

**Advances in Optical Coherence Tomography and Microscopy  
for Endoscopic Applications and Functional Neuroimaging**

by

**Aaron Dominic Aguirre**

B.S.E., Electrical Engineering, University of Michigan, Ann Arbor, 2000  
S.M., Electrical Engineering, Massachusetts Institute of Technology, 2003

Submitted to the

HARVARD-MIT DIVISION OF HEALTH SCIENCES AND TECHNOLOGY

in Partial Fulfillment of the Requirements for the Degree of

**DOCTOR OF PHILOSOPHY IN MEDICAL AND ELECTRICAL ENGINEERING**

at the

**MASSACHUSETTS INSTITUTE OF TECHNOLOGY**

June 2008

© 2008 Massachusetts Institute of Technology  
All rights reserved

Signature of Author: \_\_\_\_\_  
Harvard-MIT Division of Health Sciences and Technology  
May 15, 2008

Certified by: \_\_\_\_\_  
James G. Fujimoto, Ph.D.  
Professor of Electrical Engineering  
Thesis Supervisor

Accepted by: \_\_\_\_\_  
Martha L. Gray, Ph.D.  
Edward Hood Taplin Professor of Medical and Electrical Engineering  
Director, Harvard-MIT Division of Health Sciences and Technology



# ADVANCES IN OPTICAL COHERENCE TOMOGRAPHY AND MICROSCOPY FOR ENDOSCOPIC APPLICATIONS AND FUNCTIONAL NEUROIMAGING

Submitted to the Harvard-MIT Division of Health Sciences and Technology  
in Partial Fulfillment of the Requirements for the Degree of  
Doctor of Philosophy in Medical and Electrical Engineering

by

**Aaron Dominic Aguirre**

## ABSTRACT

Optical Coherence Tomography (OCT) is a developing medical imaging technology that generates micron resolution cross-sectional images of subsurface internal tissue structure *in situ* and in real time, without the need to remove and process specimens. Previous studies have suggested that OCT holds great potential for use in laparoscopic and endoscopic applications to detect early stage neoplastic pathologies. A minimally invasive imaging modality capable of identifying pre-malignant tissues *in vivo* could be used to guide conventional excisional biopsy and histology, thereby reducing sampling error and enabling earlier detection and treatment.

One limitation of prior endoscopic OCT imaging methods is the inability to visualize cellular features characteristic of early disease states such as neoplasia. This thesis seeks to demonstrate that advances in OCT resolution and in miniaturized imaging devices will lead to enhanced visualization of pathologic changes *in vivo* at both the tissue architectural and cellular levels. Toward this goal, three technological advances are made. First, compact and portable laser light sources for clinical ultrahigh resolution OCT are demonstrated based on supercontinuum generation in highly nonlinear optical fibers. Second, an extension of OCT called optical coherence microscopy (OCM) is developed for *in vivo* cellular imaging. High speed OCM system designs are demonstrated and characterization of OCM imaging parameters is performed. Importantly, this work demonstrates that OCM can make use of broadband laser sources to image cellular features with reduced numerical aperture compared to confocal microscopy, thereby facilitating the development of small diameter endoscopic probes. Third, two-axis scanning catheters based on micromirror technology are designed and demonstrated for ultrahigh resolution three-dimensional and *en face* OCT imaging. To demonstrate feasibility of these advances in future clinical applications, *ex vivo* imaging studies of endoscopically accessible human gastrointestinal tissues including key pathologies are performed. Results demonstrate that three-dimensional and cellular resolution optical coherence imaging can significantly improve performance over conventional OCT methods for gastrointestinal endoscopy.

Finally, this thesis also explores a new application for optical coherence tomography in neuroscience. Optical methods are currently being used to study the neurovascular response to functional activation, but most existing techniques lack depth resolution. Through correlation with video microscopy, OCT is shown to enable depth-resolved cross-sectional imaging of functional activation in the important rat somatosensory cortex model system. With further development, OCT may offer a new tool for basic and applied neuroscience research.

Thesis Supervisor: James G. Fujimoto  
Professor of Electrical Engineering and Computer Science



## Acknowledgements

It has been a true privilege to spend the past several years as a graduate student at MIT in the Division of Health Sciences and Technology (HST). I have met so many wonderful scientists, physicians, and human beings who have taken interest in my professional development and have contributed significantly to the work in this thesis.

My thesis advisor Prof. James Fujimoto has been a terrific mentor and friend. He provided me with outstanding access to intellectual and physical resources for research and unparalleled career opportunities in the emerging field of optical coherence tomography. His work ethic and careful attention to detail set a standard for excellence and rigor that has encouraged me to get the most out of my training. I would especially like to thank him for many thoughtful discussions regarding career choices and planning over the years. He was always available to impart wisdom regarding career paths, and as I transitioned during my graduate years from a PhD student to an MD-PhD student, Prof. Fujimoto provided support and encouragement while at the same time challenging me to think about the big picture of an academic career. I am grateful for his devoted interest in my development.

I would also like to thank the other members of my thesis committee, Prof. Erich Ippen from MIT and Dr. Hiroshi Mashimo from Harvard Medical School and the Boston VA Hospital. In addition to providing keen scientific insight, Prof. Ippen was a role model of true professionalism. Dr. Mashimo was an active collaborator in the endoscopy studies and provided ongoing scientific and clinical input. I also appreciate his career guidance, and I have many fond memories of the time I spent working with him at the Veterans Hospital.

Dr. James Connolly from the Beth Israel Deaconess Medical Center and Harvard Medical School was instrumental in the pathology studies performed for this thesis. In addition to clinical expertise, he made available the necessary resources to complete the studies at the surgical pathology lab. I also acknowledge the contributions of additional collaborators at the Boston VA Hospital. Dr. Qin Huang from the pathology department as well as Dr. Saleem Desai and Ms. Marisa Figuerido from the gastroenterology department were instrumental in our studies.

I am thankful to Dr. David Boas from the Massachusetts General Hospital Martinos Center and Harvard Medical School for providing the resources and mentorship to complete our studies in functional neuroimaging using OCT. I learned much from him during our collaborative projects and I appreciate the energy and enthusiasm as well as the technical expertise that he brings to his work. In addition, I acknowledge the work of Lana Ruvinskaya, who was responsible for the animal preparation during our experiments.

From the University of California, Los Angeles, I would like to acknowledge the efforts of Prof. Ming Wu, Wibool Piyawattanametha, and Dr. Li Fan in our collaboration to develop MEMS scanners for endoscopic applications. It was great working with such a competent and enthusiastic group.

From Lightlab Imaging, Inc. I acknowledge the contributions of Dr. Joseph Schmitt to our clinical endoscopic OCT studies. Dr. Schmitt is a highly-respected pioneer in optical coherence tomography imaging and provided invaluable technical insight to our group. He also made available resources from Lightlab to support our work, without which the clinical endoscopy studies could not have been accomplished.

I was fortunate to work within the Optics and Quantum Electronics Group and the Research Laboratory of Electronics at MIT. The work in this thesis would not have been possible without the resources of the Optics Group. In addition to Professors Ippen and Fujimoto, I would like to thank Prof. Franz Kaertner for his support. I also acknowledge the efforts of Ms. Cindy Kopf and Ms. Dorothy Fleischer, who served as administrative assistants to our group during my time there.

Many individuals from Prof. Fujimoto's research laboratory provided direct technical assistance as well as friendship and collegiality during this thesis work. Dr. Yu Chen was a great friend and collaborator who worked closely with me on most of the projects described in this thesis, especially our studies on ultrahigh resolution endoscopic OCT and functional brain imaging. I also acknowledge the scientific efforts of Dr. Stephane Bourquin, Dr. Ingmar Hartl, Paul Herz, Pei-Lin Hsiung, Dr. Robert Huber, Tony Ko, and Dr. Norihiko Nishizawa. In recent years, Shu-Wei Huang and Chao Zhou have brought much appreciated new energy to our projects. I was lucky to share many fun times with great officemates over the years including Drew Kowalevich, Tony Ko, Dr. Alphan Sennaroglu, Dr. Kenji Taira, Des Adler, and Tsung-Han Tsai. It was also great getting to know Josh Chung, Yu Gu, Jonathan Liu, Rohit Prasankumar, Vivek Srinivasan, Maciej Wotjkowski and all of the other great people who spent time in our group over the years.

I am indebted to the faculty, staff, and leadership of the HST program for all of the support through my doctoral and medical studies. The HST community is a rich and vibrant place to train, with endless opportunities. In particular, I want to thank Dr. Roger Mark, who was influential in my education at several points. He has been a great mentor and role model for so many HST MEMP students, and I was fortunate to work with him through the Introduction to Clinical Medicine courses and as a teaching assistant in his course. I also acknowledge Dr. Martha Gray, who served as my academic advisor as well as the co-director of HST during my tenure. I cannot forget also to thank Domingo Altarejos for help with scholarships and financial aid, Rick Mitchell and Patty Cunningham for keeping me on the right path at the medical school, and Cathy Modica for being a generally great person.

I would like to acknowledge numerous sources of external support for my graduate education including the National Defense Science and Engineering Graduate Fellowship, the Whitaker Foundation Graduate Fellowship, and the National Institutes of Health National Research Service Award (F31EB005978).

Years of hard work at MIT brought me many new friends and strengthened many of my old bonds. From MIT, I am thankful for the friendship of Joaquin Blaya, Todd Coleman, Kevin King, Jenny Mu, Alicia Quesnel, Rajiv Saigal, and Philip Sheehy. Also, my friends from Michigan remain very dear to me including Axel Berny, Brian and Sara Callaghan, Robert Casten, Garner Dewey, Sarika Gupta, Vaishalee Padgaonkar, and Seth Myers.

I am especially grateful for the support and companionship of Viviany Taqueti. It has been wonderful spending the past 5 years with her, and I look forward to great times ahead together.

My parents Nicolas and Debra Aguirre have provided and sacrificed so much so that I could have such great life opportunities, and I will always be grateful for their unwavering love and support.

Finally, I am blessed with two great brothers, Derek and Andy, who have always been my best friends. We have been lucky to work and study in Boston together for the past several years, and I am so thankful for all of their support.

# Table of Contents

<b>Abstract</b> .....	<b>3</b>
<b>Acknowledgements</b> .....	<b>5</b>
<b>Table of Contents</b> .....	<b>7</b>
<b>Chapter 1: Introduction</b>	<b>13</b>
<b>1.1 Overview</b> .....	<b>13</b>
<b>1.2 Endoscopic Surveillance for Dysplasia and Cancer in the Gastrointestinal Tract</b> .....	<b>13</b>
<b>1.3 Advanced Optical Diagnostics for Endoscopy</b> .....	<b>16</b>
1.3.1 Chromoendoscopy and Narrow Band Imaging.....	16
1.3.2 Spectroscopy Techniques for Endoscopy .....	17
1.3.3 Molecular Imaging.....	18
1.3.4 High Resolution Endoscopic Microscopy .....	18
<b>1.4 Optical Coherence Tomography</b> .....	<b>20</b>
<b>1.5 Endoscopic Optical Coherence Tomography</b> .....	<b>23</b>
<b>1.6 Statement of Work</b> .....	<b>24</b>
<b>1.7 References</b> .....	<b>26</b>
<b>Chapter 2: Ultrahigh Resolution Endoscopic OCT</b>	<b>35</b>
<b>2.1 Overview</b> .....	<b>35</b>
<b>2.2 Clinical Ultrahigh-Resolution Endoscopic OCT System Design</b> .....	<b>36</b>
<b>2.3 Endoscopic OCT Imaging Protocol and Study Parameters</b> .....	<b>41</b>
<b>2.4 Imaging Results</b> .....	<b>42</b>
2.4.1 OCT Imaging of Barrett’s Esophagus and Esophageal Adenocarcinoma .....	45
2.4.2 OCT Imaging of Gastric Polyps .....	48
<b>2.5 Discussion of Results</b> .....	<b>50</b>
<b>2.6 Prospects for Further Advances in Technology</b> .....	<b>53</b>

2.7	References .....	56
<b>Chapter 3: Supercontinuum Light Sources for Ultrahigh Resolution Optical Coherence Tomography</b>		<b>59</b>
3.1	Overview .....	59
3.2	Introduction .....	59
3.3	SESAM-Modelocked Nd:Glass Femtosecond Oscillator .....	62
3.4	<b>Broadband Continuum Generation at 1060 nm with an Ultrahigh Numerical Aperture Fiber .....</b>	<b>62</b>
3.4.1	Numerical Simulations .....	64
3.4.2	Experimental Measurements of the Continuum .....	65
3.4.3	OCT Imaging Results and Discussion .....	68
3.5	<b>Broadband Continuum Generation at 800 nm and 1300 nm with a Novel Photonic Crystal Fiber .....</b>	<b>70</b>
3.5.1	Numerical Simulations .....	71
3.5.2	Experimental Measurements of the Continuum .....	74
3.5.3	OCT Imaging Results and Discussion .....	77
3.6	Summary .....	82
3.7	References .....	83
<b>Chapter 4: Optical Coherence Microscopy</b>		<b>87</b>
4.1	Introduction .....	87
4.2	Confocal Microscopy .....	88
4.3	<b>High Transverse Resolution in Optical Coherence Tomography .....</b>	<b>90</b>
4.3.1	Depth Priority Techniques .....	91
4.3.2	Transverse Priority and <i>En Face</i> Imaging .....	93
4.3.3	<i>En Face</i> Imaging in the Time and Fourier Domain .....	94
4.4	Heterodyne Signal Detection in OCM .....	96
4.5	Advantages of OCM .....	99
4.6	Technology for OCM .....	104
4.6.1	Broadband Light Sources .....	105
4.6.2	Modulation Schemes .....	106

4.6.3	Microscope Scanner Designs .....	109
4.6.4	Controlling the Overlap of Coherence and Confocal Gating .....	112
4.6.5	Combination Microscopy Techniques .....	114
<b>4.7</b>	<b>Cellular Imaging Applications of OCM .....</b>	<b>114</b>
<b>4.8</b>	<b>Summary and Future Prospects .....</b>	<b>119</b>
<b>4.9</b>	<b>References .....</b>	<b>121</b>
 <b>Chapter 5: High Speed, Broadband OCM System for <i>In Vivo</i> Imaging</b>		<b>129</b>
<b>5.1</b>	<b>Overview .....</b>	<b>129</b>
<b>5.2</b>	<b>Introduction .....</b>	<b>129</b>
<b>5.3</b>	<b>System Design .....</b>	<b>131</b>
5.3.1	OCM Imaging Engine .....	131
5.3.2	Dispersion Compensation .....	137
5.3.3	Wavelength Dependent Source Polarization .....	142
5.3.4	Performance Characterization .....	149
<b>5.4</b>	<b>Image Autofocusing .....</b>	<b>151</b>
<b>5.5</b>	<b>Image Processing and Display .....</b>	<b>154</b>
<b>5.6</b>	<b><i>In Vivo</i> Cellular Imaging Results .....</b>	<b>158</b>
<b>5.7</b>	<b>Integrated OCM and OCM Clinical Imaging System .....</b>	<b>160</b>
<b>5.8</b>	<b>Conclusion .....</b>	<b>163</b>
<b>5.9</b>	<b>References .....</b>	<b>164</b>
 <b>Chapter 6: <i>In Vitro</i> Architectural and Cellular Imaging of Gastrointestinal Tissues with Ultrahigh Resolution OCT and OCM</b>		<b>167</b>
<b>6.1</b>	<b>Overview .....</b>	<b>167</b>
<b>6.2</b>	<b>Introduction .....</b>	<b>167</b>
<b>6.3</b>	<b>Methods .....</b>	<b>170</b>
6.3.1	Imaging System .....	170
6.3.2	Study Design and Imaging Protocol .....	171
6.3.3	Data Analysis .....	173
<b>6.4</b>	<b>Imaging Results .....</b>	<b>174</b>

6.4.1	Upper Gastrointestinal Tract .....	174
6.4.2	Lower Gastrointestinal Tract .....	177
6.4.3	Pancreas .....	179
6.4.4	Measurement of Focusing Properties Below the Tissue Surface .....	179
<b>6.5</b>	<b>Discussion .....</b>	<b>180</b>
<b>6.6</b>	<b>Images .....</b>	<b>186</b>
<b>6.7</b>	<b>References .....</b>	<b>209</b>
 <b>Chapter 7: Three-Dimensional Projection OCT Imaging of Gastrointestinal Tissues</b>		<b>213</b>
<b>7.1</b>	<b>Overview and Introduction .....</b>	<b>213</b>
<b>7.2</b>	<b>Methods .....</b>	<b>214</b>
<b>7.3</b>	<b>Results .....</b>	<b>215</b>
<b>7.4</b>	<b>Discussion .....</b>	<b>220</b>
<b>7.5</b>	<b>References .....</b>	<b>222</b>
 <b>Chapter 8: Two-axis MEMS Scanning Catheter for Ultrahigh Resolution Three-Dimensional and En Face Imaging</b>		<b>223</b>
<b>8.1</b>	<b>Overview .....</b>	<b>223</b>
<b>8.2</b>	<b>Introduction .....</b>	<b>223</b>
<b>8.3</b>	<b>Catheter Design and Characterization .....</b>	<b>224</b>
<b>8.4</b>	<b>Two and Three-dimensional Imaging Results .....</b>	<b>228</b>
<b>8.5</b>	<b>Discussion .....</b>	<b>230</b>
<b>8.6</b>	<b>References .....</b>	<b>232</b>
 <b>Chapter 9: Depth-Resolved Imaging of Functional Activation in the Rat Cerebral Cortex Using Optical Coherence Tomography</b>		<b>235</b>
<b>9.1</b>	<b>Overview .....</b>	<b>235</b>
<b>9.2</b>	<b>Introduction .....</b>	<b>235</b>
<b>9.3</b>	<b>Methods .....</b>	<b>236</b>

<b>9.4</b>	<b>Results .....</b>	<b>238</b>
<b>9.5</b>	<b>Discussion .....</b>	<b>240</b>
<b>9.6</b>	<b>References .....</b>	<b>242</b>
<b>Chapter 10: Summary and Conclusions</b>		<b>243</b>
<b>10.1</b>	<b>Summary of Work .....</b>	<b>243</b>
<b>10.2</b>	<b>Future Studies .....</b>	<b>245</b>
<b>10.3</b>	<b>Conclusions.....</b>	<b>248</b>
<b>10.4</b>	<b>References.....</b>	<b>250</b>



# Chapter 1

## Introduction

### 1.1 Overview

Excisional biopsy and histology are the time-tested gold standards for disease assessment at the tissue architectural and cellular levels, and they continue to have substantial impact on the diagnosis, staging, and management of most neoplasms. Biopsy and histology, however, are often subject to high false negative rates due to sampling errors and can pose risks to the patient, such as bleeding and infection, which also limit the ability for screening of large areas. Optical imaging technology that provides real-time, high-resolution screening of vulnerable areas with resolution at or near that of histopathology could significantly improve clinicians' capabilities to identify malignancies at curable stages [1]. The ability to assess histologic hallmarks of cancer at the tissue architectural and cellular levels, including alterations in glandular or stromal morphology, presence of abnormal mitoses and increased nuclear-to-cytoplasm ratio, without the need for tissue excision, would be a major advance in cancer diagnostics. The widespread clinical utility of such a technology, however, depends on compatibility with conventional laparoscopes and endoscopes for surgical and internal body imaging. This thesis explores new techniques for endoscopic and laparoscopic imaging that dramatically enhance the resolution and visualization capabilities of conventional optical coherence tomography (OCT) imaging for endoscopic "optical biopsy." Specifically, this work develops technology to enable ultrahigh resolution and three-dimensional endoscopic OCT imaging and cellular resolution endoscopic optical coherence microscopy (OCM). Imaging studies are performed to assess feasibility of these methods for potential future clinical applications in gastrointestinal endoscopy.

### 1.2 Endoscopic Surveillance for Dysplasia and Cancer in the Gastrointestinal Tract

Cancers of the esophagus and colon are significant sources of morbidity and mortality among malignancies. Esophageal cancer is highly lethal, with a five-year survival rate of only 16%. In 2007, approximately 15,560 new cases and 13,940 deaths were expected from cancer of the esophagus alone [2]. Colorectal cancer is among the most common forms of cancer, with approximately 155,000 new cases of colon and rectum cancer expected in 2007. It is also the third leading cause of cancer death, accounting for over 52,000 deaths in 2007, or about 10 percent of all cancer deaths [2]. Although deadly

if detected in late stages, the majority of carcinomas of the esophagus and colon are luminal in nature and have precancerous stages of progression, which makes them highly amenable to early endoscopic detection and treatment.

More than 50% of esophageal malignancies are adenocarcinomas, and the incidence of adenocarcinoma in the United States has increased significantly in the last 40 years [3-5]. The majority of esophageal adenocarcinomas are believed to develop from a precursor condition known as Barrett's esophagus. In Barrett's esophagus, a region of esophageal mucosa subject to chronic injury from gastroesophageal reflux (GERD) undergoes a metaplastic transition from normal squamous epithelium to a specialized columnar form bearing similarities to intestinal epithelium and defined by the presence of goblet cells [6]. Current diagnosis of Barrett's esophagus requires the presence of endoscopically identifiable, salmon-pink columnar mucosa extending into the tubular esophagus from the gastroesophageal junction. In addition, it requires the histologic presence of specialized intestinal metaplasia (SIM) on biopsy. Barrett's esophagus occurs in approximately 10-12% of patients with symptomatic GERD undergoing endoscopy [7].

SIM can progress through stages of low grade and high grade dysplasia characterized by cytologic and architectural disarray before transformation to adenocarcinoma. Dysplastic tissue architecture may show villiform or papillary change with crowded, irregular glands, while cellular changes are marked by decrease in mucin production, nuclear hyperchromasia and pleomorphism, increased mitotic rate with abnormal mitoses, and nuclear stratification [8]. The prevalence of dysplasia in Barrett's has been estimated between 5 and 20% [9, 10] with high-grade dysplasia associated with a 10-60% risk of developing adenocarcinoma in 3-5 years [10-12]. Endoscopic surveillance for dysplasia in patients with Barrett's esophagus results in detection of tumors at earlier stages, which in turn improves 5-year survival rates compared to non-surveillance groups [13].

Dysplasia in the esophagus is not often visible grossly and can involve a variable region of mucosa with patchy and focal distribution [14]. Current clinical surveillance protocol for dysplasia and cancer of the esophagus therefore involves thorough sampling of the endoscopically identifiable Barrett's mucosa with serial four-quadrant jumbo biopsies taken at 1-2 cm intervals [8]. Nonetheless, the prevalence of undetected adenocarcinoma from such biopsy protocols has been estimated as high as 57% [15-18]. Imaging techniques capable of identifying dysplasia and cancer *in vivo* and guiding biopsy in real time could significantly reduce sampling error and improve diagnostic yield of biopsy over standard endoscopic surveillance protocols.

Similar to esophageal adenocarcinomas, most colorectal adenocarcinomas progress through stages of dysplasia occurring in polypoid lesions [19]. Epithelial polyps are generally classified into hyperplastic, inflammatory, hamartomatous, and neoplastic, with as many as 95% of polyps belonging to the

hyperplastic and neoplastic categories [8]. Hyperplastic polyps are small (typically < 5 mm) benign lesions, while neoplastic polyps include both pre-malignant and malignant forms. Among neoplastic polyps, adenomas are the most common. Adenomas are generally asymptomatic but have varying degrees of premalignant potential depending on the size and histologic subtype. Adenomas larger than 2 cm have a 10-20% risk of carcinoma at the time of removal while those less than 1 cm have < 1% risk of harboring cancer [8, 20]. Among histologic subtypes, the degree of villous compared to tubular architecture increases the risk of adenocarcinoma [8]. By age 50, approximately 12% of individuals have adenomas, and 25% of these lesions are high risk lesions [21].

While most polypoid adenomas can be detected with standard endoscopy, many non-polypoid, flat adenomas are not readily detectable endoscopically. These lesions may have slightly raised edges or a central depression and can be difficult to distinguish from surrounding normal mucosa [8]. Importantly, some studies have suggested an increased prevalence of high-grade dysplasia and adenocarcinoma in these lesions compared to conventional adenomas [22]. This is particularly relevant in inflammatory bowel conditions such as ulcerative colitis (UC) and Crohn's disease, where neoplastic tissue is often flat rather than polypoid in form and multifocal in distribution [23]. Macroscopic heterogeneity of dysplastic and malignant lesions in the setting of gross inflammatory abnormalities makes endoscopic detection extremely challenging.

Individuals with inflammatory bowel disease, either ulcerative colitis or Crohn's disease, are at increased risk for the development of colorectal cancer (CRC). Prevalence of CRC in patients with ulcerative colitis has been estimated by meta analysis to be 3.7% overall and 5.4% in patients with pancolitis [24]. Increased risk for cancer in UC is associated with duration of the disease, degree of colonic involvement, the presence of primary sclerosing cholangitis, and the presence of severe chronic active inflammation. Studies suggest a 5% incidence of dysplasia after 10 years and a 25% incidence after 20 years, and a commonly cited rule states that the risk of cancer increases by 1%-2% per year after 10 years of disease. Although it was previously held that individuals with Crohn's disease had lower risk of colon cancer compared to those with ulcerative colitis, more recent investigations suggest that those with anatomically extensive Crohn's colitis have similar risk [23].

Standard of care in ulcerative colitis includes initial screening colonoscopy at 7-8 years from onset of disease or immediately in patients with primary sclerosing cholangitis. Practice guidelines dictate that 2-4 biopsy specimens be taken from every 10 cm of diseased bowel in addition to macroscopically atypical lesions, with the goal of taking > 30 biopsies [23]. If no dysplasia is found, patients with extensive colitis should have repeat exams in 1-2 years. Dysplasia in a discrete polyp can be resected endoscopically as long as no flat dysplasia exists immediately adjacent to the polyp or elsewhere in the colon. Presence of low grade dysplasia in flat mucosa warrants consideration of colectomy or increased frequency of

surveillance to 3-6 months. However, patients with flat high grade dysplasia or adenocarcinoma should have confirmed pathology by 2 expert pathologists followed by colectomy.

Image guided biopsy promises to reduce sampling error and improve diagnostic sensitivity in the endoscopic detection of flat dysplastic lesions in patients with long-term inflammatory bowel diseases. Developments in endoscopic mucosal resection (EMR) as a minimally invasive technique for treating early-stage gastrointestinal cancers has also lead to a demand for improved endoscopic imaging for accurate staging of the depth of tumor invasion [25].

### **1.3 Advanced Optical Diagnostics for Endoscopy**

White-light endoscopy with excisional pinch biopsy and histopathology continues to be the primary method to screen for and diagnose early stage neoplasms of the gastrointestinal tract. In current standard practice, video endoscopy is limited to low-resolution visualization of superficial mucosa over large areas, and has been described as simply an extended form of physical diagnosis [26]. White light endoscopy has typical transverse resolution of  $\sim 100$   $\mu\text{m}$  over a field of view of 100 mm and produces *en face* images without depth resolving capability [27]. Endoscopic ultrasound (EUS) has emerged as a widely available and useful cross-sectional subsurface imaging approach for staging of GI malignancies [28]. EUS can perform structural and Doppler imaging with typical structural image resolution in the range of 100 – 200  $\mu\text{m}$  and sufficient depth of image penetration to visualize submucosal tumor invasion [29, 30]. The resolution of EUS is insufficient for the visualization of fine tissue microstructure necessary to detect dysplasia, however. The inability to have direct view through the endoscope of subsurface tissue architectural and cellular features, without excisional biopsy, contributes to unacceptable false negative biopsy rates in endoscopic surveillance for dysplasia and cancer.

#### **1.3.1 Chromoendoscopy and Narrow Band Imaging**

Over the past two decades, advanced optical diagnostic techniques have emerged to address the limitations of standard clinical endoscopic methods. Chromoendoscopy refers to the use of topically applied tissue stains in conjunction with white light endoscopy. Stains utilized include Lugol's solution, methylene blue, acetic acid, and indigo carmine. Methylene blue chromoendoscopy has been shown to enhance diagnostic yields for high grade dysplasia in Barrett's esophagus [31-33]. Topical stains can also be used in conjunction with magnification endoscopes to provide improved resolution as well as contrast. Magnification endoscopes combined with high-pixel density charge-coupled devices (CCD's) have been developed with between 1.5 and 150 times magnification [34, 35]. Magnification chromoendoscopy using methylene blue was shown in a prospective randomized controlled trial to allow diagnosis of significantly more flat adenomas and small intraepithelial neoplasias compared to standard endoscopy,

thereby enabling increased diagnostic yield using chromoendoscopy targeted biopsies over random biopsy [36]. Subsequent studies confirmed these results [37, 38] leading to a new set of recommendations endorsing the use of chromoendoscopy-guided biopsy in ulcerative colitis patients [39].

Narrow band imaging (NBI) is an alternative technique to chromoendoscopy which utilizes narrow-bandwidth filters applied to standard white light endoscopy to differentially enhance contrast between capillaries and the surrounding mucosa [40]. NBI has been investigated for dysplasia and cancer in both the upper and lower gastrointestinal tracts [41, 42]. A recent comparative study in diagnosis of colorectal neoplasia demonstrated that both NBI and magnification chromoendoscopy were significantly better than conventional endoscopy but there was no significant difference between NBI and magnification chromoendoscopy [43]. NBI has the advantage over chromoendoscopy of not requiring exogenous dyes nor magnification technology and can be readily adapted to conventional endoscopes through the use of illumination filters. In addition, the ability to assess vasculature provided by NBI may prove useful in tumor staging [44].

### **1.3.2 Spectroscopy Techniques for Endoscopy**

Various spectroscopy techniques under investigation infer information about the biochemical state of tissue. Point-probe spectroscopy systems analyze a single location in the tissue utilizing non-imaging fiber-optic probes combined with spectral analysis. Elastic light scattering has been analyzed using diffuse reflectance spectroscopy [45], elastic scattering spectroscopy [46], and light scattering spectroscopy [47, 48]. These techniques have shown considerable promise in the gastrointestinal tract for detection of dysplasia and early cancers [49-54]. A recently developed light scattering spectroscopy method called four-dimensional elastic light scattering fingerprints (4D-ELF) enables simultaneous measurement of spectral, wavelength, azimuthal, and polarization dependence of scattered light [55]. This method was shown in a rat model to detect changes in mucosal blood content in the colonic microvasculature at the earliest stages of carcinogenesis, suggesting a novel biomarker for screening for early colon cancer [56]. Light scattering spectroscopy methods have also been extended to imaging geometries [57].

Raman spectroscopy is a point-probe technique which probes specific vibrational energy states of molecules such as proteins, lipids, and nucleic acids as revealed by characteristic features in the weak Raman scattering spectrum returning from tissue. In a preliminary study, Raman spectroscopy has been shown to have promise for early cancer detection in Barrett's esophagus [58].

Fluorescence spectroscopy analyzes fluorescence from either endogenous sources or exogenously applied molecules. Using endogenous autofluorescence, sensitivity of 100% and specificity of 97% were demonstrated for differentiating high grade from low grade and non-dysplastic Barrett's mucosa in a

small patient population [51]. Moreover, in this same study, a combination of autofluorescence with light scattering and diffuse reflectance spectroscopies in a multi-modal approach yielded even higher sensitivity and specificity, both 100%, suggesting an advantage to the combined approach [51].

While point probe spectroscopies offer biochemical information about the specimen, they sample a severely restricted volume and lack structural information about tissue architecture. Hence, it is desirable to implement spectroscopic imaging modalities that can be applied over larger areas for screening and can be combined with structural imaging techniques, including conventional white-light endoscopy. Wide-field autofluorescence imaging has been implemented by several groups with application in both the upper and lower GI tracts [59-63]. Results suggest improvement in detection of high grade dysplasia and early cancer using fiber-optic and video autofluorescence imaging combined with white light endoscopy [62, 63]. Exogenous contrast enhancing agents can be utilized with fluorescence imaging systems as an alternative to autofluorescence imaging. 5-aminolaevulinic acid (5-ALA) has been used in the gastrointestinal tract to augment fluorescence imaging and has shown promise in the detection of early neoplasia in both Barrett's esophagus and ulcerative colitis [64, 65].

### **1.3.3 Molecular Imaging**

With rapid advances in molecular oncology, recent research in fluorescence imaging, as well as in other non-optical imaging modalities, has led to the development of molecularly specific contrast agents which preferentially target tumor versus normal tissue [66, 67]. Targets for molecular imaging include cell-surface receptors, tyrosine kinases, apoptosis markers, proliferation markers, proteolytic enzymes, extracellular matrix targets, and glucose metabolism levels [68]. Increased protease expression in neoplastic colon polyps using a near-infrared enzyme sensing probe was demonstrated in a mouse model [69] and catheter-based systems have been developed for *in vivo* imaging use [70]. Imaging studies in mouse models suggest great promise for *in vivo* detection of colonic adenocarcinomas [71, 72]. In addition to near-infrared enzyme-activatable probes, fluorescein conjugated probes in the visible wavelength region have been developed [73, 74]. Using phage display peptide libraries screened against human colonic adenomas, Hsiung et al. discovered novel high-affinity ligands with preferential binding to dysplastic colonocytes [74].

### **1.3.4 High Resolution Endoscopic Microscopy**

Endoscopic fluorescence imaging has been extended to the cellular level with the development of methods for fiber-optic scanning confocal fluorescence endomicroscopy [75-78]. Confocal microscopy is capable of producing depth-resolved images of cellular features in human tissue with optical resolutions of  $\sim 1\text{-}3\ \mu\text{m}$ , similar to those of histopathology. Systems operate using the principle of confocal gating in

which light from a point source is imaged to a pinhole point detector. Light from outside the focal plane of interest is defocused at the detector and partially rejected thereby providing a means of preferentially selecting light returning from the sample at a specified depth. In the case of flexible fiber-optic confocal microscopes, the optical fiber serves as both the illumination and detection pinhole. Images are generated by scanning the optical focus in tissue over a specified field of view. Two approaches for tissue scanning have been used in clinical endoscopy. The optical beam can be scanned at the proximal end of the endoscope through a fiber optic coherent imaging bundle, which is inserted as a miniaturized probe through the accessory port of the endoscope [79]. Alternatively, scanning can be performed at the distal end of the endoscope with a miniaturized fiber scanner incorporated into the head of a specialized endoscope [78, 80]. Contrast enhancement is provided by exogenous contrast agents such as fluorescein, acriflavin, tetracycline, or cresyl violet [80]. The most commonly used agents are topically applied acriflavin hydrochloride, which stains superficial epithelial cells and nuclei, and intravenous fluorescein, which distributes throughout the mucosa and strongly labels the connective tissue and capillary network.

Promising results for the detection of early neoplasia in the upper and lower gastrointestinal tracts have been demonstrated with confocal fluorescence endomicroscopy. Using fluorescein contrast for *in vivo* confocal endomicroscopy, detection of intraepithelial neoplasia and cancer in the colon was possible with sensitivity of 97.4%, specificity of 99.4%, and accuracy of 99.2% [81]. Subsequent work combined confocal endomicroscopy with chromoscopy guidance to demonstrate its potential role in ulcerative colitis [82]. A prospective randomized study was performed comparing conventional random biopsy protocol with methylene blue chromoscopy-guided targeted biopsy. In the investigational group, pan-staining of the colon with methylene blue was used to identify suspicious lesions, followed by confocal imaging and biopsy. Compared to the random biopsy group, 4.75 more neoplasias could be detected with 50% fewer biopsies. Additional studies have shown that confocal fluorescence endomicroscopy can be used to quantitatively assess physiologic properties of colonic neoplasia [83] and that gastroenterologists can interpret confocal fluorescence images of gastrointestinal neoplasia with high accuracy [84]. In the upper gastrointestinal tract, fluorescein-guided endomicroscopy was capable of predicting the presence of Barrett's esophagus with a sensitivity of 98.1%, specificity of 94.1%, and accuracy of 96.8%. Furthermore, Barrett's-associated neoplastic changes were predicted with a sensitivity of 92.9% and a specificity of 98.4% [85].

Confocal fluorescence endomicroscopy produces excellent images of surface stained tissues, but has several limitations. The method relies on the use of intravenous and topically applied stains, each of which has potential toxicity and has not yet been widely accepted for use in this application. In addition, the current confocal technology provides limited penetration depth and field of view. Fluorescence confocal microscopy is limited to  $< \sim 100$   $\mu\text{m}$  in penetration depth and therefore cannot accurately assess

the basement membrane for invasion of malignant cells into the underlying supportive tissues. The depth of penetration is a fundamental limit related to the ability to optically section the tissue to isolate a single layer of cells for visualization. The field of view concern in confocal microscopy relates to the need for high magnification in order to provide high resolution and thin optical tissue sections. In the case of large mucosal lesions, the field of view limitation with confocal microscopy leads to sampling error within a lesion, which effectively limits the ability to target biopsies.

Alternative microscopy techniques are being developed which address these limitations. Confocal reflectance microscopy can be performed without exogenous tissue stains using the intrinsic contrast provided by differences in scattering properties of tissue microstructure. High quality *in vivo* cellular imaging of unstained tissues in human skin has been demonstrated with reflectance confocal microscopy [86, 87]. Using near-infrared wavelengths to perform reflectance confocal microscopy, imaging depths up to 350  $\mu\text{m}$  have been achieved [87], and normal and neoplastic conditions in the skin have been extensively studied [88-90]. Confocal reflectance microscopy has also been studied for imaging of the upper and lower gastrointestinal tracts, with results indicating the ability to visualize features of neoplastic tissue in the esophagus and colon [91-93].

Multiphoton microscopy (MPM) is another technique which can provide cellular resolution images without exogenous contrast agents [94, 95]. Multiphoton microscopy uses nonlinear excitation from short pulsed laser sources to excite fluorescence, and contrast can be generated either from applied dyes or from the intrinsic fluorescence properties of molecular constituents of tissue such as amino acids and vitamin derivatives [95, 96]. MPM uses near-infrared light to excite either two or three photon absorption and detects fluorescence in the visible wavelength range. Multiphoton imaging systems are also capable of detecting signal from second and third harmonic generation in tissue from such elements as collagen, which further enhances the image information and contrast. Multiphoton endoscopy is being investigated by several groups [97] and *ex vivo* investigations suggest superiority to confocal fluorescence microscopy in terms of both image contrast and imaging depth [98].

#### **1.4 Optical Coherence Tomography**

In the past decade, optical coherence tomography (OCT) has emerged as a promising modality for real time, high-resolution cross-sectional imaging of tissue microstructure without the need for tissue staining [99-101]. OCT is analogous to B-mode ultrasound, except it measures echo reflections of light rather than sound from tissue structures. Backscattered light reflections in tissue cannot be measured directly using electronic detectors, so OCT uses a device called a Michelson interferometer to measure echoes by low coherence interferometry.

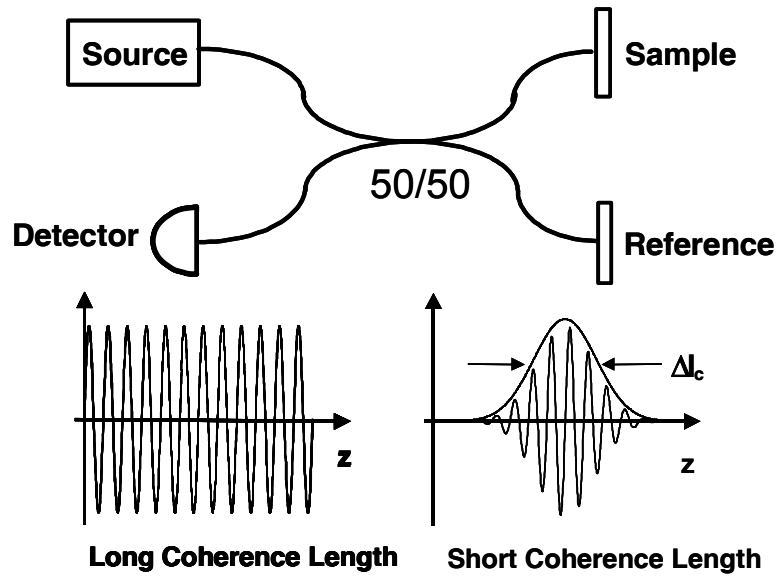


**Figure 1.1.** Optical Coherence Tomography (OCT) generates images by measuring the echo time delay of light using a fiber optical Michelson interferometer with a low coherence light source.

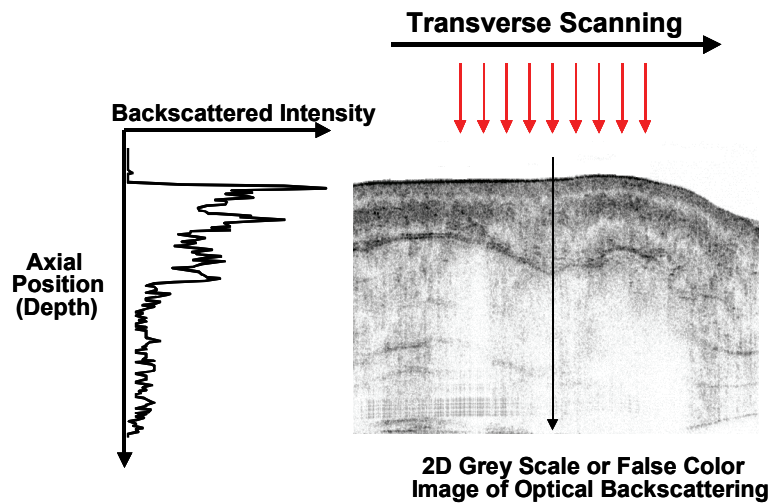


**Figure 1.2.** OCT cross-sectional images are generated by scanning a beam across tissue and measuring the backscattering intensity as a function of depth. A grey scale or false-color image can then be displayed.

Figure 1.1 illustrates the basic OCT system and principle. Light from a source is split by a fiber-optic coupler into a reference beam and a sample probe beam. Reflections from the tissue sample are recombined with a reference reflection at a detector to produce a characteristic interference signal. Depth resolution can be achieved using a light source with a broad spectral bandwidth, or short coherence length. Compared to monochromatic or long coherence length light, broadband light produces interference only when the path traveled by reference and sample beams match. The depth resolution in OCT is inversely related to the light source bandwidth. Standard resolution OCT has depth resolutions of 10-15  $\mu\text{m}$ , but ultrahigh axial resolutions of 1-2  $\mu\text{m}$  can be achieved using state of the art broadband laser technologies [102]. Figure 1.2 describes image generation in OCT. A depth profile at a fixed location in tissue can be generated by scanning the reference path with respect to the sample and plotting the backscattered intensity as a function of depth. Two dimensional cross-sectional images are then formed by scanning the beam on the sample.

The interferometric detection technique used in OCT is similar to heterodyne optical detection methods used in optical communications, which can achieve high sensitivities to weak signals in excess of -100 dB. This corresponds to measured optical reflections from tissue of 1 part in  $10^{10}$  and allows imaging to depths of 2-3 mm despite optical attenuation and scattering in tissue. This depth is shallow compared to conventional ultrasound or MRI, but the image resolution is 10x to 100x greater than these methods. Furthermore, the imaging depth is significantly greater than that of other high resolution optical methods including confocal microscopy and multiphoton microscopy. OCT also offers typical field of view of 3-5 mm in the transverse dimension, which is greater than other endoscopic microscopy techniques. Recent developments in Fourier-domain optical coherence tomography have demonstrated a large sensitivity advantage and dramatically increased imaging speeds compared to conventional time-domain OCT by using novel spectrometer-based detection or wavelength swept laser sources [103-109]. Using these approaches, OCT will be capable of rapidly imaging over large fields of view on the order of several centimeters [110, 111].

OCT is fiber optic based and can be integrated with a variety of delivery systems such as microscopes, handheld probes, endoscopes, catheters, and needles to enable minimally invasive internal body imaging [112, 113]. Inside the body at the site of interest, OCT image depth is similar to or greater than the typical sampling depth of excisional biopsy and is sufficient for evaluation of early neoplastic changes occurring in epithelial tissues. OCT imaging is currently being investigated for many clinical applications, including ophthalmology [114-118], cardiology [119-123], gastroenterology [124-126], urology [127-129], and dermatology [130-132]. In ophthalmology, the technology has been available commercially since 1996 and is rapidly becoming a standard of care.

## 1.5 Endoscopic Optical Coherence Tomography

The first demonstration of *in vivo* endoscopic OCT was done by Tearney et al. in 1997 using a 1 mm fiber optic catheter to image the GI and pulmonary tracts of the rabbit [133]. Sergeev et al. performed the first studies in humans, showing that all layers of the esophageal wall can be identified and that disruption of the well-defined stratified mucosa is observed in cancerous lesions [134]. Real time OCT imaging of the human GI tract was subsequently shown by Bouma et al. [135] and Sivak et al. [136]. In a study of 32 patients, Bouma et al. showed differentiation of Barrett's esophagus from normal esophageal mucosa and adenocarcinoma from normal and Barrett's [137]. Jackle et al. described OCT clinical studies of normal gastrointestinal tract tissues as well as colonic adenoma and carcinoma, finding distinct patterns of normal, inflammatory, premalignant, and malignant tissues in OCT images. [138, 139]. Zuccaro et al. reported OCT images of esophagus and stomach in 69 patients with distinct appearance of squamous mucosa, gastric cardia, Barrett's esophagus, and carcinoma [140]. OCT has been shown to detect specialized intestinal metaplasia in Barrett's esophagus patients with 97% sensitivity and 92% specificity [141]. More recently, Pfau et al. have suggested that OCT has potential to distinguish hyperplastic from adenomatous polyps in the colon [142]. These studies demonstrate that OCT imaging can be readily integrated with endoscopic procedures and provide useful diagnostic information.

Studies looking at the detection of dysplasia in Barrett's esophagus using OCT are emerging. In a prospective, double-blinded study, Isenberg and colleagues demonstrated sensitivity and specificity of 68% and 82%, respectively, for detection of dysplasia [143]. A second study by Evans et al., has reported sensitivity of 83% and specificity of 75% for the classification of high grade dysplasia [126]. While promising, these results do not yet establish a role for OCT in endoscopic surveillance for dysplasia [144]. Further developments in technology, and specifically improvements in resolution, will be important for further advances in this application.

In contrast to confocal microscopy, efforts to achieve cellular resolution imaging with OCT have been hindered by the limited axial and transverse resolutions of standard systems, typically in the range of 15-25  $\mu\text{m}$ . Axial resolution can be improved through the use of light sources with greater optical bandwidth. Li et al. performed ultrahigh resolution OCT imaging of Barrett's esophagus *ex vivo* using a femtosecond laser system capable of 1-2  $\mu\text{m}$  axial resolution [145]. Subsequently a portable ultrahigh resolution endoscopic OCT system was developed and demonstrated for *in vivo* imaging of the rabbit esophagus and colon with less than 5  $\mu\text{m}$  axial resolution [146]. Ultrahigh resolution endoscopic OCT is a promising advance that should enable improved visualization of fine tissue structure compared to conventional OCT. Compared to axial resolution, transverse resolution in OCT is more fundamentally limited. Cross-sectional OCT operates by fixing the focus at a specific depth in tissue and then scanning the coherence gate in the axial direction to generate an image. In order to maintain a sufficient depth of field over the

extent of the image, OCT must operate with weaker focusing and lower transverse resolution. Development of a technique to overcome the limited transverse resolution to enable cellular resolution endoscopic OCT would be a powerful advance for imaging of dysplasia and cancer.

## 1.6 Statement of Work

The aims of this thesis work were as follows. 1) To investigate *in vivo* ultrahigh resolution endoscopic OCT imaging in the human gastrointestinal tract through collaborative studies with physician investigators. 2) To develop reliable, portable light sources for *in vivo* ultrahigh resolution OCT imaging that are both widely available and highly suitable for clinical imaging studies. 3) To develop an extension of OCT called optical coherence microscopy (OCM) for cellular resolution imaging of unstained tissues. OCM images in the *en face* plane and combines confocal microscopy with OCT to provide 1-3  $\mu\text{m}$  resolution in three dimensions, thereby enabling visualization of cellular and subcellular morphology. OCM also can make use of ultrahigh OCT depth resolutions to image without the need for high numerical apertures required in confocal microscopy, thereby facilitating the development of small diameter endoscopic probes. 4) To investigate and compare the ability of ultrahigh resolution OCT and OCM to visualize architectural and cellular features characteristic of normal and pathologic conditions of the human gastrointestinal tract. 5) To develop and demonstrate miniaturized flexible endoscopes for OCT and OCM imaging based on micro-electro-mechanical systems (MEMS) scanning technology.

The written thesis is organized according to these aims. Chapter 2 presents a summary of imaging results using ultrahigh resolution OCT for imaging of the upper gastrointestinal tract. New light sources for ultrahigh resolution OCT are then discussed in Chapter 3. Compact and portable sources based on supercontinuum generation are demonstrated to be highly stable and well-suited for clinical use. Chapter 4 reviews background work on optical coherence microscopy and discusses key advantages of the technique and technical challenges for its implementation. Chapter 5 then details the design and demonstration of an OCM imaging system which addresses these challenges and enables high speed *in vivo* imaging. Chapter 5 also describes an integrated OCT and OCM imaging configuration which is capable of generating two and three dimensional image data over multiple fields of view. Chapter 6 focuses on an *ex vivo* feasibility imaging study designed to assess potential applications for optical coherence microscopy imaging in the gastrointestinal tract. The results of this study provide motivation toward the development of endoscopic OCM and the design of further studies to assess the accuracy of the technique for detecting dysplasia and cancer. Chapter 7 discusses the application of three-dimensional OCT imaging in endoscopy, with a focus on projection-based visualizations. Chapter 8 follows by describing the development of miniaturized two-axis catheter endoscope probes that can

implement arbitrary scan patterns for *en face* and three dimensional OCT. Such devices are critical to enable endoscopic three dimensional and cellular resolution imaging.

Chapter 9 departs from the focus on endoscopy to describe work conducted on a newly emerging area of application for OCT imaging – functional neuroimaging. Through *in vivo* animal studies in the important rat cortex model, OCT is demonstrated as a novel means for depth-resolved imaging of the functional neurovascular response. The results presented suggest that OCT has potential to add to a host of evolving optical tools available to the neuroscience researcher.

Chapter 10 concludes the thesis by providing a brief summary of results as well as perspectives for future studies.

## 1.7 References

- [1] F. Koenig, J. Knittel, and H. Stepp, "Diagnosing cancer in vivo," *Science*, vol. 292, pp. 1401-+, 2001.
- [2] A. Jemal, R. Siegel, E. Ward, T. Murray, J. Xu, and M. J. Thun, "Cancer statistics, 2007," *CA Cancer J Clin*, vol. 57, pp. 43-66, 2007.
- [3] X. Chen and C. S. Yang, "Esophageal adenocarcinoma: a review and perspectives on the mechanism of carcinogenesis and chemoprevention," *Carcinogenesis*, vol. 22, pp. 1119-29, 2001.
- [4] J. T. Chang and D. A. Katzka, "Gastroesophageal reflux disease, Barrett esophagus, and esophageal adenocarcinoma," *Arch Intern Med*, vol. 164, pp. 1482-8, 2004.
- [5] N. J. Shaheen, "Advances in Barrett's esophagus and esophageal adenocarcinoma," *Gastroenterology*, vol. 128, pp. 1554-66, 2005.
- [6] M. Conio, G. Lapertosa, S. Bianchi, and R. Filiberti, "Barrett's esophagus: an update," *Crit Rev Oncol Hematol*, vol. 46, pp. 187-206, 2003.
- [7] R. C. Haggitt, "Barrett's esophagus, dysplasia, and adenocarcinoma," *Hum Pathol*, vol. 25, pp. 982-93, 1994.
- [8] R. D. Odze, J. R. Goldblum, and J. M. Crawford, *Surgical Pathology of the GI Tract, Liver, Biliary Tract, and Pancreas*, 1st ed. Philadelphia: Saunders, 2004.
- [9] M. Conio, A. J. Cameron, Y. Romero, C. D. Branch, C. D. Schleck, L. J. Burgart, A. R. Zinsmeister, L. J. Melton, 3rd, and G. R. Locke, 3rd, "Secular trends in the epidemiology and outcome of Barrett's oesophagus in Olmsted County, Minnesota," *Gut*, vol. 48, pp. 304-9, 2001.
- [10] B. J. Reid, D. S. Levine, G. Longton, P. L. Blount, and P. S. Rabinovitch, "Predictors of progression to cancer in Barrett's esophagus: baseline histology and flow cytometry identify low- and high-risk patient subsets," *Am J Gastroenterol*, vol. 95, pp. 1669-76, 2000.
- [11] S. J. Spechler, "Dysplasia in Barrett's esophagus: limitations of current management strategies," *Am J Gastroenterol*, vol. 100, pp. 927-35, 2005.
- [12] N. S. Buttar, K. K. Wang, T. J. Sebo, D. M. Riehle, K. K. Krishnadath, L. S. Lutzke, M. A. Anderson, T. M. Petterson, and L. J. Burgart, "Extent of high-grade dysplasia in Barrett's esophagus correlates with risk of adenocarcinoma," *Gastroenterology*, vol. 120, pp. 1630-9, 2001.
- [13] J. M. Streitz, Jr., C. W. Andrews, Jr., and F. H. Ellis, Jr., "Endoscopic surveillance of Barrett's esophagus. Does it help?," *J Thorac Cardiovasc Surg*, vol. 105, pp. 383-7; discussion 387-8, 1993.
- [14] D. S. Levine, R. C. Haggitt, P. L. Blount, P. S. Rabinovitch, V. W. Rusch, and B. J. Reid, "An endoscopic biopsy protocol can differentiate high-grade dysplasia from early adenocarcinoma in Barrett's esophagus," *Gastroenterology*, vol. 105, pp. 40-50, 1993.
- [15] J. J. Nigro, J. A. Hagen, T. R. DeMeester, S. R. DeMeester, J. Theisen, J. H. Peters, and M. Kiyabu, "Occult esophageal adenocarcinoma: extent of disease and implications for effective therapy," *Ann Surg*, vol. 230, pp. 433-8; discussion 438-40, 1999.
- [16] M. S. Dar, J. R. Goldblum, T. W. Rice, and G. W. Falk, "Can extent of high grade dysplasia in Barrett's oesophagus predict the presence of adenocarcinoma at oesophagectomy?," *Gut*, vol. 52, pp. 486-9, 2003.
- [17] J. M. Collard, "High-grade dysplasia in Barrett's esophagus. The case for esophagectomy," *Chest Surg Clin N Am*, vol. 12, pp. 77-92, 2002.
- [18] G. W. Falk, T. W. Rice, J. R. Goldblum, and J. E. Richter, "Jumbo biopsy forceps protocol still misses unsuspected cancer in Barrett's esophagus with high-grade dysplasia," *Gastrointest Endosc*, vol. 49, pp. 170-6, 1999.
- [19] R. Cotran, V. Kumar, and T. Collins, "Robbins Pathologic Basis of Disease," 6 ed: W.B. Saunders Company, 1999.
- [20] R. T. Villavicencio and D. K. Rex, "Colonic adenomas: prevalence and incidence rates, growth rates, and miss rates at colonoscopy," *Semin Gastrointest Dis*, vol. 11, pp. 185-93, 2000.

- [21] T. F. Imperiale, D. R. Wagner, C. Y. Lin, G. N. Larkin, J. D. Rogge, and D. F. Ransohoff, "Results of screening colonoscopy among persons 40 to 49 years of age," *N Engl J Med*, vol. 346, pp. 1781-5, 2002.
- [22] T. Matsumoto, M. Iida, Y. Kuwano, S. Tada, T. Yao, and M. Fujishima, "Small nonpolypoid neoplastic lesions of the colon: endoscopic features with emphasis on their progression," *Gastrointest Endosc*, vol. 41, pp. 135-40, 1995.
- [23] S. H. Itzkowitz and N. Harpaz, "Diagnosis and management of dysplasia in patients with inflammatory bowel diseases," *Gastroenterology*, vol. 126, pp. 1634-48, 2004.
- [24] J. A. Eaden, K. R. Abrams, and J. F. Mayberry, "The risk of colorectal cancer in ulcerative colitis: a meta-analysis," *Gut*, vol. 48, pp. 526-35, 2001.
- [25] C. Ell, A. May, L. Gossner, O. Pech, E. Gunter, G. Mayer, R. Henrich, M. Vieth, H. Muller, G. Seitz, and M. Stolte, "Endoscopic mucosal resection of early cancer and high-grade dysplasia in Barrett's esophagus," *Gastroenterology*, vol. 118, pp. 670-7, 2000.
- [26] P. R. Pfau and M. V. Sivak, Jr., "Endoscopic diagnostics," *Gastroenterology*, vol. 120, pp. 763-81, 2001.
- [27] T. D. Wang and G. Triadafilopoulos, "Autofluorescence imaging: have we finally seen the light?," *Gastrointest Endosc*, vol. 61, pp. 686-8, 2005.
- [28] R. S. Kwon, D. V. Sahan, and W. R. Brugge, "Gastrointestinal cancer imaging: Deeper than the eye can see," *Gastroenterology*, vol. 128, pp. 1538-1553, 2005.
- [29] P. Fockens, "Future developments in endoscopic imaging," *Best Pract Res Clin Gastroenterol*, vol. 16, pp. 999-1012, 2002.
- [30] I. A. Scotinotis, M. L. Kochman, J. D. Lewis, E. E. Furth, E. F. Rosato, and G. G. Ginsberg, "Accuracy of EUS in the evaluation of Barrett's esophagus and high-grade dysplasia or intramucosal carcinoma," *Gastrointest Endosc*, vol. 54, pp. 689-96, 2001.
- [31] M. I. Canto, S. Setrakian, J. Willis, A. Chak, R. Petras, N. R. Powe, and M. V. Sivak, Jr., "Methylene blue-directed biopsies improve detection of intestinal metaplasia and dysplasia in Barrett's esophagus," *Gastrointest Endosc*, vol. 51, pp. 560-8, 2000.
- [32] M. I. Canto, S. Setrakian, J. E. Willis, A. Chak, R. E. Petras, and M. V. Sivak, "Methylene blue staining of dysplastic and nondysplastic Barrett's esophagus: an in vivo and ex vivo study," *Endoscopy*, vol. 33, pp. 391-400, 2001.
- [33] M. I. Canto, T. Yoshida, and L. Gossner, "Chromoscopy of intestinal metaplasia in Barrett's esophagus," *Endoscopy*, vol. 34, pp. 330-6, 2002.
- [34] K. Kubo and M. A. Fujino, "Ultra-high magnification endoscopy of the normal esophageal mucosa," *Gastrointest Endosc*, vol. 46, pp. 96-7, 1997.
- [35] P. Sharma, "Magnification endoscopy," *Gastrointest Endosc*, vol. 61, pp. 435-43, 2005.
- [36] R. Kiesslich, J. Fritsch, M. Holtmann, H. H. Koehler, M. Stolte, S. Kanzler, B. Nafe, M. Jung, P. R. Galle, and M. F. Neurath, "Methylene blue-aided chromoendoscopy for the detection of intraepithelial neoplasia and colon cancer in ulcerative colitis," *Gastroenterology*, vol. 124, pp. 880-8, 2003.
- [37] M. D. Rutter, B. P. Saunders, G. Schofield, A. Forbes, A. B. Price, and I. C. Talbot, "Pancolonial indigo carmine dye spraying for the detection of dysplasia in ulcerative colitis," *Gut*, vol. 53, pp. 256-60, 2004.
- [38] D. P. Hurlstone, M. E. McAlindon, D. S. Sanders, R. Koegh, A. J. Lobo, and S. S. Cross, "Further validation of high-magnification chromoscopic-colonoscopy for the detection of intraepithelial neoplasia and colon cancer in ulcerative colitis," *Gastroenterology*, vol. 126, pp. 376-8, 2004.
- [39] R. Kiesslich, P. R. Galle, and M. F. Neurath, "Endoscopic surveillance in ulcerative colitis: smart biopsies do it better," *Gastroenterology*, vol. 133, pp. 742-5, 2007.
- [40] T. Yoshida, H. Inoue, S. Usui, H. Satodate, N. Fukami, and S. E. Kudo, "Narrow-band imaging system with magnifying endoscopy for superficial esophageal lesions," *Gastrointest Endosc*, vol. 59, pp. 288-95, 2004.

- [41] H. Machida, Y. Sano, Y. Hamamoto, M. Muto, T. Kozu, H. Tajiri, and S. Yoshida, "Narrow-band imaging in the diagnosis of colorectal mucosal lesions: a pilot study," *Endoscopy*, vol. 36, pp. 1094-8, 2004.
- [42] M. A. Kara, F. P. Peters, W. D. Rosmolen, K. K. Krishnadath, F. J. ten Kate, P. Fockens, and J. J. Bergman, "High-resolution endoscopy plus chromoendoscopy or narrow-band imaging in Barrett's esophagus: a prospective randomized crossover study," *Endoscopy*, vol. 37, pp. 929-36, 2005.
- [43] H. M. Chiu, C. Y. Chang, C. C. Chen, Y. C. Lee, M. S. Wu, J. T. Lin, C. T. Shun, and H. P. Wang, "A prospective comparative study of narrow-band imaging, chromoendoscopy, and conventional colonoscopy in the diagnosis of colorectal neoplasia," *Gut*, vol. 56, pp. 373-9, 2007.
- [44] R. J. Atkinson and D. P. Hurlstone, "Narrow-band imaging: the next frontier in colonoscopy?," *Gastrointest Endosc*, vol. 66, pp. 317-9, 2007.
- [45] G. Zonios, L. T. Perelman, V. Backman, R. Manoharan, M. Fitzmaurice, J. Van Dam, and M. S. Feld, "Diffuse reflectance spectroscopy of human adenomatous colon polyps in vivo," *Appl Opt*, vol. 38, pp. 6628-37, 1999.
- [46] I. J. Bigio and J. R. Mourant, "Ultraviolet and visible spectroscopies for tissue diagnostics: fluorescence spectroscopy and elastic-scattering spectroscopy," *Phys Med Biol*, vol. 42, pp. 803-14, 1997.
- [47] L. T. Perelman, V. Backman, M. Wallace, G. Zonios, R. Manoharan, A. Nusrat, S. Shields, M. Seiler, C. Lima, T. Hamano, I. Itzkan, J. Van Dam, J. M. Crawford, and M. S. Feld, "Observation of periodic fine structure in reflectance from biological tissue: A new technique for measuring nuclear size distribution," *Physical Review Letters*, vol. 80, pp. 627-630, 1998.
- [48] A. Wax, C. Yang, V. Backman, K. Badizadegan, C. W. Boone, R. R. Dasari, and M. S. Feld, "Cellular organization and substructure measured using angle-resolved low-coherence interferometry," *Biophys J*, vol. 82, pp. 2256-64, 2002.
- [49] L. B. Lovat, K. Johnson, G. D. Mackenzie, B. R. Clark, M. R. Novelli, S. Davies, M. O'Donovan, C. Selvasekar, S. M. Thorpe, D. Pickard, R. Fitzgerald, T. Fearn, I. Bigio, and S. G. Bown, "Elastic scattering spectroscopy accurately detects high grade dysplasia and cancer in Barrett's oesophagus," *Gut*, vol. 55, pp. 1078-83, 2006.
- [50] A. Dhar, K. S. Johnson, M. R. Novelli, S. G. Bown, I. J. Bigio, L. B. Lovat, and S. L. Bloom, "Elastic scattering spectroscopy for the diagnosis of colonic lesions: initial results of a novel optical biopsy technique," *Gastrointest Endosc*, vol. 63, pp. 257-61, 2006.
- [51] I. Georgakoudi, B. C. Jacobson, J. Van Dam, V. Backman, M. B. Wallace, M. G. Muller, Q. Zhang, K. Badizadegan, D. Sun, G. A. Thomas, L. T. Perelman, and M. S. Feld, "Fluorescence, reflectance, and light-scattering spectroscopy for evaluating dysplasia in patients with Barrett's esophagus," *Gastroenterology*, vol. 120, pp. 1620-9, 2001.
- [52] M. B. Wallace, L. T. Perelman, V. Backman, J. M. Crawford, M. Fitzmaurice, M. Seiler, K. Badizadegan, S. J. Shields, I. Itzkan, R. R. Dasari, J. Van Dam, and M. S. Feld, "Endoscopic detection of dysplasia in patients with Barrett's esophagus using light-scattering spectroscopy," *Gastroenterology*, vol. 119, pp. 677-82, 2000.
- [53] V. Backman, M. B. Wallace, L. T. Perelman, J. T. Arendt, R. Gurjar, M. G. Muller, Q. Zhang, G. Zonios, E. Kline, J. A. McGilligan, S. Shapshay, T. Valdez, K. Badizadegan, J. M. Crawford, M. Fitzmaurice, S. Kabani, H. S. Levin, M. Seiler, R. R. Dasari, I. Itzkan, J. Van Dam, and M. S. Feld, "Detection of preinvasive cancer cells," *Nature*, vol. 406, pp. 35-6, 2000.
- [54] A. Wax, C. Yang, M. G. Muller, R. Nines, C. W. Boone, V. E. Steele, G. D. Stoner, R. R. Dasari, and M. S. Feld, "In situ detection of neoplastic transformation and chemopreventive effects in rat esophagus epithelium using angle-resolved low-coherence interferometry," *Cancer Res*, vol. 63, pp. 3556-9, 2003.
- [55] Y. L. Kim, Y. Liu, R. K. Wali, H. K. Roy, M. J. Goldberg, A. K. Kromin, K. Chen, and V. Backman, "Simultaneous measurement of angular and spectral properties of light scattering for

- characterization of tissue microarchitecture and its alteration in early precancer," *Ieee Journal of Selected Topics in Quantum Electronics*, vol. 9, pp. 243-256, 2003.
- [56] R. K. Wali, H. K. Roy, Y. L. Kim, Y. Liu, J. L. Koetsier, D. P. Kunte, M. J. Goldberg, V. Turzhitsky, and V. Backman, "Increased microvascular blood content is an early event in colon carcinogenesis," *Gut*, vol. 54, pp. 654-60, 2005.
- [57] R. S. Gurjar, V. Backman, L. T. Perelman, I. Georgakoudi, K. Badizadegan, I. Itzkan, R. R. Dasari, and M. S. Feld, "Imaging human epithelial properties with polarized light-scattering spectroscopy," *Nat Med*, vol. 7, pp. 1245-8, 2001.
- [58] C. Kendall, N. Stone, N. Shepherd, K. Geboes, B. Warren, R. Bennett, and H. Barr, "Raman spectroscopy, a potential tool for the objective identification and classification of neoplasia in Barrett's oesophagus," *J Pathol*, vol. 200, pp. 602-9, 2003.
- [59] T. D. Wang, J. Van Dam, J. M. Crawford, E. A. Preisinger, Y. Wang, and M. S. Feld, "Fluorescence endoscopic imaging of human colonic adenomas," *Gastroenterology*, vol. 111, pp. 1182-91, 1996.
- [60] T. D. Wang, J. M. Crawford, M. S. Feld, Y. Wang, I. Itzkan, and J. Van Dam, "In vivo identification of colonic dysplasia using fluorescence endoscopic imaging," *Gastrointest Endosc*, vol. 49, pp. 447-55, 1999.
- [61] J. Haringsma, G. N. Tytgat, H. Yano, H. Iishi, M. Tatsuta, T. Ogihara, H. Watanabe, N. Sato, N. Marcon, B. C. Wilson, and R. W. Cline, "Autofluorescence endoscopy: feasibility of detection of GI neoplasms unapparent to white light endoscopy with an evolving technology," *Gastrointest Endosc*, vol. 53, pp. 642-50, 2001.
- [62] K. Niepsuj, G. Niepsuj, W. Cebula, W. Zieleznik, M. Adamek, A. Sielanczyk, J. Adamczyk, J. Kurek, and A. Sieron, "Autofluorescence endoscopy for detection of high-grade dysplasia in short-segment Barrett's esophagus," *Gastrointest Endosc*, vol. 58, pp. 715-9, 2003.
- [63] M. A. Kara, F. P. Peters, F. J. Ten Kate, S. J. Van Deventer, P. Fockens, and J. J. Bergman, "Endoscopic video autofluorescence imaging may improve the detection of early neoplasia in patients with Barrett's esophagus," *Gastrointest Endosc*, vol. 61, pp. 679-85, 2005.
- [64] E. Endlicher, R. Knuechel, T. Hauser, R. M. Szeimies, J. Scholmerich, and H. Messmann, "Endoscopic fluorescence detection of low and high grade dysplasia in Barrett's oesophagus using systemic or local 5-aminolaevulinic acid sensitisation," *Gut*, vol. 48, pp. 314-9, 2001.
- [65] H. Messmann, E. Endlicher, G. Freunek, P. Rummele, J. Scholmerich, and R. Knuechel, "Fluorescence endoscopy for the detection of low and high grade dysplasia in ulcerative colitis using systemic or local 5-aminolaevulinic acid sensitisation," *Gut*, vol. 52, pp. 1003-7, 2003.
- [66] R. Weissleder, C. H. Tung, U. Mahmood, and A. Bogdanov, Jr., "In vivo imaging of tumors with protease-activated near-infrared fluorescent probes," *Nat Biotechnol*, vol. 17, pp. 375-8, 1999.
- [67] R. Weissleder and U. Mahmood, "Molecular imaging," *Radiology*, vol. 219, pp. 316-33, 2001.
- [68] U. Mahmood and M. B. Wallace, "Molecular imaging in gastrointestinal disease," *Gastroenterology*, vol. 132, pp. 11-4, 2007.
- [69] K. Marten, C. Bremer, K. Khazaie, M. Sameni, B. Sloane, C. H. Tung, and R. Weissleder, "Detection of dysplastic intestinal adenomas using enzyme-sensing molecular beacons in mice," *Gastroenterology*, vol. 122, pp. 406-14, 2002.
- [70] M. A. Funovics, R. Weissleder, and U. Mahmood, "Catheter-based in vivo imaging of enzyme activity and gene expression: feasibility study in mice," *Radiology*, vol. 231, pp. 659-66, 2004.
- [71] M. A. Funovics, H. Alencar, X. Montet, R. Weissleder, and U. Mahmood, "Simultaneous fluorescence imaging of protease expression and vascularity during murine colonoscopy for colonic lesion characterization," *Gastrointest Endosc*, vol. 64, pp. 589-97, 2006.
- [72] H. Alencar, M. A. Funovics, J. Figueiredo, H. Sawaya, R. Weissleder, and U. Mahmood, "Colonic adenocarcinomas: near-infrared microcatheter imaging of smart probes for early detection--study in mice," *Radiology*, vol. 244, pp. 232-8, 2007.

- [73] R. Keller, G. Winde, H. J. Terpe, E. C. Foerster, and W. Domschke, "Fluorescence endoscopy using a fluorescein-labeled monoclonal antibody against carcinoembryonic antigen in patients with colorectal carcinoma and adenoma," *Endoscopy*, vol. 34, pp. 801-7, 2002.
- [74] P. L. Hsiung, J. Hardy, S. Friedland, R. Soetikno, C. B. Du, A. P. Wu, P. Sahbaie, J. M. Crawford, A. W. Lowe, C. H. Contag, and T. D. Wang, "Detection of colonic dysplasia in vivo using a targeted heptapeptide and confocal microendoscopy," *Nat Med*, vol. 14, pp. 454-8, 2008.
- [75] P. M. Delaney, M. R. Harris, and R. G. King, "Fiberoptic Laser-Scanning Confocal Microscope Suitable for Fluorescence Imaging," *Applied Optics*, vol. 33, pp. 573-577, 1994.
- [76] A. R. Rouse and A. F. Gmitro, "Multispectral imaging with a confocal microendoscope," *Optics Letters*, vol. 25, pp. 1708-1710, 2000.
- [77] A. R. Rouse, A. Kano, J. A. Udovich, S. M. Kroto, and A. F. Gmitro, "Design and demonstration of a miniature catheter for a confocal microendoscope," *Applied Optics*, vol. 43, pp. 5763-5771, 2004.
- [78] A. L. Polglase, W. J. McLaren, S. A. Skinner, R. Kiesslich, M. F. Neurath, and P. M. Delaney, "A fluorescence confocal endomicroscope for in vivo microscopy of the upper- and the lower-GI tract," *Gastrointest Endosc*, vol. 62, pp. 686-95, 2005.
- [79] V. Becker, T. Vercauteren, C. H. von Weyhern, C. Prinz, R. M. Schmid, and A. Meining, "High-resolution miniprobe-based confocal microscopy in combination with video mosaicing (with video)," *Gastrointest Endosc*, vol. 66, pp. 1001-7, 2007.
- [80] A. Hoffman, M. Goetz, M. Vieth, P. R. Galle, M. F. Neurath, and R. Kiesslich, "Confocal laser endomicroscopy: technical status and current indications," *Endoscopy*, vol. 38, pp. 1275-83, 2006.
- [81] R. Kiesslich, J. Burg, M. Vieth, J. Gnaendiger, M. Enders, P. Delaney, A. Polglase, W. McLaren, D. Janell, S. Thomas, B. Nafe, P. R. Galle, and M. F. Neurath, "Confocal laser endoscopy for diagnosing intraepithelial neoplasias and colorectal cancer in vivo," *Gastroenterology*, vol. 127, pp. 706-13, 2004.
- [82] R. Kiesslich, M. Goetz, K. Lammersdorf, C. Schneider, J. Burg, M. Stolte, M. Vieth, B. Nafe, P. R. Galle, and M. F. Neurath, "Chromoscopy-guided endomicroscopy increases the diagnostic yield of intraepithelial neoplasia in ulcerative colitis," *Gastroenterology*, vol. 132, pp. 874-82, 2007.
- [83] T. D. Wang, S. Friedland, P. Sahbaie, R. Soetikno, P. L. Hsiung, J. T. Liu, J. M. Crawford, and C. H. Contag, "Functional imaging of colonic mucosa with a fibered confocal microscope for real-time in vivo pathology," *Clin Gastroenterol Hepatol*, vol. 5, pp. 1300-5, 2007.
- [84] A. Meining, D. Saur, M. Bajbouj, V. Becker, E. Peltier, H. Hofler, C. H. von Weyhern, R. M. Schmid, and C. Prinz, "In vivo histopathology for detection of gastrointestinal neoplasia with a portable, confocal miniprobe: an examiner blinded analysis," *Clin Gastroenterol Hepatol*, vol. 5, pp. 1261-7, 2007.
- [85] R. Kiesslich, L. Gossner, M. Goetz, A. Dahlmann, M. Vieth, M. Stolte, A. Hoffman, M. Jung, B. Nafe, P. R. Galle, and M. F. Neurath, "In Vivo Histology of Barrett's Esophagus and Associated Neoplasia by Confocal Laser Endomicroscopy," *Clin Gastroenterol Hepatol*, 2006.
- [86] M. Rajadhyaksha, M. Grossman, D. Esterowitz, R. H. Webb, and R. R. Anderson, "In vivo confocal scanning laser microscopy of human skin: melanin provides strong contrast," *J Invest Dermatol*, vol. 104, pp. 946-52, 1995.
- [87] M. Rajadhyaksha, S. Gonzalez, J. M. Zavislan, R. R. Anderson, and R. H. Webb, "In vivo confocal scanning laser microscopy of human skin II: Advances in instrumentation and comparison with histology," *Journal of Investigative Dermatology*, vol. 113, pp. 293-303, 1999.
- [88] R. G. B. Langley, M. Rajadhyaksha, P. J. Dwyer, A. J. Sober, T. J. Flotte, and R. R. Anderson, "Confocal scanning laser microscopy of benign and malignant melanocytic skin lesions in vivo," *Journal of the American Academy of Dermatology*, vol. 45, pp. 365-376, 2001.

- [89] K. J. Busam, K. Hester, C. Charles, D. L. Sachs, C. R. Antonescu, S. Gonzalez, and A. C. Halpern, "Detection of clinically amelanotic malignant melanoma and assessment of its margins by in vivo confocal scanning laser microscopy," *Arch Dermatol*, vol. 137, pp. 923-9, 2001.
- [90] M. Huzaira, F. Rius, M. Rajadhyaksha, R. R. Anderson, and S. Gonzalez, "Topographic variations in normal skin, as viewed by in vivo reflectance confocal microscopy," *Journal of Investigative Dermatology*, vol. 116, pp. 846-852, 2001.
- [91] H. Inoue, T. Igari, T. Nishikage, K. Ami, T. Yoshida, and T. Iwai, "A novel method of virtual histopathology using laser-scanning confocal microscopy in-vitro with untreated fresh specimens from the gastrointestinal mucosa," *Endoscopy*, vol. 32, pp. 439-43, 2000.
- [92] M. Sakashita, H. Inoue, H. Kashida, J. Tanaka, J. Y. Cho, H. Satodate, E. Hidaka, T. Yoshida, N. Fukami, Y. Tamegai, A. Shiokawa, and S. Kudo, "Virtual histology of colorectal lesions using laser-scanning confocal microscopy," *Endoscopy*, vol. 35, pp. 1033-8, 2003.
- [93] P. W. Chiu, H. Inoue, H. Satodate, T. Kazawa, T. Yoshida, M. Sakashita, and S. E. Kudo, "Validation of the quality of histological images obtained of fresh and formalin-fixed specimens of esophageal and gastric mucosa by laser-scanning confocal microscopy," *Endoscopy*, vol. 38, pp. 236-40, 2006.
- [94] W. Denk, J. H. Strickler, and W. W. Webb, "Two-photon laser scanning fluorescence microscopy," *Science*, vol. 248, pp. 73-6, 1990.
- [95] W. R. Zipfel, R. M. Williams, R. Christie, A. Y. Nikitin, B. T. Hyman, and W. W. Webb, "Live tissue intrinsic emission microscopy using multiphoton-excited native fluorescence and second harmonic generation," *Proc Natl Acad Sci U S A*, vol. 100, pp. 7075-80, 2003.
- [96] W. R. Zipfel, R. M. Williams, and W. W. Webb, "Nonlinear magic: multiphoton microscopy in the biosciences," *Nat Biotechnol*, vol. 21, pp. 1369-77, 2003.
- [97] B. A. Flusberg, E. D. Cocker, W. Piyawattanametha, J. C. Jung, E. L. Cheung, and M. J. Schnitzer, "Fiber-optic fluorescence imaging," *Nat Methods*, vol. 2, pp. 941-50, 2005.
- [98] J. N. Rogart, J. Nagata, C. S. Loeser, R. D. Roorda, H. Aslanian, M. E. Robert, W. R. Zipfel, and M. H. Nathanson, "Multiphoton imaging can be used for microscopic examination of intact human gastrointestinal mucosa ex vivo," *Clin Gastroenterol Hepatol*, vol. 6, pp. 95-101, 2008.
- [99] D. Huang, E. A. Swanson, C. P. Lin, J. S. Schuman, W. G. Stinson, W. Chang, M. R. Hee, T. Flotte, K. Gregory, C. A. Puliafito, and J. G. Fujimoto, "Optical coherence tomography," *Science*, vol. 254, pp. 1178-1181, 1991.
- [100] J. G. Fujimoto, M. E. Brezinski, G. J. Tearney, S. A. Boppart, B. Bouma, M. R. Hee, J. F. Southern, and E. A. Swanson, "Optical biopsy and imaging using optical coherence tomography," *Nature Medicine*, vol. 1, pp. 970-972, 1995.
- [101] J. G. Fujimoto, "Optical coherence tomography for ultrahigh resolution in vivo imaging," *Nature Biotechnology*, vol. 21, pp. 1361-1367, 2003.
- [102] W. Drexler, U. Morgner, F. X. Kartner, C. Pitris, S. A. Boppart, X. D. Li, E. P. Ippen, and J. G. Fujimoto, "In vivo ultrahigh-resolution optical coherence tomography," *Optics Letters*, vol. 24, pp. 1221-1223, 1999.
- [103] M. Wojtkowski, T. Bajraszewski, P. Targowski, and A. Kowalczyk, "Real-time in vivo imaging by high-speed spectral optical coherence tomography," *Opt Lett*, vol. 28, pp. 1745-7, 2003.
- [104] R. Leitgeb, C. K. Hitzenberger, and A. F. Fercher, "Performance of Fourier domain vs. time domain optical coherence tomography," *Optics Express*, vol. 11, pp. 889-894, 2003.
- [105] M. A. Choma, M. V. Sarunic, C. H. Yang, and J. A. Izatt, "Sensitivity advantage of swept source and Fourier domain optical coherence tomography," *Optics Express*, vol. 11, pp. 2183-2189, 2003.
- [106] J. F. de Boer, B. Cense, B. H. Park, M. C. Pierce, G. J. Tearney, and B. E. Bouma, "Improved signal-to-noise ratio in spectral-domain compared with time-domain optical coherence tomography," *Opt Lett*, vol. 28, pp. 2067-9, 2003.

- [107] N. Nassif, B. Cense, B. H. Park, S. H. Yun, T. C. Chen, B. E. Bouma, G. J. Tearney, and J. F. de Boer, "In vivo human retinal imaging by ultrahigh-speed spectral domain optical coherence tomography," *Opt Lett*, vol. 29, pp. 480-2, 2004.
- [108] S. H. Yun, G. J. Tearney, J. F. de Boer, N. Iftimia, and B. E. Bouma, "High-speed optical frequency-domain imaging," *Optics Express*, vol. 11, pp. 2953-2963, 2003.
- [109] R. Huber, M. Wojtkowski, and J. G. Fujimoto, "Fourier Domain Mode Locking (FDML): A new laser operating regime and applications for optical coherence tomography," *Optics Express*, vol. 14, pp. 3225-3237, 2006.
- [110] S. H. Yun, G. J. Tearney, B. J. Vakoc, M. Shishkov, W. Y. Oh, A. E. Desjardins, M. J. Suter, R. C. Chan, J. A. Evans, I. K. Jang, N. S. Nishioka, J. F. de Boer, and B. E. Bouma, "Comprehensive volumetric optical microscopy in vivo," *Nat Med*, vol. 12, pp. 1429-33, 2006.
- [111] D. C. Adler, Y. Chen, R. Huber, J. Schmitt, J. Connolly, and J. G. Fujimoto, "Three-dimensional endomicroscopy using optical coherence tomography," *Nature Photonics*, vol. 1, pp. 709-716, 2007.
- [112] G. J. Tearney, S. A. Boppart, B. E. Bouma, M. E. Brezinski, N. J. Weissman, J. F. Southern, and J. G. Fujimoto, "Scanning single-mode fiber optic catheter-endoscope for optical coherence tomography," *Optics Letters*, vol. 21, pp. 543-5, 1996.
- [113] X. Li, C. Chudoba, T. Ko, C. Pitris, and J. G. Fujimoto, "Imaging needle for optical coherence tomography," *Optics Letters*, vol. 25, pp. 1520-2, 2000.
- [114] M. R. Hee, C. A. Puliafito, C. Wong, J. S. Duker, E. Reichel, J. S. Schuman, E. A. Swanson, and J. G. Fujimoto, "Optical coherence tomography of macular holes," *Ophthalmology*, vol. 102, pp. 748-756, 1995.
- [115] J. S. Schuman, M. R. Hee, A. V. Arya, T. Pedut-Kloizman, C. A. Puliafito, J. G. Fujimoto, and E. A. Swanson, "Optical coherence tomography: a new tool for glaucoma diagnosis," *Current Opinion in Ophthalmology*, vol. 6, pp. 89-95, 1995.
- [116] M. R. Hee, C. A. Puliafito, C. Wong, J. S. Duker, E. Reichel, B. Rutledge, J. S. Schuman, E. A. Swanson, and J. G. Fujimoto, "Quantitative assessment of macular edema with optical coherence tomography," *Archives of Ophthalmology*, vol. 113, pp. 1019-1029, 1995.
- [117] M. R. Hee, C. A. Puliafito, J. S. Duker, E. Reichel, J. G. Coker, J. R. Wilkins, J. S. Schuman, E. A. Swanson, and J. G. Fujimoto, "Topography of diabetic macular edema with optical coherence tomography," *Ophthalmology*, vol. 105, pp. 360-370, 1998.
- [118] W. Drexler and J. G. Fujimoto, "State-of-the-art retinal optical coherence tomography," *Prog Retin Eye Res*, vol. 27, pp. 45-88, 2008.
- [119] M. E. Brezinski, G. J. Tearney, N. J. Weissman, S. A. Boppart, B. E. Bouma, M. R. Hee, A. E. Weyman, E. A. Swanson, J. F. Southern, and J. G. Fujimoto, "Assessing atherosclerotic plaque morphology: comparison of optical coherence tomography and high frequency intravascular ultrasound," *Heart*, vol. 77, pp. 397-403, 1997.
- [120] M. E. Brezinski, G. J. Tearney, B. E. Bouma, J. A. Izatt, M. R. Hee, E. A. Swanson, J. F. Southern, and J. G. Fujimoto, "Optical coherence tomography for optical biopsy. Properties and demonstration of vascular pathology," *Circulation*, vol. 93, pp. 1206-13, 1996.
- [121] G. J. Tearney, M. E. Brezinski, S. A. Boppart, B. E. Bouma, N. Weissman, J. F. Southern, E. A. Swanson, and J. G. Fujimoto, "Catheter-based optical imaging of a human coronary artery," *Circulation*, vol. 94, pp. 3013, 1996.
- [122] G. J. Tearney, H. Yabushita, S. L. Houser, H. T. Aretz, I. K. Jang, K. H. Schlendorf, C. R. Kauffman, M. Shishkov, E. F. Halpern, and B. E. Bouma, "Quantification of macrophage content in atherosclerotic plaques by optical coherence tomography," *Circulation*, vol. 107, pp. 113-9, 2003.
- [123] I. K. Jang, G. J. Tearney, B. MacNeill, M. Takano, F. Moselewski, N. Iftima, M. Shishkov, S. Houser, H. T. Aretz, E. F. Halpern, and B. E. Bouma, "In vivo characterization of coronary atherosclerotic plaque by use of optical coherence tomography," *Circulation*, vol. 111, pp. 1551-5, 2005.

- [124] J. A. Izatt, M. D. Kulkarni, H.-W. Wang, K. Kobayashi, and M. V. Sivak, Jr., "Optical coherence tomography and microscopy in gastrointestinal tissues," *IEEE Journal of Selected Topics in Quantum Electronics*, vol. 2, pp. 1017-28, 1996.
- [125] G. J. Tearney, M. E. Brezinski, J. F. Southern, B. E. Bouma, S. A. Boppart, and J. G. Fujimoto, "Optical biopsy in human gastrointestinal tissue using optical coherence tomography," *The American journal of gastroenterology*, vol. 92, pp. 1800-4, 1997.
- [126] J. A. Evans, J. M. Poneris, B. E. Bouma, J. Bressner, E. F. Halpern, M. Shishkov, G. Y. Lauwers, M. Mino-Kenudson, N. S. Nishioka, and G. J. Tearney, "Optical coherence tomography to identify intramucosal carcinoma and high-grade dysplasia in Barrett's esophagus," *Clin Gastroenterol Hepatol*, vol. 4, pp. 38-43, 2006.
- [127] G. J. Tearney, M. E. Brezinski, J. F. Southern, B. E. Bouma, S. A. Boppart, and J. G. Fujimoto, "Optical biopsy in human urologic tissue using optical coherence tomography," *The Journal of urology*, vol. 157, pp. 1915-9, 1997.
- [128] A. V. D'Amico, M. Weinstein, X. Li, J. P. Richie, and J. Fujimoto, "Optical coherence tomography as a method for identifying benign and malignant microscopic structures in the prostate gland," *Urology*, vol. 55, pp. 783-7, 2000.
- [129] Y. T. Pan, T. Q. Xie, C. W. Du, S. Bastacky, S. Meyers, and M. L. Zeidel, "Enhancing early bladder cancer detection with fluorescence-guided endoscopic optical coherence tomography," *Opt Lett*, vol. 28, pp. 2485-7, 2003.
- [130] J. Welzel, E. Lankenau, R. Birngruber, and R. Engelhardt, "Optical coherence tomography of the human skin," *Journal of the American Academy of Dermatology*, vol. 37, pp. 958-63, 1997.
- [131] J. Welzel, C. Reinhardt, E. Lankenau, C. Winter, and H. H. Wolff, "Changes in function and morphology of normal human skin: evaluation using optical coherence tomography," *Br J Dermatol*, vol. 150, pp. 220-5, 2004.
- [132] T. Gambichler, G. Moussa, M. Sand, D. Sand, P. Altmeyer, and K. Hoffmann, "Applications of optical coherence tomography in dermatology," *J Dermatol Sci*, vol. 40, pp. 85-94, 2005.
- [133] G. J. Tearney, M. E. Brezinski, B. E. Bouma, S. A. Boppart, C. Pitvis, J. F. Southern, and J. G. Fujimoto, "In vivo endoscopic optical biopsy with optical coherence tomography," *Science*, vol. 276, pp. 2037-2039, 1997.
- [134] A. M. Sergeev, V. M. Gelikonov, G. V. Gelikonov, F. I. Feldchtein, R. V. Kuranov, N. D. Gladkova, N. M. Shakhova, L. B. Suopova, A. V. Shakhov, I. A. Kuznetzova, A. N. Denisenko, V. V. Pochinko, Y. P. Chumakov, and O. S. Streltsova, "In vivo endoscopic OCT imaging of precancer and cancer states of human mucosa," *Optics Express*, vol. 1, 1997.
- [135] B. E. Bouma and G. J. Tearney, "Power-efficient nonreciprocal interferometer and linear-scanning fiber-optic catheter for optical coherence tomography," *Optics Letters*, vol. 24, pp. 531-3, 1999.
- [136] M. V. Sivak, Jr., K. Kobayashi, J. A. Izatt, A. M. Rollins, R. Ung-Runyawee, A. Chak, R. C. Wong, G. A. Isenberg, and J. Willis, "High-resolution endoscopic imaging of the GI tract using optical coherence tomography," *Gastrointestinal endoscopy*, vol. 51(4) Pt 1, pp. 474-9, 2000.
- [137] B. E. Bouma, G. J. Tearney, C. C. Compton, and N. S. Nishioka, "High-resolution imaging of the human esophagus and stomach in vivo using optical coherence tomography," *Gastrointestinal endoscopy*, vol. 51(4) Pt 1, pp. 467-74, 2000.
- [138] S. Jäckle, N. Gladkova, F. Feldchtein, A. Terentjeva, B. Brand, G. Gelikonov, V. Gelikonov, A. Sergeev, A. Fritscher-Ravens, J. Freund, U. Seitz, S. Schröder, and N. Soehendra, "In vivo endoscopic optical coherence tomography of esophagitis, Barrett's esophagus, and adenocarcinoma of the esophagus," *Endoscopy*, vol. 32, pp. 750-5, 2000.
- [139] S. Jäckle, N. Gladkova, F. Feldchtein, A. Terentjeva, B. Brand, G. Gelikonov, V. Gelikonov, A. Sergeev, A. Fritscher-Ravens, J. Freund, U. Seitz, S. Soehendra, and N. Schröder, "In vivo endoscopic optical coherence tomography of the human gastrointestinal tract--toward optical biopsy," *Endoscopy*, vol. 32, pp. 743-9, 2000.

- [140] G. Zuccaro, N. Gladkova, J. Vargo, F. Feldchtein, E. Zagaynova, D. Conwell, G. Falk, J. Goldblum, J. Dumot, J. Ponsky, G. Gelikonov, B. Davros, E. Donchenko, and J. Richter, "Optical coherence tomography of the esophagus and proximal stomach in health and disease," *The American journal of gastroenterology*, vol. 96, pp. 2633-9, 2001.
- [141] J. M. Poneros, S. Brand, B. E. Bouma, G. J. Tearney, C. C. Compton, and N. S. Nishioka, "Diagnosis of specialized intestinal metaplasia by optical coherence tomography," *Gastroenterology*, vol. 120, pp. 7-12, 2001.
- [142] P. R. Pfau, M. V. Sivak, Jr., A. Chak, M. Kinnard, R. C. Wong, G. A. Isenberg, J. A. Izatt, A. Rollins, and V. Westphal, "Criteria for the diagnosis of dysplasia by endoscopic optical coherence tomography," *Gastrointest Endosc*, vol. 58, pp. 196-202, 2003.
- [143] G. Isenberg, M. V. Sivak, Jr., A. Chak, R. C. Wong, J. E. Willis, B. Wolf, D. Y. Rowland, A. Das, and A. Rollins, "Accuracy of endoscopic optical coherence tomography in the detection of dysplasia in Barrett's esophagus: a prospective, double-blinded study," *Gastrointest Endosc*, vol. 62, pp. 825-31, 2005.
- [144] M. B. Wallace, "Detecting dysplasia with optical coherence tomography," *Clin Gastroenterol Hepatol*, vol. 4, pp. 36-7, 2006.
- [145] X. D. Li, S. A. Boppart, J. Van Dam, H. Mashimo, M. Mutinga, W. Drexler, M. Klein, C. Pitris, M. L. Krinsky, M. E. Brezinski, and J. G. Fujimoto, "Optical coherence tomography: advanced technology for the endoscopic imaging of Barrett's esophagus," *Endoscopy*, vol. 32, pp. 921-30, 2000.
- [146] P. R. Herz, Y. Chen, A. D. Aguirre, J. C. Fujimoto, H. Mashimo, J. Schmitt, A. Koski, J. Goodnow, and C. Petersen, "Ultrahigh resolution optical biopsy with endoscopic optical coherence tomography," *Optics Express*, vol. 12, 2004.

## Chapter 2

### Ultrahigh Resolution Endoscopic OCT

#### 2.1 Overview

Previous work on endoscopic OCT has been performed with resolutions in the range of 10 – 20  $\mu\text{m}$ . An important focus of this thesis is the development of new technology for improving resolution in OCT, with a particular emphasis on endoscopic applications. This chapter describes work performed as part of a large collaborative effort on the development and application of ultrahigh resolution endoscopic OCT (UHR EOCT) for human clinical imaging in the upper gastrointestinal tract. First, the ultrahigh resolution endoscopic OCT system design and performance are described. Axial image resolutions of less than 5  $\mu\text{m}$  in tissue were achieved using a compact, solid-state Cr:Forsterite laser source. Images were acquired and visualized in real-time at 4 frames per second. Second, imaging studies in human patients are discussed. UHR EOCT imaging of normal mucosal tissues in the upper gastrointestinal tract are contrasted with images from patients with Barrett's esophagus and esophageal adenocarcinoma. In addition, an interesting case study is discussed to motivate potential applications for OCT imaging in the stomach. Finally, the results of these studies are discussed with respect to key advantages and limitations of endoscopic OCT. This discussion therefore provides perspective and motivation for the subsequent work detailed in this thesis.

The contributions of several individuals to this chapter must be appropriately acknowledged in advance. This project involved physician investigators under the direction of Dr. Hiroshi Mashimo at the Boston Veteran's Affairs (VA) Healthcare System, technology support from Dr. Joseph Schmitt and colleagues at Lightlab Imaging, and contributions from several researchers at the Massachusetts Institute of Technology. Lightlab Imaging provided fiber-optic imaging catheters as well as a platform imaging engine that was modified for ultrahigh resolution for these studies. Visiting researcher Karl Schneider developed the Cr:Forsterite laser source and former student Paul Herz led the ultrahigh resolution system integration and initial demonstrations during his doctoral studies [1]. Post-doctoral associate Yu Chen has been instrumental in all aspects of the study and is largely responsible for managing the logistics of the clinical studies. In addition, several of the figures in this chapter were prepared by him. Former student Pei-Lin Hsiung also contributed substantially to both the technical and clinical aspects of the

endoscopy study. The majority of the results described in this chapter were reported in two journal manuscripts [2, 3].

## 2.2 Clinical Ultrahigh-Resolution Endoscopic OCT System Design

The ultrahigh resolution endoscopic system was based on an imaging engine developed by Lightlab Imaging. Lightlab Imaging was founded in 1998 to develop optical coherence tomography for cardiovascular and endoscopic applications. In 2002, it became a subsidiary of Goodman Co. Ltd., a Japanese corporation specializing in devices for interventional cardiology. Efforts in endoscopic and bronchoscopic imaging at Lightlab have been done in joint collaboration with Pentax, a major Japanese manufacturer of endoscopic equipment.

The OCT engine housed an electro-optic module, a reference arm assembly, and signal-processing electronics and it interfaced to an external actuator and catheter probe. The standard light source used in the electro-optic module consists of a pair of InGaP superluminescent diodes (SLEDs) with partially overlapping spectra in the 1250 – 1350 nm wavelength range, which together give a polarized source with a bandwidth of 75 nm and approximately 20 mW output power. In these studies, the system was modified to utilize a custom-built Cr:Forsterite solid-state laser source, which produced > 200 nm bandwidth and was engineered for compactness and portability for the clinical setting [3, 4]. Figure 2.1 illustrates the ultrahigh resolution endoscopic OCT system incorporating the Cr:Forsterite laser. Light from the laser first passed through a non-reciprocal optical circulator and into a fiber-optic coupler, which delivered 90% of the light to the sample arm and 10% to the reference arm. This configuration is power-conserving by limiting the amount of power directed to the reference arm compared to the sample arm. The reference arm illumination was directed onto a high speed rotating delay scanner, which provided a linear scan of the optical path length at up to 3125 scans per second. This high speed allowed high pixel density imaging at several frames per second to minimize artifact from subject motion during *in vivo* imaging.

To optimize resolution in ultrahigh resolution OCT, chromatic dispersion must be closely balanced between the reference and sample arms of the interferometer. The simplest approach to balancing dispersion requires matching of the materials in reference and sample arms. In the ultrahigh resolution endoscopic system, an air gap coupling apparatus was used in the sample arm to match the air path in the reference delay scanner. Furthermore, glass blanks of different materials were inserted in the reference arm to compensate any dispersion mismatch generated by the sample arm optics. Generally speaking, the birefringence mismatch between the two arms of the interferometer in an OCT system must also be balanced to achieve optimal signal. In this system, however, a polarization diversity scheme was used to eliminate the deleterious effects of variation in sample arm birefringence incurred during imaging. These

effects are particularly relevant when using circularly scanned catheters, which incur periodic polarization modulation during rotation of the catheter. In addition, the polarization diversity schemes removed the effects of sample polarization due either to propagation through birefringent structures or to polarization dependent scattering properties [5]. Polarization diversity was achieved using a polarizing beam splitter (PBS) in the detection path and a polarization controller (PC) in the reference path. The reference polarization state was set to equalize the optical reference power on each of the two detectors, representing orthogonal polarization states. This ensured uniform heterodyne gain for each of the two detected polarization states.

Due to the rapid delay scan, the heterodyne carrier frequency of the OCT interference signal at each detector in this system was approaching 20 MHz. Analog-to-digital conversion was performed on two 14-bit channels at 40 MHz each to satisfy Nyquist sampling criteria, which requires at least two points per fringe or twice the highest frequency component of the acquired signal [6]. Real-time digital demodulation was performed using onboard digital mixers and filters and a field-programmable gate array computed the polarization-insensitive image intensity as the square root of the sum of the squares of the two detector signals. Images were then displayed on a logarithmic scale to represent the entire dynamic range within the standard image format consisting of 256 intensity levels. Images were typically displayed using a sepia colormap rather than standard grayscale or inverse grayscale, as it has been determined that addition of a single color to the colormap enhances visual perception of image quality [7].

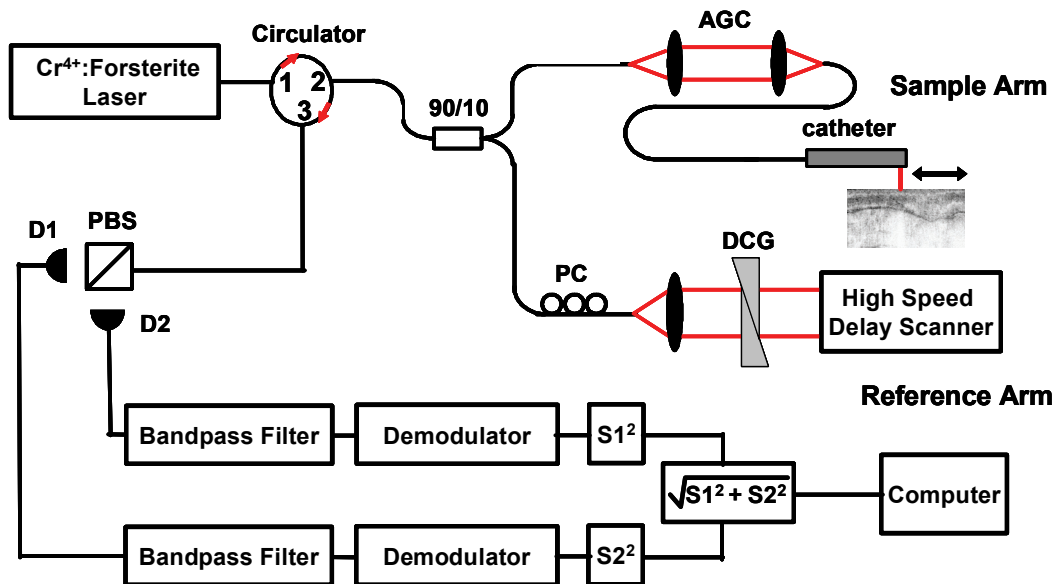


**Figure 2.1.** Schematic of the ultrahigh resolution endoscopic OCT system used for gastrointestinal imaging. PC, polarization controller; AGC, air-gap coupling; PBS, polarizing beam splitter; DCG, dispersion compensating glass. Figure is modified slightly from [3].

High resolution optical coherence tomography using a Cr:Forsterite laser source was previously demonstrated in the laboratory setting [8]. In this work, the authors showed that propagation of the high peak power Cr:Forsterite pulse in a standard single mode fiber resulted in unacceptable nonlinear effects and spectral modulation that distorted the axial point spread function. They overcame these effects by using a length of dispersion shifted fiber to eliminate phase matching necessary to support four-photon mixing. The remaining interaction between self-phase modulation and normal dispersion resulted in the generation of a broadened spectrum capable of producing OCT axial resolutions as short as 6  $\mu\text{m}$ . They subsequently used this source to demonstrate endoscopic imaging in the rabbit model with  $\sim 10 \mu\text{m}$  resolution [9].

The Cr:Forsterite laser developed for these studies was a modified and enhanced version of the earlier system suitable for clinical studies outside of the laboratory. The laser used a prismless cavity design based on broadband double-chirped mirrors [10] to compensate intracavity dispersion. A compact 5 Watt Ytterbium (Yb) fiber laser served as the pump source. The pump and the entire laser cavity were laid out on a 60 cm x 40 cm breadboard. The laser produced a maximum of 120 mW modelocked output power and a spectral bandwidth of  $\sim 59 \text{ nm}$ . A dispersion-shifted, Germanium-doped, highly nonlinear fiber was used to broaden the optical spectrum. Coupling between 50 and 70 mW into the fiber typically resulted in a spectrum of over 200 nm centered at  $\sim 1240 \text{ nm}$ . Figure 2.2a shows an example broadened spectrum as well as the characteristic spectrum passing through the imaging system. The optical components in the system had limited spectral bandwidth and could not fully support the source output spectrum, particularly the shorter wavelengths. Nonetheless, the transmitted spectrum was sufficient to provide  $\sim 5 \mu\text{m}$  axial resolution in air, which corresponds to  $\sim 3.7 \mu\text{m}$  resolution in tissue. This corresponds to a factor of 3 – 4 improvement compared to previously used clinical OCT systems. The axial point spread function is provided as figure 2.2b.

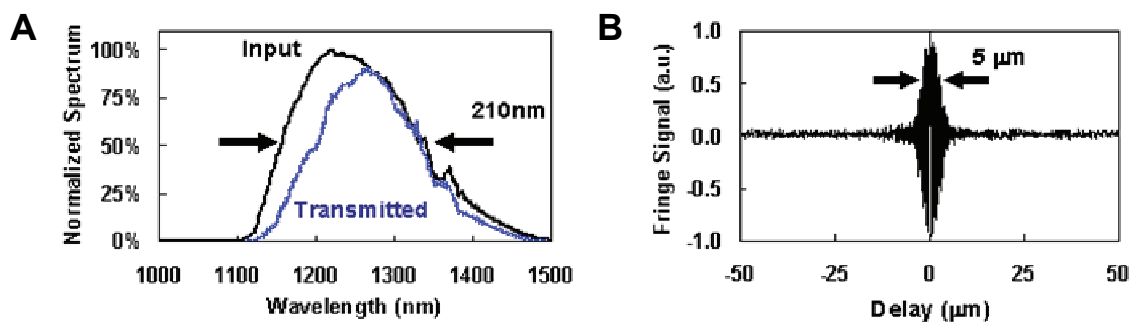


**Figure 2.2.** Optical imaging performance of the compact Cr:Forsterite laser source. The laser output spectrum (A) has a full width at half maximum of  $\sim 210 \text{ nm}$ , although the spectrum transmitted through the system is reduced by the limited optical bandwidth of the interferometer. The resulting axial image resolution (B) measures  $\sim 5 \mu\text{m}$  in air, corresponding to  $\sim 3.7 \mu\text{m}$  in tissue. Figure is modified slightly from [3].

The imaging catheter is one of the most critical components in the endoscopic system. Catheters for this study were provided by Lightlab Imaging based on their ImageWire technology. The devices were in principal similar to previously used catheter endoscopes designed for OCT, which consisted of single-mode fibers threaded through a 1-mm diameter torque cable and attached to a graded-index (GRIN) lens and microprism [11]. The ImageWire was modified from the earlier prototypes, however, to improve performance and allow for easier and more consistent manufacturing. Rather than the GRIN lens and microprism, the ImageWire focused using a fused-fiber assembly consisting of coreless single mode fiber lengths with a short segment of multimode fiber interspersed. The multimode fiber effectively acted as a converging lens. A 45 degree polish was placed on one end of the coreless fiber to deflect the beam away from the catheter. The entire fiber optical assembly was covered with a transparent plastic sheath that allowed for easy sanitation after use. The sheathed catheter had an outer diameter of 1.8 mm and a  $1/e^2$  beam diameter focal spot size of 15  $\mu\text{m}$ , with the focus located at a working distance of 0.5 mm from the outer wall of the device. Figure 2.3a shows the catheter device inserted through the 2.8 mm diameter accessory port of a standard clinical endoscope, while figure 2.3b shows the catheter imaging in the field of view of the endoscope. Use of miniaturized imaging catheters with existing clinical endoscopes is a major advantage of endoscopic OCT and allows for ready integration with established clinical protocol as well as potential for use with advanced endoscopic procedures such as endoscopic retrograde cholangiopancreatography (ERCP) [12].

Scanning of the catheter is typically performed in one of two ways, which are illustrated in figure 2.3c and 2.3d. The catheter can be scanned rotationally and the image generated from a map of backscatter as a function of radius  $R$  and angle  $\Theta$ . The first demonstration of endoscopic OCT in an animal model used this method [9] as have several subsequent studies in the human gastrointestinal tract [13, 14]. Rotational scanning is typically performed at the proximal end of the catheter device by rotating the inner fiber assembly with respect to the outer sheath. An air gap coupling apparatus is required to allow free rotation of the distal end [11]. The circular scan method has the advantage of being less sensitive to catheter beam positioning relative to the tissue surface and has shown to be particularly useful for applications such as intravascular imaging where it provides information on lesion thickness and impingement into the vessel lumen. An important disadvantage of the rotational method, however, is a loss of pixel sampling resolution at larger radii versus shorter radii in the image. The second approach to catheter scanning is to perform linear translation of the device such that cross-sectional images are generated along the catheter axis. Actuation is usually performed at the proximal end of the fiber in a “push-pull” manner using a mechanical actuator. The linear translation approach has the advantage of enabling uniform pixel density throughout the image range, which has been shown to provide improved image quality for gastrointestinal

imaging [15]. The disadvantage of this method is the relative difficulty in positioning the optical beam orthogonally to the mucosal surface. Deliberate rotation from the proximal end is generally imprecise, making it challenging to orient the beam for optimum signal intensity. A third hybrid scanning approach involves rotationally scanning the catheter while pulling-back along the catheter axis. This results in a spiral scan pattern and can be useful for large area coverage in intravascular applications or in endoscopy [3]. In the work conducted for this thesis, the longitudinal “push-pull” scan method was used in order to provide uniformly sampled, high pixel density images that fully display the ultrahigh image resolutions. Actuation was performed with a voice coil translator that allowed rapid displacement over 3-5 mm of the inner catheter with respect to the outer sheath at several cycles per second [1].

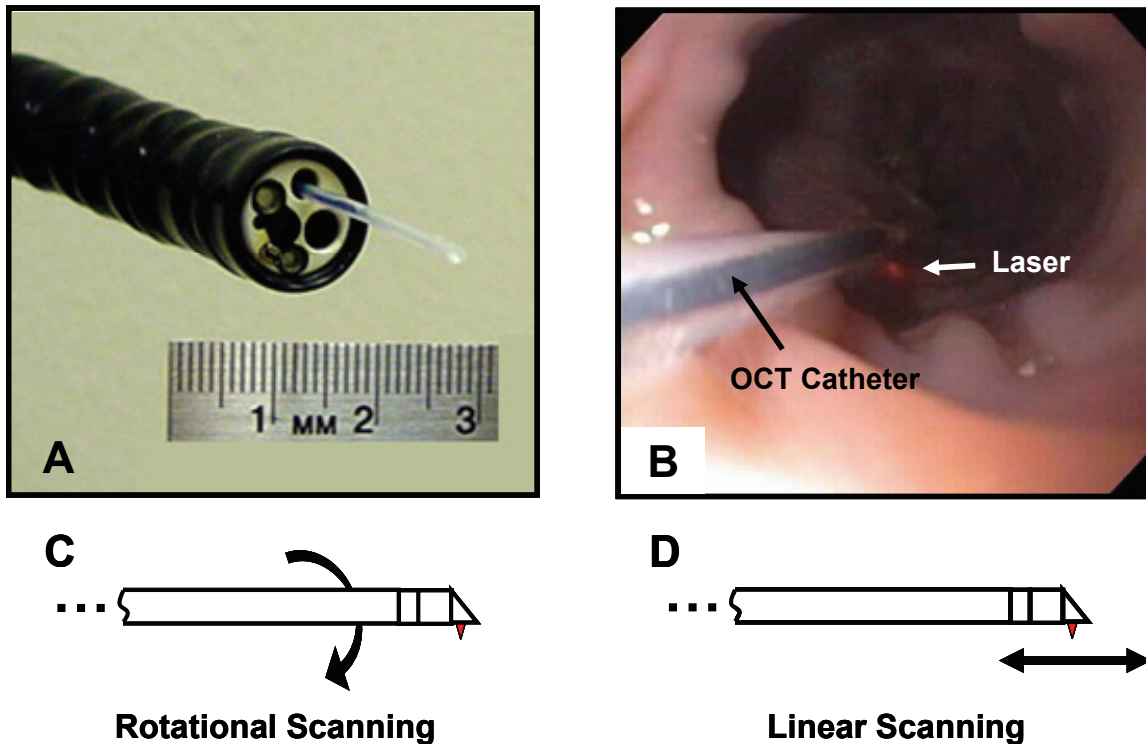


**Figure 2.3.** Fiber-optic imaging catheter and scanning methods. The catheter measures 1.8 mm in outer diameter and easily passes through the standard 2.8 mm diameter accessory port of a clinical endoscope (A). Imaging can be performed under direct endoscopic view (B). Rotational scanning (C) or linear scanning (D) is typically performed to generate a two-dimensional cross-sectional image. In this study, linear scanning was the method of choice.

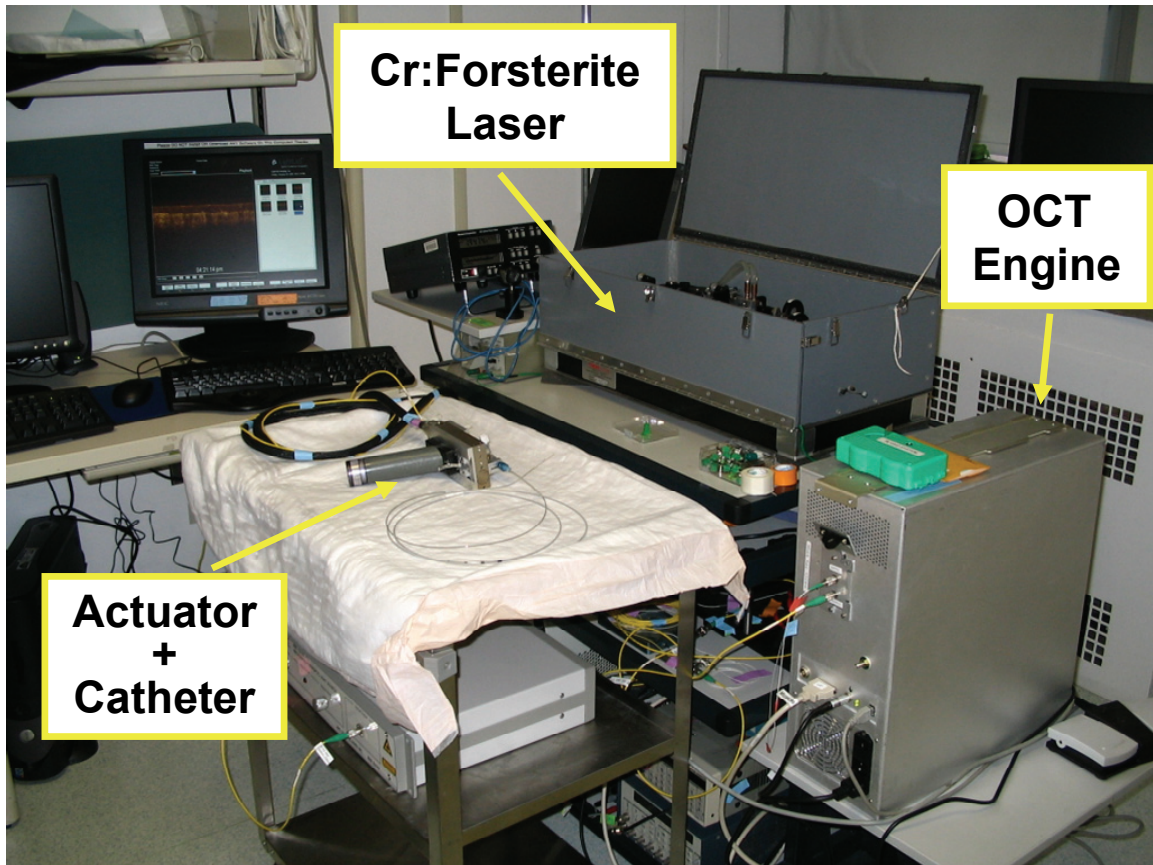


**Figure 2.4.** Photograph of the ultrahigh resolution endoscopic OCT system in the GI endoscopy suite.

Figure 2.4 presents a photograph of the integrated ultrahigh resolution endoscopic OCT system in the gastrointestinal endoscopy suite. The compact Cr:Forsterite laser, complete with pump source and chiller, is placed on a robust mobile cart. The imaging engine also mounts on this cart as well as the accessory electronics and the air gap coupling apparatus. The computer controlling the system is placed on the table next to the cart. Typically, a second monitor (not shown) is mounted above the patient's bed next to the video endoscopy screen, allowing the endoscopist simultaneous assessment of the endoscopic view and the OCT image.

### **2.3 Endoscopic OCT Imaging Protocol and Study Parameters**

OCT imaging was performed in the esophagus and stomach of patients undergoing upper GI endoscopy at the Boston Veteran Affairs Medical Center (VAMC). Informed consent was obtained under a protocol approved jointly by the Institutional Review Board (IRB) of Boston VAMC, the Committee on Human Studies at Harvard Medical School and the Committee on the Use of Humans as

Experimental Subjects (COUHES) of Massachusetts Institute of Technology. Before the endoscopic procedure, the OCT imaging catheter was disinfected by immersion in Cidex® solution (ortho-phthalaldehyde solution, Division of Ethicon, Inc., CA, USA) and rinsed with sterile water. The disinfected imaging catheter was inserted through the accessory channel of the endoscope. While in the field of view of the endoscope, the catheter was positioned to the areas of interest by maneuvering the tip of the endoscope. The side of the distal end of the catheter was placed in gentle contact with the tissue surface during image acquisition to maintain mechanical stability for minimizing motion artifacts. A visible wavelength (670 nm) light source served as an aiming beam to facilitate the visualization and identification of the OCT imaging plane.

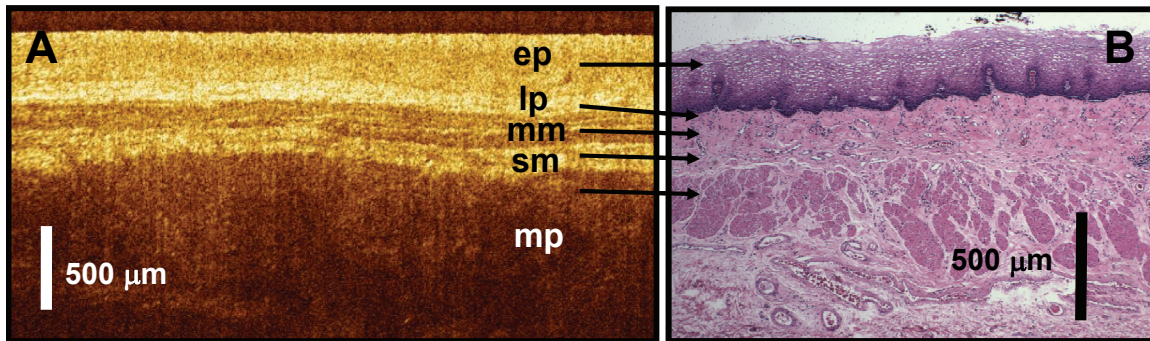
OCT images were acquired in real time at a rate of 4 frames per second. The images measured 3 mm in length (600 pixels) and 2.5 mm in depth (1,600 pixels). This aspect ratio includes scaling in the depth dimension to account for the approximate index of refraction of tissue of 1.38. The video outputs of both the endoscopic CCD view and the computer monitor OCT view were saved on SVHS tapes simultaneously for post-analysis and registration of imaging sites. In addition, an audio stream was recorded during the procedure to capture important commentary for later offline use in image interpretation and analysis. Pinch biopsies of the imaged regions suspected for pathology were obtained after the completion of the OCT imaging procedure. In select cases, larger specimens were resected by endoscopic mucosal resection (EMR) procedures. All biopsy and EMR specimens were immersed in 10% buffered formalin and submitted for routine histology processing, H&E staining, and pathologic evaluation.

This study was designed as a pilot observational study to evaluate new technology for *in vivo* imaging. A total of 50 patients with previous history of Barrett's esophagus were imaged. Images from both normal and abnormal areas in the upper GI tract were acquired and later classified according to the results of pinch biopsy histology. The pathologic diagnoses on biopsy specimens included Barrett's esophagus without dysplasia (18), indefinite for dysplasia (6), low-grade dysplasia (16), high-grade dysplasia (4) and adenocarcinoma (2).

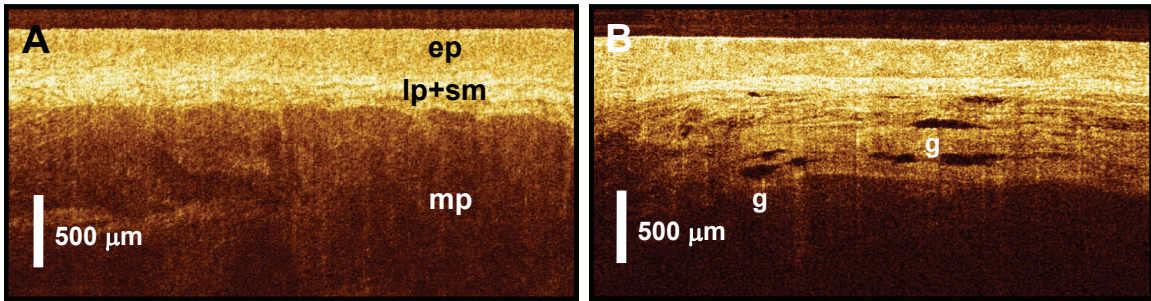
## **2.4 Imaging Results**

Figure 2.5 shows example images of normal stratified squamous esophageal mucosa. Representative histology is provided for reference. Consistent with previous studies, the distinct layered architecture of the squamous esophagus was visible on OCT. A five layered structure could typically be visualized, consisting of 1) a homogeneously scattering stratified epithelium (ep), 2) a highly scattering lamina propria (lp), 3) a weakly scattering and layered mucularis mucosa (mm), 4) a band of submucosa (sm), and 5) the deep muscularis propria (mp). Normal variants in the images of the layered esophagus are

shown in figure 2.6. Due to the fact that the longitudinal fibers of the muscularis layer occur in bundles, and a given cross-sectional OCT image may not intercept one of these bundles, one may see a three-layered pattern in which the lamina propria and submucosa blend together. In addition, the presence of large submucosal glands could frequently be detected. Squamous esophagus could clearly be differentiated from normal columnar gastric epithelium, which is shown together with the endoscopic photograph in figures 2.7a and 2.7b. On endoscopic view, the prominent gastric folds can be identified. In contrast to the layered architecture of the esophagus on OCT, gastric architecture is characterized on the images by relatively lower penetration depth and a distinct pattern of gastric pits and tubular glands. Corresponding histology in figure 2.7d illustrates this pattern of columnar surface epithelium with mucous cells. An OCT image of the squamo-columnar border in figure 2.8 further highlights the differences between normal squamous and junctoinal columnar epithelium. Variations in gastric architecture were evident in the fundus and pylorus, as shown in figure 2.9. Vertical pits in the body and fundus are shorter and straighter compared to the longer, more branching pit architecture of the pylorus.



**Figure 2.5.** UHR E-OCT image of normal squamous esophagus with representative histology. On OCT (A), a typical five layered appearance is visible including the epithelium (ep), lamina propria (lp), muscularis mucosa (mm), submucosa (sm), and muscularis propria (mp). The histology (B) is from a surgically resected specimen from another patient. Note that the muscularis layer can be difficult to detect on a given cross-section. In this histology specimen, it appears as only a few stray fibers rather than the distinct band seen on OCT. Figure 2.6 presents a similar appearance on OCT.



**Figure 2.6.** Normal variants in esophageal mucosa visualized on OCT. A three-layered mucosa (a) can be seen when the cross-sectional imaging plane does not intersect a bundle of muscularis fibers. Submucosal glands (g) can also be visualized frequently, as seen in (b).

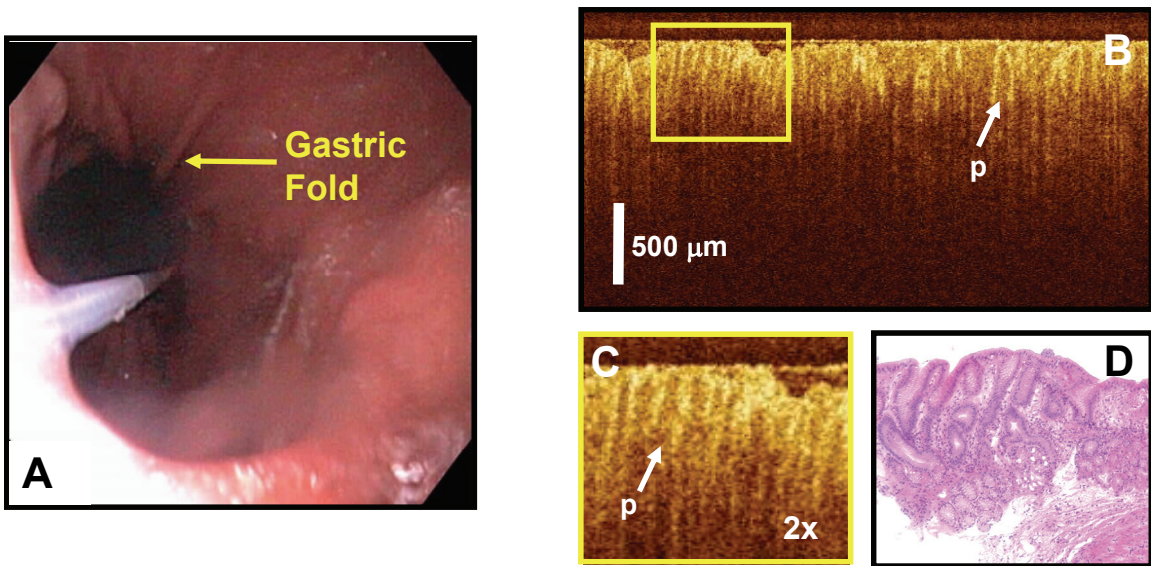


**Figure 2.7.** Gastric architecture visualized on OCT. Prominent mucosal folds are visible in the stomach on the endoscope view (A). On OCT (B,C), a distinct pattern of pits (p) is visible, which correlates well with histology (D). Histology in (D) is shown at the same scale as the image (B).

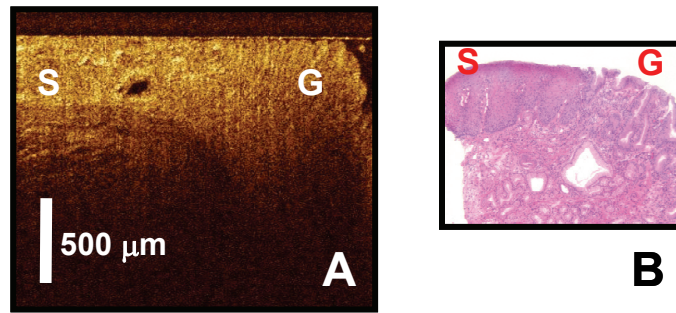


**Figure 2.8.** UHR EOCT image of the squamo-columnar junction. Squamous (S) and gastric (G) regions are clearly differentiated on OCT (A) with good correlation with histology (B). Histology is shown at the same scale as the OCT image.

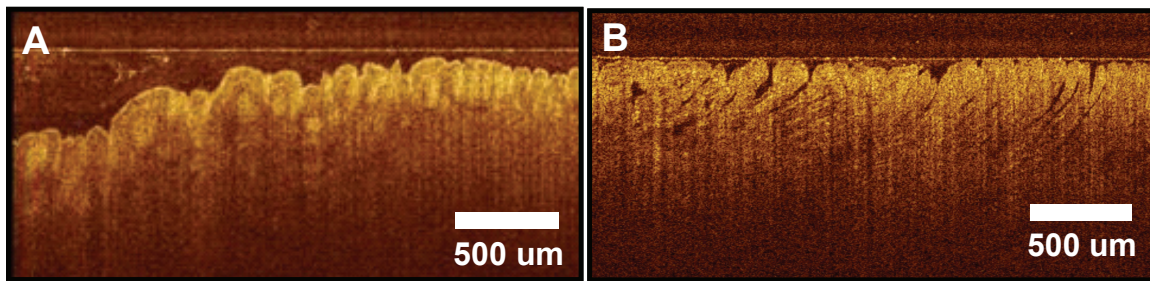


**Figure 2.9.** Variations in gastric mucosal architecture seen on OCT. The vertical pits in the body and fundus (A) are shorter and straighter compared to the longer, more branching pit architecture of the pylorus (B).

#### 2.4.1 OCT Imaging of Barrett’s Esophagus and Esophageal Adenocarcinoma

Selected images from three patients with Barrett’s esophagus are presented in figure 2.10. The endoscope view shows the transition between the light pink color of the normal squamous epithelium to the darker, salmon-colored columnar epithelium. As was seen in previous studies with standard resolution [16], UHR EOCT OCT images demonstrate loss of the distinct layered structure of the esophagus and the regular pit pattern of gastric mucosa. Irregularly spaced glands of varying sizes are prominent in the images, and a heterogenous tissue structure appears throughout the mucosa. The heterogeneity likely results from closely packed areas of Barrett’s glands and columnar epithelium, with highly scattering lamina propria interspersed. In the enlarged OCT images, the columnar epithelium bordering dilated glands can clearly be distinguished from the underlying lamina propria. In addition, select images show the presence of low scattering spaces in the epithelial layer, which is suggestive of the presence of goblet cells. Goblet cells are the histologic hallmark of specialized intestinal metaplasia of

the esophagus. Previous studies with standard resolution have not been able to identify individual goblet cells [16-18]. Corresponding histology for each of the cases confirmed the presence of specialized intestinal metaplasia with goblet cells in the regions imaged.

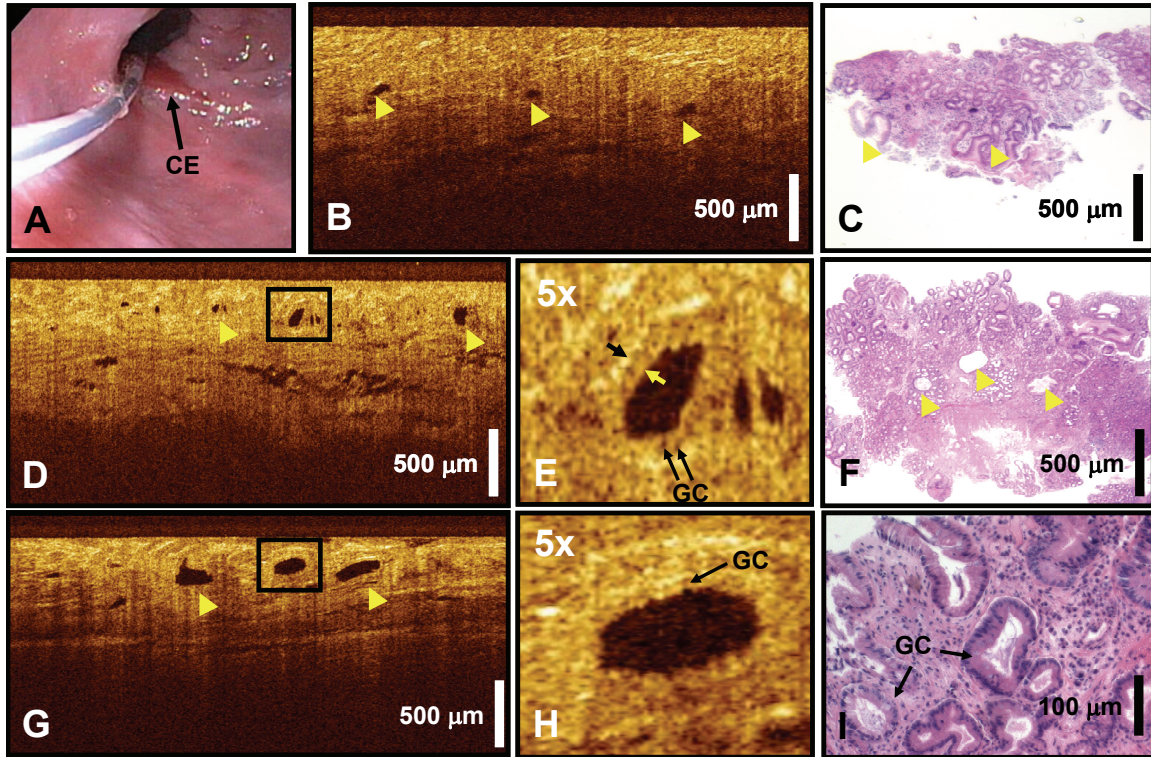


**Figure 2.10.** UHR EOCT images of Barrett's Esophagus. Images are taken from three separate patients. The typical endoscopic view (A) from one of the patients shows salmon-colored columnar epithelium. OCT images (B,D,G) demonstrate absence of the gastric pit or the layered squamous architecture, as well as irregularly-spaced Barrett's glands of varying sizes (arrowheads). Zoom views (E,H) of the glandular structure demonstrate that UHR OCT can visualize the columnar epithelial layer surrounding the glands. In addition, vacuous inclusions in the epithelial layer can be visualized in many glands, suggesting that UHR EOCT may be able to visualize the barrel-shaped goblet cells (GC), which are the hallmark trait of specialized intestinal metaplasia (SIM) of the esophagus. Corresponding histology (C to B; F to D,E; I to G,H) shown at the same scale as the OCT images confirmed the diagnosis of SIM. Histology view in (I) shows the presence of goblet cells in the Barrett's epithelium.

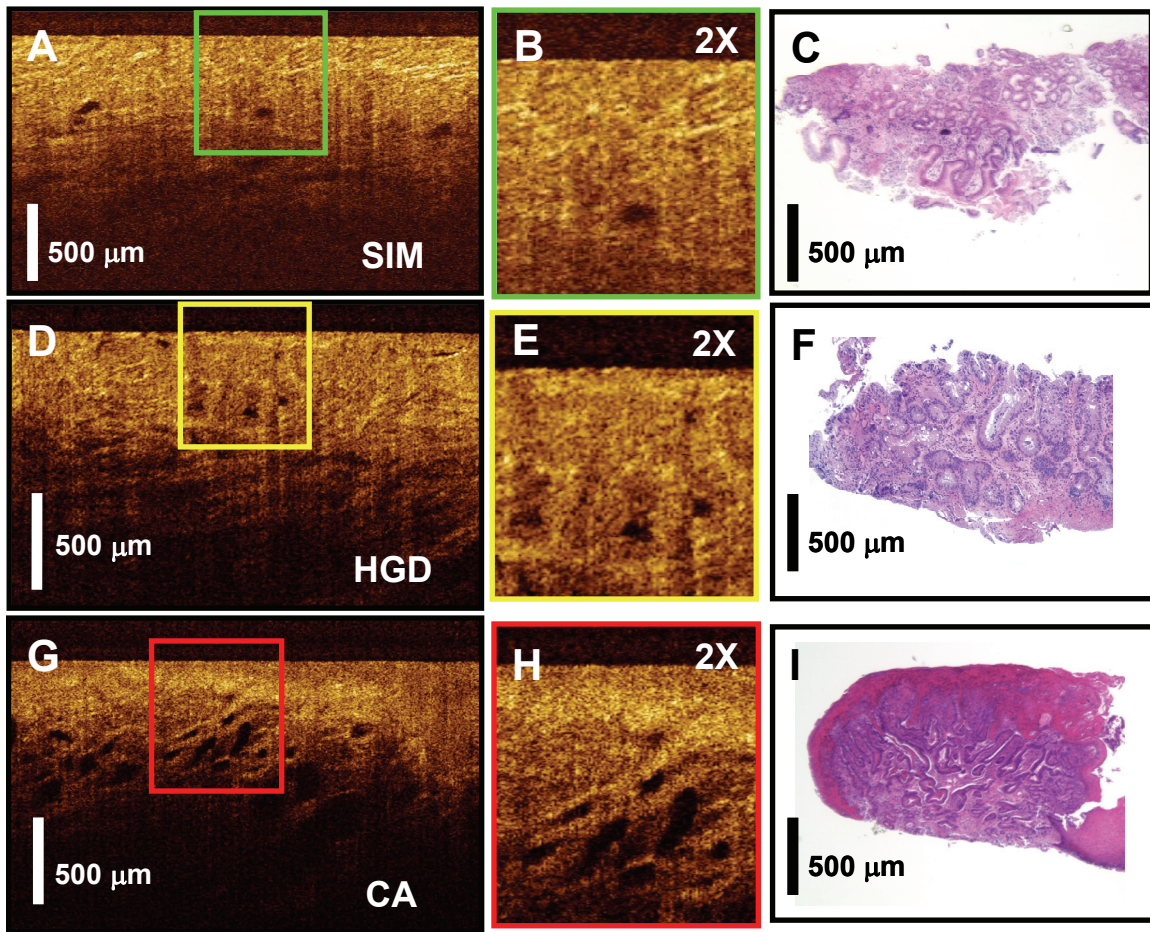


**Figure 2.11.** Image comparison of Barrett's without dysplasia, Barrett's with dysplasia, and invasive adenocarcinoma. Images are taken from three separate patients. A trend toward increasing glandular irregularity is noted in the progression from Barrett's (A,B) to high grade dysplasia (D,E) to invasive adenocarcinoma (G,H). Corresponding histology reviewed by a pathologist (C to A, F to D, I to G) was used to classify the images.

Figure 2.11 compares UHR EOCT images from separate patients of Barrett's esophagus, high grade dysplasia, and invasive adenocarcinoma. Image classification was again determined by histologic confirmation in the region imaged. In the sequence going from Barrett's to high grade dysplasia to adenocarcinoma, there is a trend on UHR EOCT images toward increasing glandular irregularity and density. In this study, images of high grade dysplasia tended in general to exhibit lower overall backscattering intensity as well as a finer tissue heterogeneity pattern compared to Barrett's epithelium without dysplasia. This can likely be attributed to denser packing of the glands with less intervening stroma. Moreover, the glandular entities themselves in high grade dysplasia tended to show irregular morphology, including cribriform architecture. Figure 2.11g shows the presence of elongated, highly

irregular glands of adenocarcinoma invading beneath a relatively intact squamous epithelium. Note the complete absence of the mucosal layers typically present beneath squamous epithelium.

#### **2.4.2 OCT Imaging of Gastric Polyps**

Figures 2.12 and 2.13 present OCT imaging results from a case of gastric polyposis. The patient was a 78 year-old female with a history of colorectal cancer who was evaluated by esophagogastroduodenoscopy (EGD) for previous diagnosis of Barrett's esophagus and the presence multiple gastric polyps. Innumerable polyps of widely varying shapes and sizes were present throughout the stomach, as shown on the endoscopic view in figure 2.12a. Prior to OCT imaging, endoscopic ultrasound (EUS) was performed to assess the possibility of invasion through the underlying muscularis. As shown in figure 2.12b, the EUS confirmed the presence of an intact muscularis (arrows). Two large polyps were selected for OCT imaging. The first was an elongated, pedunculated polyp (+) measuring 1.6 cm in length. The second was a friable, mass (\*) measuring approximately 2 cm in largest dimension. After imaging, these polyps were resected by snare polypectomy and sent for histology.

The pedunculated polyp was classified as a hyperplastic, while the friable mass was a mixed hyperplastic and adenomatous specimen with voluminous low-grade dysplasia and focal high grade. Two pathologists reviewed the slides and confirmed the diagnosis. The endoscope views of the hyperplastic and adenomatous polyps are shown in figures 2.13a and 2.13b. OCT images of the hyperplastic polyp in figures 2.13c and 2.13d show both cystic and glandular regions in the polyp. Areas of cystic dilation (2.13c) could be clearly differentiated from areas of dense glandular structure (2.13d) with accurate histologic correlation (figures 2.13f and 2.13g). By comparison, OCT images of the adenomatous polyp in 2.13e show dense tissue structure, presumably due to tightly packed glandular features. Images of the adenomatous polyp in general showed greater penetration depth with finer heterogeneity in scattered intensity compared to the hyperplastic polyp.

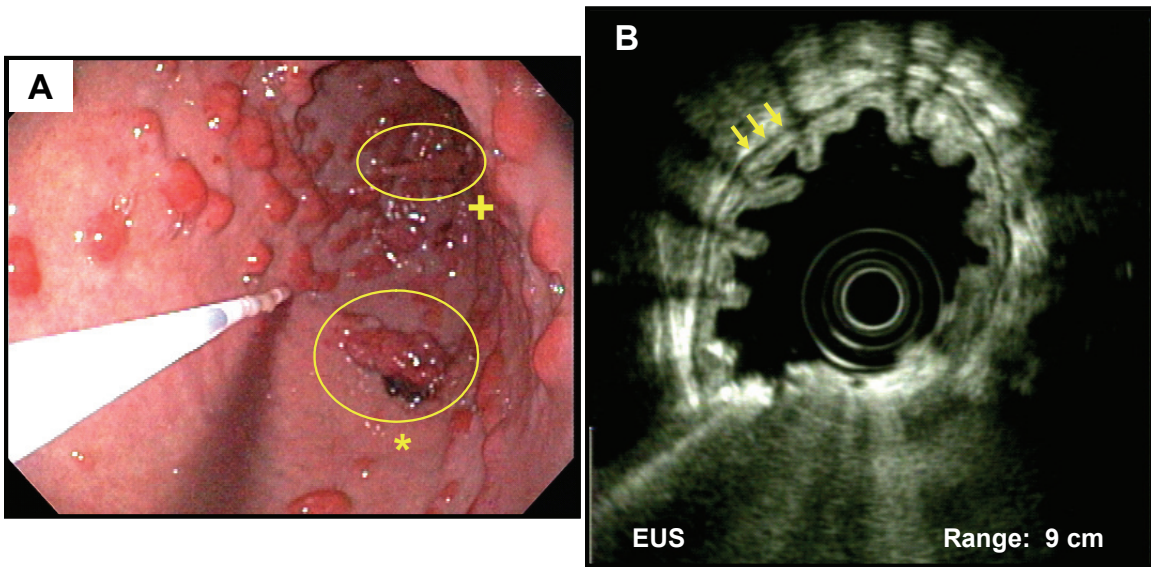


**Figure 2.12.** UHR EOCCT imaging of gastric polyps. The endoscopic view (A) shows innumerable polyps of varying sizes throughout the stomach. The OCT catheter is seen in the field of view of the scope. Endoscopic ultrasound (B) confirmed the presence of an intact muscularis layer (arrows).

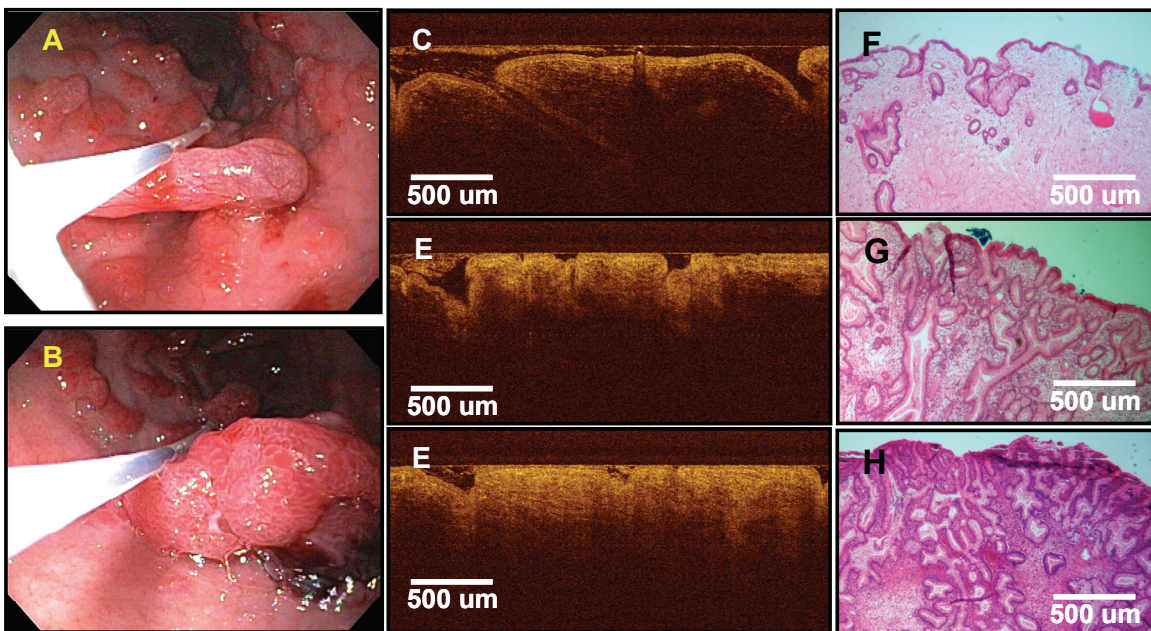


**Figure 2.13.** Image comparison of hyperplastic and adenomatous polyps. The specimen in (A) is a hyperplastic polyp while that in (B) is an adenomatous lesion. In the hyperplastic specimen, OCT differentiates cystic regions (C,F) from glandular regions (D,G). The OCT image of the adenomatous specimen (E) illustrates densely packed glandular morphology. Presence of diffuse low grade dysplasia was confirmed on histology (H).

## 2.5 Discussion of Results

The results of this study demonstrate ultrahigh resolution endoscopic OCT imaging in a series of patients previously diagnosed with Barrett’s esophagus. The optical resolution of the instrument measured  $\sim 4 \text{ um} \times 15 \text{ um}$  (axial x lateral), which is 3-4 times improvement in the axial dimension and between 1.3 - 2 times improvement in the transverse dimension compared to most previous studies. Table 2.1 compares the performance specifications for the instruments used by several groups for endoscopic OCT. Data was taken from several recent references [15, 16, 19-24]. The UHR EOCT system maintained state of the art performance in all categories while significantly enhancing resolution. In addition to broad optical bandwidth, the portable Cr:Forsterite light source used in this study provided excellent noise characteristics and superior output power to enable high sensitivity imaging. Moreover, the source was integrated with a highly engineered commercial prototype complete with an all digital receiver and polarization diversity detection.

<b>Parameter</b>	<b>Bouma [15] 1999</b>	<b>Rollins [20] 1999</b>	<b>Jackle [23] 2000</b>	<b>Li [21] 2000</b>	<b>UHR EOCT</b>
<b>Wavelength</b>	<b>1310 nm</b>	<b>1310 nm</b>	<b>1270 nm</b>	<b>1310 nm</b>	<b>1260 nm</b>
<b>Optical Resolution (lat x axial)</b>	<b>25 um x 10 um</b>	<b>25 um x 11 um</b>	<b>20 um x 12 um</b>	<b>13 um x 13 um</b>	<b>15 um x 3.7 um</b>
<b>Scan Method</b>	<b>Linear</b>	<b>Radial</b>	<b>Linear</b>	<b>Linear</b>	<b>Linear</b>
<b>Scan Size (w x d)</b>	<b>5.5 mm x 2.5 mm</b>	<b>3.5 mm radius</b>	<b>1.7 mm x 1.2 mm</b>	<b>4 mm x 2.5 mm</b>	<b>3 mm x 2.5 mm</b>
<b>Pixel Sampling (w x d)</b>	<b>512 x 256</b>	<b>600 x 600</b>	<b>200 x 200</b>	<b>512 x 512</b>	<b>600 x 1600</b>
<b>Nyquist Image Resolution (w x d)</b>	<b>11 um x 10 um</b>	<b>Varies x 11.7 um</b>	<b>17 um x 12 um</b>	<b>16 um x 10 um</b>	<b>10 um x 3 um</b>
<b>Incident Power</b>	<b>5 mW</b>	<b>5 mW</b>	<b>1.5 mW</b>	<b>5 mW</b>	<b>10 – 20 mW</b>
<b>Imaging Speed</b>	<b>4 fps</b>	<b>6.7 fps</b>	<b>0.33 fps</b>	<b>4 fps</b>	<b>4 fps</b>
<b>Probe Diameter</b>	<b>2.0 mm</b>	<b>2.4 mm</b>	<b>2.7 mm</b>	<b>1.0 mm</b>	<b>1.8 mm</b>

**Table 2.1.** Comparison of system performance for endoscopic OCT systems.

The UHR EOCT images provided enhanced visualization of fine tissue microstructural features compared to standard resolution endoscopic OCT. Because of the smaller optical volume sampled by the high resolution system, the coherent speckle in the images was reduced in size compared to traditional systems. Speckle noise degrades image quality and serves to reduce effective resolution by obscuring fine structural features. With UHR EOCT, the squamous mucosal layers as well as the gastric pit architecture could be clearly defined. In addition, subtle features in Barrett's mucosa could be appreciated, including the epithelial layer surrounding some glandular entities. Moreover, small inclusions in the epithelial layer suggestive of goblet cells were noted in several images. Goblet cells could not be visualized with previous OCT systems [16]. Typical goblet cells measure approximately 20 um in diameter, which is near or below the resolution limit of previous system designs. However, the improved performance of the UHR EOCT system brings the goblet cell within the resolution limit of the system, potentially enabling recognition. The goblet cell is the histologic hallmark of Barrett's esophagus, and the ability to recognize it *in situ* may improve the accuracy of endoscopic OCT for the diagnosis of Barrett's esophagus. Granted, the previously reported numbers of 97 % sensitivity and 92% specificity are quite high already [16]. However, this study has not been repeated with a larger patient population, nor has a study of intraobserver variability been performed. Given that a single experienced observer classified images in that study, it is reasonable to expect that these numbers may vary among less experienced observers. The improved image quality provided by UHR EOCT will likely offer additional power to the previously reported image criteria for diagnosis of Barrett's esophagus and may enable new criteria based upon previously unappreciated image features.

UHR EOCT should also be an important advance for the detection of high grade dysplasia in Barrett's esophagus. This study was not designed nor powered to determine the ability of UHR EOCT to identify dysplasia in the setting of Barrett's esophagus; however, enhanced image quality compared to previously reported results raises hope that the method can also help to improve upon existing work in this area. UHR EOCT visualized fine glandular structures, and the small speckle size allowed better appreciation of tissue heterogeneity, which is related to structure below the resolution and contrast limit of the instrument. Previous work with standard resolution EOCT has reported sensitivity of 68%, specificity of 82%, and diagnostic accuracy of 78% in a prospective, double-blind study [25]. Furthermore, the diagnostic accuracy for four endoscopists ranged from 56% to 98%. A second study looked at defining image criteria for high grade dysplasia on EOCT images [19]. This work reported 83% sensitivity and 75% specificity for the diagnosis for intramucosal adenocarcinoma or high grade dysplasia grouped together. The results from this study were based on a single highly experienced observer, however, and no assessment of intraobserver variability was determined. As with the diagnosis of

Barrett's, improvements in resolution and image quality should contribute to further developing diagnostic criteria for reading EOCT images.

Recent work suggests that computer aided diagnosis will improve the accuracy of endoscopic OCT for the diagnosis of Barrett's esophagus and dysplasia [25, 26]. Computer algorithms based upon texture analysis and principal component analysis will allow standardization of image interpretation across users and may allow appreciation of subtle image features not recognized by a human observer. UHR EOCT, with enhanced visualization of fine tissue structure, should improve performance of these algorithms.

UHR EOCT images of adenocarcinoma suggest a role for the technology in surveying tumor margins. In figure 2.11g, invasive malignant glands are shown beneath a squamous epithelium. This demonstrates the ability to image with high resolution several hundred microns below the surface. Imaging of lesion margins may be particularly relevant during endoscopic mucosal resection. As endoscopic methods advance, it is likely that an increasing number of therapeutic procedures will be performed. The ability to visualize subsurface features with EOCT may prove important in monitoring therapy as well as in aiding diagnosis.

In addition to surveillance in Barrett's esophagus, endoscopic OCT may prove important for surveillance in polyposis syndromes of the upper and lower gastrointestinal tracts. The results in figure 2.13 suggest that UHR EOCT may be useful in distinguishing polyp subtypes in the stomach. In settings where resection of the portion of the affected organ is undesirable or not possible due to pre-existing conditions, frequent surveillance may be the most appropriate option. Moreover, forceps biopsy sampling may provide inadequate tissue for correct diagnosis in gastric polyps with histologic heterogeneity [27]. An imaging method that can rapidly survey polyps for targeted biopsies may be clinically useful in the setting of polyposis syndromes.

The study described in this chapter had some limitations. First, the *in vivo* OCT images were difficult to register with pinch biopsy histology. Endoscopes with a single accessory channel were used, which required sequential imaging and pinch biopsy. Imaging was often performed over visually identifiable landmarks to improve the correlation accuracy with histology. In most cases, however, correlation could be achieved with only 5-10 mm accuracy. This limits the certainty to which one can classify OCT images based on the histologic diagnosis, particularly in the case of focal processes. Another group has developed a more sophisticated approach using a dual channel endoscope and a modified EMR cap to allow nearly simultaneous sampling of EOCT images and pinch biopsy [25]. Such approaches are surely important to implement in future studies using UHR EOCT. This study was also limited in its design to an observational study and was not powered to provide statistical assessment of the improvement over standard resolution systems. Further studies should focus on providing quantitative measures of improvement. Finally, the study was limited by the complexity of the technology. The Cr:Forsterite laser

was very sensitive to environmental conditions and required daily alignment and adjustment in the clinical environment. It required consistent attention from research scientists and was not suitable for routine operation by physicians.

## 2.6. Prospects for Further Advances in Technology

A number of key technology developments promise to advance research efforts in endoscopic OCT. Commercially available femtosecond oscillators can provide improved reliability and portability compared to the Cr:Forsterite used in this study. In addition, new wavelength regions can be investigated. Most previous work has been done at 1300 nm because of the increased penetration provided by the longer NIR wavelength. For detection of dysplasia, however, the resolution may be the most important parameter to optimize rather than the penetration depth. Shorter wavelengths around 800 nm will provide higher resolution at the expense of penetration depth. Furthermore, the wavelength window around 1060 nm has not yet been well explored for imaging in scattering tissue. Previous work suggests that 1060 nm may offer a compromise between 800 nm and 1300 nm, and could in fact be an optimal wavelength for ultrahigh resolution OCT imaging in certain tissues [28-31].

In addition, newly developed Fourier domain detection methods for OCT promise to dramatically improve imaging speeds for endoscopic applications [32-37]. Developments in swept source OCT are particularly promising [38-40]. In one study, imaging speeds of up to 370,000 lines/second were achieved, enabling real time volumetric imaging [41]. Subsequently, swept source OCT has been demonstrated for wide area coverage, endoscopic volumetric microscopy *in vivo* [42-44]. In surveillance applications where sampling errors can occur, the ability to comprehensively image large areas of tissue may be particularly important. When combined with computer aided diagnosis algorithms, this may enable new approaches to fast screening of large areas which will reduce false negative rates that limit traditional pinch biopsy approaches.

Fast three-dimensional imaging will allow visualization of tissue microstructure in arbitrary imaging planes. Figure 2.14 provides an example of three-dimensional imaging in a gastrointestinal specimen. The images are from the gastric polyps shown in figure 2.13. Imaging was performed *ex vivo* after polyp resection with a benchtop time-domain UHR OCT microscope. In 2.14a, multiple slices are shown to illustrate the ability to section in any plane. *En face* image sections of the hyperplastic polyp and the adenomatous polyp are shown in figures 2.14b and 2.14c, respectively. The *en face* images were rendered from consecutive cross-sectional images and contain 385 x 370 pixels with aspect ratio of 1.15 x 1.85 mm. These views highlight distinct features in the tissue architecture which were difficult to visualize in the cross-sectional images. In particular, hyperplastic pits with a stellate appearance are evident in 2.14b while adenomatous crypts with thickened tubular epithelium can be seen in figure 2.14c.

The complementary views provided by *en face* and cross-sectional planes may prove useful in distinguishing hyperplastic versus adenomatous lesions.

Three-dimensional datasets can also be processed in novel ways to extract further information. Figure 2.15 presents two such methods of display. In 2.15a and 2.15b, the hyperplastic and adenomatous polyps viewed *en face* in figure 2.14 are shown in a three-dimensional rendered format. This view highlights the surface contours of the specimen. In 2.15c and 2.15d, the same datasets are shown collapsed in an *en face* projection. Projection views are commonly used in all forms of medical imaging, including CT, MR, and optical. The sum intensity projection used here enables a two-dimensional *en face* representation to incorporate the perception of depth. This representation of the OCT data gives a perspective which is strikingly similar to that provided by magnification endoscopy. The ability to relate the OCT dataset to an existing clinical method would make the technique more user-friendly and ultimately aid in its clinical acceptance.

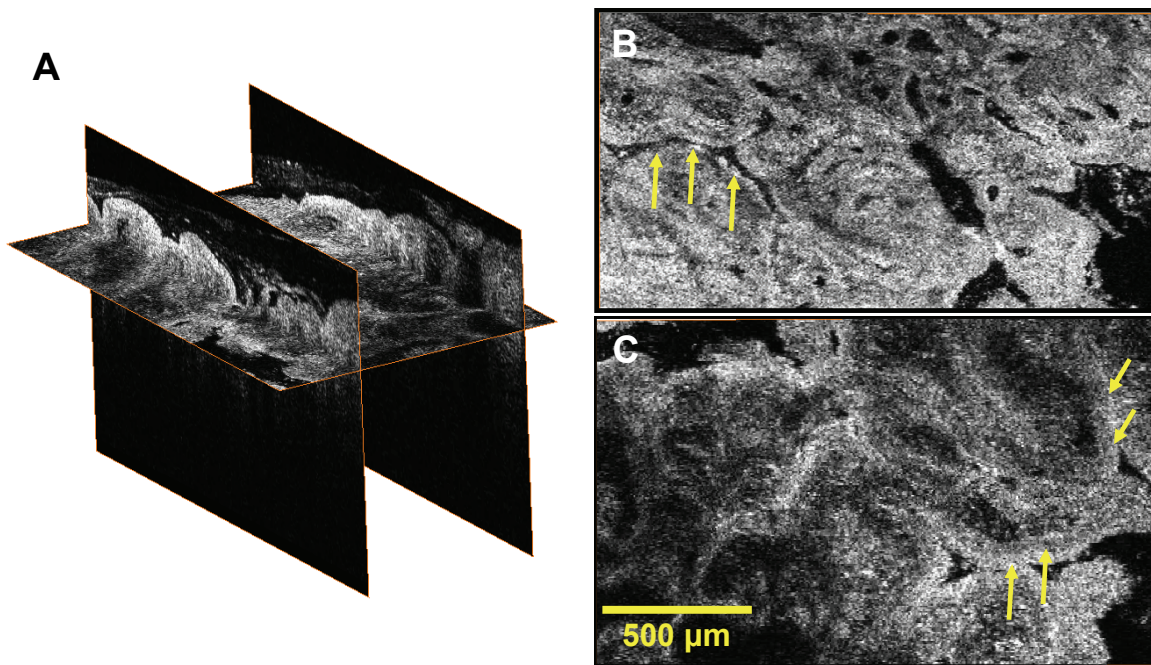


**Figure 2.14.** Ultrahigh resolution, three-dimensional imaging of two gastric polyp specimens. Arbitrary section planes can be viewed from the acquired dataset (A). The *en face* view illustrates star-shaped crypts in the hyperplastic polyp (B, arrows) as well as thickened crypt epithelium in the adenomatous polyp (C, arrows).

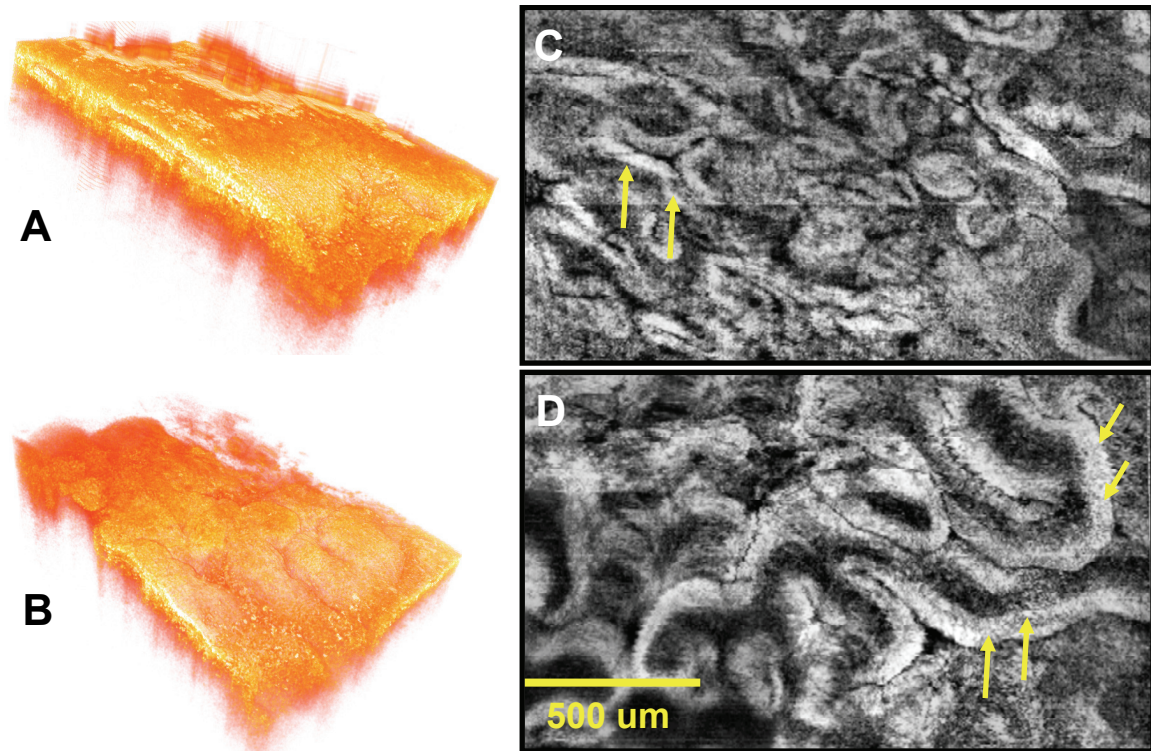


**Figure 2.15.** Alternate presentation modes for three-dimensional OCT volume data sets. (A,B) Rendered format. (C,D) *En face* projection view.

Further improvements in resolution are also under development. Even with novel light sources for ultrahigh resolution, traditional OCT approaches are not capable of reliably visualizing cellular features. Endoscopic confocal microscopy methods are being developed to enable real-time cellular resolution [45, 46]. Moreover, optical coherence microscopy (OCM) is an extension of optical coherence tomography to the confocal limit [47]. Development of endoscopic OCM systems promises to bring OCT imaging to the cellular level.

## 2.7 References

- [1] P. R. Herz, "Minimally invasive diagnostic imaging using high resolution Optical Coherence Tomography," in *Dept. of Electrical Engineering and Computer Science*. Cambridge: Massachusetts Institute of Technology, 2004, pp. 244.
- [2] Y. Chen, A. D. Aguirre, P. L. Hsiung, S. Desai, P. R. Herz, M. Pedrosa, Q. Huang, M. Figueiredo, S. W. Huang, A. Koski, J. M. Schmitt, J. G. Fujimoto, and H. Mashimo, "Ultrahigh resolution optical coherence tomography of Barrett's esophagus: preliminary descriptive clinical study correlating images with histology," *Endoscopy*, vol. 39, pp. 599-605, 2007.
- [3] P. R. Herz, Y. Chen, A. D. Aguirre, J. G. Fujimoto, H. Mashimo, J. Schmitt, A. Koski, J. Goodnow, and C. Petersen, "Ultrahigh resolution optical biopsy with endoscopic optical coherence tomography," *Optics Express*, vol. 12, pp. 3532-3542, 2004.
- [4] K. Schneider, "Compact and Portable Modelocked Cr:Forsterite Laser," Massachusetts Institute of Technology, 2002, pp. 22.
- [5] J. M. Schmitt and S. H. Xiang, "Cross-polarized backscatter in optical coherence tomography of biological tissue," *Optics Letters*, vol. 23, pp. 1060-2, 1998.
- [6] A. V. Oppenheim, R. W. Schaffer, and J. R. Buck, *Discrete-Time Signal Processing*, 2nd ed. Upper Saddle River: Prentice Hall, 1998.
- [7] J. Schmitt, "Personal Communication," A. D. Aguirre, Ed. Cambridge, 2003.
- [8] B. E. Bouma, G. J. Tearney, I. P. Bilinsky, B. Golubovic, and J. G. Fujimoto, "Self-phase-modulated Kerr-lens mode-locked Cr:forsterite laser source for optical coherence tomography," *Optics Letters*, vol. 21, pp. 1839-1841, 1996.
- [9] G. J. Tearney, M. E. Brezinski, B. E. Bouma, S. A. Boppart, C. Pitris, J. F. Southern, and J. G. Fujimoto, "In vivo endoscopic optical biopsy with optical coherence tomography," *Science*, vol. 276, pp. 2037-9, 1997.
- [10] F. X. Kartner, N. Matuschek, T. Schibli, U. Keller, H. A. Haus, C. Heine, R. Morf, V. Scheuer, M. Tilsch, and T. Tschudi, "Design and fabrication of double-chirped mirrors," *Optics Letters*, vol. 22, pp. 831-833, 1997.
- [11] G. J. Tearney, S. A. Boppart, B. E. Bouma, M. E. Brezinski, N. J. Weissman, J. F. Southern, and J. G. Fujimoto, "Scanning single-mode fiber optic catheter-endoscope for optical coherence tomography," *Optics Letters*, vol. 21, pp. 543-5, 1996.
- [12] J. M. Ponerros, G. J. Tearney, M. Shiskov, P. B. Kelsey, G. Y. Lauwers, N. S. Nishioka, and B. E. Bouma, "Optical coherence tomography of the biliary tree during ERCP," *Gastrointest Endosc*, vol. 55, pp. 84-8, 2002.
- [13] M. V. Sivak, Jr., K. Kobayashi, J. A. Izatt, A. M. Rollins, R. Ung-Runyawee, A. Chak, R. C. Wong, G. A. Isenberg, and J. Willis, "High-resolution endoscopic imaging of the GI tract using optical coherence tomography," *Gastrointest Endosc*, vol. 51, pp. 474-9, 2000.
- [14] P. R. Pfau, M. V. Sivak, Jr., A. Chak, M. Kinnard, R. C. Wong, G. A. Isenberg, J. A. Izatt, A. Rollins, and V. Westphal, "Criteria for the diagnosis of dysplasia by endoscopic optical coherence tomography," *Gastrointest Endosc*, vol. 58, pp. 196-202, 2003.
- [15] B. E. Bouma and G. J. Tearney, "Power-efficient nonreciprocal interferometer and linear-scanning fiber-optic catheter for optical coherence tomography," *Optics Letters*, vol. 24, pp. 531-3, 1999.
- [16] J. M. Ponerros, S. Brand, B. E. Bouma, G. J. Tearney, C. C. Compton, and N. S. Nishioka, "Diagnosis of specialized intestinal metaplasia by optical coherence tomography," *Gastroenterology*, vol. 120, pp. 7-12, 2001.
- [17] A. Chak, M. B. Wallace, and J. M. Ponerros, "Optical coherence tomography of Barrett's esophagus," *Endoscopy*, vol. 37, pp. 587-90, 2005.
- [18] J. M. Ponerros, "Diagnosis of Barrett's esophagus using optical coherence tomography," *Gastrointest Endosc Clin N Am*, vol. 14, pp. 573-88, x, 2004.

- [19] J. A. Evans, J. M. Ponerros, B. E. Bouma, J. Bressner, E. F. Halpern, M. Shishkov, G. Y. Lauwers, M. Mino-Kenudson, N. S. Nishioka, and G. J. Tearney, "Optical coherence tomography to identify intramucosal carcinoma and high-grade dysplasia in Barrett's esophagus," *Clin Gastroenterol Hepatol*, vol. 4, pp. 38-43, 2006.
- [20] A. M. Rollins, R. Ung-arunyawee, A. Chak, R. C. K. Wong, K. Kobayashi, M. V. Sivak, Jr., and J. A. Izatt, "Real-time in vivo imaging of human gastrointestinal ultrastructure by use of endoscopic optical coherence tomography with a novel efficient interferometer design," *Optics Letters*, vol. 24, pp. 1358-60, 1999.
- [21] X. D. Li, S. A. Boppart, J. Van Dam, H. Mashimo, M. Mutinga, W. Drexler, M. Klein, C. Pitris, M. L. Krinsky, M. E. Brezinski, and J. G. Fujimoto, "Optical coherence tomography: advanced technology for the endoscopic imaging of Barrett's esophagus," *Endoscopy*, vol. 32, pp. 921-30, 2000.
- [22] G. Zuccaro, N. Gladkova, J. Vargo, F. Feldchtein, E. Zagaynova, D. Conwell, G. Falk, J. Goldblum, J. Dumot, J. Ponsky, G. Gelikonov, B. Davros, E. Donchenko, and J. Richter, "Optical coherence tomography of the esophagus and proximal stomach in health and disease," *Am J Gastroenterol*, vol. 96, pp. 2633-9, 2001.
- [23] S. Jackle, N. Gladkova, F. Feldchtein, A. Terentjeva, B. Brand, G. Gelikonov, V. Gelikonov, A. Sergeev, A. Fritscher-Ravens, J. Freund, U. Seitz, S. Soehendra, and N. Schroder, "In vivo endoscopic optical coherence tomography of the human gastrointestinal tract--toward optical biopsy," *Endoscopy*, vol. 32, pp. 743-9, 2000.
- [24] S. Brand, J. M. Ponerros, B. E. Bouma, G. J. Tearney, C. C. Compton, and N. S. Nishioka, "Optical coherence tomography in the gastrointestinal tract," *Endoscopy*, vol. 32, pp. 796-803, 2000.
- [25] G. Isenberg, M. V. Sivak, Jr., A. Chak, R. C. Wong, J. E. Willis, B. Wolf, D. Y. Rowland, A. Das, and A. Rollins, "Accuracy of endoscopic optical coherence tomography in the detection of dysplasia in Barrett's esophagus: a prospective, double-blinded study," *Gastrointest Endosc*, vol. 62, pp. 825-31, 2005.
- [26] X. Qi, M. V. Sivak, D. L. Wilson, and A. M. Rollins, "Computer aided diagnosis (CAD) of dysplasia in Barrett's esophagus (BE) using endoscopic optical coherence tomography (EOCT)," *Gastroenterology*, vol. 126, pp. A351-A351, 2004.
- [27] G. Oberhuber and M. Stolte, "Gastric polyps: an update of their pathology and biological significance," *Virchows Arch*, vol. 437, pp. 581-90, 2000.
- [28] G. J. Tearney and Massachusetts Institute of Technology. Dept. of Electrical Engineering and Computer Science., "Optical biopsy of in vivo tissue using optical coherence tomography," 1996, pp. 220 leaves.
- [29] Y. M. Wang, J. S. Nelson, Z. P. Chen, B. J. Reiser, R. S. Chuck, and R. S. Windeler, "Optimal wavelength for ultrahigh-resolution optical coherence tomography," *Optics Express*, vol. 11, pp. 1411-1417, 2003.
- [30] S. Bourquin, A. D. Aguirre, I. Hartl, P. Hsiung, T. H. Ko, J. G. Fujimoto, T. A. Birks, W. J. Wadsworth, U. Bunting, and D. Kopf, "Ultrahigh resolution real time OCT imaging using a compact femtosecond Nd : Glass laser and nonlinear fiber," *Optics Express*, vol. 11, pp. 3290-3297, 2003.
- [31] H. Lim, Y. Jiang, Y. Wang, Y. C. Huang, Z. Chen, and F. W. Wise, "Ultrahigh-resolution optical coherence tomography with a fiber laser source at 1 microm," *Opt Lett*, vol. 30, pp. 1171-3, 2005.
- [32] R. Leitgeb, C. K. Hitzenberger, and A. F. Fercher, "Performance of Fourier domain vs. time domain optical coherence tomography," *Optics Express*, vol. 11, pp. 889-894, 2003.
- [33] J. F. de Boer, B. Cense, B. H. Park, M. C. Pierce, G. J. Tearney, and B. E. Bouma, "Improved signal-to-noise ratio in spectral-domain compared with time-domain optical coherence tomography," *Opt Lett*, vol. 28, pp. 2067-9, 2003.

- [34] M. A. Choma, M. V. Sarunic, C. H. Yang, and J. A. Izatt, "Sensitivity advantage of swept source and Fourier domain optical coherence tomography," *Optics Express*, vol. 11, pp. 2183-2189, 2003.
- [35] N. Nassif, B. Cense, B. H. Park, S. H. Yun, T. C. Chen, B. E. Bouma, G. J. Tearney, and J. F. de Boer, "In vivo human retinal imaging by ultrahigh-speed spectral domain optical coherence tomography," *Opt Lett*, vol. 29, pp. 480-2, 2004.
- [36] M. Wojtkowski, T. Bajraszewski, P. Targowski, and A. Kowalczyk, "Real-time in vivo imaging by high-speed spectral optical coherence tomography," *Opt Lett*, vol. 28, pp. 1745-7, 2003.
- [37] M. Wojtkowski, V. J. Srinivasan, T. H. Ko, J. G. Fujimoto, A. Kowalczyk, and J. S. Duker, "Ultrahigh-resolution, high-speed, Fourier domain optical coherence tomography and methods for dispersion compensation," *Optics Express*, vol. 12, pp. 2404-2422, 2004.
- [38] S. H. Yun, G. J. Tearney, J. F. de Boer, N. Iftimia, and B. E. Bouma, "High-speed optical frequency-domain imaging," *Optics Express*, vol. 11, pp. 2953-2963, 2003.
- [39] R. Huber, M. Wojtkowski, K. Taira, J. G. Fujimoto, and K. Hsu, "Amplified, frequency swept lasers for frequency domain reflectometry and OCT imaging: design and scaling principles," *Optics Express*, vol. 13, pp. 3513-3528, 2005.
- [40] R. Huber, M. Wojtkowski, and J. G. Fujimoto, "Fourier Domain Mode Locking (FDML): A new laser operating regime and applications for optical coherence tomography," *Optics Express*, vol. 14, pp. 3225-3237, 2006.
- [41] R. Huber, D. C. Adler, and J. G. Fujimoto, "Buffered Fourier domain mode locking: unidirectional swept laser sources for optical coherence tomography imaging at 370,000 lines/s," *Optics Letters*, vol. 31, pp. 2975-2977, 2006.
- [42] S. H. Yun, G. J. Tearney, B. J. Vakoc, M. Shishkov, W. Y. Oh, A. E. Desjardins, M. J. Suter, R. C. Chan, J. A. Evans, I. K. Jang, N. S. Nishioka, J. F. de Boer, and B. E. Bouma, "Comprehensive volumetric optical microscopy in vivo," *Nat Med*, vol. 12, pp. 1429-33, 2006.
- [43] B. J. Vakoc, M. Shishko, S. H. Yun, W. Y. Oh, M. J. Suter, A. E. Desjardins, J. A. Evans, N. S. Nishioka, G. J. Tearney, and B. E. Bouma, "Comprehensive esophageal microscopy by using optical frequency-domain imaging (with video)," *Gastrointest Endosc*, vol. 65, pp. 898-905, 2007.
- [44] D. C. Adler, Y. Chen, R. Huber, J. Schmitt, J. Connolly, and J. G. Fujimoto, "Three-dimensional endomicroscopy using optical coherence tomography," *Nature Photonics*, vol. 1, pp. 709-716, 2007.
- [45] R. Kiesslich, J. Burg, M. Vieth, P. Delaney, D. Janell, S. Thomas, P. R. Galle, and M. F. Neurath, "Subsurface analysis of colon neoplasias by confocal laser colonoscopy and virtual histology: A novel diagnostic tool for predicting cancer during screening colonoscopy," *Gastrointestinal Endoscopy*, vol. 59, pp. Ab97-Ab97, 2004.
- [46] R. Kiesslich, J. Burg, M. Vieth, J. Gnaendiger, M. Enders, P. Delaney, A. Polglase, W. McLaren, D. Janell, S. Thomas, B. Nafe, P. R. Galle, and M. F. Neurath, "Confocal laser endoscopy for diagnosing intraepithelial neoplasias and colorectal cancer in vivo," *Gastroenterology*, vol. 127, pp. 706-713, 2004.
- [47] J. A. Izatt, M. R. Hee, G. M. Owen, E. A. Swanson, and J. G. Fujimoto, "Optical coherence microscopy in scattering media," *Optics Letters*, vol. 19, pp. 590-2, 1994.

## Chapter 3

# Supercontinuum Light Sources for Ultrahigh Resolution Optical Coherence Tomography

### 3.1 Overview

Work in the previous chapter was performed with a portable Cr:Forsterite laser source. While the performance was excellent, the laser lacked the stability and reliability for routine use in the clinical setting by users who are not trained to work with femtosecond lasers. Moreover, the Forsterite laser was not commercially available and therefore restricted in use only to research groups with sufficient expertise to build the source themselves. This chapter covers the development of light sources for ultrahigh resolution OCT imaging based on a commercially available femtosecond oscillator and the phenomenon of continuum generation in highly nonlinear fibers. The results demonstrate that femtosecond laser sources for ultrahigh resolution OCT can be made reliable and widely available for OCT imaging in highly scattering tissues.

### 3.2 Introduction

Optical coherence tomography (OCT) enables high-resolution cross-sectional imaging of tissue microstructure without the need for tissue excision and processing [1] and has therefore been investigated for minimally invasive imaging in several areas of biology and medicine [2]. OCT performs optical imaging in scattering tissue using low-coherence interferometry, and the axial range resolution scales inversely with the optical bandwidth,  $\Delta\lambda$ , of the light source as  $\lambda_0^2/\Delta\lambda$ , where  $\lambda_0$  is the center wavelength of the source. Traditional OCT imaging systems are based on superluminescent diode light sources, which enable imaging resolutions of 10 – 15  $\mu\text{m}$ . Broadband modelocked Ti:Al<sub>2</sub>O<sub>3</sub> lasers have been demonstrated to extend the axial resolution to 1-5  $\mu\text{m}$  in tissue [3, 4], leading to the term ultrahigh resolution OCT. These sources directly provide broad bandwidth and high power and are well suited for real time biomedical imaging, particularly in the relatively transparent tissues of the eye [5]. The high cost and complexity of femtosecond Ti:Al<sub>2</sub>O<sub>3</sub> sources has driven the development of lower cost alternatives for ultrahigh resolution OCT imaging, including low-threshold Ti:Al<sub>2</sub>O<sub>3</sub> lasers capable of using low-power pump lasers [6, 7], continuum generation in highly nonlinear fibers [8], diode-pumped

Cr:LiCAF lasers [9], thermal light sources [10], superluminescent Ti:Al<sub>2</sub>O<sub>3</sub> sources [11, 12], and multiplexed superluminescent diode sources [13]. As a result of these developments as well as commercialization of suitable Ti:Al<sub>2</sub>O<sub>3</sub> laser sources, ultrahigh resolution OCT imaging in the 800 nm wavelength range is becoming widely available to the research community.

*In vivo* OCT imaging in scattering tissues other than the eye is typically performed at 1300 nm to take advantage of reduced scattering and enhanced penetration at the longer near-infrared wavelength [14]. Suitably broadband ultrafast lasers for ultrahigh resolution are not common at this wavelength and research has therefore focused on spectral broadening techniques using nonlinear mechanisms in optical fibers. A Cr:forsterite femtosecond laser with the bandwidth of the output pulse broadened in a dispersion shifted fiber has been used to achieve < 5  $\mu\text{m}$  axial resolution [15, 16]. The realization of supercontinuum generation in photonic crystal fibers (PCF's) [17] has enabled ultrahigh resolution OCT at wavelengths throughout the visible and near infrared [18-20]. OCT was performed at 1300 nm with resolutions as high as 2.5  $\mu\text{m}$  using a portion of the broadband continuum produced by a Ti:Al<sub>2</sub>O<sub>3</sub> pump laser and a PCF with zero dispersion at 800 nm [18]. Broadband continuum from highly nonlinear fibers has also been used to demonstrate ultrahigh resolution OCT in the wavelength range around 1000 nm as an alternative to 800 nm and 1300 nm [21-24]. This wavelength range has generated considerable interest for imaging in scattering tissues due to the optimal characteristics of water dispersion at 1000 nm [25]. Similarly, ultrahigh resolution OCT imaging using continuum generation at 1500 nm has recently been demonstrated [26].

Using continuum generation, reliable commercially available femtosecond lasers can be used to access different wavelengths throughout the near-infrared region. However, higher exposure limits for non-ocular tissues necessitate higher power sources for OCT imaging at wavelengths other than 800 nm. Controlling the continuum generation to simultaneously achieve high power and broad bandwidth with small spectral modulation and low amplitude noise is of primary interest. Broadening by self-phase modulation in the normal dispersion region of highly nonlinear fibers has proven effective in achieving these goals [27]. Using a portable Cr:Forsterite and spectral broadening in a dispersion shifted fiber, axial resolution of < 5  $\mu\text{m}$  has been achieved for *in vivo* endoscopic imaging [16]. Compact Cr:forsterite lasers are not commercially available, which will limit this technique for use at 1300 nm to investigators with significant femtosecond laser experience. Pumping near the zero dispersion wavelength of a PCF can generate very broad spectra extending beyond 1300 nm, but can result in unacceptably strong spectral modulation and noise amplification [28-30]. Furthermore, spectral filtering of a wavelength region away from the pump wavelength is inefficient and results in low source output power. A compact erbium fiber laser combined with a highly nonlinear fiber has been demonstrated for  $\sim 2$   $\mu\text{m}$  axial resolution at 1300 nm but had only 4 mW of output power due to inefficient spectral conversion [31]. A continuous-wave,

all-fiber Raman light source based on a microstructured fiber was capable of  $< 5 \mu\text{m}$  resolution in tissue with  $> 300 \text{ mW}$  output power from a  $10 \text{ W}$  pump source, but the continuum suffered from excess intensity noise [32].

Photonic crystal fiber technology is extremely powerful because it enables customization of the fiber dispersion profile, which can be used to control the nonlinear processes responsible for continuum generation. Recently, a novel photonic crystal fiber with two closely spaced zero dispersion wavelengths centered around  $860 \text{ nm}$  was reported for the generation of stable, compressible double peak spectra using a modelocked  $\text{Ti:Al}_2\text{O}_3$  laser broadened by a combination of self-phase modulation and four-wave mixing [33]. Unlike supercontinuum produced when a standard PCF is pumped near the zero dispersion wavelength, the continuum from the new PCF design was relatively insensitive to parameters of the input  $\text{Ti:Al}_2\text{O}_3$  pulse resulting in stable, low-noise spectra. In addition, the pump energy was efficiently depleted during the continuum generation to produce high brightness spectral peaks at higher and lower wavelengths, with the location of the peaks set by the zero dispersion wavelengths of the fiber.

In this chapter, broadband, stable light sources for ultrahigh resolution OCT imaging are demonstrated using supercontinuum generation in highly nonlinear fibers. A combination of numerical simulation and experiment has been used to optimize these sources. A commercially available, turnkey  $\text{Nd:Glass}$  femtosecond laser was used for the experiments. First, the  $\text{Nd:Glass}$  oscillator was combined with self-phase modulation in a high numerical aperture, normal dispersion fiber to demonstrate imaging at  $1060 \text{ nm}$  with  $< 5 \mu\text{m}$  axial resolution and  $> 100 \text{ mW}$  output power. Second, a novel PCF design with two closely spaced zero dispersion wavelengths was investigated for a broadband, stable continuum light source for ultrahigh resolution OCT imaging at either  $800 \text{ nm}$  or  $1300 \text{ nm}$ . By injecting pulses at  $1064 \text{ nm}$  from the  $\text{Nd:Glass}$  laser into the fiber, it was shown numerically and experimentally that a stable continuum can be generated with high brightness double peaks centered at  $800 \text{ nm}$  and  $1300 \text{ nm}$ , two primary wavelengths of interest to the OCT imaging community. The experimentally measured continuum achieved  $> 110 \text{ nm}$  bandwidth and  $30 \text{ mW}$  power in the  $800 \text{ nm}$  spectral peak and  $> 150 \text{ nm}$  and  $48 \text{ mW}$  in the  $1300 \text{ nm}$  peak, thereby enabling ultrahigh resolution imaging with  $< 5 \mu\text{m}$  in tissue at both wavelengths. In addition, numerical simulations were used to investigate the conditions for achieving a smooth, modulation free spectrum for optimal OCT imaging. In combination, this work suggests that a single commercially available oscillator combined with various highly nonlinear fibers can be used to generate stable, high brightness spectra for ultrahigh resolution OCT imaging throughout the near infrared wavelength region.

This work was performed in collaboration with scientists at HighQ Laser Production GmbH, located in Austria. Drs. Daniel Kopf and Wolfgang Seitz were instrumental for their collaboration in configuring and maintaining the  $\text{Nd:Glass}$  oscillator, and Dr. Max Lederer provided useful insight into the nonlinear

fiber experiments. From MIT, Dr. Norihiko Nishizawa performed the numerical simulations and provided consistent insight into all of the experimental studies. Dr. Nishizawa was visiting from Nagoya University in Japan at the time. Dr. Stephane Bourquin also contributed to early work with the high numerical aperture fiber.

### **3.3 SESAM-Modelocked Nd:Glass Femtosecond Oscillator**

The diode pumped femtosecond Nd:Glass laser (High Q Laser Production, IC199) used for this work generated a 52 MHz train of 84 fs pulses with 165 mW average power at 1064 nm center wavelength. The compact, prismless cavity had dimensions of only 50.8 cm x 20 cm x 7.5 cm and was pumped by two 1 W laser diodes. Self-starting soliton modelocking was achieved using a semiconductor saturable absorber mirror (SESAM) and intracavity dispersion was managed using chirped mirrors. Figure 3.1 presents a photograph of the laser as well as the experimental characterization. The compact laser head enclosure shown in figure 3.1a allowed only minimal adjustment of two parameters, the end mirror and the position of the SESAM. Turnkey operation was possible with little to no adjustment required from day to day by the user. Furthermore, an even smaller diode-pumped unit with comparable performance was available from the manufacturer. This unit, shown in figure 3.1b next to a standard compact disc, had a size of only 18cm × 10cm × 5.5cm. This demonstrates the ability to construct extremely portable, turnkey operation femtosecond lasers.

Characterization of the Nd:Glass oscillator used for the studies in this chapter is shown in figure 3.1c-e. The optical spectrum (3.1c) from the laser measured  $> 16$  nm full width at half maximum (FWHM), while the autocorrelation (3.1d) had a FWHM duration of 84 fs. Output power was stable to  $\pm 1$  mW over 12 hours of operation.

### **3.4 Broadband Continuum Generation at 1060 nm with an Ultrahigh Numerical Aperture Fiber**

The light source described in the previous chapter consisted of a Cr:Forsterite laser spectrally broadened in a high nonlinearity fiber with strong normal dispersion. By analogy, it should also be possible to spectrally broaden the Nd:Glass laser output using normal dispersion fibers. The combination of the commercially available oscillator with a high nonlinearity fiber could provide a more robust alternative to the broadened Cr:Forsterite laser. Moreover, the wavelength band around 1060 nm could provide improved imaging depth compared to the 800 nm window and improved resolution compared to 1300 nm sources.

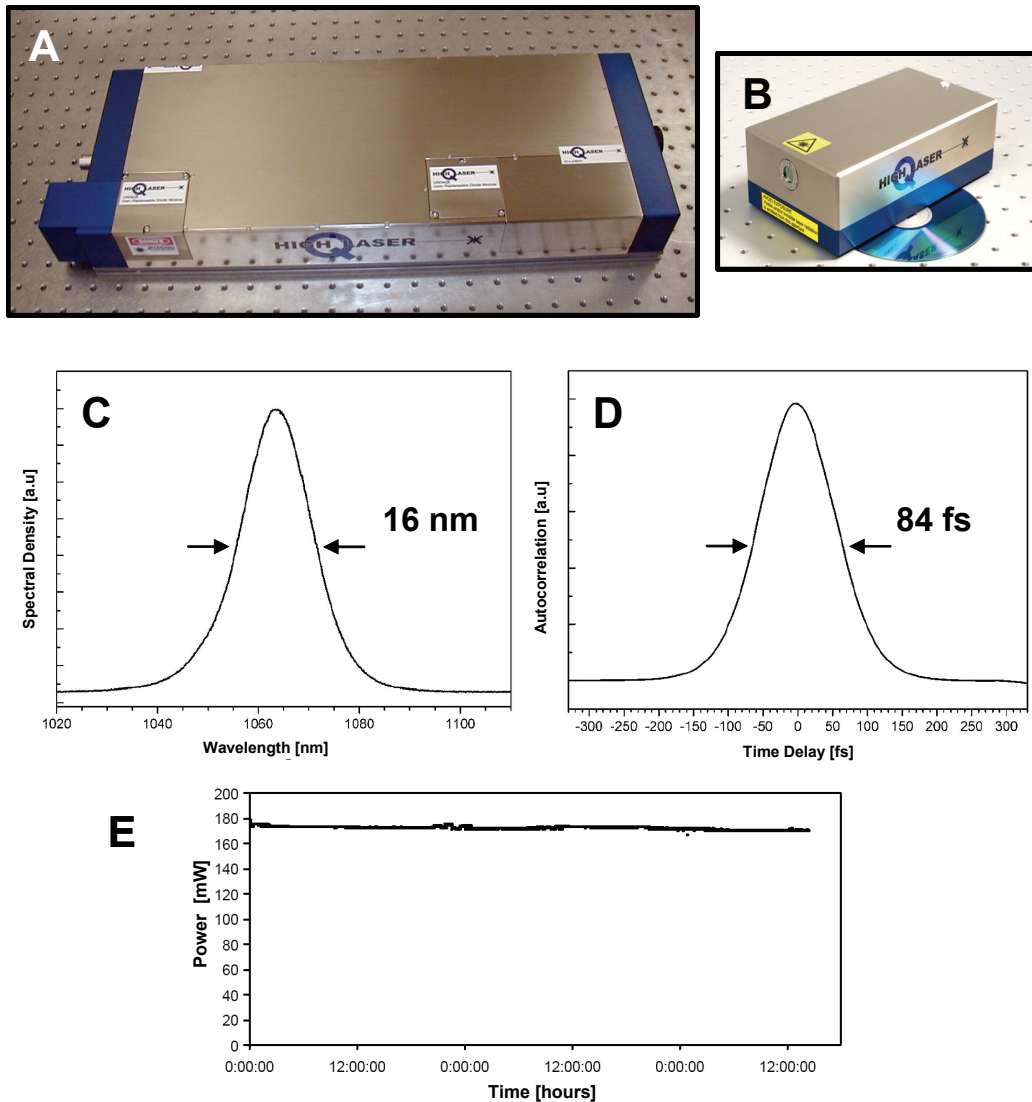


**Figure 3.1.** Photograph and performance characterization of the Nd:Glass femtosecond laser. The unit used for these studies (A) measured 50.8 x 20 x 7.5 cm and can be made even more compact (B). The optical spectrum (C) measured > 16 nm full-width-at-half maximum and the autocorrelation had a duration of ~ 84 fs. Power was stable to +/- 1 mW over hours of operation (E).

Several fibers with normal dispersion were tested with the Nd:Glass oscillator through both numerical simulations and experiment. These included microstructured photonic crystal fibers as well as more standard solid core fibers with rare-earth doped glass and high numerical aperture. The fiber that produced the best results was an ultrahigh high numerical aperture fiber with a germanium-doped core (Nufern, UHNA3). The fiber had a mode field diameter of 2.5  $\mu\text{m}$  at 1100nm and a second mode cutoff wavelength of 850 nm. The numerical aperture was 0.35 and bend loss measured < 0.001 dB for 100 turns of 25 mm radius. Figure 3.2 presents the simulated dispersion characteristics for this class of fibers, as determined by the manufacturer. Plots are shown for fibers with cutoffs of 800 nm and 900 nm, and

the result for the 850 nm cutoff fiber should be bracketed by these curves. The fiber had strong normal dispersion measuring approximately -125 ps/nm/km. Furthermore, the dispersion was relatively flat over the source bandwidth.

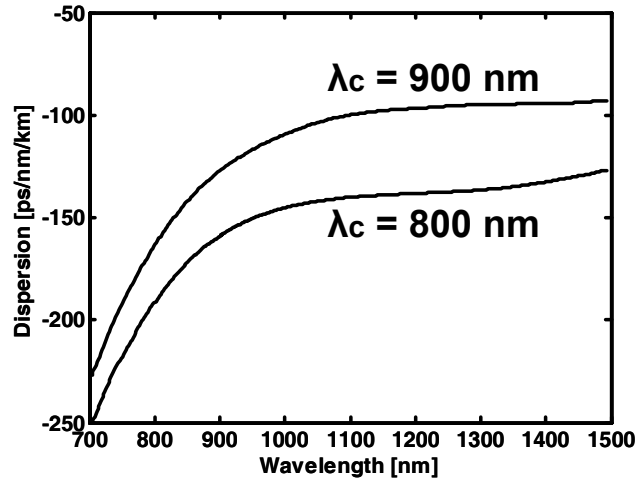


**Figure 3.2.** Simulated dispersion profiles for the class of ultrahigh NA fibers used in these studies. The fiber selected for further use and for OCT imaging had a second mode cutoff of 850 nm and therefore had a dispersion profile bracketed by the two curves shown here. Data supplied by Nufern Inc.

### 3.4.1 Numerical Simulations

Numerical simulations were conducted to understand the evolution of the broadened spectrum in the ultrahigh numerical aperture fiber. Dr. Norihiko Nishizawa performed the simulations, and the details of the procedure have been described previously [34, 35]. In summary, pulse propagation in the fiber was modeled by solving the generalized nonlinear Schrodinger equation using the split-step Fourier method. Dispersion terms up to 10th order were included as well as absorption losses from Rayleigh scattering, infrared absorption, and OH ion absorption. Dispersion parameters were estimated from the simulated dispersion profile provided above. Third order effects including self-phase modulation (SPM) and four-wave mixing (FWM) were included in the simulations as well as the effect of self-steepening (SS). Stimulated Raman scattering (SRS) was ignored. A sech<sup>2</sup> pulse with 75 fs full width at half maximum duration and 20 kW peak power at the Nd:Glass center wavelength of 1064 nm was used for the simulations.

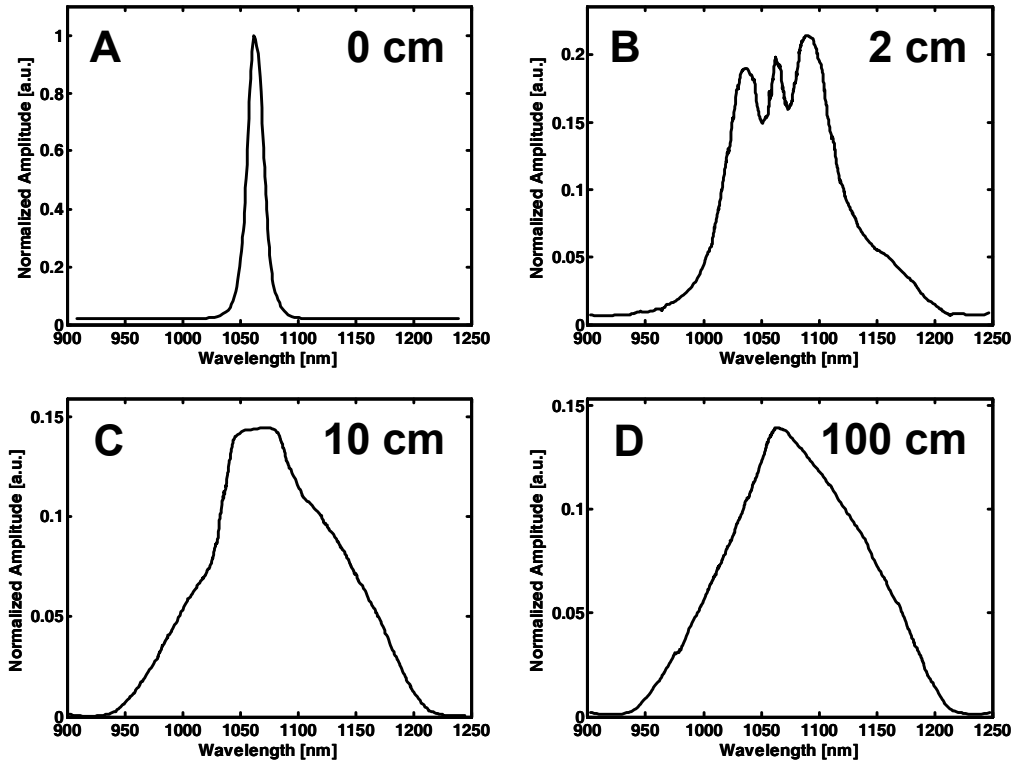


**Figure 3.3.** Numerical simulations for spectral broadening in the ultrahigh NA fiber. The input spectrum (A) and broadened spectra for lengths of 2 cm, 10 cm, and 100 cm are shown in (B), (C), and (D), respectively.

Figure 3.3 presents the length dependence of the continuum evolution in the high NA fiber. After 2 cm, the spectrum has already broadened significantly, with spectral structure characteristic of self-phase modulation. At 10 cm propagation length, the spectrum has further broadened and the spectral modulation has been smoothed. At 100 cm, the spectrum has fully evolved, reaching a full-width-at-half-maximum (FWHM) width approaching 200 nm. In addition, the spectrum is smooth and without fine structure. These results are consistent with the fact that propagation in the normal dispersion regime is dominated by self-phase modulation and chromatic dispersion. Pulse broadening due to dispersion limits the nonlinear interaction length over which SPM acts.

### 3.4.2 Experimental Measurements of the Continuum

The output of the Nd:Glass laser was coupled into the high NA fiber using an aspheric lens with focal length 3.1 mm. For 165 mW average output power, typical coupled power was approximately 105 mW, which corresponds to a coupling efficiency of 64 %. A length of 1 m of high NA fiber was spliced to a standard single mode fiber for 1060 nm wavelength (Corning, HI-1060). A representative measured spectrum at the output of the high NA fiber is provided in figure 3.4. The spectrum in 3.4a was measured

using an optical spectrum analyzer with 1 nm resolution (ANDO). The FWHM spectral width measures 228 nm with a spectral shape that agrees well with the simulation results. The measured axial point spread function achieved with a dispersion balanced fiber-optic Michelson interferometer is provided in figure 3.4b. The resolution of 4.0  $\mu\text{m}$  in air corresponds to a value of 2.9  $\mu\text{m}$  in tissue when scaled by the approximate index of refraction of 1.38. The theoretical point spread function corresponding to the calculated autocorrelation of the spectrum is provided on log and linear scales in figures 3.4c and 3.4d, respectively. The theoretical axial response width of 2.6  $\mu\text{m}$  is smaller than the measured value because the fiber optic measurement interferometer did not support the full bandwidth of the source. Importantly, the smooth shape of the spectrum leads to low coherence sidelobe levels, as evident on the calculated log point spread function in figure 3.4d. The highest sidelobe peaks in 3.4d are at least -40 dB down from the main peak. Since OCT images have large dynamic range and are typically displayed on a log scale, it is essential that the log point spread function falls quickly to the electronic noise floor. Sharp spectral features raise the wings of the point spread function and make it difficult to distinguish a weak reflector in the adjacent presence of a strong reflector, an occurrence referred to as blindness in the OCT literature [36].

The noise characteristics of the Nd:Glass oscillator were measured with and without the nonlinear fiber using a fast photodiode and a low-noise radio-frequency (RF) spectrum analyzer (Advantest). The noise spectrum was obtained by recording the RF spectrum of the laser pulse train at high spectral resolution over small frequency spans and fusing individual recordings together to generate a composite noise spectrum. The measurements were made at the first harmonic of the laser repetition rate and normalized to the carrier power. The composite result plotted on a log-log scale is presented in figure 3.5. As expected for measurements of the integrated noise power, the noise spectra are virtually identical. The noise rolls off quickly after frequencies of  $10^5$  and has reached the instrument detection sensitivity limit for frequencies above  $10^6$ . This suggests that OCT systems operating with MHz carrier frequencies will have a signal to noise advantage using this light source.

Notably, both the spectral shape and the output power of the fiber-coupled continuum light source were remarkably stable over time and highly suitable for use over hours with minimal to no realignment necessary. A high quality, three-axis fiber coupling stage minimized fluctuations in output power, making the light source an excellent candidate for clinical imaging experiments.

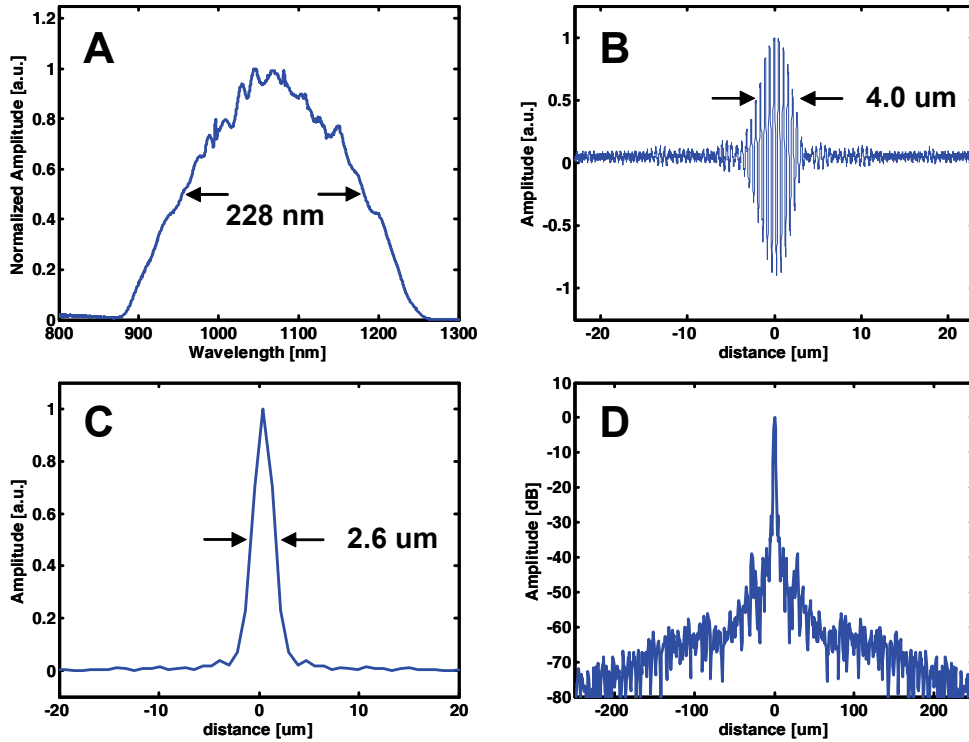


**Figure 3.4.** Measured optical spectrum and corresponding experimental and theoretical axial point spread functions. The recorded spectrum (A) corresponds well to the numerical result. An axial point spread function of 4.0  $\mu\text{m}$  in air was achieved (B), although the theoretical limit corresponding to the spectral width was 2.6  $\mu\text{m}$  (C). The calculated response on a log scale (D) shows coherence sidelobes of -40 dB below the main peak.

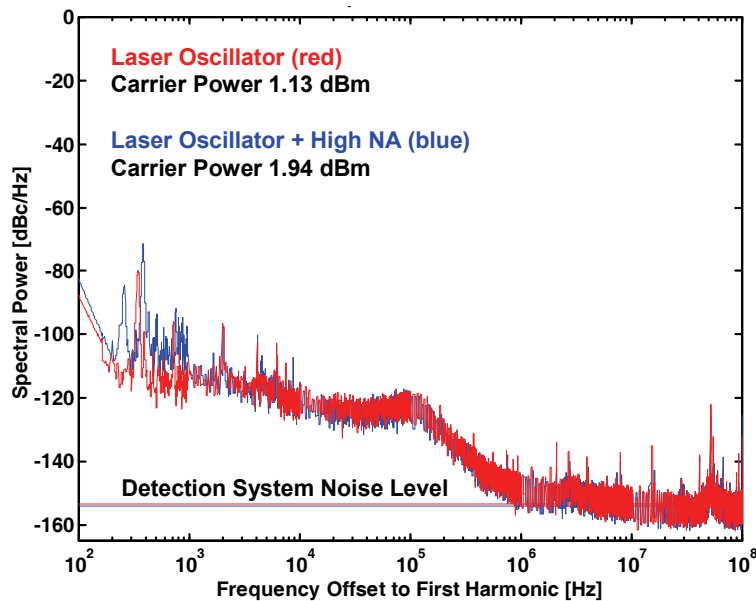


**Figure 3.5.** Noise measurements for the high numerical aperture continuum source.

### 3.4.3 OCT Imaging Results and Discussion

An OCT imaging system optimized for performance at 1060 nm was constructed based on the schematic shown in figure 3.6. The output of the high NA fiber was input to a fiber optic coupler, which divided the power equally between a reference arm and a sample arm. High quality broadband fiber optic circulators and couplers with unequal split ratios were not as readily available at 1060 nm as at 1300 nm, so the interferometer made use of a single coupler with an equal split ratio. This restricted the sample power compared to the system design described in the previous chapter, but this was not a significant issue due to the very high output power of the light source. The sample exposure limit could still be reached for *in vivo* imaging. As with the 1300 nm endoscopic system, scanning was performed with a high speed rotating linear scanner. A benchtop microscope with XYZ translation stages for sample scanning was used for initial evaluation of imaging performance. Detection of the interference signal was performed with a photodiode and transimpedance amplifier and log demodulation was performed after bandpass filtering the signal. Analog to digital conversion was handled through a personal computer, which also controlled the rotating depth scanner and the microscope translation stages.

Sample images acquired *ex vivo* of human tissue samples using the system are presented in figure 3.7. The images were acquired at 2 frames per second with 30 mW on the sample. Lateral resolution measured 10  $\mu\text{m}$  and the field of view was 1.3 mm in depth by 2 mm in lateral dimension with 1344 x 1000 pixels. Image aspect ratio is corrected by dividing the scale of the depth dimension by  $n = 1.38$ , which is an approximate average index of refraction of tissue. Image A shows a scan of fibroadipose tissue in a human breast specimen. The high resolution system readily resolves the fine boundaries between adipose cells and clearly distinguishes the border between adipose and fibrous tissue. Corresponding histology provided in 3.7b further highlights the excellent image quality provided by the ultrahigh resolution OCT system. An image of human thyroid tissue is provided in figure 3.7c. The ultrahigh resolution OCT system enables clear visualization of the thyroid follicles as well as the thyroid epithelium. Again, the corresponding histology is provided in figure 3.7d.

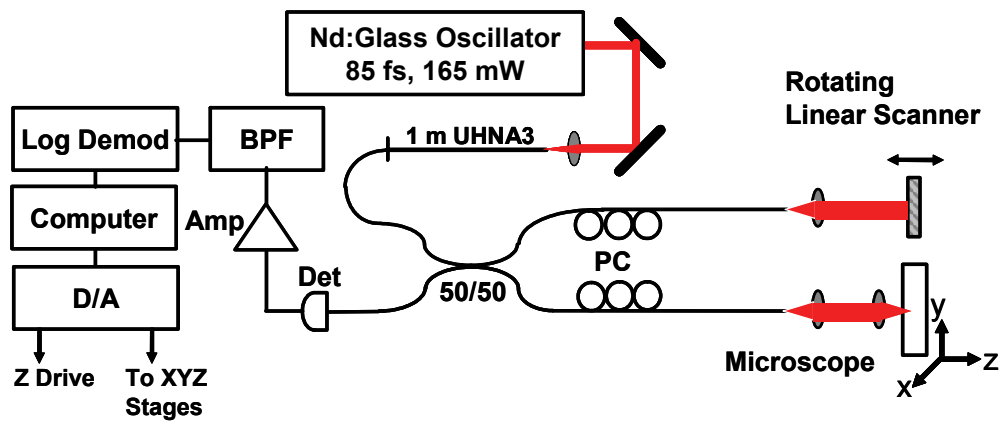


**Figure 3.6.** High-speed, time-domain OCT imaging system at 1060 nm. D/A, digital to analog converter. Amp, amplifier. BPF, bandpass filter. Det, detector. PC, personal computer.

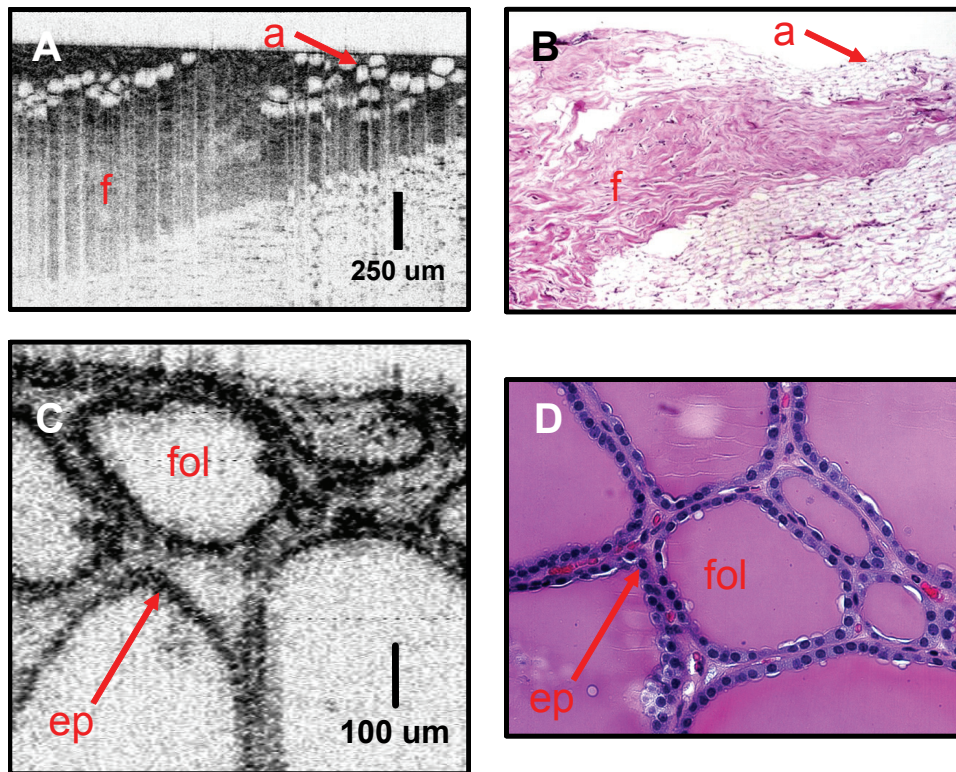


**Figure 3.7.** Ultrahigh resolution OCT images of human tissue samples acquired at 1  $\mu$ m wavelength. Fibroadipose tissue from human breast is shown in (A) along with corresponding histology in (B). Adipose (a) and fibrous (f) tissue can be readily distinguished. Human thyroid is shown in (C) and (D). fol, follicle. Ep, epithelium. Histology is shown at the same scale as the OCT images.

### 3.5 Broadband Continuum Generation at 800 nm and 1300 nm with a Novel Photonic Crystal Fiber

This work was based on a commercially available photonic crystal fiber with a parabolic dispersion profile and two closely spaced zero dispersion wavelengths (Crystal Fibre A/S, NL-1050-ZERO-2). Figure 3.8 presents a high magnification photograph of the fiber core as well as the fiber dispersion profile supplied by the manufacturer. Zero dispersion wavelengths were nominally present at  $\sim 1022$  nm and  $\sim 1075$  nm with the parabolic maximum of  $\sim 0.6$  ps/nm/km in the anomalous region at 1050 nm and monotonically decreasing dispersion at wavelengths below and above the zero dispersion points. The fiber was non-polarization maintaining and used a microstructured cladding with air holes to guide light in a pure silica core. It had high nonlinearity of  $\sim 0.37$  (Wkm) $^{-1}$  with a small mode field diameter of  $\sim 2.2$   $\mu\text{m}$  and high numerical aperture of 0.37.

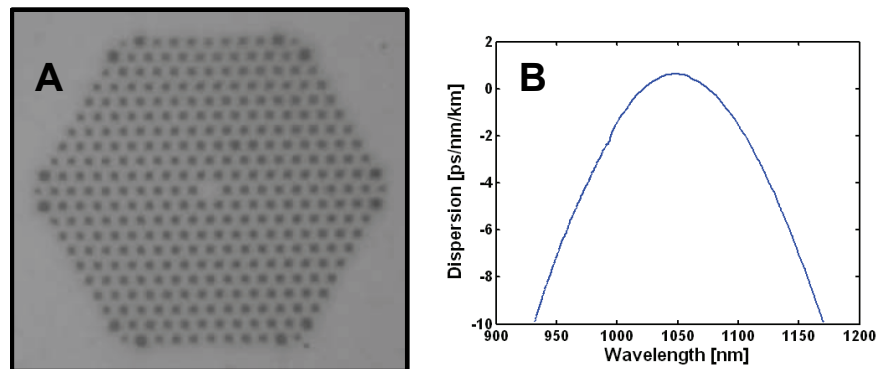


**Figure 3.8.** Photograph (A) and dispersion profile (B) of the photonic crystal fiber. Picture and data provided by Crystal Fiber A/S, Denmark.

#### 3.5.1 Numerical Simulations

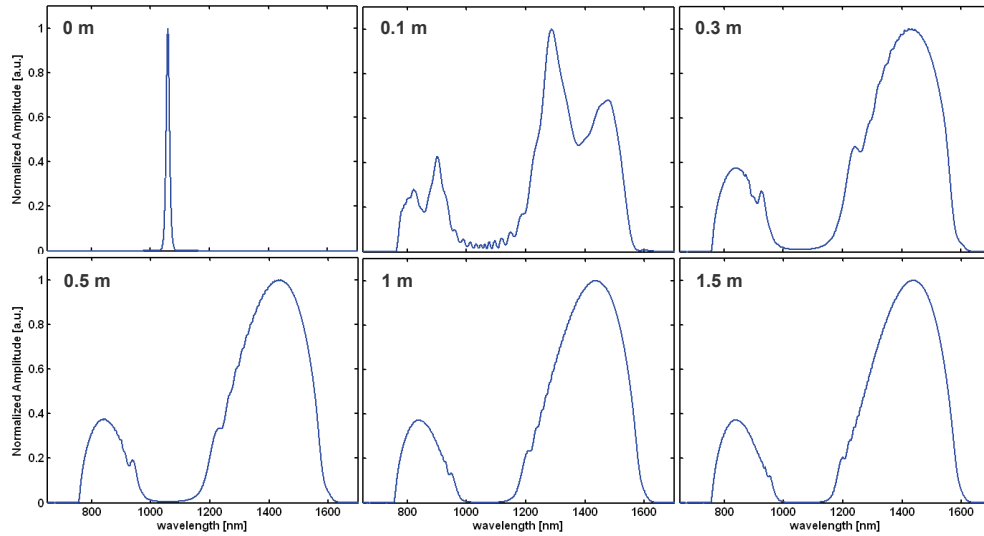
Numerical simulations were conducted to study continuum generation in the novel PCF for OCT imaging applications. A similar simulation approach as the one described above was used. To most closely match the experimental setup, a  $\text{sech}^2$  pulse with 85 fs full width at half maximum duration and 18 kW peak power at the Nd:Glass center wavelength of 1064 nm was used for the simulations.

Figure 3.9 presents numerical results for the length dependence of the continuum, with spectra displayed on a linear scale. As demonstrated for a similar fiber design previously [33], this continuum rapidly evolves into a double peak structure with nearly complete depletion of the pump wavelength. These results predict that the main spectral peaks can be localized to the important OCT imaging wavelength regions near 800 nm and 1300 nm. The input spectrum is rapidly broadened within 10 cm to a full spectral width of more than one octave between 700 nm and 1500 nm. Additional propagation in the fiber leads to further depletion of the region between the two spectral peaks as well as filling in and

smoothing of the main peaks. Slight modulation appears on the inner facing edges of the spectral peaks between 0.5 and 1.0 m, and propagation after 0.5 m results in little change in the spectrum.

Several theoretical and experimental studies have been performed to elucidate mechanisms of supercontinuum generation in typical photonic crystal fibers when pumping in the anomalous dispersion region near the zero-dispersion wavelength [37-41]. When using picosecond or nanosecond pulses, stimulated Raman scattering and parametric four-wave mixing are dominant [41], while the use of femtosecond pulses leads to spectral broadening through fission of higher-order solitons into red-shifted fundamental solitons and blue-shifted nonsolitic radiation [42]. By contrast, the mechanism for supercontinuum generation in PCF's with two closely spaced zero dispersion wavelengths has been attributed by Hilligsoe, et al. to a combination of self-phase modulation and phase-matched four-wave mixing, with relative suppression of the Raman scattering, self-steepening, and soliton fission mechanisms [33]. These authors report that self-phase modulation is the dominant broadening mechanism and provides seed wavelengths for four-wave mixing, which leads to efficient depletion of wavelengths between the zero dispersion points. Additional non-degenerate four wave mixing also contributes to extending the depleted region between the main peaks beyond the region between the zero dispersion wavelengths [33]. Subsequent work has questioned the role of four-wave mixing in the spectral broadening and has demonstrated a role of generation of dispersive waves followed by soliton self frequency shift (SSFS) if the separation between the zero dispersion wavelengths is large enough [43]. Additional work on the fundamental mechanisms in such fibers is necessary to fully understand the discrepancies in these studies.

In the studies for this thesis, the fiber chosen had a very narrow anomalous dispersion region between the zero dispersion wavelengths, which makes soliton effects unlikely due to the rapid shift of energy outside of the zero dispersion wavelengths to the normal dispersion region [43]. Comparison of the characteristic lengths of dispersion,  $L_D$ , and nonlinearity,  $L_{NL}$ , for peak power  $P_o$ , pulse width  $T_o$ , and dispersion  $\beta_2$  at the pump wavelength reinforces that pulse evolution is initially dominated by high nonlinearity since  $L_D / L_{NL} \equiv (\gamma P_o T_o^2) / |\beta_2| \approx 10^4 \gg 1$  [35]. Small group-velocity dispersion in the region of the pump wavelength and high fiber nonlinearity allows self-phase modulation to dominate dispersive broadening over the first several centimeters resulting in fast spectral broadening. The main spectral peaks lie in the normal dispersion region and dispersive broadening subsequently leads to a reduction in peak power. With continued propagation, nearly complete depletion of the region between the main peaks results, potentially due to phase-matched four-wave mixing [33]. Further theoretical studies will be required to confirm the precise mechanisms of continuum generation in this fiber.



**Figure 3.9.** Simulated fiber length dependence of the continuum spectrum generated by 85 fs, 18 kW peak power pulses at 1060 nm. Nearly complete depletion of the pump wavelength is observed along with creation of two high brightness main peaks centered near 800 nm and 1300 nm.

To further understand how to control spectral shape for OCT applications, the effect of varying the pump wavelength with respect to the zero dispersion wavelengths was simulated. Previous results suggested that the spectral extent is not very sensitive to the position of the pump wavelength and that the relative power between the two main lobes can be adjusted by choice of the pump wavelength position [33]. The simulations presented here present somewhat different results using the photonic crystal fiber designed for 1050 nm. This fiber has extremely small anomalous dispersion in the region between the zero dispersion wavelengths, which may complicate the wavelength dependence by enhancing additional nonlinear mechanisms. Figure 3.10 presents spectra resulting from simulations of 85 fs, 18 kW peak power pulses propagated through a 2 m length of the photonic crystal fiber at various center wavelengths around the depletion region. At each pump wavelength, the majority of the spectral power remains in the long wavelength peak, and for pump wavelengths near the lower zero dispersion wavelength, the continuum can extend farther into the infrared. The short wavelength edge of the spectrum remains relatively fixed with respect to changing pump wavelength. The asymmetry in the spectrum seems to depend on higher order dispersion terms. In addition, the depletion region between the main spectral lobes increases in span with pump wavelengths in the normal dispersion ranges. This could be due to enhanced four-wave mixing processes resulting from stronger seed energy deposited by self-phase modulation around the zero dispersion wavelengths [33].

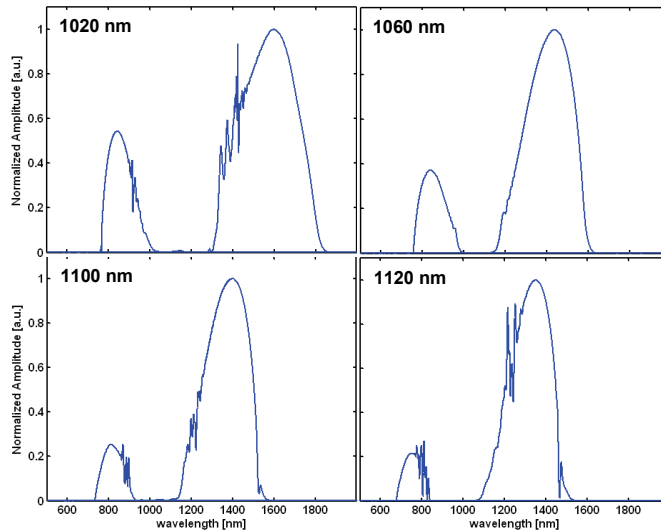


**Figure 3.10.** Simulated pump wavelength dependence for optimal continuum generation. Input pulses of 85 fs, 18 kW peak power illustrate differences in continuum as a function of pump wavelength.

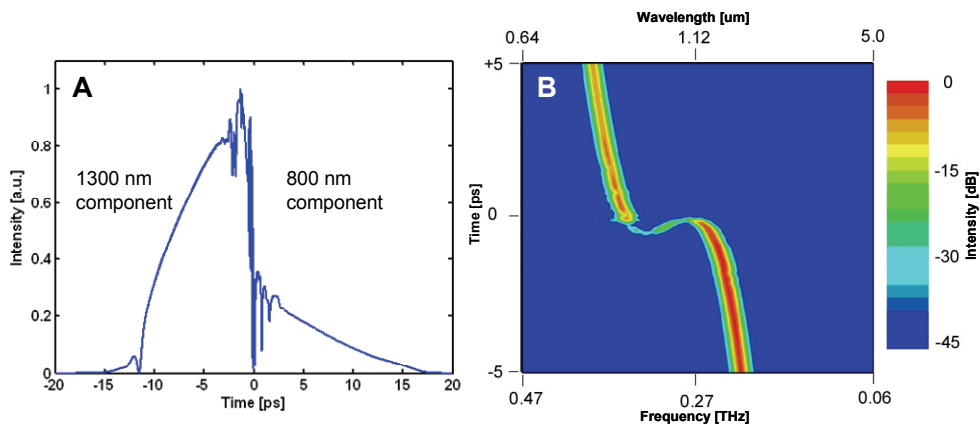


**Figure 3.11.** Time-frequency characteristics of the continuum for input pump pulse center wavelength of 1120 nm. The temporal profile (A) and spectrogram (B) illustrate how temporal overlap of spectral components can lead to temporal and spectral structure by cross-phase modulation.

For OCT imaging, spectral shape is a critical determinant of image quality since non-Gaussian spectra with large modulation can lead to large coherence wings on the interference point spread function [36]. The simulations presented here indicate that smooth, twin peak spectra can be achieved when the wavelength of the pump pulse is located between the two zero dispersion wavelengths.

The increased fine spectral modulation for pump wavelengths in the normal dispersion region results from cross phase modulation due to temporally overlapped spectral components. Figure 3.11 displays the temporal pulse profile and spectrogram corresponding to the 1120 nm pulse with spectral profile shown in

figure 3.10. The short wavelength spectral components trail the long wavelength components for the most part, but temporal overlap between wavelengths on the edges of the depletion region leads to cross-phase modulation. This overlap is minimized for pump wavelengths located between the zero dispersion points. Further investigation will be necessary to completely understand the mechanisms behind the wavelength dependence of this continuum. Since choosing the optimal pump wavelength is largely equivalent to optimizing the fiber dispersion profile for a fixed pump wavelength, custom photonic crystal design and fabrication should enable ultrahigh resolution OCT with several commercially available femtosecond oscillators.

### 3.5.2 Experimental Measurements of the Continuum

The experimental setup used to measure the continuum spectrum is shown in figure 3.12. The ends of a 1 m length of PCF were flat-cleaved using a standard cleaver and mounted on high-precision 3-axis stages for coupling into and out of the fiber. The laser output was coupled directly into a 1 m length of photonic crystal fiber using a 3.3 mm focal length aspheric lens and was recollimated at the output using a 3.1 mm aspheric lens. An isolator was tested and found to be unnecessary because the oscillator was relatively insensitive to feedback from the fiber end facet reflection. The fiber was non-polarization maintaining, and adjustment of the input via a half-wave plate also did not appreciably alter the continuum spectrum.

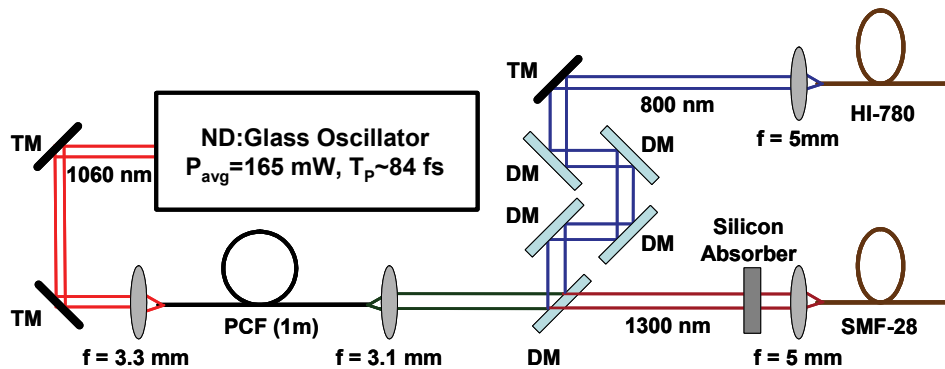


**Figure 3.12.** Experimental setup for the continuum generation light source at 800 nm and 1300 nm for ultrahigh resolution OCT imaging. Spectral filtering is performed using broadband dielectric mirrors and a silicon absorber to ensure removal of the opposite wavelength for OCT imaging. TM, turning mirror; DM, dielectric mirror.

To enable OCT imaging at both 800 nm and 1300 nm, the spectrum had to be filtered with high purity to prevent interference from the unused wavelength region. The 800 nm continuum was filtered using 5 bounces on dielectric mirrors with broadband antireflection coatings centered at 800 nm. These mirrors have typical reflectances of  $> 99\%$  across the wavelength range around 800 nm while transmitting with

low loss the wavelengths at 1300 nm, thereby providing 60-70 dB of spectral separation of the two continuum main lobes. Rejection of residual 800 nm light from the 1300 nm continuum was achieved with a polished silicon absorber. After spectral filtering, the 800 nm and 1300 nm light was separately coupled into standard single mode fibers designed for those wavelengths using 5 mm focal length aspheric lenses.

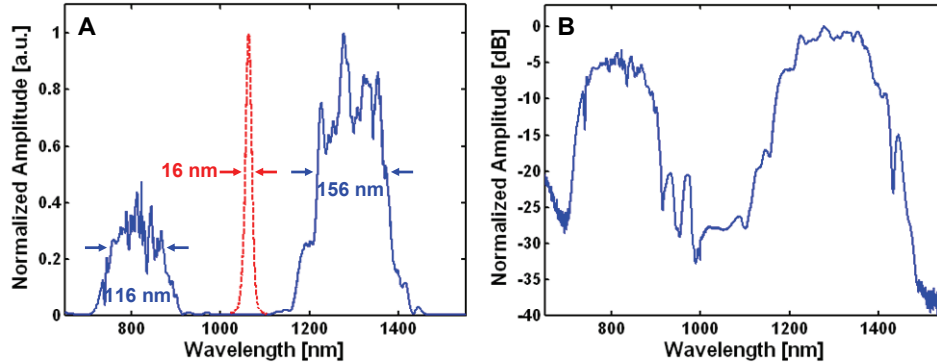


**Figure 3.13.** Experimental measurement of continuum spectrum on (A) linear and (B) log scales. The pump laser spectrum is also shown in (A). These spectra are created from concatenation of individually measured spectra in the 800 nm and 1300 nm wavelength regions.

The measured continuum spectrum is presented in figure 3.13. The pump spectrum is also shown in figure 3.13a. The continuum spectrum shown is a concatenation of spectra measured separately with 0.5 nm resolution after filtering the 800 nm and 1300 nm spectra. Separate measurement of the spectral regions enabled more precise representation of spectral shape and relative amplitude, since the power in both wavelength regions could be individually measured and fiber coupling to the optical spectrum analyzer could be optimized to minimize chromatic focusing aberrations. The effect of filtering on the combined spectrum was minimized by concatenating the spectra at 1000 nm in the depleted region between the two main peaks. The silicon absorption edge and the dielectric mirror reflectivity both drop sharply around this wavelength. The linear spectrum in figure 3.13a agrees reasonably well with previously presented simulation results. Bandwidths of 156 nm and 116 nm are achieved at 1300 nm and 800 nm, respectively. The simulated spectrum shown in figure 3.9 for 1060 nm pump wavelength extends further into the infrared than the measured spectrum. This may be due to leakage losses in the PCF at the long wavelengths [33] or perhaps to deviation from the specified dispersion profile. As shown in figure 3.10, the extent of the long wavelength side of the continuum also depends on the pump wavelength relative to the two zero dispersion points. Power in the spectra recorded before coupling to the single mode fibers measured  $\sim 30$  mW at 800 nm and  $\sim 48$  mW at 1300 nm. For average incident pump power of 165 mW, the measured output power corresponds to  $\sim 48\%$  coupling efficiency. At 800 nm, 8-11 mW was available in the single mode HI-780 fiber, while at 1300 nm 25-30 mW was coupled

into SMF-28. As predicted in the simulation, energy is efficiently depleted from the pump wavelength and transferred to the two spectral bands around 800 nm and 1300 nm. The spectrum is shown on a log scale in figure 3.13b. The region between the two spectral main lobes after filtering is shown to be  $> 20$  dB below the main spectral lobe amplitude.

The modulation seen on the spectrum in 3.13a is greater than expected based on numerical simulations for an injected pulse at 1064 nm. There are several possible reasons for this. First, there may be some error in the approximation of the higher order dispersion terms from the available measured data of the fiber dispersion profile. The form of the continuum is strongly dependent on the dispersion characteristics of the PCF. The observation that the short wavelength component is centered closer to 800nm in the experimental measurements compared to the numerical results may also indicate deviation from the manufacturer's dispersion specification. In addition, the dispersion profile may vary slightly over the length of the fiber, since it depends on physical air hole structure on the micron scale. It was observed that, while the general form of the continuum remained fixed, the spectral modulation varied slightly when the fiber was reconnected and when the fiber ends were switched such that the propagation direction was reversed. The spectral shape of the continuum was also sensitive to very small adjustments of the XYZ coupling stage without significant coupled power variation suggesting that the precise way in which the mode is launched into the fiber must be considered. It is possible that light propagating in the microstructured cladding may cause modulation on the spectrum. To minimize these effects, steps will be taken in future experiments to control the coupling with even higher precision stages.

Occasionally, severe degradation was observed in coupled power into the PCF. This was the result of increased scattering from dust or moisture at the tip and subsequent fiber end facet damage. This effect was seen at both the input and output coupling ends and is a well known observation with photonic crystal fibers, since the fine air-silica microstructure is extremely sensitive to ambient environmental conditions. This effect could be minimized by covering the bare end facet, but in future work the use of commercially available options for fiber end facet protection will likely improve long term power stability. Photonic crystal fibers are now readily available with integrated collimating lenses or with hermetically sealed end facets.

Excess amplitude noise has been measured previously on continuum spectra measured from photonic crystal fibers as the result of temporal instability and nonlinearly amplified quantum noise [28]. Prior work with PCF's using two closely spaced zero dispersion wavelengths, however, has measured relatively low noise continuum because of the suppression of several higher order nonlinear mechanisms including soliton fission [33]. To verify that this holds for the continuum presented in figure 3.13, the intensity noise in the filtered wavelength regions of 800 nm and 1300 nm was measured separately using an RF spectrum analyzer.

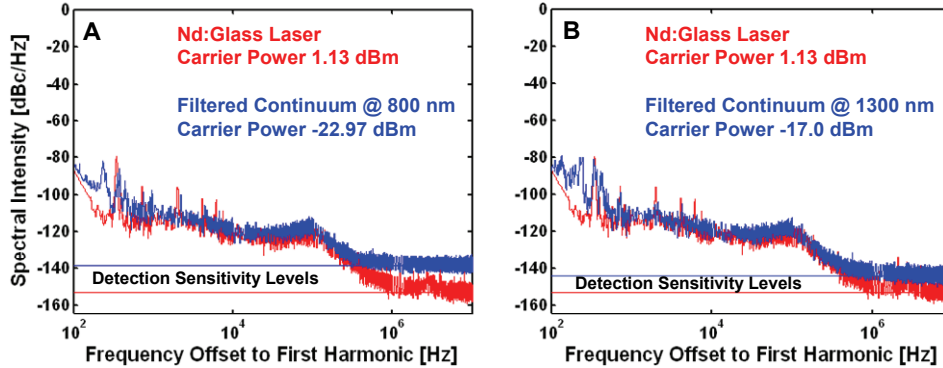


**Figure 3.14.** Experimental measurement of RF noise spectra for the filtered wavelength regions around (A) 800 nm and (B) 1300 nm. The noise spectra are compared to the RF spectrum for the Nd:Glass oscillator alone.

Figure 3.14 shows the recorded RF noise spectra acquired using a fast photodiode. The measurements were made at the first harmonic of the laser repetition rate and normalized to the carrier power. Detected first harmonic carrier power was 1.13 dBm for the oscillator alone and -22.97 dBm and -17.0 dBm for the wavelength regions of 800 nm and 1300 nm, respectively. The noise decreases nearly exponentially at frequencies above  $10^5$  Hz and is consistent with previous measurements of the amplitude noise spectrum for continuum generated predominantly by self-phase modulation in a high numerical aperture fiber [24]. The noise spectra largely track that of the oscillator alone implying that OCT imaging can be performed with high sensitivity due to the lack of excess amplitude noise.

### 3.5.3 OCT Imaging Results and Discussion

The continuum spectrum presented in figure 3.13 was used with time-domain, ultrahigh resolution OCT systems to demonstrate imaging in biological tissue. Figure 3.15 shows the generalized system diagram, which was implemented at both 800 nm and 1300 nm. Light from the filtered continuum was coupled into a dual-balanced interferometer consisting of two 50/50 splitters. At the final splitter, light was divided between a reference beam and a sample beam. Optical path length scanning of the reference beam was performed using a retroreflecting galvanometer, while the sample beam was focused by a 1:1 microscope to a small spot size approximately equal to the fiber mode field diameter,  $\sim 6 \mu\text{m}$  at 800 nm and  $\sim 9 \mu\text{m}$  at 1300 nm. Dispersion compensating glass was used in the reference arm to match the dispersion of the sample arm optics. Sample scanning was achieved using mechanical translation with a computer controlled stage.

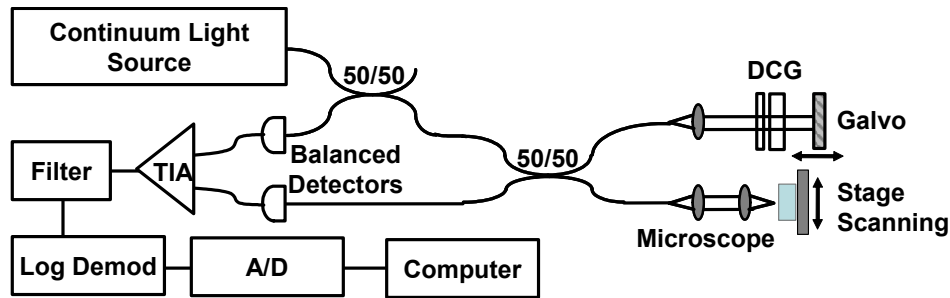


**Figure 3.15.** OCT system diagram. Similar systems were implemented at both 800 nm and 1300 nm for these experiments. DCG, dispersion compensating glass; TIA, transimpedance amplifier; A/D, analog to digital converter.

Light returning from the sample and reference arms interfered at the balanced detectors, which subtracted common-mode noise while adding the interference terms. The electronic OCT signal was amplified, filtered, and logarithmically demodulated before being sampled by a computer for display. Different couplers, sample arm optics, and photodiode detectors were used for the 800 nm and 1300 nm wavelengths, but the galvanometer, scanning stage, and filtering/demodulating electronics were common for both systems. Filtering was performed at 205 kHz center frequency with 53 kHz bandwidth. For axial scan depth of 2 mm at both wavelengths, this corresponded to 38 Hz, 133 mm/s scanning at 1300 nm and 25.4 Hz, 84.5 mm/s scanning at 800 nm. These imaging speeds were slower than usual for most time-domain OCT systems, but were sufficient for evaluating the imaging performance of the continuum light source.

System performance characterization is presented for both wavelengths in figure 3.16. System resolutions and point spread functions were characterized by measuring reflections from a mirror with neutral density filters in the sample arm. Minimum neutral density attenuation was chosen to prevent saturation of the transimpedance amplifier, which occurred for  $> 2.5$  OD. Figures 3.16a and 3.16b compare the point spread function on a linear scale for both wavelengths. At 800 nm, 3.0  $\mu\text{m}$  full width at half maximum (FWHM) was achieved, which for index of refraction in tissue of 1.38 provided  $\sim 2.2$   $\mu\text{m}$  in tissue. At 1300 nm, 6.5  $\mu\text{m}$  FWHM provided  $\sim 4.7$   $\mu\text{m}$  in tissue. Both point spread functions were symmetric and correlated well to the Fourier transform interference bandwidths presented in figure 3.16e and 3.16f, indicating that dispersion mismatch is minimized. The interference bandwidths indicate that some spectral shaping in the OCT system resulted in reduction of optical bandwidth on the short wavelength edges of the spectra. The couplers used in this study have been previously demonstrated to support broad optical bandwidth [4, 18]. Spectral shaping likely resulted from wavelength dependent focusing aberration in the optics as well as some multimode leakage in long optical fibers bringing light to the OCT system setup. This can be improved with further attention to system design.

Figure 3.16c and 3.16d present the logarithmically demodulated output signals for 800 nm and 1300 nm, respectively. The traces have been normalized and scaled to reflect the 50 dB sample arm attenuation (2.5 OD filter, double-pass) used to measure them. At both wavelengths, the sidelobe coherence artifacts on the point spread functions were present at  $\sim 25$ -30 dB. These results correlated well to the expected point spread function obtained by Fourier transforming the input optical bandwidths to the systems indicating that the source of the coherence artifact was the spectral modulation. Sidelobe levels of 40-50 dB are desirable for OCT imaging, and further work to investigate spectral smoothing in the PCF will be important for performance improvement. Sensitivities were recorded as the minimum detectable reflection levels below the sample power for the systems. Measured values were  $\sim -103$  dB for 1.0 mW sample exposure at 800 nm and  $\sim -107$  dB for 3.0 mW sample exposure at 1300 nm. Reference arm optical power on the detectors was set to achieve shot noise limited sensitivity with maximum dynamic range.

Figure 3.17 presents representative OCT imaging results in biological tissue at 800 nm and 1300 nm. Imaging was performed of formalin fixed hamster cheek pouch, which provides an excellent and durable tissue model for evaluation and comparison of light source performance. OCT imaging was performed with axial resolutions in tissue of 2.2  $\mu\text{m}$  and 4.7  $\mu\text{m}$  at 800 nm and 1300 nm, respectively. Transverse resolutions ( $1/e^2$  diameter) at 800 nm and 1300 nm measured approximately 6  $\mu\text{m}$  and 9  $\mu\text{m}$ , respectively. Acquired images were  $\sim 1$  mm x 1.5 mm (transverse x axial) in dimension with 1000 x 2000 pixels. Vertical scale was corrected to account for the index of refraction of tissue. Sample power was 3.7 mW at 1300 nm and 1.0 mW at 800 nm.

Examination of the 800 nm and 1300 nm images in figure 3.17 illustrates that fine features in the fixed tissue specimen can be visualized with high resolution. Some blurring of the images results from the sidelobe coherence artifact, but this can be improved with further optimization of the continuum light source. Enhanced penetration depth at 1300 nm is evident in the images. The OCT system at 1300 nm had a larger depth of field by a factor of  $\sim 2$  corresponding to the larger fiber spot size at this wavelength. In addition, there was reduced scattering and enhanced penetration of longer wavelengths in tissue. This has been an important reason for imaging in the 1300 nm wavelength range in highly scattering tissues. In the formalin fixed tissue sample, there was some shrinkage compared to the unfixed *in vivo* images which have been presented previously, but the layered structure is preserved. The epithelium (e), connective tissue (c), and muscular layers (m) are visible with high contrast.

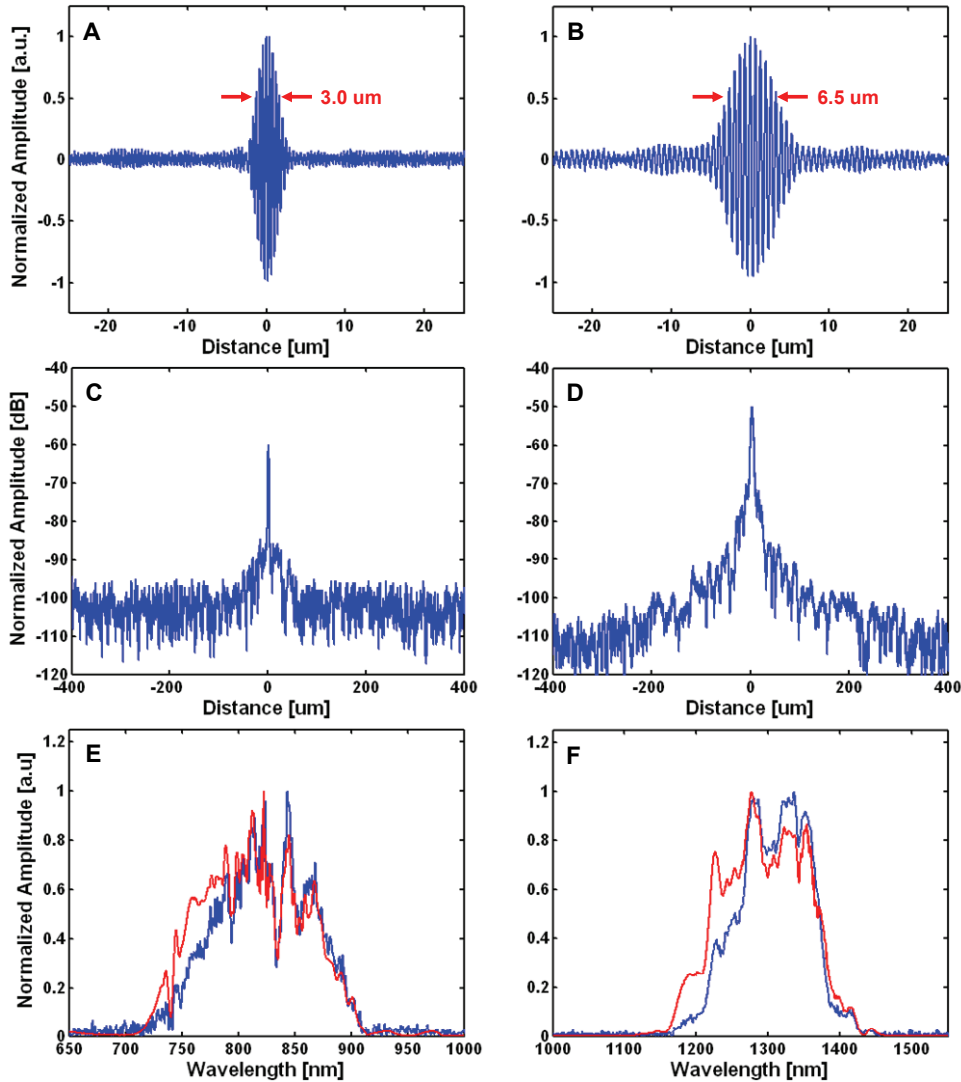


**Figure 3.16.** Ultrahigh resolution OCT performance evaluation. Linear (A,B) and logarithmic (C,D) point spread functions are shown for both 800 nm (A,C) and 1300 nm (B,D). The Fourier transform of the point spread functions in (A) and (B) are shown in blue in (E) and (F) to indicate the interference bandwidth. They are overlapped with the input source spectra shown in red.

The OCT imaging results presented here suggest that ultrahigh resolution OCT can be achieved at both 800 nm and 1300 nm with a single compact, stable, and user-friendly source with sufficient output power for *in vivo* imaging applications. While it is unlikely that continuum generation sources will find widespread use for ultrahigh resolution retinal imaging at 800 nm due to the availability of broadband superluminescent diode (SLD) sources [13], they offer a very promising alternative to SLD's for ultrahigh resolution imaging in other applications where more power and/or longer wavelengths are required. The 1300 nm source demonstrated here, for example, may with further development provide a widely available replacement for the Cr:Forsterite modelocked laser source currently used in ultrahigh resolution

endoscopic OCT [16]. It is feasible that the light source and fiber can be integrated into a single package to provide a completely turn-key operation, high power ultrahigh resolution OCT source at 1300 nm. Currently, the performance of this light source is not equal to the Cr:Forsterite source due to coherence artifact from spectral modulation, but based on the numerical simulations presented in section 2 and on the work of others [33, 43-45], it appears that generation of smoother continuum will be realizable with further optimization of such fibers. Dispersion management solutions using combinations of fibers with different dispersion profiles [46] or tapering of photonic crystal fibers are particularly promising [44]. It should be noted that, while these sources were demonstrated for time-domain ultrahigh resolution OCT imaging, they can also be implemented with spectrometer based spectral domain OCT systems for high speed, ultrahigh resolution OCT at 800 nm and 1300 nm [47-50].

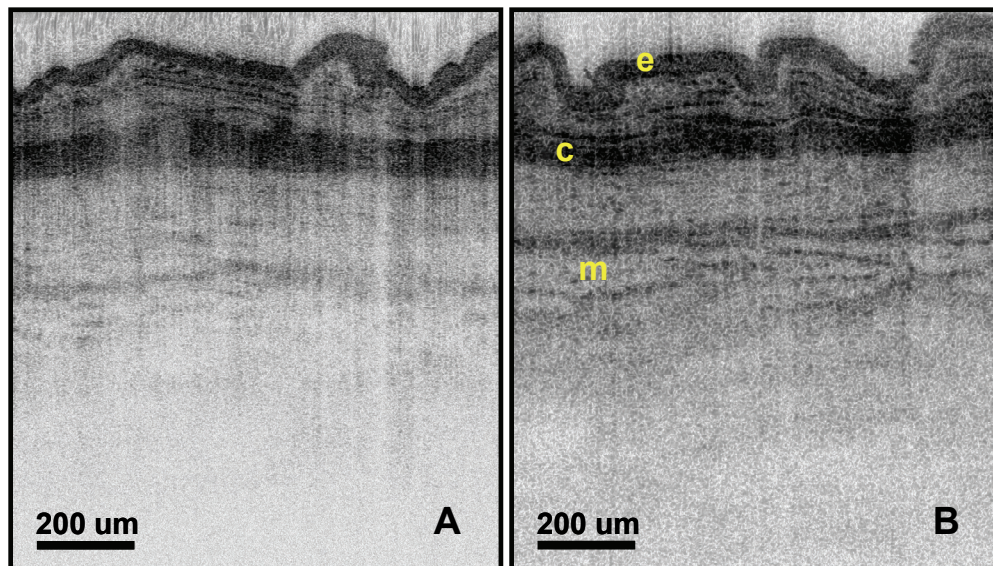


**Figure 3.17.** Ultrahigh resolution OCT images of formalin fixed hamster cheek pouch at (A) 800 nm and (B) 1300 nm. Enhanced image penetration is noticeable at 1300 nm and important features such as the epithelium (e), connective tissue bands (c), and muscular layers (m) can be distinguished.

The paradigm of using theoretical analysis and numerical simulation to custom design photonic crystal fibers that achieve a desired spectral distribution will be extremely powerful for applications such as OCT that are critically dependent on the precise spectral characteristics. The novel PCF design with two closely spaced zero dispersion wavelengths offers a solution to the problems of excess noise and low power efficiency that have hindered the use of supercontinuum generation for ultrahigh resolution OCT in the 1300 nm wavelength range. Furthermore, the ability to tune the wavelengths of the main peaks by setting the zero dispersion wavelengths opens up the possibility that investigators can achieve ultrahigh resolution imaging at any wavelength throughout the near infrared by using a single pump laser source

with a specific fiber. This would greatly expand the capabilities of research groups by enabling multiple expensive laser systems to be replaced with a single system and several optical fibers.

### **3.6. Summary**

We have developed and demonstrated light sources for ultrahigh resolution OCT imaging at 800 nm, 1060 nm, and 1300 nm based on supercontinuum generation in highly nonlinear optical fibers. The fibers included a high numerical aperture germanium doped fiber and a novel photonic crystal fiber with two closely spaced zero dispersion wavelengths. The sources were developed entirely with commercially available components, including the optical fibers and the turnkey Nd:Glass femtosecond oscillator. High sensitivity imaging was achieved with  $< 5 \mu\text{m}$  axial resolution in tissue at all three wavelengths. The high numerical aperture source at 1060 nm provided excellent performance and was highly suitable for *in vivo* clinical imaging. It provides a widely available, user-friendly option for ultrahigh resolution OCT in applications such as endoscopy. With the photonic crystal fiber source, coherence artifacts from spectrum modulation degraded the performance somewhat. To address this, numerical simulations were used to study the conditions for generating smooth spectral peaks in the PCF. Results suggest that optimization of the continuum can be achieved by tuning the pump dispersion wavelength relative to the zero dispersion wavelengths of the fiber. This work provides preliminary data that should motivate additional development and optimization of similar photonic crystal based light sources for ultrahigh resolution OCT.

### 3.7 References

- [1] D. Huang, E. A. Swanson, C. P. Lin, J. S. Schuman, W. G. Stinson, W. Chang, M. R. Hee, T. Flotte, K. Gregory, C. A. Puliafito, and et al., "Optical coherence tomography," *Science*, vol. 254, pp. 1178-81, 1991.
- [2] J. G. Fujimoto, "Optical coherence tomography for ultrahigh resolution in vivo imaging," *Nat Biotechnol*, vol. 21, pp. 1361-7, 2003.
- [3] B. Bouma, G. J. Tearney, S. A. Boppart, M. R. Hee, M. E. Brezinski, and J. G. Fujimoto, "High-resolution optical coherence tomographic imaging using a mode-locked Ti:Al<sub>2</sub>O<sub>3</sub> laser source," *Optics Letters*, vol. 20, pp. 1486-1488, 1995.
- [4] W. Drexler, U. Morgner, F. X. Kartner, C. Pitris, S. A. Boppart, X. D. Li, E. P. Ippen, and J. G. Fujimoto, "In vivo ultrahigh-resolution optical coherence tomography," *Optics Letters*, vol. 24, pp. 1221-1223, 1999.
- [5] W. Drexler, U. Morgner, R. K. Ghanta, F. X. Kartner, J. S. Schuman, and J. G. Fujimoto, "Ultrahigh-resolution ophthalmic optical coherence tomography," *Nat Med*, vol. 7, pp. 502-7, 2001.
- [6] A. M. Kowalewicz, T. R. Schibli, F. X. Kartner, and J. G. Fujimoto, "Ultralow-threshold Kerr-lens mode-locked Ti:Al<sub>2</sub>O<sub>3</sub> laser," *Optics Letters*, vol. 27, pp. 2037-2039, 2002.
- [7] A. Unterhuber, B. Povazay, B. Hermann, H. Sattmann, W. Drexler, V. Yakovlev, G. Tempea, C. Schubert, E. M. Anger, P. K. Ahnelt, M. Stur, J. E. Morgan, A. Cowey, G. Jung, T. Le, and A. Stingl, "Compact, low-cost Ti:Al<sub>2</sub>O<sub>3</sub> laser for in vivo ultrahigh-resolution optical coherence tomography," *Opt Lett*, vol. 28, pp. 905-7, 2003.
- [8] D. L. Marks, A. L. Oldenburg, J. J. Reynolds, and S. A. Boppart, "Study of an ultrahigh-numerical-aperture fiber continuum generation source for optical coherence tomography," *Optics Letters*, vol. 27, pp. 2010-12, 2002.
- [9] P. C. Wagenblast, T. H. Ko, J. G. Fujimoto, F. X. Kaertner, and U. Morgner, "Ultrahigh-resolution optical coherence tomography with a diode-pumped broadband Cr<sup>3+</sup>: LiCAF laser," *Optics Express*, vol. 12, pp. 3257-3263, 2004.
- [10] L. Vabre, A. Dubois, and A. C. Boccara, "Thermal-light full-field optical coherence tomography," *Optics Letters*, vol. 27, pp. 530-2, 2002.
- [11] A. M. Kowalewicz, T. Ko, I. Hartl, J. G. Fujimoto, M. Pollnau, and R. P. Salathe, "Ultrahigh resolution optical coherence tomography using a superluminescent light source," *Optics Express*, vol. 10, 2002.
- [12] C. Grivas, T. C. May-Smith, D. P. Shepherd, R. W. Eason, M. Pollnau, and M. Jelinek, "Broadband single-transverse-mode fluorescence sources based on ribs fabricated in pulsed laser deposited Ti : sapphire waveguides," *Applied Physics a-Materials Science & Processing*, vol. 79, pp. 1195-1198, 2004.
- [13] T. H. Ko, D. C. Adler, J. G. Fujimoto, D. Mamedov, V. Prokhorov, V. Shidlovski, and S. Yakubovich, "Ultrahigh resolution optical coherence tomography imaging with a broadband superluminescent diode light source," *Optics Express*, vol. 12, pp. 2112-2119, 2004.
- [14] J. M. Schmitt, A. Knüttel, M. Yadlowsky, and M. A. Eckhaus, "Optical-coherence tomography of a dense tissue: statistics of attenuation and backscattering," *Phys Med Biol*, vol. 39, pp. 1705-20, 1994.
- [15] B. E. Bouma, G. J. Tearney, I. P. Bilinsky, B. Golubovic, and J. G. Fujimoto, "Self-phase-modulated Kerr-lens mode-locked Cr:forsterite laser source for optical coherence tomography," *Optics Letters*, vol. 21, pp. 1839-1841, 1996.
- [16] P. R. Herz, Y. Chen, A. D. Aguirre, J. G. Fujimoto, H. Mashimo, J. Schmitt, A. Koski, J. Goodnow, and C. Petersen, "Ultrahigh resolution optical biopsy with endoscopic optical coherence tomography," *Optics Express*, vol. 12, pp. 3532-3542, 2004.

- [17] J. K. Ranka, R. S. Windeler, and A. J. Stentz, "Visible continuum generation in air-silica microstructure optical fibers with anomalous dispersion at 800 nm," *Optics Letters*, vol. 25, pp. 25-27, 2000.
- [18] I. Hartl, X. D. Li, C. Chudoba, R. K. Hganta, T. H. Ko, J. G. Fujimoto, J. K. Ranka, and R. S. Windeler, "Ultrahigh-resolution optical coherence tomography using continuum generation in an air-silica microstructure optical fiber," *Optics Letters*, vol. 26, pp. 608-610, 2001.
- [19] B. Povazay, K. Bizheva, A. Unterhuber, B. Hermann, H. Sattmann, A. F. Fercher, W. Drexler, A. Apolonski, W. J. Wadsworth, J. C. Knight, P. S. J. Russell, M. Vetterlein, and E. Scherzer, "Submicrometer axial resolution optical coherence tomography," *Optics Letters*, vol. 27, pp. 1800-2, 2002.
- [20] W. Drexler, "Ultrahigh-resolution optical coherence tomography," *J Biomed Opt*, vol. 9, pp. 47-74, 2004.
- [21] H. Lim, Y. Jiang, Y. Wang, Y. C. Huang, Z. Chen, and F. W. Wise, "Ultrahigh-resolution optical coherence tomography with a fiber laser source at 1 microm," *Opt Lett*, vol. 30, pp. 1171-3, 2005.
- [22] B. Povazay, K. Bizheva, B. Hermann, A. Unterhuber, H. Sattmann, A. F. Fercher, W. Drexler, C. Schubert, P. K. Ahnelt, M. Mei, R. Holzwarth, W. J. Wadsworth, J. C. Knight, and P. S. Russel, "Enhanced visualization of choroidal vessels using ultrahigh resolution ophthalmic OCT at 1050 nm," *Optics Express*, vol. 11, pp. 1980-1986, 2003.
- [23] Y. Wang, Y. Zhao, J. S. Nelson, Z. Chen, and R. S. Windeler, "Ultrahigh-resolution optical coherence tomography by broadband continuum generation from a photonic crystal fiber," *Opt Lett*, vol. 28, pp. 182-4, 2003.
- [24] S. Bourquin, A. D. Aguirre, I. Hartl, P. Hsiung, T. H. Ko, J. G. Fujimoto, T. A. Birks, W. J. Wadsworth, U. Bunting, and D. Kopf, "Ultrahigh resolution real time OCT imaging using a compact femtosecond Nd : Glass laser and nonlinear fiber," *Optics Express*, vol. 11, pp. 3290-3297, 2003.
- [25] Y. Wang, J. S. Nelson, Z. Chen, B. J. Reiser, R. S. Chuck, and R. S. Windeler, "Optimal wavelength for ultrahigh-resolution optical coherence tomography," *Optics Express*, vol. 11, 2003.
- [26] N. Nishizawa, Y. Chen, P. Hsiung, E. P. Ippen, and J. G. Fujimoto, "Real-time, ultrahigh-resolution, optical coherence tomography with an all-fiber, femtosecond fiber laser continuum at 1.5 microm," *Opt Lett*, vol. 29, pp. 2846-8, 2004.
- [27] T. Hori, N. Nishizawa, T. Goto, and M. Yoshida, "Wideband and nonmechanical sonogram measurement by use of an electronically controlled, wavelength-tunable, femtosecond soliton pulse," *Journal of the Optical Society of America B-Optical Physics*, vol. 20, pp. 2410-2417, 2003.
- [28] K. L. Corwin, N. R. Newbury, J. M. Dudley, S. Coen, S. A. Diddams, B. R. Washburn, K. Weber, and R. S. Windeler, "Fundamental amplitude noise limitations to supercontinuum spectra generated in a microstructured fiber," *Applied Physics B-Lasers and Optics*, vol. 77, pp. 269-277, 2003.
- [29] A. Apolonski, B. Povazay, A. Unterhuber, W. Drexler, W. J. Wadsworth, J. C. Knight, and P. S. Russell, "Spectral shaping of supercontinuum in a cobweb photonic-crystal fiber with sub-20-fs pulses," *Journal of the Optical Society of America B-Optical Physics*, vol. 19, pp. 2165-2170, 2002.
- [30] N. R. Newbury, B. R. Washburn, K. L. Corwin, and R. S. Windeler, "Noise amplification during supercontinuum generation in microstructure fiber," *Optics Letters*, vol. 28, pp. 944-946, 2003.
- [31] K. Bizheva, B. Povazay, B. Hermann, H. Sattmann, W. Drexler, M. Mei, R. Holzwarth, T. Hoelzenbein, V. Wacheck, and H. Pehamberger, "Compact, broad-bandwidth fiber laser for sub-2-microm axial resolution optical coherence tomography in the 1300-nm wavelength region," *Opt Lett*, vol. 28, pp. 707-9, 2003.

- [32] P. L. Hsiung, Y. Chen, T. H. Ko, J. G. Fujimoto, C. J. S. de Matos, S. V. Popov, J. R. Taylor, and V. P. Gapontsev, "Optical coherence tomography using a continuous-wave, high-power, Raman continuum light source," *Optics Express*, vol. 12, pp. 5287-5295, 2004.
- [33] K. M. Hilligsoe, T. V. Andersen, H. N. Paulsen, C. K. Nielsen, K. Molmer, S. Keiding, R. Kristiansen, K. P. Hansen, and J. J. Larsen, "Supercontinuum generation in a photonic crystal fiber with two zero dispersion wavelengths," *Optics Express*, vol. 12, pp. 1045-1054, 2004.
- [34] T. Hori, N. Nishizawa, T. Goto, and M. Yoshida, "Experimental and numerical analysis of widely broadened supercontinuum generation in highly nonlinear dispersion-shifted fiber with a femtosecond pulse," *Journal of the Optical Society of America B-Optical Physics*, vol. 21, pp. 1969-1980, 2004.
- [35] G. P. Agrawal, *Nonlinear fiber optics*, 3rd ed. San Diego: Academic Press, 2001.
- [36] S. R. Chinn and E. A. Swanson, "Blindness Limitations in Optical Coherence Domain Reflectometry," *Electronics Letters*, vol. 29, pp. 2025-2027, 1993.
- [37] G. Genty, M. Lehtonen, H. Ludvigsen, J. Broeng, and M. Kaivola, "Spectral broadening of femtosecond pulses into continuum radiation in microstructured fibers," *Optics Express*, vol. 10, pp. 1083-1098, 2002.
- [38] A. V. Husakou and J. Herrmann, "Supercontinuum generation of higher-order solitons by fission in photonic crystal fibers," *Physical Review Letters*, vol. 8720, pp. -, 2001.
- [39] A. L. Gaeta, "Nonlinear propagation and continuum generation in microstructured optical fibers," *Optics Letters*, vol. 27, pp. 924-926, 2002.
- [40] B. R. Washburn, S. E. Ralph, and R. S. Windeler, "Ultrashort pulse propagation in air-silica microstructure fiber," *Optics Express*, vol. 10, pp. 575-580, 2002.
- [41] S. Coen, A. H. L. Chau, R. Leonhardt, J. D. Harvey, J. C. Knight, W. J. Wadsworth, and P. S. J. Russell, "Supercontinuum generation by stimulated Raman scattering and parametric four-wave mixing in photonic crystal fibers," *Journal of the Optical Society of America B-Optical Physics*, vol. 19, pp. 753-764, 2002.
- [42] A. V. Husakou and J. Herrmann, "Supercontinuum generation, four-wave mixing, and fission of higher-order solitons in photonic-crystal fibers," *Journal of the Optical Society of America B-Optical Physics*, vol. 19, pp. 2171-2182, 2002.
- [43] M. H. Frosz, P. Falk, and O. Bang, "The role of the second zero-dispersion wavelength in generation of supercontinua and bright-bright soliton-pairs across the zero-dispersion wavelength," *Optics Express*, vol. 13, pp. 6181-6192, 2005.
- [44] P. Falk, M. H. Frosz, and O. Bang, "Supercontinuum generation in a photonic crystal fiber with two zero-dispersion wavelengths tapered to normal dispersion at all wavelengths," *Optics Express*, vol. 13, pp. 7535-7540, 2005.
- [45] H. Wang and A. M. Rollins, "Optimization of dual-band continuum light source for ultrahigh-resolution optical coherence tomography," *Applied Optics*, vol. 46, pp. 1787-1794, 2007.
- [46] T. Hori, J. Takayanagi, N. Nishizawa, and T. Goto, "Flatly broadened, wideband and low noise supercontinuum generation in highly nonlinear hybrid fiber," *Optics Express*, vol. 12, pp. 317-324, 2004.
- [47] M. Wojtkowski, T. Bajraszewski, P. Targowski, and A. Kowalczyk, "Real-time in vivo imaging by high-speed spectral optical coherence tomography," *Opt Lett*, vol. 28, pp. 1745-7, 2003.
- [48] M. Wojtkowski, V. J. Srinivasan, T. H. Ko, J. G. Fujimoto, A. Kowalczyk, and J. S. Duker, "Ultrahigh-resolution, high-speed, Fourier domain optical coherence tomography and methods for dispersion compensation," *Optics Express*, vol. 12, pp. 2404-2422, 2004.
- [49] N. Nassif, B. Cense, B. H. Park, S. H. Yun, T. C. Chen, B. E. Bouma, G. J. Tearney, and J. F. de Boer, "In vivo human retinal imaging by ultrahigh-speed spectral domain optical coherence tomography," *Opt Lett*, vol. 29, pp. 480-2, 2004.
- [50] S. H. Yun, G. J. Tearney, B. E. Bouma, B. H. Park, and J. F. de Boer, "High-speed spectral-domain optical coherence tomography at 1.3  $\mu$  m wavelength," *Optics Express*, vol. 11, pp. 3598-3604, 2003.



## Chapter 4

### Optical Coherence Microscopy

#### 4.1 Introduction

Cellular imaging of human tissues has been recognized for the past decade as an enabling advance in many clinical applications of optical coherence tomography (OCT). Current diagnosis and management of numerous human diseases, including cancers and various inflammatory and autoimmune conditions, depend upon biopsy and histopathologic analysis of cellular and subcellular features. Imaging cells with traditional OCT methods, however, has not been possible due to the limited transverse resolution of such techniques.

The term optical coherence microscopy (OCM) refers to optical coherence tomography methods with high transverse spatial resolution. OCM uses higher numerical aperture focusing than conventional OCT and therefore must generate *en face* rather than cross-sectional images in order to avoid the depth of field limitation in the cross-sectional plane. OCM is a powerful technique that can achieve the high resolutions sufficient for cellular imaging in human tissues. By using coherence gated detection, unwanted scattered light can be dramatically reduced, improving image contrast and enabling imaging to greater depths than possible with confocal microscopy. At the same time, coherence gating in OCM enables the use of lower numerical aperture focusing than required for classic confocal microscopy. Therefore, OCM promises to be a key technology to enable cellular level, internal body imaging in future endoscopic applications.

Two general approaches for OCM have been described to date in the literature. The point-scanning, or “flying spot,” approach is based directly upon the principle of confocal microscopy in which a single point of illumination in the scattering medium is imaged to a pinhole point detector. The pinhole imposes a spatial gate on photons returning from the sample and serves to preferentially reject light from outside the focal plane. Two-dimensional *en face* images are created by raster scanning the point focus. Traditional fiber-optic OCT systems are inherently confocal and implement the point-scanning technique. As the transverse spot size is reduced in the OCM limit, the confocal axial response becomes comparable to the axial coherence gate and the combined confocal and coherence gating creates both important advantages and challenges. In contrast to point-scanning OCM systems, the second approach to OCM

involves full-field illumination and detection [1-3]. The full-field technique is similar to conventional white-light interference microscopy and produces *en face* images through parallel illumination and detection. Full-field OCM / OCT techniques typically use CCD based detection and have achieved impressive image quality. The full-field methods have the advantage of simplicity and highly parallel data acquisition, but because of their inherent sensitivity to motion, *in vivo* imaging is challenging.

The work in this thesis focuses on point-scanning, confocal OCM implementations, and this meaning of optical coherence microscopy should henceforth be assumed. This chapter provides a comprehensive review of prior and concurrent work on OCM methods as well as an overview of OCM image formation. It also discusses several of the challenges and advantages of the technique and describes system design approaches for high resolution OCM, with a focus on enabling technological developments. Finally, examples of cellular level imaging in human tissues are presented. Subsequent chapters detail the OCM system developed and the OCM imaging studies performed for this thesis.

The majority of this thesis chapter is to be published separately as a book chapter [4].

## 4.2 Confocal Microscopy

Confocal microscopy was first proposed by Marvin Minsky in the late 1950s [5]. Imaging can be performed in reflectance or fluorescence modes, depending on the specific application. Figure 4.1 illustrates the basic principle of confocal microscopy in reflection geometry. A point source illuminates a sample plane through a focusing objective lens. The backscattered light from the focal plane is recollected by the objective lens and focused through a pinhole detector. Unwanted scattered light from outside the focal plane is also collected by the objective, but this light is defocused at the detector and is therefore rejected. The spatial discrimination against out of focus scattered light is known as confocal gating. The combination of focused illumination and spatially filtered detection reduces blurring, increases effective resolution, and improves contrast through improved signal to noise ratio [6]. The single point transverse resolution of a confocal microscope is typically defined as the full width at half maximum (FWHM) of the transverse point spread function. For a focused Gaussian beam, the transverse spot  $dx$  can be characterized by the  $1/e^2$  radius of the transverse intensity response [7], which is given as

$$dx = \frac{0.46\lambda}{NA} \quad (1)$$

The axial response of a confocal microscope to a perfectly reflecting plane at the focus under Gaussian beam assumptions can similarly be described as

$$dz = \frac{1.4n\lambda}{NA^2} \quad (2)$$

where  $dz$  represents the FWHM of the axial irradiance [8]. As shown, the transverse resolution varies inversely with the numerical aperture (NA) of the objective lens, while the axial resolution or axial sectioning capability of the confocal microscope varies inversely with the square of the NA. Hence, image quality in scattering objects requires the use of high magnification, high-NA objectives. With such high NA lenses, typically NA 0.7 – 1.2, confocal microscopy systems can achieve 3 – 5  $\mu\text{m}$  axial sectioning capability and better than 1  $\mu\text{m}$  transverse resolution [9].

To generate an image in two dimensions, several scanning approaches have been demonstrated, including sample scanning, objective scanning, and beam scanning [7]. The use of laser sources marked a major development in confocal microscopy [10, 11] and enabled high speed, high resolution point scanning systems at multiple wavelengths. Typically, the confocal scanning laser microscope (CLSM) samples an *en face* scan plane by rapidly raster scanning the beam on tissue.

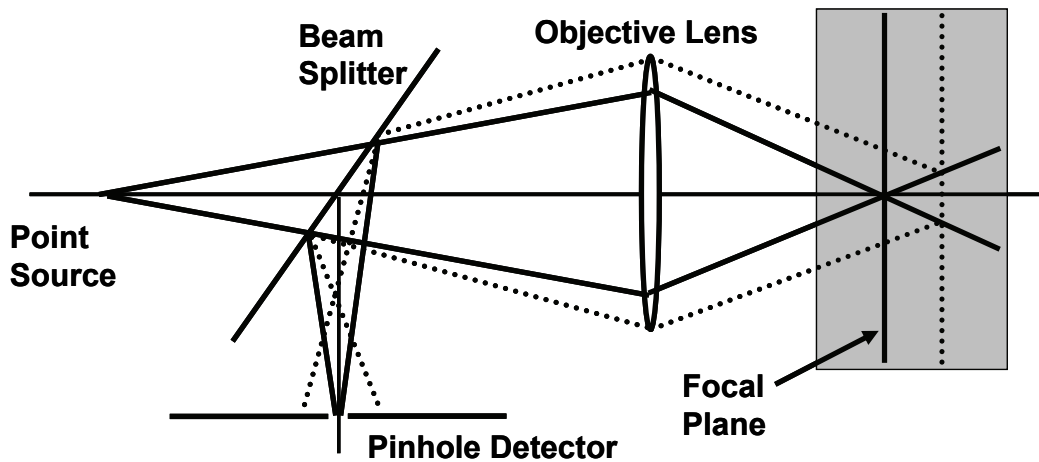


**Figure 4.1.** Schematic illustrating the principle of reflectance confocal microscopy.

Confocal laser scanning microscopy was demonstrated for *in vivo* cellular imaging of human tissues at visible wavelengths [8]. Advances in instrumentation and design led to the development of video-rate reflectance systems capable of reliable imaging in clinical applications [12-14]. These systems offer high power illumination and extension to deeper penetrating wavelengths in the near infrared. Operating at wavelengths of 800 nm and 1064 nm, the systems provide transverse resolution of 0.5 - 1  $\mu\text{m}$  and axial sectioning capacity of 3 - 5  $\mu\text{m}$ . Results of reflectance imaging of human skin [9, 15-18], oral mucosa [19], and cervix [20] have demonstrated the capability to image normal and pathologic cellular features *in vivo* with impressive correlation of confocal images with histology. Commercial versions of the CLSM imaging system now offer new tools for clinical diagnostic applications in dermatology and other specialties where open access to tissue specimens is possible. In addition, endoscope compatible reflectance confocal microscopes are being developed [21, 22].

Using exogenous fluorescence dyes to provide contrast, fluorescence confocal endoscopy has been developed for clinical application in the gastrointestinal tract [23-26]. Excellent *in vivo* image quality has generated excitement about this technology and has set a standard for reflectance-based endoscopic methods to match. Because excitation of fluorophores is performed with visible wavelengths, however, the penetration depth is quite limited with the fluorescence approach. In addition, exogenous dyes have toxicities which may limit clinical applicability. Reflectance-based, endoscopic confocal or optical coherence microscopy methods that can provide comparable image quality at greater depths, but without the need for exogenous contrast, would therefore be an important advance.

### 4.3 High Transverse Resolution in Optical Coherence Tomography

Compared with confocal microscopy, conventional optical coherence tomography systems work in the opposite focusing limit. In OCT, the focal spot size is restricted using relatively low NA lenses in order to preserve a sufficient depth of field for cross sectional imaging. As the NA of the OCT optics increases, the depth of field decreases and signal loss occurs at depths away from the focus. Figure 4.2 compares these focusing limits and their implications for OCT image formation. Images are acquired by setting the focus to a defined position in the tissue and detecting light from different depths by coherence ranging, either in the time domain or in the frequency domain. In confocal microscopy, the goal is precisely to use high NA focusing to restrict the depth of field such that light outside of the focal plane is rejected. *En face* images are then formed by rapidly raster scanning the beam.

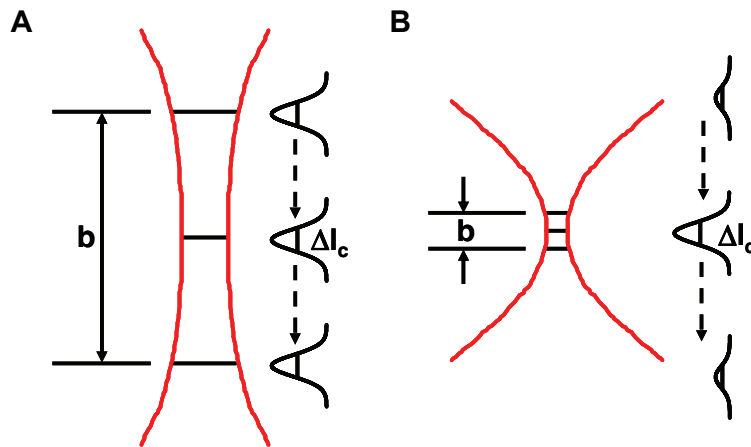


**Figure 4.2.** Focusing limits for OCT imaging. Use of a low numerical aperture lens (A) preserves depth of field across the entire depth scan while a higher aperture lens (B) leads to restricted confocal parameter and signal loss at the edges of the depth scan. Confocal parameter,  $b$ ; Coherence length  $l_c$ .

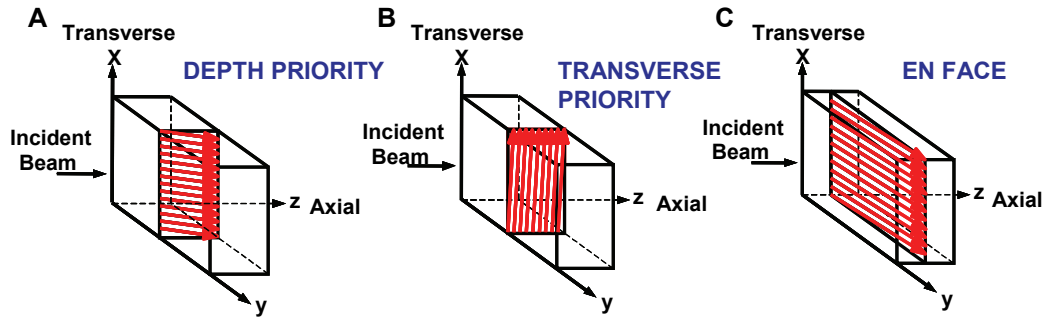


**Figure 4.3.** Image scanning protocols for optical coherence tomography.

Several solutions to overcome the depth of field restriction in OCT have been demonstrated in the literature. These methods can be classified into three types according to the image acquisition scan protocol, as illustrated in figure 4.3. Depth priority methods maintain the cross-sectional imaging plane of conventional OCT by rapidly acquiring along the depth axis while scanning the transverse beam position at the image frame rate. Transverse priority OCT techniques also scan a cross-sectional plane. In contrast, however, the transverse beam position is scanned to rapidly acquire the transverse axis, while varying the depth axis at the frame rate. The third option is to acquire an *en face* image plane analogous to confocal laser scanning microscopy.

#### 4.3.1 Depth Priority Techniques

The most direct strategy for maintaining high transverse resolution across the image using depth priority scanning is to coordinate the optical focus depth with the depth scanning of the coherence gate. This approach has been termed focus tracking in the literature and has been used by Schmitt et al. to generate high quality cross-sectional images of human skin with 3  $\mu\text{m}$  transverse resolution [27]. Depth scanning was synchronized with focus scanning by mounting the reference reflector and the focusing objective on a single translation stage. The disadvantage of this setup is the relatively limited axial scan rates that can be achieved using mechanical translation of the objective. Image acquisition required nearly 30 seconds for 256 lines. Lexer et al. devised a different scheme for high speed focus tracking based on a novel microscope design that shifts the beam focus through the object without changing the reference path length [28]. Images were acquired of an *ex vivo* human cornea specimen in approximately one second with 5  $\mu\text{m}$  transverse resolution. The ability to scan the focus without translating the optical path required careful choice of the microscope magnification, which limits overall design flexibility. Other groups have investigated fast focus adjustment using a variable focus micromachined mirror [29, 30] or lens [31]. Application of these devices in the future for endoscopic applications is promising.

A disadvantage of focus tracking approaches is their incompatibility with high speed, Fourier domain detection techniques. In Fourier domain OCT, backscattered or backreflected light is acquired from all

depths simultaneously in the frequency or Fourier domain and axial scan information is subsequently reconstructed using a Fourier transform. Fourier domain OCT methods have been shown to have a significant speed and sensitivity advantage compared with time-domain OCT [32-34]. Two basic Fourier domain implementations have been demonstrated. Spectral / Fourier domain OCT uses a broadband light source and a spectrometer with a charge-coupled device (CCD) in the detection arm. Swept source / Fourier domain OCT uses a frequency swept laser source and individual photodiode detectors. In either implementation, depth scanning of the coherence gate is not performed, and it is therefore impossible to perform focus-tracking to extend depth of field. The increases in speed and sensitivity, however, have made Fourier domain detection the method of choice for most OCT imaging applications, such as ophthalmology [35, 36]. Strategies for improving the transverse resolution which are compatible with both time and Fourier domain detection are therefore desirable.

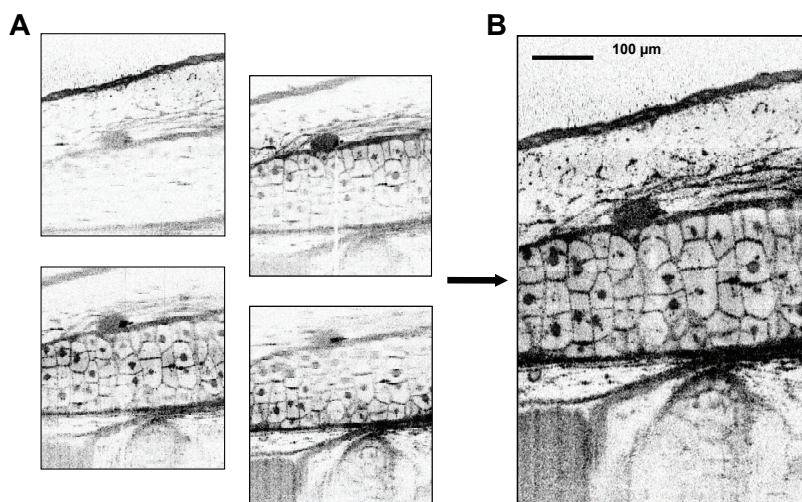


**Figure 4.4.** C-mode scanning in optical coherence tomography. Acquisition of individual images with high transverse resolution but restricted depth of field can be reconstructed to form a single image with extended depth of field. Images are reproduced from Drexler et al. [37]

One technique for improving transverse resolution that works for all OCT implementations has been termed C-mode scanning in analogy to ultrasound. This method was demonstrated for OCT by Drexler et al. using an ultrahigh resolution OCT system with 1  $\mu\text{m}$  axial x 3  $\mu\text{m}$  transverse resolution [37]. Figure 4.4 presents the concept of C-mode scanning. Multiple OCT images with high axial and transverse resolution were acquired with the focal position set at different depths. The individual images in figure 4.4a clearly demonstrate the limited depth of focus. These images were overlapped and fused in figure 4.4b to form a single image with extended depth of field. Cellular and subcellular structures in the *Xenopus laevis* tadpole are visualized. C-mode scanning techniques have also been demonstrated for Fourier domain OCT [38]. Like focus-tracking, C-mode scanning still requires translation of the focal

position in depth, albeit at a much slower rate. The number of images required scales inversely with the desired transverse resolution. As the focal spot and depth of field for an individual image is reduced, more images are required, which reduces the overall frame rate that can be achieved in the composite image. To address this limitation, Yang et al. developed a multi-focus fiber probe capable of simultaneously generating images at different depths in tissue [39]. In the initial demonstration, four simultaneous images were acquired while maintaining a spot diameter of 9-14  $\mu\text{m}$ .

Other techniques are being developed to increase the image depth of field without any focus translation or offset. Ding et al. proposed the use of an axicon lens in the OCT probe to generate a long focal volume [40]. In phantom imaging experiments, a 6 mm focusing depth range with 10  $\mu\text{m}$  transverse resolution was demonstrated. Axicons produce a cylindrical Bessel beam field distribution with an extended central lobe lying along the optical axis of the lens and are typically used in the form of refracting cone lenses. Unfortunately, there is a trade-off between signal intensity and focusing range since the axicon distributes the focal energy along the focusing range and the central lobe of the Bessel field carries only a fraction of the total power compared with a focused Gaussian beam. In double pass reflection geometry, the squared signal loss limits the utility for high sensitivity imaging in biological tissues. Leitgeb et al. has improved upon the initial axicon demonstration by using the improved sensitivity of spectral domain detection in combination with a modified confocal detection scheme [41]. Transverse resolution of  $\sim 1.5 \mu\text{m}$  was maintained over 200  $\mu\text{m}$  image range with a sensitivity of 105 dB. Techniques such as these are compelling for high speed, cross-sectional cellular imaging and will undoubtedly be the subject of further research.

Another approach for increasing transverse resolution without focus adjustment is the use of post-processing algorithms. Image processing is attractive for increasing resolution since the algorithms require minimal to no modifications to existing OCT setups and can be applied offline to large volumes of data. Ralston et al. have introduced synthetic aperture inverse scattering methods for reducing transverse blurring in OCT images [42]. Depth of field and resolution improvement was demonstrated in scattering phantoms and in the weakly scattering *Xenopus* tadpole specimen with 15  $\mu\text{m}$  transverse resolutions. Subsequent research demonstrated simulations showing that inverse scattering theory can be applied to OCT images to provide spatially invariant resolution over the full depth range [43]. The performance of these algorithms in the high NA confocal limit and in highly scattering biological media is under investigation.

#### **4.3.2 Transverse Priority and *En Face* Imaging**

Transverse priority image acquisition requires rapid transverse scanning of the beam on tissue and slow depth scanning, as illustrated in figure 4.3b. Podoleanu et al. suggested transverse priority scanning

for performing OCT imaging of the retina and skin [44]. As in C-mode scanning, transverse-priority acquisition enables a slow translation of the focus in tissue at the image frame rate. If focus-tracking is implemented to coordinate the depth scan and focus translation, then no image fusion is required and data collection is very efficient. Cobb et al. demonstrated continuous focus tracking to achieve *ex vivo* OCT images of excised rabbit esophagus at 1 frame/s with transverse resolution of 10.5  $\mu\text{m}$  [45]. Transverse scanning was performed at 1.37 kHz using a miniaturized probe, and the reference path length was adjusted to compensate for index of refraction path length shifts produced by the air-tissue interface.

To date, *en face* imaging has proven to be the most robust approach for achieving fine enough transverse resolution for cellular imaging in scattering tissues. In the *en face* plane, the position of the coherence gate can be matched to the position of the optical focus while the beam is raster scanned in two transverse dimensions on the sample. In this manner, high speed focus tracking tactics are not required and the image acquisition rate is limited only by the speed of the XY scanner. Furthermore, high NA can be used to achieve high axial and transverse resolutions, in the confocal limit. The implementation of *en face* optical coherence microscopy was first demonstrated by Izatt and colleagues [46], although it has a history in the development of confocal interference microscopes [47-51]. Izatt and others demonstrated that broadband coherence gating can significantly enhance the imaging depth of conventional confocal microscopy [46, 52, 53]. Subsequently, Izatt et al. showed that *en face* OCM could generate high quality images of cellular features deep below the surface in human gastrointestinal tissues [54]. *In vivo*, *en face* optical coherence tomography was implemented for imaging in the skin and retina, although systems were limited to relatively low transverse resolution and were not capable of visualizing cellular features [44, 55]. In comparison, the development of *en face* optical coherence microscopy for *in vivo* cellular imaging applications has been slow. In part, this is related to the numerous exciting developments in OCT imaging, which have spread the efforts of researchers across many fronts. In addition, however, OCM technology development for cellular imaging presents unique challenges and requires additional complexity compared with other OCT methods. The remainder of this chapter is devoted to discussing the challenges and the advantages of *en face* OCM imaging and to describing progress toward *in vivo* cellular imaging applications.

### 4.3.3 *En Face* Imaging in the Time and Fourier Domain

Given the dramatic speed advantages of Fourier domain versus time domain OCT for cross-sectional imaging, it is worth discussing the relative performance of the two approaches for *en face* imaging. For imaging in the *en face* plane, time domain detection approaches can actually have an advantage in terms of imaging speed compared with Fourier domain detection. The reason for this is precisely the same property of Fourier domain detection that creates the sensitivity advantage for cross-sectional imaging.

Using spectral / Fourier domain detection or swept-source / Fourier domain detection, signals from multiple depths are detected simultaneously. In order to acquire an *en face* image, an entire three-dimensional volume must effectively be acquired. This places a tremendous demand upon the Fourier-domain OCT system axial line rate in order to achieve high frame rates in the *en face* plane. For a typical image of 500 x 500 pixels, acquisition speeds of 8 frames/s would require an astonishing axial scan rate of 2 million axial lines per second. This is far beyond the specifications of typical spectral / Fourier domain or swept source / Fourier domain systems reported in the literature. For spectral / Fourier domain systems with line rate of 29 kHz [35], acquisition of a 500 x 500 scan volume would take over 8 seconds. Similarly, swept source / Fourier domain systems operating at 15-20 kHz [38, 56, 57] would require 12-17 seconds for the same volume.

By contrast, time domain OCT imaging systems can be adjusted to efficiently acquire signals from only a single *en face* plane. Rather than scanning in depth to generate a Doppler frequency for detection, *en face* imaging systems use phase modulation in the reference arm to provide an external carrier [54]. The reference path is set to the focus depth such that only one depth is sampled at any given transverse position. Image acquisition rate is then determined by signal to noise constraints and by the maximum speed of the XY scanners. In addition, the intrinsic sensitivity advantage of Fourier domain detection vanishes when only a single *en face* plane is of interest. For a given image acquisition time, the increase in line rate required for sampling a three-dimensional volume in Fourier domain detection cancels the sensitivity advantage compared with sampling a single *en face* plane in time domain. These characteristics currently make time domain the method of choice for high speed *en face* imaging at rates of 4-8 frames per second and higher.

There are of course advantages to performing *en face* OCT and OCM imaging using Fourier domain detection. Sampling of an entire volume can be quite powerful. An arbitrary *en face* plane can be chosen from the volume or structures can be rendered in three dimensions. In addition, Fourier domain detection can provide greatly increased phase stability compared with time domain detection. Choma et al. [58] and Joo et al. [59] demonstrated this property and implemented spectral / Fourier domain phase microscopy using common path interferometer designs. Other OCT/OCM methods have also shown to have advantages in the spectral / Fourier domain, including numerical dispersion compensation [60] and spectroscopic OCM [61]. Moreover, imaging speeds are increasing rapidly, particularly in the case of swept source / Fourier domain imaging. Axial line rates of 115 kHz were demonstrated using a short cavity swept laser [62] while rates as high as 370 kHz have been shown using a novel long cavity laser design [63, 64]. This latter result, based on a fundamentally different approach to swept laser sources called Fourier-domain modelocking (FDML) is particularly promising for high speed volumetric imaging. Imaging performance is improved compared with previous swept sources and promises to scale to even

higher scan rates in the future. Figure 4.5 presents an example volume data set of the human finger acquired *in vivo* at 3.5 volumes/second with 256 x 128 x 256 pixels. Continued development of this method should enable real-time volumetric and *en face* imaging based on swept source / Fourier domain detection techniques.

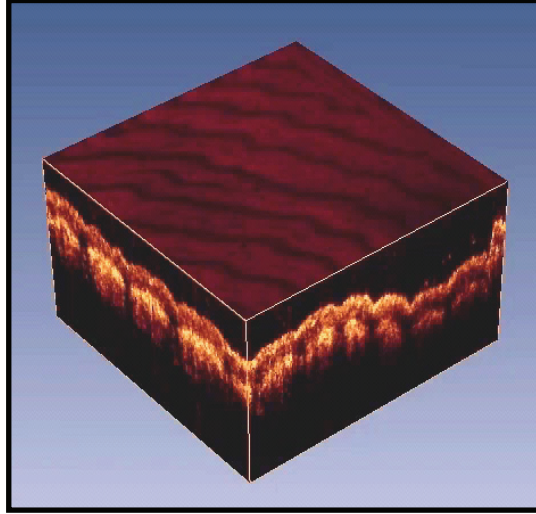


**Figure 4.5.** Three-dimensional volume dataset acquired with a Fourier-domain modelocked (FDML) swept source OCT system. The volume measures 3.5 mm x 3.5 mm x 2 mm and was acquired at 232 kHz axial scan rate with 906 Hz frame rate and 3.5 Hz volume rate. FDML lasers enable high speed volumetric imaging which should make possible high speed OCM imaging based on the swept source method. The image is reproduced from Huber et al. [63]

#### 4.4 Heterodyne Signal Detection in OCM

A schematic of a fiber-optic, time-domain OCM system is depicted in Figure 4.6. It consists of a broadband light source, an interferometer, photodetectors, an apparatus to modulate the reference arm phase, and a sample arm confocal microscope. Light from the low coherence light source is split equally by the 50/50 coupler between the reference arm and the sample arm. The reference and sample reflectivities are denoted  $R_r$  and  $R_s$ , respectively. A wavelength dependent phase delay  $\phi(\omega, t)$  can be imparted by the reference phase modulator. Light returning from the sample and the reference path interferes at the detector. Ignoring the transverse dependence of the fiber mode profile, the time averaged photocurrent at the detector can be written as [65]

$$i_D = \left\langle \frac{\eta e}{h\nu} \frac{|E_R + E_S|^2}{2\eta_f} \right\rangle \quad (3)$$

where  $\eta$  is the detector quantum efficiency,  $e$  is the electronic charge,  $h\nu$  is the photon energy and  $\eta_f$  is the intrinsic impedance of the fiber core material. The detector response time is taken to be much

longer than the coherence time for a low-coherence source but much shorter than the heterodyne signal beat oscillations. For a polychromatic, low-coherence source, the oscillating component of the heterodyne signal depends on the sum of the interference due to monochromatic plane waves and can be determined by integration of the cross-spectral interference term over the bandwidth of the light source. Ignoring the sample arm confocal response and assuming pure phase delay scanning from the reference arm modulator, the heterodyne photocurrent can then be written in terms of the optical frequency  $\omega$  and center frequency  $\omega_o$  as

$$i_D(\Delta l) \propto R_R R_S \{F^{-1}[S_o(\omega)]\} \cos(\omega_o \Delta t_p) = R_R R_S G_o \left( \frac{2\Delta l}{v_g} \right) \cos \left[ \frac{2\omega_o \Delta l}{v_p} + \phi(\omega_o, t) \right] \quad (4)$$

where

$$v_p = \frac{2\Delta l}{\Delta \tau_p} \quad (5)$$

and

$$v_g = \frac{2\Delta l}{\Delta \tau_g} \quad (6)$$

describe the phase velocity  $v_p$  and group velocity  $v_g$  in terms of the phase delay  $\Delta \tau_p$ , group delay  $\Delta \tau_g$ , and the difference in path length  $\Delta l = l_S - l_R$  between the sample and reference arms. The source power spectrum  $S_o(\omega)$  is related to the autocorrelation  $G_o(\Delta \tau_g)$  by the Fourier transform with respect to the group delay. The autocorrelation is a measure of the degree of temporal coherence of the source. Using the concept of the time-bandwidth product in Fourier transform theory, it is clear that the width of the interference signal envelope decreases for larger bandwidth or shorter coherence length light sources. In the case of a Gaussian light source, the full width at half maximum (FWHM) of the interference signal in free space can be shown to relate to the center wavelength  $\lambda_o$  and spectral bandwidth  $\Delta \lambda$  as [65]

$$\Delta l_{FWHM} = \frac{2 \ln 2}{\pi} \left( \frac{\lambda_o^2}{\Delta \lambda} \right) \quad (7)$$

This expression is typically used for the specification of the coherence gate or axial resolution of a low-coherence interferometry system. Figure 4.7 displays the coherence-gated axial resolution versus bandwidth for near infrared imaging wavelengths of interest in OCT and OCM.

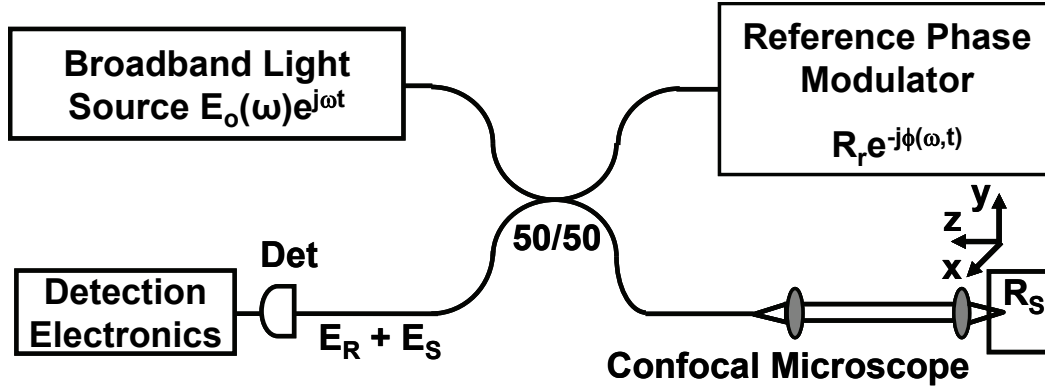


**Figure 4.6.** Schematic time-domain OCM imaging system. The system consists of a broadband light source, fiber-optic coupler, reference arm phase modulator, sample arm confocal microscope, and detection electronics.

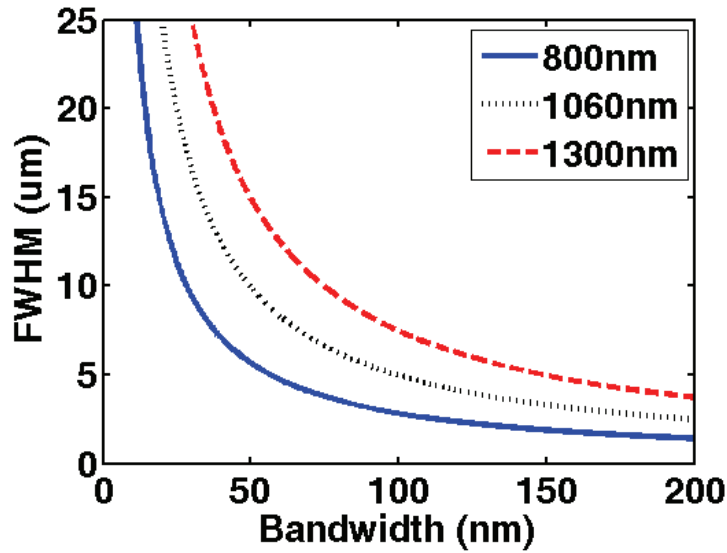


**Figure 4.7.** Coherence gated axial resolution as a function of spectral bandwidth for various center wavelengths. Broad bandwidth sources produce short coherence gates and high axial resolutions for imaging. FWHM, full-width at half maximum.

Izatt et al. described the heterodyne signal in OCM by incorporating a sample reflection in confocal geometry [54]. The influence of the sample arm confocal microscope is determined by the convolution of the field reflectivity function  $R_S(x, y, z)$  with the confocal impulse response  $[h_l(x, y, z)]^2$ . The appropriate confocal point spread function for a fiber-based microscope has been described by Gu et al [66]. For an axially distributed reflectivity which is present in scattering media, the heterodyne signal can be written as an integral over the sample arm path length  $l_S$ . Replacing  $R_S$  in (4) with the confocal response and integrating over the sample path, the heterodyne current becomes

$$i_D(l_R) \propto \int_{-\infty}^{\infty} dl_S R_R \left[ R_S(l_S) \otimes [h_I(l_S)]^2 \right] G_o \left( \frac{2\Delta l}{v_g} \right) \cos \left[ \frac{2\omega_o \Delta l}{v_p} + \phi(\omega_o, t) \right] \quad (8)$$

where the (x,y) dependence of  $r_s$  and  $h_I$  have been ignored for simplicity. The heterodyne component is the convolution of the sample arm confocal response with the carrier dependent source autocorrelation term. For a single scatterer at a depth location  $l_{S0}$  with reflectivity  $R_S(l_{S0})$ , the heterodyne current reduces to [54]

$$i_D(l_R) \propto R_R R_S(l_{S0}) \sqrt{I_C(l_{S0})} G_o \left( \frac{2(l_{S0} - l_R)}{v_g} \right) \cos \left[ \frac{2\omega_o(l_{S0} - l_R)}{v_p} + \phi(\omega_o, t) \right] \quad (9)$$

where  $I_C$  represents the confocal intensity response and, by definition,  $l_S = 0$  corresponds to the position of the focus.

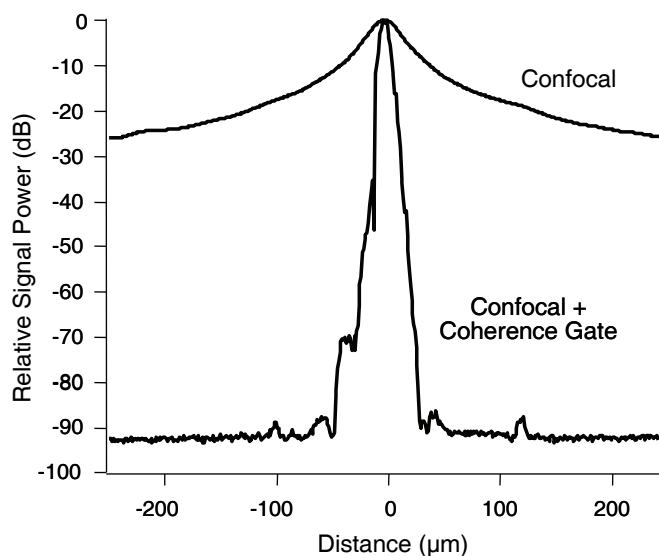
From (9) it is evident that control of the positions and widths of the confocal and coherence gates are decoupled. The confocal gate width is determined by the NA of the focusing objective and its position is set by the focus position. For the coherence gate, the width is determined by the light source bandwidth, and, for fixed focus position, the depth location is set by the reference arm path length  $l_R$ . Maximum heterodyne signal occurs when the reference and sample arm path lengths match  $l_{S0} = l_R$  such that the coherence and confocal gates overlap. The sensitivity of the heterodyne signal to the relative position of the gates scales with the NA of the objective lens. For high NA, the confocal parameter  $b$  as shown in figure 4.2b is quite small and results in a small depth of field for imaging. When the reference path length is set to the microscope focus,  $l_R = 0$ , the heterodyne amplitude is subject to the multiplication of the coherence and confocal gate point spread functions.

In contrast to OCT systems using time domain detection, *en face* OCM systems do not generate images by depth scanning. Instead, a phase modulation technique is used to introduce a carrier frequency to the heterodyne signal. Raster scanning the beam in an *en face* pattern encodes the image information as a function of time. After photodetection, the heterodyne image signal is filtered to remove noise and demodulated with either analog electronics or digital processing. The demodulated signal amplitude versus beam position constitutes the OCM image.

#### 4.5 Advantages of OCM

For imaging in scattering media, combined confocal and coherence gating can have advantages compared with confocal gating alone. Coherence and confocal gating reject unwanted out of focus scattered light using distinct mechanisms. The confocal gate rejects light based on spatial imaging

constraints, while the coherence gate rejects photons based on the path length they travel in tissue. The multiplicative effect of the two gates can be stronger than either gate individually, achieving greater image contrast and image penetration in scattering tissue. Moreover, as Wang et al. point out, the typical Gaussian coherence gate has a functional response which is not only more effective than the confocal gate but also more effective than the exponential extinction of incident light in tissue [67]. Figure 4.8 compares measured point spread functions on a log scale from an early OCM demonstration [46]. At depths of several tens of micrometers from the focus, the coherence gate rejects scattered light with orders of magnitude better efficiency than the confocal gate alone. In addition, the confocal axial response is affected by aberrations when focusing into tissue, which causes broadening of the peak of the point spread function and increases the wings of the response [68]. Combined coherence and confocal gating can help to minimize reductions in contrast due to loss of confocal axial resolution.



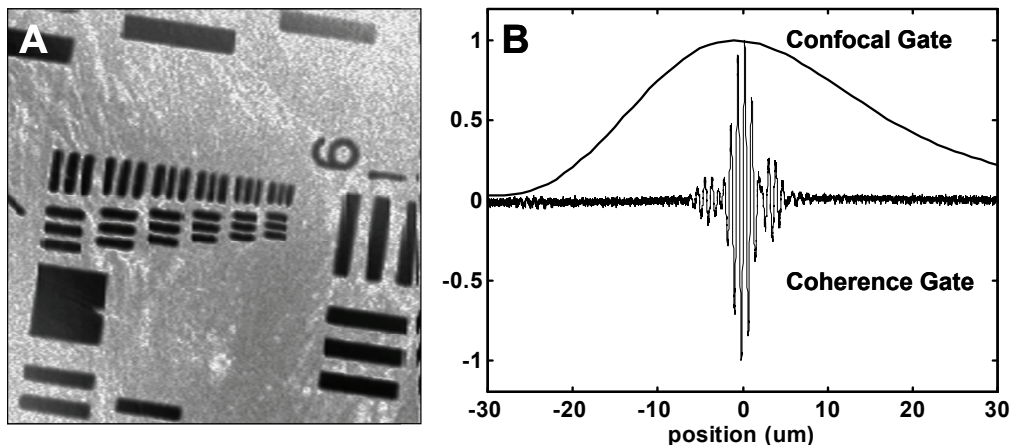
**Figure 4.8.** Measured confocal and coherence-gated axial resolutions for a typical OCM imaging system. Data is presented on a log scale and demonstrates the improved rejection of out of focus scattered light using combined confocal and coherence-gating compared with confocal gating alone. Figure is reproduced from Izatt et al. [46]

Image penetration depth limits in confocal microscopy and their enhancement using coherence gating have been studied by several investigators [46, 53, 69-71]. Using single scattering theory, and signal to background noise considerations, Izatt et al. estimated the confocal penetration limit to be in the range of 5 – 8 mean free paths (MFP) [46]. Schmitt et al. used Monte Carlo simulations to investigate the role of multiple scattering and concluded that penetration depth is actually limited to the range of 2 – 4 MFP [70, 71]. Smithpeter et al. subsequently used experimental measurements to predict a similar penetration depth of about 3 - 4 MFP in amelanotic tissue [69]. Coherence gating has been shown to enhance image

penetration by rejecting multiply scattered light, particularly from superficial depths. Based on the shot-noise quantum detection limit, initial estimates of imaging depth improvement were placed at 2 - 3 times compared with confocal gating alone [46]. As researchers became more aware of the sensitivity of coherence-gating methods to multiple scattering, these expectations were tempered. In highly scattering media, contrast in OCT and OCM images is limited by the ratio of single scattered to multiple scattered light, not by the quantum sensitivity limit [72]. Furthermore, the system sensitivity to multiple scattering is a function of both the optical properties of the tissue as well as the system design parameters, including the numerical aperture. Given these constraints, precise quantification of the image depth enhancement will depend upon the specifics of the application. Nonetheless, several initial studies in human tissues have demonstrated significant improvement using coherence gating. In one study, Izatt et al. demonstrated imaging of cellular features in colonic crypts at depths up to 500  $\mu\text{m}$  [54]. Another study by Clark et al. demonstrated an average depth improvement of 33% over confocal microscopy in human oral mucosa [73].

Closely linked to the notion of imaging depth in optical coherence microscopy is the question of resolution degradation in OCM images deep in scattering media, since image quality is dependent upon both contrast and resolution. Bizheva and Boas studied these questions using both simulation and experiment over a range of typical OCM parameters for scattering anisotropy and imaging NA [74]. Their results indicate relatively small changes in axial resolution at both low and high NA when imaging in media with low scattering anisotropy of 0.2. However, in media of high scattering anisotropy of 0.9, axial resolution degradation is quite rapid after 3-4 MFP. Moreover, degradation is more pronounced at lower NA compared with higher NA. With respect to transverse resolution, their results show no significant change up to 7 MFP for either low or high anisotropy and some resolution degradation after 7 MFP. Further studies such as these will be important to determine optimal parameters for deep cellular imaging in highly scattering tissues.

Combined coherence and confocal gating can have additional advantages beyond imaging depth improvement. One such advantage lies in the ability to use ultrahigh axial resolutions provided by very broad bandwidth light sources. Results from confocal microscopy in human skin demonstrate that achieving an axial resolution of  $< 5 \mu\text{m}$  is important for high contrast imaging of cellular features [8]. Such an optical slice axial thickness is similar to the conventional section thickness used in histopathology. Because the axial resolution depends inversely on the square of the NA ( $1/\text{NA}^2$ ), achieving a 5  $\mu\text{m}$  axial resolution with confocal microscopy alone requires high NA objectives, typically in the range of 0.7 – 1.2 NA. Most OCM systems to date have operated in this limit, using the confocal axial section as the dominant gating method with the coherence gate acting mostly to reduce the background from out of focus scattered light.



**Figure 4.9.** Optical coherence microscopy using a femtosecond laser source. High transverse resolution of  $< 2 \mu\text{m}$  allows visualization of even the smallest elements of the USAF 1951 resolution target (A). This transverse resolution was achieved with a reduced numerical aperture compared with that typically used for confocal microscopy, resulting in a confocal axial resolution of only  $\sim 30 \mu\text{m}$ . A short coherence gate of  $\sim 3 \mu\text{m}$  was then used to compensate for the lower confocal resolution. Images reproduced from Aguirre et al. [75]

The development of ultrahigh resolution OCT techniques opened the possibility of using the coherence gate rather than the confocal gate to set the optical section thickness [37]. Transverse resolution of  $1 - 2 \mu\text{m}$  can be maintained with much lower NA, since the transverse spot size only scales inversely with the NA ( $1/\text{NA}$ ). This implies that OCM with ultrahigh axial coherence resolution can achieve high contrast cellular imaging with significantly reduced NA compared with confocal microscopy. Figure 4.9 demonstrates this operating limit. A confocal microscope with an axial resolution of  $\sim 30 \mu\text{m}$  was combined with a broad bandwidth modelocked Ti:Al<sub>2</sub>O<sub>3</sub> solid-state laser light source [75]. The coherence gate measures  $\sim 3 \mu\text{m}$  and provides most of the optical sectioning power of this microscope. The effective NA of the microscope was only  $\sim 0.22$ . Figure 4.9a illustrates that high transverse resolution is still maintained. The smallest elements measuring  $2.2 \mu\text{m}$  in width on the USAF 1951 resolution target can be visualized. Figure 4.10 demonstrates that high contrast cellular images in human tissue can be achieved, despite the low confocal axial resolution. The images were taken *in vivo* at 4 frames per second using a novel modulator design capable of supporting large optical bandwidth (described in section 4.6.2). Figures 4.10a and 4.10b present images from the *Xenopus laevis* tadpole, a commonly used model organism in developmental biology studies. Cell nuclei and membranes as well as small vessels and blood cells are visible. Figures 4.10c and 4.10d show images of human skin *in vivo*. Epidermal cells and the lumen of a sweat duct can be clearly identified.

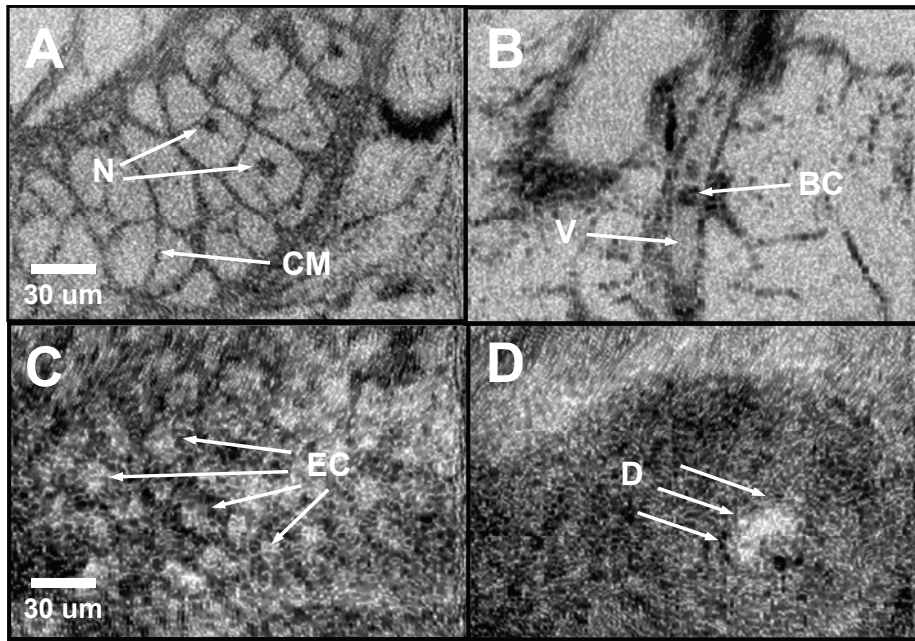


**Figure 4.10.** *In vivo* cellular imaging with optical coherence microscopy. Images of *Xenopus* tadpole (A,B) show cell membranes (CM), cell nuclei (N), and individual blood cells (BC) in a vessel (V). Epidermal cells (EC) and a duct (D) structure are also in images of human skin (C,D). Images reproduced from Aguirre et al. [75]

The ability to image with reduced NA makes OCM an enabling technology for endoscopic imaging. Miniaturization of high NA objectives is a challenging optical design problem [76]. Using a broad bandwidth light source to provide ultrahigh axial coherence resolutions can reduce the numerical aperture requirement, therefore allowing smaller and simpler probe designs. Figure 4.11 further highlights this advantage. Confocal axial and transverse resolutions are plotted versus numerical aperture. OCM can achieve sufficient transverse resolutions in the range of 0.2 - 0.5 NA and lower, despite the rapid degradation of the axial resolution seen in confocal microscopy.

An added advantage of OCM using lower NA lenses with lower magnification is the ability to achieve larger fields of view and longer working distance compared with confocal microscopy. Improved field of view allows the user to survey larger regions of tissue and helps to provide context to the microscopic features visualized with OCM. Furthermore, the larger confocal axial resolution affords the possibility of acquiring multiple depth sections by scanning the coherence gate relative to the focus. This may be useful for applications such as characterizing the three dimensional shape and size of cells in a particular tissue layer. This type of imaging cannot be done in confocal microscopy without translating the focus.

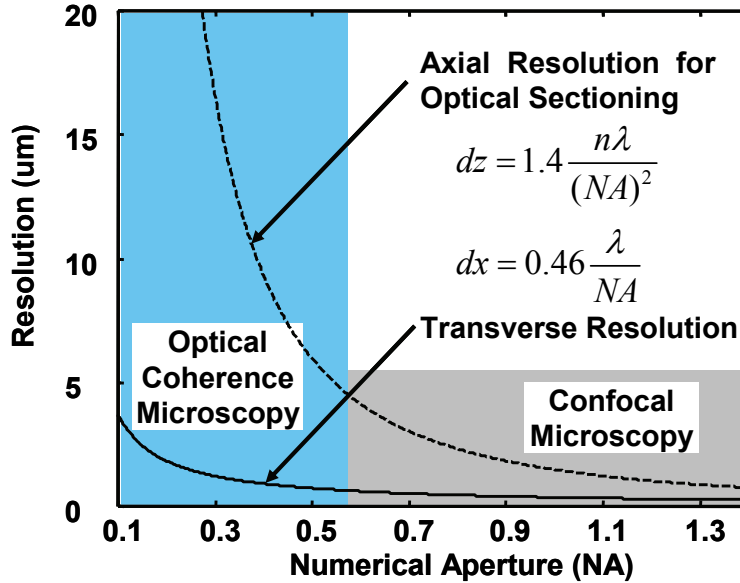


**Figure 4.11.** Operating ranges for optical coherence microscopy compared with confocal microscopy.

#### 4.6 Technology for OCM

Cellular imaging with OCM comes at the cost of increased system complexity compared with conventional OCT as well as confocal microscopy. System designs must incorporate the core features of a confocal microscope, including a two-axis scanner and reasonably high NA lens, in addition to the heterodyne interferometer and detection electronics necessary in OCT. To achieve ultrahigh coherence axial resolutions, very broadband light sources must be used. Furthermore, modulation schemes capable of supporting these large spectral bandwidths must be developed. For *in vivo* imaging, the imaging speed is also a critical parameter. Visualization of cellular and subcellular features requires sufficient speed to eliminate motion artifacts and transverse blurring. Based on work with confocal microscopy, a minimum speed of  $\sim 8$  frames per second is required, even with the use of contact tissue stabilization schemes [8]. This necessitates fast raster scanning and high speed phase modulation methods. High speed imaging also requires high power light sources to overcome signal loss due to reduced pixel dwell times. At near-infrared wavelengths, permissible tissue exposures for high speed imaging are in the range of 10 - 20 mW. Typical system throughput including coupler loss and optical transmission loss can be quite low, however, and this can substantially increase the light source output power requirements to obtain sufficient tissue illumination. Finally, an OCM system must have some mechanism to ensure overlap of the confocal and coherence gates in scattering tissue. This section reviews progress on technology for OCM that will enable high speed *in vivo* imaging.

#### 4.6.1 Broadband Light Sources

Chapter 3 of this thesis describes progress in light source development for OCT in detail. Light source requirements for OCM essentially parallel the requirements for OCT. Near infrared wavelengths between 800 nm and 1300 nm are desirable to take advantage of lower absorption and scattering in tissue compared with visible wavelengths. Within this range, the shorter wavelengths near 800 nm provide increased contrast and better resolution for a fixed optical bandwidth compared with the longer wavelengths near 1300 nm. Nonetheless, the increased penetration depth at longer near infrared wavelengths is attractive for imaging below the surface in scattering tissues. Most studies with OCM to date have used superluminescent diode light sources, with typical bandwidths in the range of 40 – 80 nm and output powers between 1 and 20 mW. Figure 4.12a presents a measured spectrum from a typical superluminescent diode at 1300 nm. The coherence gate can be computed from the autocorrelation of the spectrum and has a width of 13.5  $\mu\text{m}$ , as shown in figure 4.12b. Superluminescent diodes offer compact, stable, turnkey solutions and have been widely applied in clinical studies with OCT.

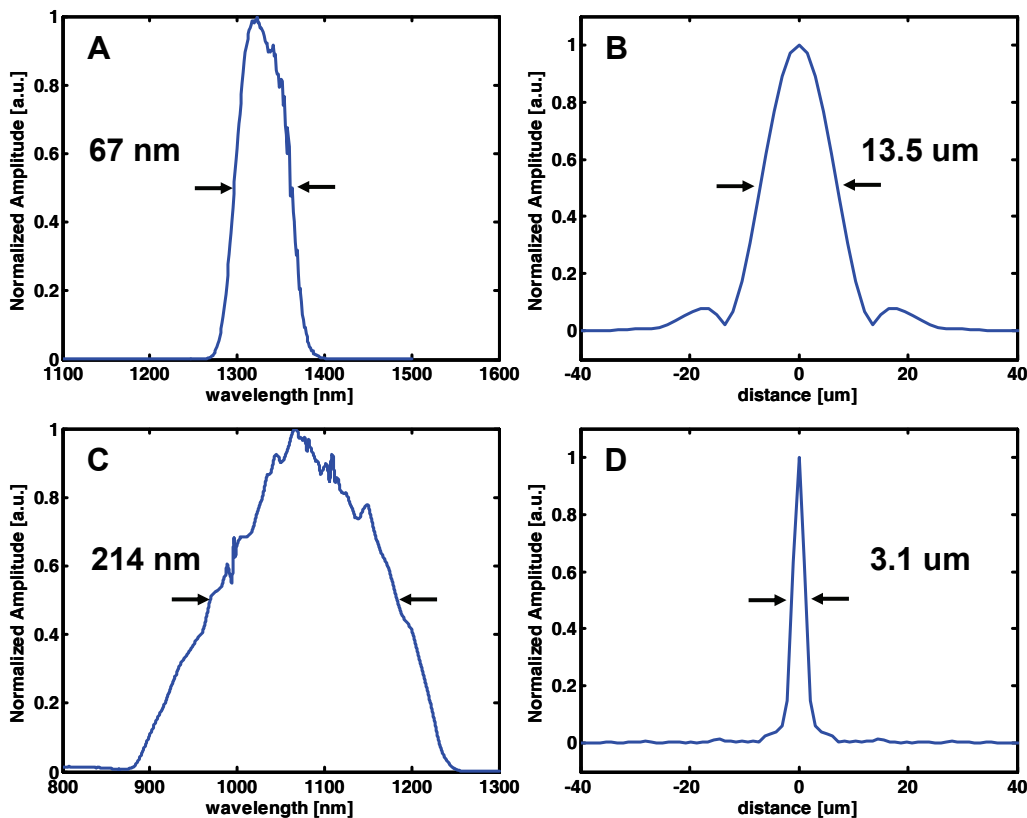


**Figure 4.12.** Comparison of light sources for optical coherence microscopy. A typical superluminescent diode source provides a spectrum of around 70 nm (A), which corresponds to an axial resolution of about 14  $\mu\text{m}$  (B). State of the art femtosecond lasers and continuum generation can provide much broader spectra and higher axial resolution. Shown here are results achieved using a compact Nd:Glass oscillator. Spectral bandwidth (C) measures over 200 nm, corresponding to an axial resolution of about 3  $\mu\text{m}$  (D).

More recent developments in femtosecond solid state lasers have enabled ultrahigh resolution OCT with coherence gates of less than 5  $\mu\text{m}$ . These systems offer superior performance in terms of bandwidth and output power compared with the SLD's, but they are typically expensive as well as complex to build and operate. The use of supercontinuum generation in highly nonlinear fibers has enabled the application of commercially available femtosecond lasers for OCT. Such commercial laser sources can be made highly stable and compact, compared with research prototypes, which allows the development of portable systems for clinical investigations outside of the research laboratory. Figures 4.12c and 4.12d present the measured spectrum and the computed coherence gate for a laser light source of this type [77]. Using a compact Nd:Glass femtosecond laser oscillator coupled into a Germanium-doped, high numerical aperture, nonlinear fiber, an optical spectrum of over 200 nm centered at 1060 nm was generated using self phase modulation nonlinearity. This enables resolutions of  $\sim 3 \mu\text{m}$  in air. Moreover, the average power was  $> 100 \text{ mW}$ , enabling high speed imaging. The wavelength range around 1060 nm is compelling for use in scattering tissues because it offers both increased penetration compared with the 800 nm region and improved resolution compared with 1300 nm. Some studies suggest that this wavelength window is an optimum choice for ultrahigh resolution imaging [78], and continuous wave lasers around 1060 nm have been extensively used for confocal imaging [8, 79].

#### **4.6.2 Modulation Schemes**

Several modulation techniques have been applied for OCM imaging. The basic goal is to provide a phase delay to the reference arm light, without imparting significant group delay that would cause the coherence gate to shift relative to the confocal gate. The first OCM system demonstrated by Izatt et al. used a piezo-electric fiber stretcher to dither the reference path length by a fraction of a wavelength [46]. A similar approach employs a piezo-electric stack to vibrate the reference mirror [54, 73, 80]. To date, most of the cellular resolution OCM imaging results have used this method. It uses a relatively simple interferometer design which supports broad optical bandwidth and facilitates matching of dispersion between the reference and sample paths. This technique is limited, however, to relatively slow modulation rates and therefore does not allow real-time imaging. The maximum modulation rate reported to date was  $\sim 377 \text{ kHz}$ , which enabled an image acquisition time of 3 seconds with an 85 Hz line rate. The piezo-electric stack modulators also have the disadvantage of requiring demodulation at two harmonics of the modulation frequency in order to optimize signal detection [54]. In a fiber based interferometer, the signal at either harmonic suffers from modulation due to slow drifts in the fiber path lengths. The modulation can be removed by appropriate choice of piezo drive amplitude and computation of the sum of the demodulated powers at two harmonics, but this comes at the cost of increased complexity in the detection and signal processing.

An alternative approach to reference arm phase modulation involves the use of a rapid scanning optical delay line (RSOD) similar to those designed for OCT [81, 82]. The RSOD uses a grating and lens combination to perform an optical Fourier transform. A scanning mirror in the Fourier plane of the delay line imparts a wavelength dependent phase shift which, when passing back through the lens-grating combination, produces a group delay scan in the time domain. In addition, offsetting the optical beam from the scanning mirror center axis allows the generation of a phase delay scan, which adds a Doppler frequency shift to the heterodyne signal. Zvyagin et al. demonstrated that, with proper choice of grating, lens, and offset parameters, the RSOD can also be set to generate phase delay without group delay [83]. Aguirre et al. utilized this configuration to construct a broadband optical phase modulator for OCM imaging [75]. Figure 4.13 presents this design as well as performance characterization. The modulator consists of an all-reflective geometry and is shown in top and side views in Figures 4.13a and 4.13b, respectively. The input beam diffracts from the grating and onto a curved mirror, which then focuses the beam onto a scanning galvanometer mirror. The return beam is offset vertically from the input beam and strikes a retro-reflecting mirror, which sends it back through the modulator to retrace its path. The double-pass geometry helps to minimize beam walk-off created by the scanning mirror while also doubling the delay. The reflective design eliminates chromatic aberration encountered with lens geometries. Importantly, this design also does not introduce additional chromatic dispersion that could degrade the OCM point spread function. Figure 4.13c shows the input and backcoupled spectra from the RSOD modulator. The modulator easily supports a bandwidth of nearly 180 nm FWHM. Figure 4.13d shows the heterodyne interference signal produced from a mirror during a continuous phase delay scan of the modulator. Using resonant galvanometer scanners, RSOD modulators such as this are capable of producing modulation frequencies in the MHz range [82]. Moreover, the offset between the grating and the focusing element in the RSOD can be adjusted to provide dispersion compensation. The modulator design shown in figure 4.13 was used to produce *in vivo* cellular images at 4 frames per second, as shown in figure 4.10 above. The RSOD modulator has the disadvantage of requiring that the fast axis of the *en face* raster scan be synchronized to the modulator scanner. In addition, the geometry does not easily permit incorporation of a fast depth scanner to synchronize the coherence and confocal gates.

Acousto-optic (AO) and electro-optic (EO) modulators are excellent solutions for high speed modulation. Several investigators have used EO modulators in OCT to provide a highly phase stable Doppler shift at 1300 nm wavelength [84-86]. Electro-optic modulators can be driven at very high modulation rates in the GHz range, well beyond what would be needed for even the fastest OCM system. For OCM, the EO modulator is usually driven with a sawtooth waveform with an amplitude equal to  $V_{\pi}$ . In a double-pass geometry, a phase shift of  $2\pi$  is acquired, resulting in a repetitive sinusoidal carrier modulation. Linear, broadband EO phase modulators are not widely available at wavelengths outside of

the standard telecommunications band encompassing 1300 nm – 1500 nm. Moreover, typical LiNbO<sub>3</sub> crystals used in EO modulators are highly birefringent. For unpolarized superluminescent diode sources, this does not present a significant problem. However, with polarized broadband laser sources that have complex polarization evolution in the fiber, the polarization dependence of EO modulators can make them difficult to use and potentially necessitate polarization control or diversity approaches.

Acousto-optic modulators have also been applied for cross-sectional, transverse-priority and *en face* OCT imaging [45, 87, 88]. AO modulators are available at many wavelengths and provide a pure frequency shift rather than a phase modulation, but typical frequency shifts are in the tens of MHz range. To reduce the frequency shift to a lower value more suitable for OCT or OCM imaging, a modified approach can be used in which a pair of AO modulators is cascaded with opposite frequency shifts offset in magnitude by a small amount. For example, Xie et al. used AO modulators with frequencies of +55 MHz and -54 MHz giving a round-trip, double pass net frequency shift of 2 MHz [87]. This approach requires the added complexity of two separate modulators and drive electronics, but like the EO modulation schemes, it can provide a highly stable modulation. In addition, AO modulators are generally polarization insensitive.

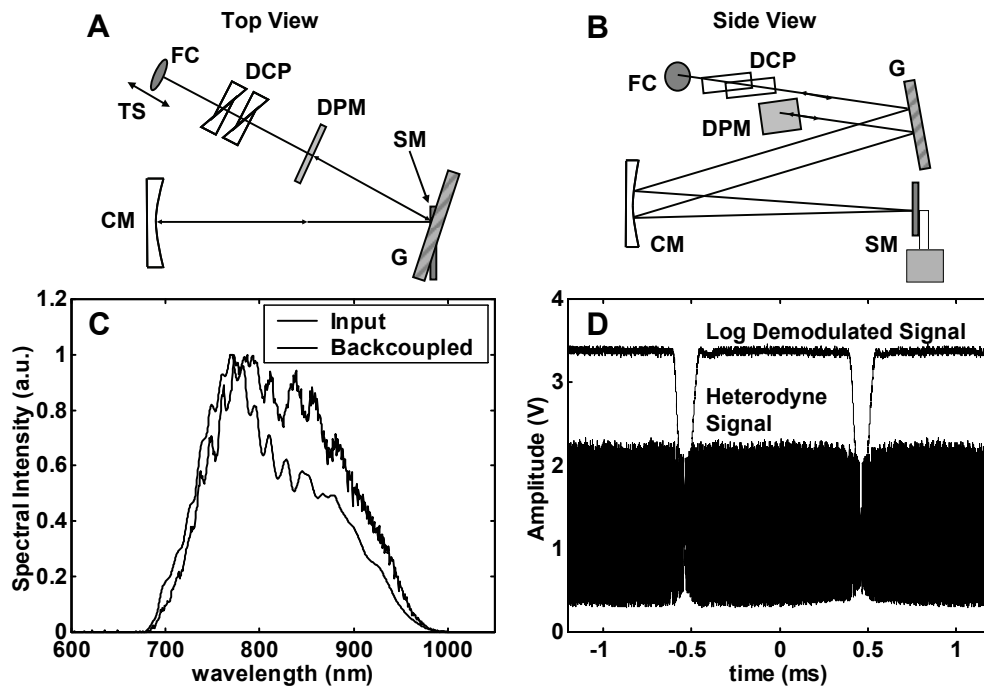


**Figure 4.13.** Broadband modulator for OCM based on the rapid scanning optical delay line. The all-reflective design (A,B) supports large optical bandwidth (C) and produces a pure phase delay for *en face* OCM imaging.

Dispersion compensation is another important challenge in using either an EO or AO modulators with broadband OCT or OCM systems. The optical materials used in modulators introduce large amounts of dispersion in the reference arm which must be balanced or compensated in order to preserve the axial point spread function. This issue has been addressed primarily by using rapid scanning optical delay lines (RSODs) to remove second order dispersion [85, 89]. An RSOD alone, however, cannot remove higher order terms. One approach that enables compensation of high order dispersion is to place identical optical materials as are used in the reference arm modulator in the sample arm. Wiesauer et al. used this strategy to achieve  $< 3$   $\mu\text{m}$  axial resolution in a free-space *en face* OCT system [90]. However, this approach is undesirable for use in endoscopy or other applications using fiber-optic sample probes, since it would require free space coupling out of and into the fiber in order to introduce the dispersion compensation material. Chen et al. demonstrated a simple and elegant modification to the RSOD compensation technique which allows dispersion management up to third order by using a length of single-mode optical fiber in the sample arm [91]. This technique was theoretically analyzed and experimentally demonstrated for EO as well as AO modulators and a resolution of  $\sim 2.8$   $\mu\text{m}$  was achieved with an AO modulator at 800 nm wavelength. The same group subsequently developed a technique for optimization of the spectral throughput of AO modulators which supports more than 200 nm bandwidth at 800 nm [92]. With the development of suitably broadband dispersion compensation approaches, AO and EO modulators promise to be widely used for high speed *in vivo* OCM imaging in the future.

Two interesting approaches to *en face* imaging have been demonstrated which do not require modulators in the reference arm. The first approach makes use of the inherent modulation imparted by raster scanning the beam with a galvanometer mirror. In the case when the scan field in the sample arm is curved, a sampling function based on Newton rings can be used [93]. Alternately, an offset of the beam on the galvanometer scanner mirror can be used to produce a parallel fringe sampling function [94]. A second approach uses homodyne detection based on 3x3 optical couplers [95]. The homodyne method takes advantage of the inherent phase shifts between the ports of the coupler to obtain amplitude and phase information. Images of a *Xenopus* tadpole were demonstrated with sensitivity of  $\sim 90$  dB and transverse resolution of 9.4  $\mu\text{m}$ . OCM schemes that do not require modulation can result in simpler system designs and are therefore promising for further study.

#### **4.6.3 Microscope Scanner Designs**

Microscope design principles for OCM imaging are similar to those for confocal microscopy in epi-reflection mode. The microscope consists of three basic subsystems: 1) an XY scanning apparatus, 2) collimation and relay optics, 3) a focusing objective. The XY scanner should ideally maintain the same optical path length to the focus across the entire scan field in order to ensure overlap of the confocal and

coherence gates. The most direct way to do this is would be to mechanically scan the microscope and sample with respect to each other using translation stages. For high speed imaging, however, beam steering is the preferred method. Galvanometer mirror scanners have been widely used for OCM, because rotating polygon scanners typically used for video rate confocal microscopes [8] introduce an unwanted path length shift across the scan. Resonant scanning galvanometers can offer fast axis scan rates, as high as 10-15 kHz, which are sufficient for video rate imaging with high line density per image.

Collimation and relay optics are typically composed of multiple-element achromatic lenses designed and coated for use at near-infrared wavelengths. Focusing objectives are generally chosen to provide field flatness, which aids in reference path length matching across the field of view. Furthermore, water immersion lenses are often used for imaging in biological tissue to minimize aberrations from refractive index mismatch. However, high quality focusing objectives designed for the near infrared are not widely available, and therefore most systems have used lenses designed for visible wavelengths. This leads to poor optical throughput as well as focusing aberrations. As near IR imaging methods, including multiphoton and harmonic microscopies as well as OCT, become more established, it can be expected that near IR objective lenses will become more readily available.

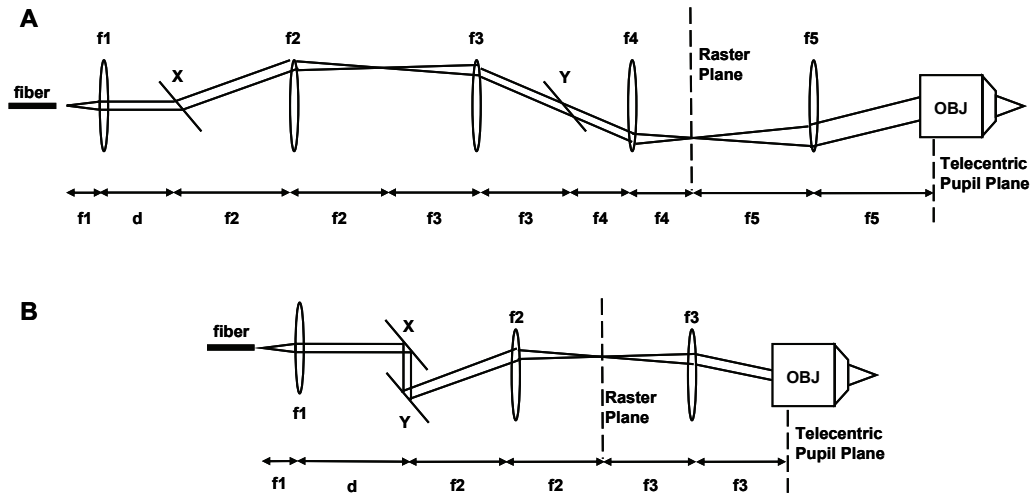


**Figure 4.14.** Fiber-optic confocal microscope designs typically used for OCM. A true telecentric design (A) separates the transverse scanners and precisely images the points of angular scan on each axis to the telecentric plane of the objective. An approximate geometry (B) which uses a pair of closely spaced galvanometer scanners can also work well but introduces aberration.

Figure 4.14 illustrates two examples of benchtop OCM microscope designs for use with galvanometer scanners and an infinity corrected objective lens. The design in figure 4.14a is a true telecentric design. The beam from the fiber is collimated and directed onto the center of the first galvanometer scanner. The center point of this galvanometer is then relay imaged to the center point of the second scanner by lenses

f2 and f3. A final telescope, formed by lenses f4 and f5, then images the scanners to the telecentric pupil plane in the objective lens. This design offers true telecentricity in that the beam can be made to pivot on both axes about the telecentric plane. The disadvantage of this design is that it requires several lenses and a relatively large optical path. A second design, shown in figure 4.14b, uses a closely-spaced pair of galvanometers after the collimator. The center point between the mirrors is imaged by a single telescope to the telecentric pupil plane. This configuration can provide only approximate telecentricity, since neither of the pivoting mirrors can be exactly imaged to the correct pupil plane in the objective. The spacing between the galvanometers should be minimized to reduce the degree of field curvature that results. This design offers compactness, and is more amenable to use with handheld imaging devices.

The development of miniaturized microscopes for endoscopic confocal and OCM imaging is a critical enabling step necessary for widespread application of these techniques for human clinical imaging. Two separate challenges must be overcome: design of small diameter, high NA objective lenses and development of miniaturized, fast two-axis scanners. These issues have been the topic of significant research efforts in recent years. Ideally, the device diameter would be a maximum of 3-4 mm in order to enable its use through the standard accessory ports of clinical endoscopes. As described above, OCM has the important advantage that it can image with lower NA compared with confocal microscopy, which facilitates the development of the small diameter objective lenses required. Several approaches for developing compact endoscopic scanning devices have been investigated. Some groups are pursuing fiber imaging bundles for confocal [21, 24, 96-99] and optical coherence imaging [100]. Fused coherent fiber bundles consist of thousands of individual fibers which preserve spatial relationship between proximal and distal ends. Each fiber in the bundle serves as an image pixel, and scanning can be performed at the proximal end of the fiber bundle using conventional galvanometer scanners. Bundles tend to have poor optical efficiency, however, and image pixelation can degrade resolution and contrast. In addition, phase differences between individual fiber paths can present problems for phase sensitive heterodyne detection methods.

Single-mode fiber scanners have much better optical efficiency, but require miniaturized scanners located at the distal tip of the fiber optic probe. Two-dimensional scanning of the input fiber tip has been used by several groups for endoscopy, confocal microscopy and multiphoton microscopy [101-104]. Liu et al. demonstrated a piezo-electric fiber scanning probe with 2.4 mm diameter and a fast line scan rate of 2.8 kHz [104]. Piezo-electric devices typically require resonance drives to achieve sufficient deflection, which limits their ability to scan arbitrary XY scan patterns. Nonetheless, the ability to generate fast scans in such a small footprint make piezo-electric devices highly attractive for future endoscopic applications. Two-axis micro-electro-mechanical systems (MEMS) may also enable a wide range of fiber optic endoscope devices for OCT and OCM. Two-axis MEMS scanning mirrors have been demonstrated

for confocal microscopy applications [105] and one and two axis scanners have been designed for optical coherence tomography applications [106-110].

Figure 4.15 illustrates one implementation of a two-axis MEMS scanning catheter used for 3D and *en face* ultrahigh resolution OCT imaging. The scanner, shown in the scanning electron micrograph in figure 4.15a, has a large 1 mm diameter mirror for high resolution imaging. It uses angular vertical comb (AVC) drive actuators on the mirror and on the outer gimbal to actuate in two dimensions over large angles of  $> 8$  degrees with only  $\sim 50$  V applied bias [110]. The mirror and gimbal axes can achieve high resonance frequencies of over 1 kHz for high speed imaging. The mirror was incorporated into a small diameter catheter, as shown in figure 4.15b. The device consists of an outer aluminum housing with maximum diameter of  $\sim 5$  mm. A fiber collimator delivers light to an achromatic objective lens (not visible in the schematic) which focuses the beam. The MEMS scanner is used in a post-objective scanning configuration with the focused beam reflected from the scanner. The scanner directs the beam at 90 degrees out of the device for side-view imaging. This post-objective scanning configuration minimizes optical aberration. Figure 4.15c shows a three-dimensional rendering of hamster cheek pouch acquired *ex vivo* with the miniaturized catheter. While catheter designs such as this are continuing to advance, other challenges such as focus adjustment and tissue stabilization remain to be addressed. Therefore, *in vivo* endoscopic confocal and OCM imaging remains a difficult problem.

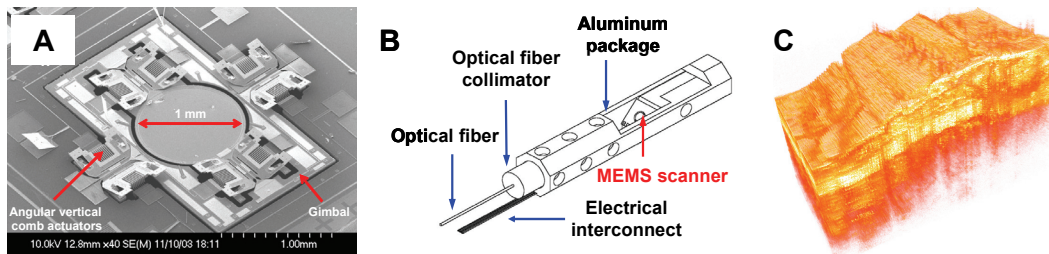


**Figure 4.15.** Two-axis MEMS scanning catheter endoscope for three-dimensional and *en face* imaging. A large 1 mm diameter MEMS mirror (A) was integrated into a 5 mm diameter catheter package (B). Three-dimensional imaging was demonstrated *ex vivo* of the hamster oral mucosa.

#### 4.6.4 Controlling the Overlap of Coherence and Confocal Gating

OCM is critically sensitive to the overlap of the confocal and coherence gates determined by matching of the reference and sample arm optical path lengths. Focusing into a sample with a discontinuity in index of refraction leads to a reduction in signal amplitude and loss of resolution because the confocal and coherence gates shift relative to each other. Optical path length (OPL) is defined as

$$OPL = n \cdot l \quad (10)$$

If the reference and sample refractive indices are matched,  $n_S = n_R$ , the reference arm OPL remains equal to the sample arm OPL as the focus is translated deeper into the sample. This does not hold true when the refractive index of the sample is different from that of the reference arm. In this case, a physical thickness of  $\delta l$  over which  $n_S \neq n_R$  produces an OPL mismatch of

$$\Delta L_{OPL} = (n_S - n_R) \cdot \delta l = \Delta n \cdot \delta l. \quad (11)$$

The index mismatch is particularly important when using dry objectives and can be minimized by the use of water immersion objectives. Given the turbulent nature of the index of refraction in tissue [111], path length mismatch cannot be insured in general by matching the reference path to the microscope focus outside of tissue. Furthermore, fiber optic imaging probes such as catheters or handheld microscopes are subject to path length shifts between the reference and sample arms produced by stretching and bending of the optical fiber as the probe is positioned for *in vivo* imaging. The sensitivity to path length changes between the reference and sample arms is exacerbated when the confocal and coherence gates are both very small. Using broadband laser sources to provide ultrahigh coherence axial resolutions, as in figure 4.9, allows the confocal gate to be longer than in standard confocal microscopy. This helps to make the gate overlap less sensitive to index variations.

To ensure optimum image quality in highly scattering tissue, some form of overlap alignment between the confocal and coherence gates is desirable. This is most easily done by adjusting the reference arm path length. Schmitt et al. used a focus-tracking scanner with the reference mirror and the sample objective mounted on the same translation scanner [27]. As the objective was translated by a distance  $\Delta z$  toward the sample, the optical pathlength in the reference arm increased by an amount  $2\Delta l$ . Since focus tracking requires a change of  $\Delta l = n^2 \Delta z$  and  $n^2 \approx 2$  for biological tissues, this technique provided approximate overlap alignment of the confocal and coherence gates across the depth scan. This approach does not work for fiber optic systems with separate reference and sample paths. Most investigators have instead used manual adjustment of the reference path length with a translation stage. The position of the focus was determined using image intensity as the metric. For *in vivo* imaging applications, high speed adjustment is required. This can be done by incorporating a galvanometer scanner in the reference path to quickly scan depth and provide a depth profile of image intensity. The focal position can then be determined and the DC offset to the depth scanner adjusted to ensure overlap of confocal and coherence gates. This method is essentially an autofocus technique, analogous to the autofocus methods used in digital cameras. The ability to rapidly and automatically align overlap for OCM in tissue is important to ensure optimum image quality at different depths.

#### 4.6.5 Combination Microscopy Techniques

Multi-modality imaging methods combining OCM with confocal, multiphoton, or harmonic microscopy have been pursued by several investigators. OCM can provide structural information about tissue architectural or cellular features with complementary contrast mechanisms to other microscopy methods. Fluorescence imaging, for example, can provide information about biochemical tissue constituents or even gene expression when using appropriate exogenous probes. Beaufreire et al. first demonstrated simultaneous OCM and two-photon microscopy in a free space optical setup [112]. Co-registered reflectance and fluorescence images of cell nuclei in live drosophila embryo illustrated the potential for the multi-modal method. Tang et al. extended this technique using a broadband 12-fs femtosecond laser source, providing coherence axial resolution of  $\sim 1.5 \mu\text{m}$  [113]. They demonstrated second-harmonic generation (SHG), two-photon fluorescence, and OCM reflectance images registered to the same micrometer-sized sample volume. Yazdanfar et al. developed a combined second harmonic and optical coherence microscope with interferometric detection of the epidirected SHG [114]. Heterodyne detection can potentially improve the penetration depth over traditional SHG microscopy. Vinegoni et al. demonstrated a combined optical coherence and multiphoton microscope using spectral domain detection methods [115]. Dunkers et al. demonstrated simultaneous confocal fluorescence and optical coherence microscopy for imaging of tissue engineering constructs [116]. The use of both methods allowed simultaneous acquisition of structural and functional information from fluorescently stained osteoblasts cultured in a polymeric scaffold.

#### 4.7 Cellular Imaging Applications of OCM

As mentioned earlier, investigation of OCM imaging applications has generally lagged behind similar studies with OCT and confocal microscopy, in part because of the technical challenges. Indeed, only a handful of papers exist in the literature demonstrating cellular imaging with OCM. Applications to date include imaging of plants [117], developmental biology specimens [75, 118], human skin [75], human oral mucosa [73], and human colonic mucosa [54]. Of the human imaging studies, to date, only imaging of human skin has been performed *in vivo*. However, the promise of minimally invasive imaging at the cellular level *in vivo* will undoubtedly push these applications forward in the future. One of the most critical areas of investigation is likely to be early cancer detection. Excisional biopsy and histology are the time-tested gold standards for disease assessment at the tissue and cellular levels, and they continue to be the dominant method used for the diagnosis, staging, and management of many neoplasms. Biopsy and histology, however, can be subject to high false negative rates due to sampling errors, and can pose risks to the patient, such as bleeding and infection, which also limit the ability to screen large areas. Optical imaging technology that provides real-time, high-resolution screening of vulnerable areas with

resolution at or near that of histopathology can significantly improve clinicians' capabilities to identify malignancies at curable stages. The ability to visualize the histologic hallmarks of cancer at the tissue architectural and cellular levels, including alterations in glandular or stromal morphology, presence of abnormal mitoses and increased nuclear-to-cytoplasm ratio, *in situ* and in real time, without the need for tissue excision and processing, would be a major advance in cancer diagnostics.

Clark and colleagues have performed an *ex vivo* investigation of OCM for detection of oral neoplasia [73]. Their system imaged at 800 nm using a superluminescent diode light source. The combined coherence and confocal gated microscope provided an axial resolution of 7.8  $\mu\text{m}$  and a transverse resolution of 2.3  $\mu\text{m}$  with a field of view of up to 250  $\mu\text{m}$ . Figure 4.16 presents data from their work comparing OCM images of normal squamous epithelium and squamous cell carcinoma of the oral mucosa. The images were treated with acetic acid to increase nuclear contrast [20] and compared with conventional hematoxylin and eosin histology sections processed after imaging. The histology (a) and OCM (c) images of normal mucosa exhibit consistent nuclear area and spacing compared with the tightly packed tumor cells and irregular nuclei of squamous cell carcinoma shown in (b) and (d).

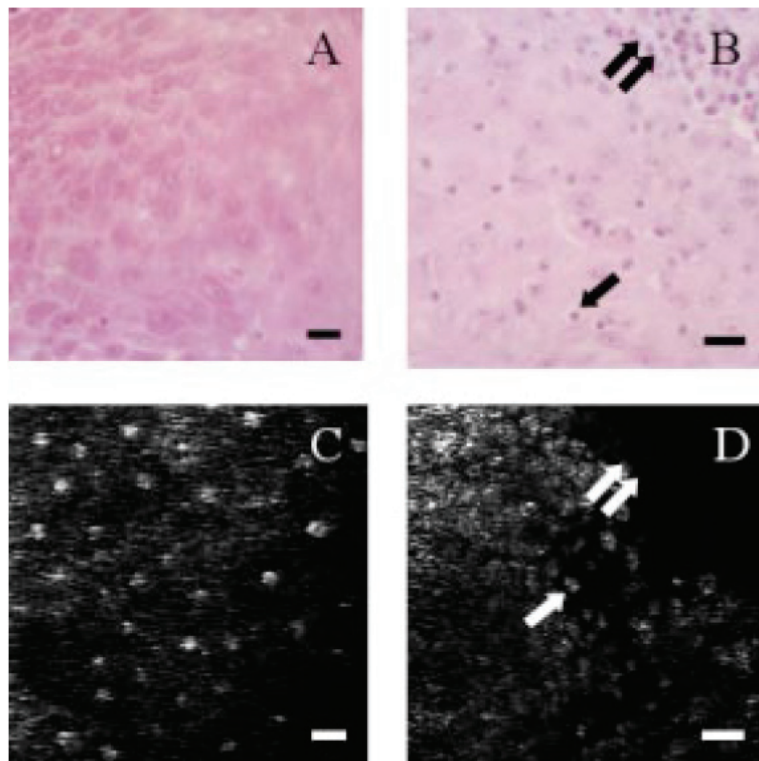


**Figure 4.16.** Histology and OCM images of normal and cancerous squamous epithelium of the human oral mucosa *ex vivo*. The normal histology (A) and OCM images (C) demonstrate consistent nuclear area and spacing, while the cancerous histology (B) and images (D) show tightly packed tumor cells (arrows) and irregular nuclei. Scale bars 20  $\mu\text{m}$ . Images reproduced from Clark et al. [73]

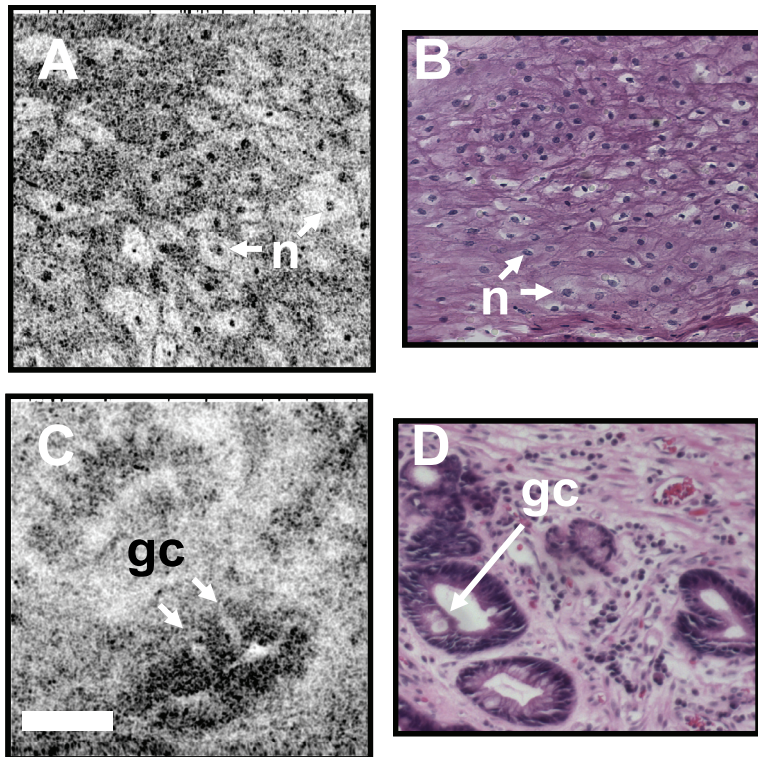


**Figure 4.17.** OCM images and histology of normal squamous esophagus and Barrett's esophagus *ex vivo*. Normal squamous mucosa (A,B) exhibits a characteristic pattern of squamous cells with centrally-located, highly scattering nuclei (n). Images of Barrett's epithelium exhibit the presence of intestinalized glands with hallmark barrel-shaped goblet cells (gc). Scale bar, 100  $\mu\text{m}$ , pertains to all images.

Building on the preliminary results by Izatt et al. [54], Aguirre and colleagues have explored the role of OCM for cellular imaging in the esophagus and colon [119]. Details of this study are described in chapter 6 of this thesis. Images were acquired *ex vivo* using a high speed OCM imaging system operating at 1060 nm wavelength with transverse resolution of  $< 2 \mu\text{m}$  and axial coherence gated resolution of  $< 5 \mu\text{m}$  over a field of view of up to 400  $\mu\text{m}$  square. Figures 4.17 and 4.18 present sample data from this study. The image in figure 4.17a illustrates the characteristic pattern of squamous cells in the esophagus. Corresponding histology is shown in figure 4.17b. In the OCM images as well as histology, cell nuclei can be clearly differentiated from the surrounding cytoplasm and individual membranes which delineate cell boundaries. Figures 4.17c and 4.17d show an example of Barrett's esophagus. Barrett's esophagus is a condition in which chronic gastrointestinal reflux leads to a metaplastic change in the esophageal mucosa from the normal squamous architecture to a columnar architecture with similar features to colonic mucosa. The presence of Barrett's metaplasia is a predisposing risk factor for the development of dysplasia and adenocarcinoma of the esophagus. The hallmark histopathologic feature of Barrett's is the presence of barrel-shaped goblet cells. OCM identifies the glandular architecture of the Barrett's mucosa

as well as the presence of goblet cells in the columnar epithelium. Figure 4.18 shows a comparison of OCM images of normal and dysplastic colonic mucosa. The normal colonic mucosa shown in the OCM images and histology of figures 4.18a and 4.18b, respectively, exhibits a regular pattern of round crypts with numerous goblet cells and nuclei restricted to the basal aspect of the columnar epithelium. In contrast, figures 4.18c and 4.18d present images and histology from a tubular adenoma with low grade dysplasia. Glands in the adenoma are larger and exhibit significant eccentricity compared with the small round crypts present in normal mucosa. In addition, the adenomatous glands show the presence of cigar-shaped nuclei extending beyond the basal third of the columnar epithelium. OCM images correlate well with histology and demonstrate the ability to identify key histologic features of normal and pathologic tissues.

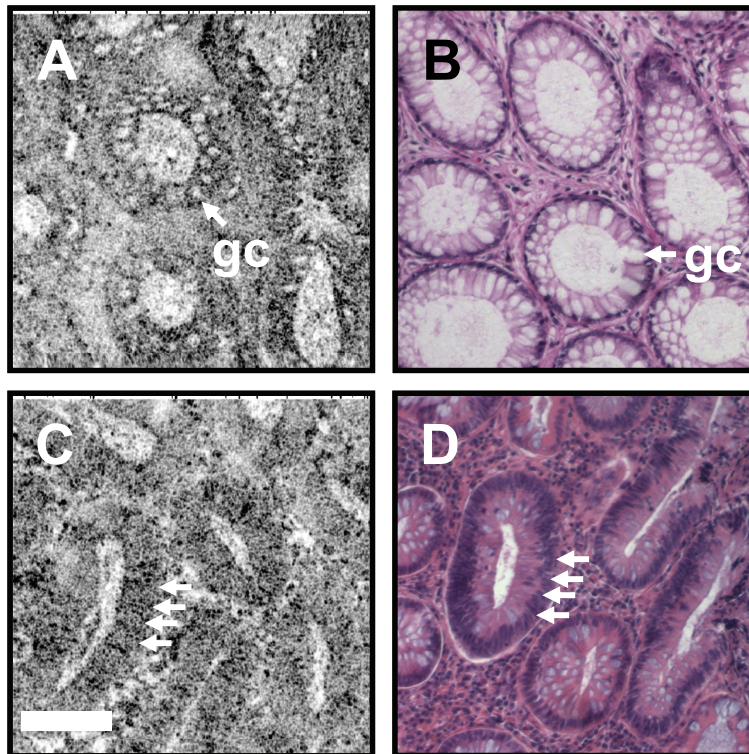


**Figure 4.18.** OCM images and histology of normal and dysplastic colon *ex vivo*. Normal colonic mucosa (A,B) shows the presence of round crypts with goblet cells (gc) and basally situated nuclei. Adenomatous dysplastic crypts (C,D) have increased eccentricity and exhibit characteristic cigar-shaped nuclei (arrows) in an epithelium which appears thickened. Scale bar, 100  $\mu$ m.

OCM achieves high resolution in three-dimensions for visualization of cellular and subcellular morphology. However, due to the high magnification of the objective lens, the field of view in OCM is generally restricted to the range of 500  $\mu\text{m}$ . From a clinical perspective, OCM is essentially a point-sampling technique and will therefore suffer from sampling error in screening and diagnostic applications. One solution to this limitation involves the combination of OCM with conventional OCT imaging. Figure 4.19 presents an example data set to illustrate this point. The data was acquired with a combined OCT and OCM microscope with an adjustable objective lens magnification. The microscope allowed precise registration of *en face* OCM images to OCT cross sectional image data. Figure 4.19a shows an ultrahigh resolution OCT image of squamous mucosa of the cervix. Transverse resolution was measured to be  $\sim 12$   $\mu\text{m}$  with axial resolution of  $< 3$   $\mu\text{m}$ , and the field of view was 3 mm in length. OCT provides cross-sectional visualization of the epithelial layer thickness, with clear delineation of the basement membrane and underlying lamina propria. The lamina propria appears highly scattering compared with the stratified squamous epithelium. As shown by the 3x zoom view in figure 4.19b, OCT cannot clearly delineate cellular structure due to its limited transverse resolution. *En face* OCM images of the same region delineated by this zoom view allow cellular resolution with  $< 2$   $\mu\text{m}$  resolution over a restricted field of view. Figures 4.19c, 4.19d, and 4.19e were obtained at imaging depths of 60  $\mu\text{m}$ , 150  $\mu\text{m}$ , and 400  $\mu\text{m}$  below the surface, respectively. The regular pattern of squamous cells is evident in figure 4.19c, while figure 4.19d shows the ridges of lamina propria projecting through the lower epithelial layers. A highly scattering rim of basal cells can be seen surrounding the islands of lamina propria. Figure 4.19e shows the disorganized loose connective tissue deep below the tissue surface.

The concept of imaging over multiple fields of view to allow visualization of tissue architecture at varying resolutions is a promising approach in clinical applications such as endoscopic surveillance for dysplasia or resection of tumor margins. In these scenarios a clinically useful imaging solution should provide both high resolution to enable visualization of important architectural and cellular features as well as broad area coverage to avoid sampling error and excessive false negative rates. With high imaging speeds that are now available using OCT with Fourier domain detection techniques, it may be soon possible to survey large areas of tissue *in vivo*, which would allow the user to identify areas of interest for closer inspection. OCM could then be used to look directly at cellular and glandular features in these focal regions. This mode of operation would be similar to the approach used by pathologists when viewing conventional histopathology slides. A lower magnification is first used to gain an appreciation for the overall tissue architecture including layers and glandular organization. Then a high magnification is used to investigate cellular features. Both views provide important information used for making a diagnosis. OCT and OCM can function as complementary imaging methods in an analogous way. OCT

can survey large areas of tissue architectural morphology in a cross-sectional view, while OCM can provide high, cellular level resolution in an *en face* view.

The fact that OCM and OCT imaging engines can be designed to have a majority of components in common makes the two techniques readily amenable to integration into a single instrument. Moreover, the ability of OCM to image with lower NA than confocal microscopy alone, will enable more flexibility in probe development for internal body imaging. Combined OCM/OCT imaging probes using zoom lens technology will allow the user to switch readily between modes and generate both cross-sectional and *en face* views sequentially through the same optical path.

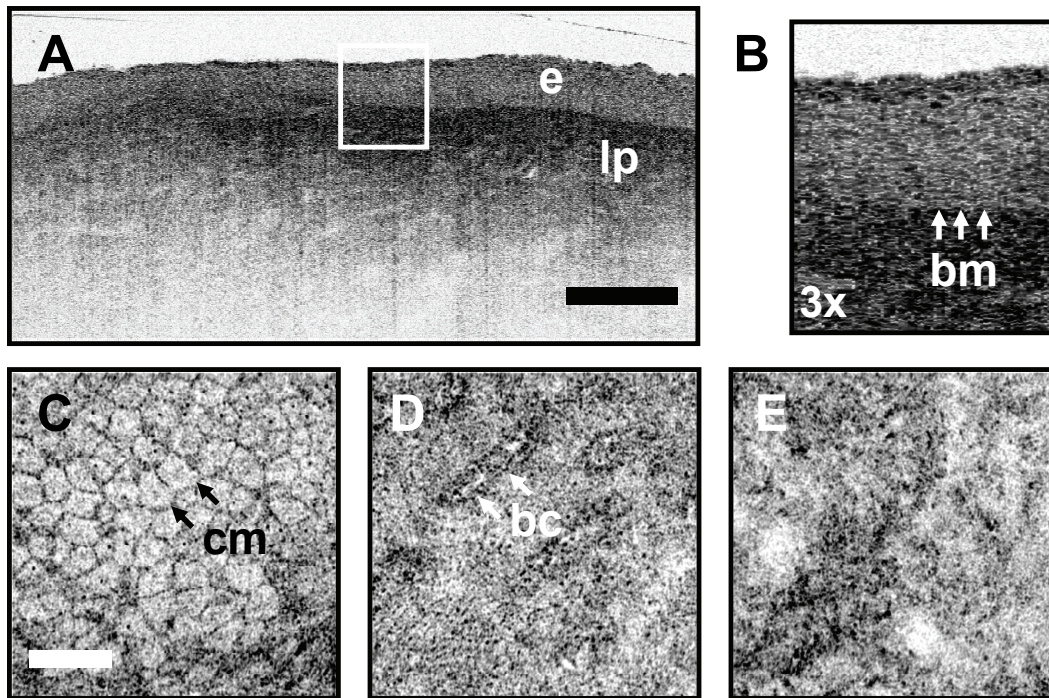


**Figure 4.19.** Co-registered OCT and OCM imaging of normal cervix. Ultrahigh resolution OCT (A,B) clearly identifies the layers of the cervical mucosa and delineates the basement membrane (bm) separating the epithelium from the underlying lamina propria. OCM images at progressive depths identify cell membranes (cm) in the upper epithelium (C) as well as the rim of basal cells (bc) surrounding the ridges of lamina propria (D). OCM can image deep into the lamina propria, shown here by an image of the loose connective tissue at 400 um depth (E). Scale bars, (A) 500 um, (C-E) 100 um.

#### 4.8 Summary and Future Prospects

This chapter has reviewed several important developments in optical coherence microscopy during the past 15 – 20 years. Techniques are progressing rapidly and numerous new system designs are becoming available for high speed imaging. Miniaturized two-axis scanning technologies are also being developed for endoscopic and laparoscopic applications. In addition, *ex vivo* tissue imaging studies are

establishing the validity of OCM imaging in various organ systems. OCM undoubtedly represents an important advance in OCT imaging generally, but the clinical implications remain to be explored. OCM has several important advantages compared with confocal microscopy, but the imaging technology is generally more complex. Nevertheless, OCM promises to provide powerful new approaches to make the concept of real-time, in situ, cellular-resolution optical biopsy a clinical reality.

#### 4.9 References

- [1] A. Dubois, K. Grieve, G. Moneron, R. Lecaque, L. Vabre, and C. Boccara, "Ultrahigh-resolution full-field optical coherence tomography," *Appl Opt*, vol. 43, pp. 2874-83, 2004.
- [2] A. Dubois, G. Moneron, K. Grieve, and A. C. Boccara, "Three-dimensional cellular-level imaging using full-field optical coherence tomography," *Phys Med Biol*, vol. 49, pp. 1227-34, 2004.
- [3] A. Dubois, L. Vabre, A. C. Boccara, and E. Beaufrepaire, "High-resolution full-field optical coherence tomography with a Linnik microscope," *Appl Opt*, vol. 41, pp. 805-12, 2002.
- [4] A. D. Aguirre and J. G. Fujimoto, "Optical Coherence Microscopy," in *Optical Coherence Tomography: Technology and Applications*, W. Drexler and J. G. Fujimoto, Eds. Germany: Springer, 2008.
- [5] M. Minsky, "Microscopy apparatus." U.S.A, 1961.
- [6] D. R. Sandison and W. W. Webb, "Background rejection and signal-to-noise optimization in confocal and alternative fluorescence microscopes," *Applied Optics*, vol. 33, pp. 603-615, 1994.
- [7] T. Corle and G. Kino, *Confocal Scanning Optical Microscopy and Related Imaging Systems*. San Diego: Academic Press, 1996.
- [8] M. Rajadhyaksha, R. R. Anderson, and R. H. Webb, "Video-rate confocal scanning laser microscope for imaging human tissues in vivo," *Applied Optics*, vol. 38, pp. 2105-2115, 1999.
- [9] M. Rajadhyaksha, S. Gonzalez, J. M. Zavislan, R. R. Anderson, and R. H. Webb, "In vivo confocal scanning laser microscopy of human skin II: Advances in instrumentation and comparison with histology," *Journal of Investigative Dermatology*, vol. 113, pp. 293-303, 1999.
- [10] P. Davidovits and M. D. Egger, "Scanning laser microscope," *Nature*, vol. 223, pp. 831, 1969.
- [11] P. Davidovits and M. D. Egger, "Scanning Laser Microscope for Biological Investigations," *Applied Optics*, vol. 10, pp. 1615-1619, 1971.
- [12] M. Rajadhyaksha, M. Grossman, D. Esterowitz, R. H. Webb, and R. R. Anderson, "In vivo confocal scanning laser microscopy of human skin: melanin provides strong contrast," *J Invest Dermatol*, vol. 104, pp. 946-52, 1995.
- [13] W. M. White, M. Rajadhyaksha, S. Gonzalez, R. L. Fabian, and R. R. Anderson, "Clinical, real-time confocal imaging of human oral mucosa in vivo.," *Journal of Investigative Dermatology*, vol. 110, pp. 588-588, 1998.
- [14] S. Gonzalez, Y. Gilaberte-Calzada, A. Gonzalez-Rodriguez, A. Torres, and M. C. Mihm, Jr., "In vivo reflectance-mode confocal scanning laser microscopy in dermatology," *Adv Dermatol*, vol. 20, pp. 371-87, 2004.
- [15] M. Rajadhyaksha, G. Menaker, T. Flotte, P. Dwyer, and S. Gonzalez, "Confocal Examination of Nonmelanoma Cancers in Thick Skin Excisions to Potentially Guide Mohs Micrographic Surgery Without Frozen Histopathology," *Journal of Investigative Dermatology*, vol. 117, pp. 1137-1143, 2001.
- [16] M. Huzaira, F. Rius, M. Rajadhyaksha, R. Anderson, and S. Gonzalez, "Topographic variations in normal skin, as viewed by in vivo reflectance confocal microscopy," *Journal of Investigative Dermatology*, vol. 116, pp. 846-852, 2001.
- [17] R. Langley, M. Rajadhyaksha, P. Dwyer, A. Sober, T. Flotte, and R. Anderson, "Confocal Scanning Laser Microscopy of Benign and Malignant Melanocytic Skin Lesions In Vivo," *Journal of the American Academy of Dermatology*, vol. 45, pp. 365-376, 2001.
- [18] S. Gonzalez, "Characterization of psoriasis in vivo by confocal reflectance microscopy," *Journal of Medicine*, vol. 30, pp. 337-356, 1999.
- [19] W. M. White, M. Rajadhyaksha, R. L. Fabian, and R. R. Anderson, "Noninvasive imaging of human oral mucosa in vivo by confocal reflectance microscopy," *Laryngoscope*, vol. 109, pp. 1709-17, 1999.

- [20] R. A. Drezek, T. Collier, C. K. Brookner, A. Malpica, R. Lotan, R. R. Richards-Kortum, and M. Follen, "Laser scanning confocal microscopy of cervical tissue before and after application of acetic acid," *American Journal of Obstetrics and Gynecology*, vol. 182, pp. 1135-1139, 2000.
- [21] K. B. Sung, C. Liang, M. Descour, T. Collier, M. Follen, and R. Richards-Kortum, "Fiber-optic confocal reflectance microscope with miniature objective for in vivo imaging of human tissues," *IEEE Trans Biomed Eng*, vol. 49, pp. 1168-72, 2002.
- [22] C. Pitris, B. E. Bouma, M. Shiskov, and G. J. Tearney, "A GRISM-based probe for spectrally encoded confocal microscopy," *Optics Express*, vol. 11, pp. 120-124, 2003.
- [23] A. L. Polglase, W. J. McLaren, S. A. Skinner, R. Kiesslich, M. F. Neurath, and P. M. Delaney, "A fluorescence confocal endomicroscope for in vivo microscopy of the upper- and the lower-GI tract," *Gastrointest Endosc*, vol. 62, pp. 686-95, 2005.
- [24] A. R. Rouse, A. Kano, J. A. Udovich, S. M. Kroto, and A. F. Gmitro, "Design and demonstration of a miniature catheter for a confocal microendoscope," *Applied Optics*, vol. 43, pp. 5763-5771, 2004.
- [25] P. M. Delaney, M. R. Harris, and R. G. King, "Fiberoptic Laser-Scanning Confocal Microscope Suitable for Fluorescence Imaging," *Applied Optics*, vol. 33, pp. 573-577, 1994.
- [26] R. Kiesslich, J. Burg, M. Vieth, J. Gnaendiger, M. Enders, P. Delaney, A. Polglase, W. McLaren, D. Janell, S. Thomas, B. Nafe, P. R. Galle, and M. F. Neurath, "Confocal laser endoscopy for diagnosing intraepithelial neoplasias and colorectal cancer in vivo," *Gastroenterology*, vol. 127, pp. 706-713, 2004.
- [27] J. M. Schmitt, S. L. Lee, and K. M. Yung, "An optical coherence microscope with enhanced resolving power in thick tissue," *Optics Communications*, vol. 142, pp. 203-207, 1997.
- [28] F. Lexer, C. K. Hitzenberger, W. Drexler, S. Molebny, H. Sattmann, M. Sticker, and A. F. Fercher, "Dynamic coherent focus OCT with depth-independent transversal resolution," *Journal of Modern Optics*, vol. 46, pp. 541-53, 1999.
- [29] B. Qi, A. P. Himmer, L. M. Gordon, X. D. V. Yang, L. D. Dickensheets, and I. A. Vitkin, "Dynamic focus control in high-speed optical coherence tomography based on a microelectromechanical mirror," *Optics Communications*, vol. 232, pp. 123-128, 2004.
- [30] V. X. Yang, Y. Mao, B. A. Standish, N. R. Munce, S. Chiu, D. Burnes, B. C. Wilson, I. A. Vitkin, P. A. Himmer, and D. L. Dickensheets, "Doppler optical coherence tomography with a micro-electro-mechanical membrane mirror for high-speed dynamic focus tracking," *Opt Lett*, vol. 31, pp. 1262-4, 2006.
- [31] A. Divetia, T. H. Hsieh, J. Zhang, Z. P. Chen, M. Bachman, and G. P. Li, "Dynamically focused optical coherence tomography for endoscopic applications," *Applied Physics Letters*, vol. 86, pp. -, 2005.
- [32] R. Leitgeb, C. K. Hitzenberger, and A. F. Fercher, "Performance of Fourier domain vs. time domain optical coherence tomography," *Optics Express*, vol. 11, pp. 889-894, 2003.
- [33] M. A. Choma, M. V. Sarunic, C. H. Yang, and J. A. Izatt, "Sensitivity advantage of swept source and Fourier domain optical coherence tomography," *Optics Express*, vol. 11, pp. 2183-2189, 2003.
- [34] J. F. de Boer, B. Cense, B. H. Park, M. C. Pierce, G. J. Tearney, and B. E. Bouma, "Improved signal-to-noise ratio in spectral-domain compared with time-domain optical coherence tomography," *Opt Lett*, vol. 28, pp. 2067-9, 2003.
- [35] N. Nassif, B. Cense, B. H. Park, S. H. Yun, T. C. Chen, B. E. Bouma, G. J. Tearney, and J. F. de Boer, "In vivo human retinal imaging by ultrahigh-speed spectral domain optical coherence tomography," *Opt Lett*, vol. 29, pp. 480-2, 2004.
- [36] M. Wojtkowski, T. Bajraszewski, P. Targowski, and A. Kowalczyk, "Real-time in vivo imaging by high-speed spectral optical coherence tomography," *Opt Lett*, vol. 28, pp. 1745-7, 2003.
- [37] W. Drexler, U. Morgner, F. X. Kartner, C. Pitris, S. A. Boppart, X. D. Li, E. P. Ippen, and J. G. Fujimoto, "In vivo ultrahigh-resolution optical coherence tomography," *Optics Letters*, vol. 24, pp. 1221-1223, 1999.

- [38] R. Huber, M. Wojtkowski, J. G. Fujimoto, J. Y. Jiang, and A. E. Cable, "Three-dimensional and C-mode OCT imaging with a compact, frequency swept laser source at 1300 nm," *Optics Express*, vol. 13, pp. 10523-10538, 2005.
- [39] V. X. Yang, N. Munce, J. Pekar, M. L. Gordon, S. Lo, N. E. Marcon, B. C. Wilson, and I. A. Vitkin, "Micromachined array tip for multifocus fiber-based optical coherence tomography," *Opt Lett*, vol. 29, pp. 1754-6, 2004.
- [40] Z. Ding, H. Ren, Y. Zhao, J. S. Nelson, and Z. Chen, "High-resolution optical coherence tomography over a large depth range with an axicon lens," *Optics Letters*, vol. 27, pp. 243-5, 2002.
- [41] R. A. Leitgeb, M. Villiger, A. H. Bachmann, L. Steinmann, and T. Lasser, "Extended focus depth for Fourier domain optical coherence microscopy," *Opt Lett*, vol. 31, pp. 2450-2, 2006.
- [42] T. S. Ralston, D. L. Marks, F. Kamalabadi, and S. A. Boppart, "Deconvolution methods for mitigation of transverse blurring in optical coherence tomography," *IEEE Trans Image Process*, vol. 14, pp. 1254-64, 2005.
- [43] T. S. Ralston, D. L. Marks, P. S. Carney, and S. A. Boppart, "Inverse scattering for optical coherence tomography," *J Opt Soc Am A Opt Image Sci Vis*, vol. 23, pp. 1027-37, 2006.
- [44] A. G. Podoleanu, J. A. Rogers, D. A. Jackson, and S. Dunne, "Three dimensional OCT images from retina and skin," *Optics Express*, vol. 7, pp. 292-298, 2000.
- [45] M. J. Cobb, X. Liu, and X. Li, "Continuous focus tracking for real-time optical coherence tomography," *Opt Lett*, vol. 30, pp. 1680-2, 2005.
- [46] J. A. Izatt, M. R. Hee, G. M. Owen, E. A. Swanson, and J. G. Fujimoto, "Optical coherence microscopy in scattering media," *Optics Letters*, vol. 19, pp. 590-2, 1994.
- [47] T. Sawatari, "Optical Heterodyne Scanning Microscope," *Applied Optics*, vol. 12, pp. 2768-2772, 1973.
- [48] D. K. Hamilton and C. J. R. Sheppard, "A Confocal Interference Microscope," *Optica Acta*, vol. 29, pp. 1573-1577, 1982.
- [49] M. Gu and C. J. R. Sheppard, "Fiberoptic Confocal Scanning Interference Microscopy," *Optics Communications*, vol. 100, pp. 79-86, 1993.
- [50] M. Gu and C. J. R. Sheppard, "Experimental Investigation of Fiberoptic Confocal Scanning Microscopy - Including a Comparison with Pinhole Detection," *Micron*, vol. 24, pp. 557-565, 1993.
- [51] H. Zhou, C. J. R. Sheppard, and M. Gu, "A compact confocal interference microscope based on a four-port single-mode fibre coupler," *Optik*, vol. 103, pp. 45-48, 1996.
- [52] M. Kempe and W. Rudolph, "Analysis of heterodyne and confocal microscopy for illumination with broad-bandwidth light," *Journal of Modern Optics*, vol. 43, pp. 2189-2204, 1996.
- [53] M. Kempe, W. Rudolph, and E. Welsch, "Comparative study of confocal and heterodyne microscopy for imaging through scattering media," *Journal of the Optical Society of America a-Optics Image Science and Vision*, vol. 13, pp. 46-52, 1996.
- [54] J. A. Izatt, M. D. Kulkarni, H.-W. Wang, K. Kobayashi, and M. V. Sivak, Jr., "Optical coherence tomography and microscopy in gastrointestinal tissues," *IEEE Journal of Selected Topics in Quantum Electronics*, vol. 2, pp. 1017-28, 1996.
- [55] A. G. Podoleanu, M. Seeger, G. M. Dobre, D. J. Webb, D. A. Jackson, and F. W. Fitzke, "Transversal and longitudinal images from the retina of the living eye using low coherence reflectometry," *Journal of Biomedical Optics*, vol. 3, pp. 12-20, 1998.
- [56] S. H. Yun, G. J. Tearney, J. F. de Boer, N. Iftimia, and B. E. Bouma, "High-speed optical frequency-domain imaging," *Optics Express*, vol. 11, pp. 2953-2963, 2003.
- [57] R. Huber, M. Wojtkowski, K. Taira, J. G. Fujimoto, and K. Hsu, "Amplified, frequency swept lasers for frequency domain reflectometry and OCT imaging: design and scaling principles," *Optics Express*, vol. 13, pp. 3513-3528, 2005.
- [58] M. A. Choma, A. K. Ellerbee, C. Yang, T. L. Creazzo, and J. A. Izatt, "Spectral-domain phase microscopy," *Opt Lett*, vol. 30, pp. 1162-4, 2005.

- [59] C. Joo, T. Akkin, B. Cense, B. H. Park, and J. F. de Boer, "Spectral-domain optical coherence phase microscopy for quantitative phase-contrast imaging," *Opt Lett*, vol. 30, pp. 2131-3, 2005.
- [60] M. Wojtkowski, V. J. Srinivasan, T. H. Ko, J. G. Fujimoto, A. Kowalczyk, and J. S. Duker, "Ultrahigh-resolution, high-speed, Fourier domain optical coherence tomography and methods for dispersion compensation," *Optics Express*, vol. 12, pp. 2404-2422, 2004.
- [61] C. Xu, C. Vinegoni, T. S. Ralston, W. Luo, W. Tan, and S. A. Boppart, "Spectroscopic spectral-domain optical coherence microscopy," *Opt Lett*, vol. 31, pp. 1079-81, 2006.
- [62] W. Y. Oh, S. H. Yun, G. J. Tearney, and B. E. Bouma, "115 kHz tuning repetition rate ultrahigh-speed wavelength-swept semiconductor laser," *Optics Letters*, vol. 30, pp. 3159-3161, 2005.
- [63] R. Huber, M. Wojtkowski, and J. G. Fujimoto, "Fourier Domain Mode Locking (FDML): A new laser operating regime and applications for optical coherence tomography," *Optics Express*, vol. 14, pp. 3225-3237, 2006.
- [64] R. Huber, D. C. Adler, and J. G. Fujimoto, "Buffered Fourier domain mode locking: Unidirectional swept laser sources for optical coherence tomography imaging at 370,000 lines/s," *Opt Lett*, vol. 31, pp. 2975-7, 2006.
- [65] M. Hee, "Optical Coherence Tomography: Theory," in *Handbook of Optical Coherence Tomography*, B. Bouma and G. Tearney, Eds. New York: Marcel Dekker, 2002.
- [66] M. Gu, C. J. R. Sheppard, and X. Gan, "Image-Formation in a Fiberoptic Confocal Scanning Microscope," *Journal of the Optical Society of America a-Optics Image Science and Vision*, vol. 8, pp. 1755-1761, 1991.
- [67] H.-W. Wang, J. Izatt, and M. Kulkarni, "Optical Coherence Microscopy," in *Handbook of Optical Coherence Tomography*, B. Bouma and G. Tearney, Eds. New York: Marcel Dekker, 2002, pp. 275-298.
- [68] C. J. R. Sheppard, M. Gu, K. Brain, and H. Zhou, "Influence of Spherical-Aberration on Axial Imaging of Confocal Reflection Microscopy," *Applied Optics*, vol. 33, pp. 616-624, 1994.
- [69] C. L. Smithpeter, A. K. Dunn, A. J. Welch, and R. Richards-Kortum, "Penetration depth limits of in vivo confocal reflectance imaging," *Applied Optics*, vol. 37, pp. 2749-2754, 1998.
- [70] J. M. Schmitt and K. BenLetaief, "Efficient monte carlo simulation of confocal microscopy in biological tissue," *Journal of the Optical Society of America a-Optics Image Science and Vision*, vol. 13, pp. 952-961, 1996.
- [71] J. M. Schmitt, A. Knuttel, and M. Yadlowsky, "Confocal Microscopy in Turbid Media," *Journal of the Optical Society of America a-Optics Image Science and Vision*, vol. 11, pp. 2226-2235, 1994.
- [72] J. M. Schmitt and A. Knuttel, "Model of optical coherence tomography of heterogeneous tissue," *Journal of the Optical Society of America A (Optics, Image Science and Vision)*, vol. 14, pp. 1231-42, 1997.
- [73] A. L. Clark, A. Gillenwater, R. Alizadeh-Naderi, A. K. El-Naggar, and R. Richards-Kortum, "Detection and diagnosis of oral neoplasia with an optical coherence microscope," *J Biomed Opt*, vol. 9, pp. 1271-80, 2004.
- [74] K. Bizheva, "Low Coherence Interferometry in Turbid Media: The Effect of Multiply Scattered Light Detection on Image Quality," in *Department of Physics and Astronomy*. Boston: Tufts University, 2001, pp. 168.
- [75] A. D. Aguirre, P. Hsiung, T. H. Ko, I. Hartl, and J. G. Fujimoto, "High-resolution optical coherence microscopy for high-speed, in vivo cellular imaging," *Opt Lett*, vol. 28, pp. 2064-6, 2003.
- [76] C. Liang, K. B. Sung, R. R. Richards-Kortum, and M. R. Descour, "Design of a high-numerical-aperture miniature microscope objective for an endoscopic fiber confocal reflectance microscope," *Appl Opt*, vol. 41, pp. 4603-10, 2002.
- [77] S. Bourquin, A. D. Aguirre, I. Hartl, P. Hsiung, T. H. Ko, J. G. Fujimoto, T. A. Birks, W. J. Wadsworth, U. Bunting, and D. Kopf, "Ultrahigh resolution real time OCT imaging using a

- compact femtosecond Nd : Glass laser and nonlinear fiber," *Optics Express*, vol. 11, pp. 3290-3297, 2003.
- [78] Y. M. Wang, J. S. Nelson, Z. P. Chen, B. J. Reiser, R. S. Chuck, and R. S. Windeler, "Optimal wavelength for ultrahigh-resolution optical coherence tomography," *Optics Express*, vol. 11, pp. 1411-1417, 2003.
- [79] K. B. Sung, C. Liang, M. Descour, T. Collier, M. Follen, A. Malpica, and R. Richards-Kortum, "Near real time in vivo fibre optic confocal microscopy: sub-cellular structure resolved," *J Microsc*, vol. 207, pp. 137-45, 2002.
- [80] B. M. Hoeling, A. D. Fernandez, R. C. Haskell, and D. C. Petersen, "Phase modulation at 125 kHz in a Michelson interferometer using an inexpensive piezoelectric stack driven at resonance," *Review of Scientific Instruments*, vol. 72, pp. 1630-1633, 2001.
- [81] G. J. Tearney, B. E. Bouma, and J. G. Fujimoto, "High-speed phase- and group-delay scanning with a grating-based phase control delay line," *Optics Letters*, vol. 22, pp. 1811-13, 1997.
- [82] A. M. Rollins, M. D. Kulkarni, S. Yazdanfar, R. Ung-arunyawee, and J. A. Izatt, "In vivo video rate optical coherence tomography," *Optics Express*, vol. 3, 1998.
- [83] A. V. Zvyagin and D. D. Sampson, "Achromatic optical phase shifter-modulator," *Optics Letters*, vol. 26, pp. 187-189, 2001.
- [84] V. Westphal, S. Yazdanfar, A. M. Rollins, and J. A. Izatt, "Real-time, high velocity-resolution color Doppler optical coherence tomography," *Optics Letters*, vol. 27, pp. 34-6, 2002.
- [85] J. F. de Boer, C. E. Saxer, and J. S. Nelson, "Stable carrier generation and phase-resolved digital data processing in optical coherence tomography," *Applied Optics*, vol. 40, pp. 5787-90, 2001.
- [86] Y. Zhao, Z. Chen, C. Saxer, S. Xiang, J. F. de Boer, and J. S. Nelson, "Phase-resolved optical coherence tomography and optical Doppler tomography for imaging blood flow in human skin with fast scanning speed and high velocity sensitivity," *Optics Letters*, vol. 25, pp. 114-16, 2000.
- [87] T. Q. Xie, Z. G. Wang, and Y. T. Pan, "High-speed optical coherence tomography using fiberoptic acousto-optic phase modulation," *Optics Express*, vol. 11, pp. 3210-3219, 2003.
- [88] M. Pircher, E. Goetzinger, R. Leitgeb, and C. K. Hitzenberger, "Transversal phase resolved polarization sensitive optical coherence tomography," *Phys Med Biol*, vol. 49, pp. 1257-63, 2004.
- [89] T. Q. Xie, Z. G. Wang, and Y. T. Pan, "Dispersion compensation in high-speed optical coherence tomography by acousto-optic modulation," *Applied Optics*, vol. 44, pp. 4272-4280, 2005.
- [90] K. Wiesauer, M. Pircher, E. Goetzinger, S. Bauer, R. Engelke, G. Ahrens, G. Grutzner, C. K. Hitzenberger, and D. Stifter, "En-face scanning optical coherence tomography with ultra-high resolution for material investigation," *Optics Express*, vol. 13, pp. 1015-1024, 2005.
- [91] Y. C. Chen and X. D. Li, "Dispersion management up to the third order for real-time optical coherence tomography involving a phase or frequency modulator," *Optics Express*, vol. 12, pp. 5968-5978, 2004.
- [92] Y. C. Chen, X. M. Liu, M. J. Cobb, M. T. Myaing, T. Sun, and X. D. Li, "Optimization of optical spectral throughput of acousto-optic modulators for high-speed optical coherence tomography," *Optics Express*, vol. 13, pp. 7816-7822, 2005.
- [93] A. G. Podoleanu, G. M. Dobre, D. J. Webb, and D. A. Jackson, "Coherence imaging by use of a Newton rings sampling function," *Optics Letters*, vol. 21, pp. 1789-1791, 1996.
- [94] A. G. Podoleanu, G. M. Dobre, and D. A. Jackson, "En-face coherence imaging using galvanometer scanner modulation," *Optics Letters*, vol. 23, pp. 147-149, 1998.
- [95] Z. Yaqoob, J. Fingler, X. Heng, and C. Yang, "Homodyne en face optical coherence tomography," *Opt Lett*, vol. 31, pp. 1815-7, 2006.
- [96] J. Knittel, L. Schnieder, G. Buess, B. Messerschmidt, and T. Possner, "Endoscope-compatible confocal microscope using a gradient index-lens system," *Optics Communications*, vol. 188, pp. 267-273, 2001.
- [97] P. M. Lane, A. L. P. Dlugan, R. Richards-Kortum, and C. E. MacAulay, "Fiber-optic confocal microscopy using a spatial light modulator," *Optics Letters*, vol. 25, pp. 1780-1782, 2000.

- [98] Y. S. Sabharwal, A. R. Rouse, L. Donaldson, M. F. Hopkins, and A. F. Gmitro, "Slit-scanning confocal microendoscope for high-resolution in vivo imaging," *Applied Optics*, vol. 38, pp. 7133-7144, 1999.
- [99] A. F. Gmitro and D. Aziz, "Confocal Microscopy through a Fiberoptic Imaging Bundle," *Optics Letters*, vol. 18, pp. 565-567, 1993.
- [100] T. Xie, D. Mukai, S. Guo, M. Brenner, and Z. Chen, "Fiber-optic-bundle-based optical coherence tomography," *Opt Lett*, vol. 30, pp. 1803-5, 2005.
- [101] F. Helmchen, M. S. Fee, D. W. Tank, and W. Denk, "A miniature head-mounted two-photon microscope: High-resolution brain imaging in freely moving animals," *Neuron*, vol. 31, pp. 903-912, 2001.
- [102] L. D. Swindle, S. G. Thomas, M. Freeman, and P. M. Delaney, "View of normal human skin in vivo as observed using fluorescent fiber-optic confocal microscopic imaging," *Journal of Investigative Dermatology*, vol. 121, pp. 706-712, 2003.
- [103] E. J. Seibel and Q. Y. J. Smithwick, "Unique features of optical scanning, single fiber endoscopy," *Lasers in Surgery and Medicine*, vol. 30, pp. 177-183, 2002.
- [104] X. Liu, M. J. Cobb, Y. Chen, M. B. Kimmey, and X. Li, "Rapid-scanning forward-imaging miniature endoscope for real-time optical coherence tomography," *Opt Lett*, vol. 29, pp. 1763-5, 2004.
- [105] D. L. Dickensheets and G. S. Kino, "Silicon-micromachined scanning confocal optical microscope," *Journal of Microelectromechanical Systems*, vol. 7, pp. 38-47, 1998.
- [106] Y. Pan, H. Xie, and G. K. Fedder, "Endoscopic optical coherence tomography based on a microelectromechanical mirror," *Optics Letters*, vol. 26, pp. 1966-8, 2001.
- [107] J. M. Zara, S. Yazdanfar, K. D. Rao, J. A. Izatt, and S. W. Smith, "Electrostatic micromachine scanning mirror for optical coherence tomography," *Opt Lett*, vol. 28, pp. 628-30, 2003.
- [108] J. T. W. Yeow, V. X. D. Yang, A. Chahwan, M. L. Gordon, B. Qi, I. A. Vitkin, B. C. Wilson, and A. A. Goldenberg, "Micromachined 2-D scanner for 3-D optical coherence tomography," *Sensors and Actuators a-Physical*, vol. 117, pp. 331-340, 2005.
- [109] A. Jain, A. Kopa, Y. T. Pan, G. K. Fedder, and H. K. Xie, "A two-axis electrothermal micromirror for endoscopic optical coherence tomography," *Ieee Journal of Selected Topics in Quantum Electronics*, vol. 10, pp. 636-642, 2004.
- [110] W. Piyawattanametha, P. R. Patterson, D. Hah, H. Toshiyoshi, and M. C. Wu, "Surface- and bulk-micromachined two-dimensional scanner driven by angular vertical comb actuators," *Journal of Microelectromechanical Systems*, vol. 14, pp. 1329-1338, 2005.
- [111] J. M. Schmitt and G. Kumar, "Turbulent nature of refractive-index variations in biological tissue," *Optics Letters*, vol. 21, pp. 1310-1312, 1996.
- [112] E. Beaurepaire, L. Moreaux, F. Amblard, and J. Mertz, "Combined scanning optical coherence and two-photon-excited fluorescence microscopy," *Optics Letters*, vol. 24, pp. 969-971, 1999.
- [113] S. Tang, T. B. Krasieva, Z. Chen, and B. J. Tromberg, "Combined multiphoton microscopy and optical coherence tomography using a 12-fs broadband source," *J Biomed Opt*, vol. 11, pp. 20502, 2006.
- [114] S. Yazdanfar, L. H. Laiho, and P. T. C. So, "Interferometric second harmonic generation microscopy," *Optics Express*, vol. 12, pp. 2739-2745, 2004.
- [115] C. Vinegoni, T. Ralston, W. Tan, W. Luo, D. L. Marks, and S. A. Boppart, "Integrated structural and functional optical imaging combining spectral-domain optical coherence and multiphoton microscopy," *Applied Physics Letters*, vol. 88, pp. -, 2006.
- [116] J. P. Dunkers, M. T. Cicerone, and N. R. Washburn, "Collinear optical coherence and confocal fluorescence microscopies for tissue engineering," *Optics Express*, vol. 11, pp. 3074-3079, 2003.
- [117] J. W. Hettinger, M. de la Pena Mattozzi, W. R. Myers, M. E. Williams, A. Reeves, R. L. Parsons, R. C. Haskell, D. C. Petersen, R. Wang, and J. I. Medford, "Optical coherence microscopy. A technology for rapid, in vivo, non-destructive visualization of plants and plant cells," *Plant Physiol*, vol. 123, pp. 3-16, 2000.

- [118] B. M. Hoeling, A. D. Fernandez, R. C. Haskell, E. Huang, W. R. Myers, D. C. Petersen, S. E. Ungersma, R. Y. Wang, M. E. Williams, and S. E. Fraser, "An optical coherence microscope for 3-dimensional imaging in developmental biology," *Optics Express*, vol. 6, pp. 136-146, 2000.
- [119] A. D. Aguirre and J. G. Fujimoto, "*Ex Vivo* Cellular Imaging of Normal and Pathologic Tissues from the Human Gastrointestinal Tract Using Optical Coherence Microscopy," Massachusetts Institute of Technology, 2006.



## Chapter 5

### High Speed, Broadband OCM System for *In Vivo* Imaging

#### 5.1 Overview

The previous chapter reviewed prior work on optical coherence microscopy and provided an overview of system design goals and constraints as well as imaging applications. The current chapter describes the development of a high speed, broadband OCM system based on an electro-optic phase modulator. The system design was highly suitable for *in vivo* OCM imaging applications and is limited in imaging speed only by the maximum line rate of the beam scanners. Furthermore, the system implemented a robust solution to the problem of controlling the overlap of confocal and coherence gates for optimal image signal and resolution. The system configuration provided for integration with a variety of delivery devices such as catheters, handheld probes, and benchtop imaging microscopes. Finally, the OCM system was portable and ready for use in the clinical environment.

#### 5.2 Introduction

Optical coherence tomography (OCT) and confocal laser scanning microscopy (CLSM) are developing techniques for *in vivo* imaging of tissue microstructure [1, 2]. Optical coherence microscopy (OCM) extends the capabilities of OCT and confocal microscopy by combining high-sensitivity, coherence-gated detection with confocal optical sectioning to improve rejection of unwanted scattered light from outside the imaging plane [3]. The improved axial sectioning provided by optical coherence gating enables greater imaging depth and contrast compared to confocal microscopy alone [3, 4]. Furthermore, by scanning an *en face* image plane with the coherence gate matched to the confocal gate, OCM does not suffer from depth of field limitations present in standard depth scanning OCT and can achieve transverse image resolutions on the micron level. Cellular imaging in human tissue has been demonstrated with OCM [5-7].

Optical coherence microscopy can achieve cellular imaging in scattering tissues with lower numerical aperture compared to confocal microscopy because axial sectioning is performed with a combination of coherence and confocal gating. Using short coherence gates produced by broadband laser sources, OCM can achieve thin optical sections using coherence gating and can therefore image with lower numerical aperture [6]. To perform high resolution OCM imaging with very short coherence gates, OCM systems must support broad optical bandwidths similar to ultrahigh resolution OCT [8]. Development of high-resolution, real-time OCM systems has been limited by the lack of high-speed, broadband phase modulators. Grating phase delay scanners have been adapted for high-speed OCM and shown to support nearly 200 nm bandwidth [6]. These scanners use a grating and lens to produce spectral dispersion and a galvanometer mirror to produce a Fourier plane phase shift, resulting in a group and/or phase delay. By choosing the grating and lens correctly, the group delay can be set to zero to produce a pure phase modulation. Using such a grating phase modulator, axial resolution of  $\sim 3$   $\mu\text{m}$  was achieved and high quality *in vivo* images of human skin and *Xenopus laevis* tadpole were achieved with this system. A disadvantage of this type of modulator is the need for a rapid scanning galvanometer to generate the phase delay. This limits the modulation rate that can be achieved and requires that the lateral scan be synchronized to the modulator scanner. Synchronization can be difficult when incorporating resonant scanning devices as is typical with miniaturized scanners for endoscopic applications [9]. In addition, the grating phase modulator layout does not allow easy incorporation of a depth scanning galvanometer to rapidly adjust the position of the coherence gate. Rapid depth scanning is necessary to perform conventional OCT. It is also important for fast synchronization of the confocal and coherence gates for *in vivo* imaging.

Several groups have used acousto-optic (AO) [10-12] or electro-optic (EO) modulators [13-15] for OCT imaging. Both solutions have been shown to provide highly stable carrier frequencies suitable for phase sensitive imaging. The application of these modulators for ultrahigh coherence axial resolutions, however, has required advances in dispersion management to compensate for the large unbalanced chromatic dispersion introduced by the modulator crystal in the reference arm [12, 16]. With appropriate dispersion compensation, AO and EO modulators offer excellent options for high speed OCM imaging.

This chapter describes a novel OCM system design based on an electro-optic waveguide phase modulator for imaging at 1060 nm wavelength. The system was designed for use with a broadband light source consisting of the output from an Nd:Glass oscillator spectrally broadened in a high numerical aperture fiber [17], as described in chapter 3 of this thesis. Using a strategy slightly modified from previously reported dispersion compensation approaches, the system enabled coherence axial resolutions of 3.7  $\mu\text{m}$ . To allow the modulator to be used with the polarized broadband continuum, a novel polarization compensation approach was developed. In addition, a rapid linear-scanning galvanometer

was incorporated into the reference arm of the system to enable fast depth scanning and precise control of the position of the coherence gate. The scanner was used to implement a new algorithm for rapid, automated alignment of the optical coherence gate with the focus plane of the confocal microscope in highly scattering tissue during imaging. The algorithm was analogous to autofocus strategies used in modern digital cameras, and its implementation ensured optimal image quality for real-time imaging. It also made the OCM system much easier to operate and improved the reliability of the instrument. *Ex vivo* and *in vivo* cellular imaging results from human tissues are reported and parameters for image display and optimization are discussed. Finally, the integration of the OCM system into a portable unit for clinical investigation is discussed.

### 5.3 System Design

#### 5.3.1 OCM Imaging Engine

Figure 5.1 illustrates the OCM system design. An Nd:Glass oscillator (HighQ Laser) generating 85 fs pulses with  $> 165$  mW output power was coupled into a 1 m length of high numerical aperture (NA) germanium-doped optical fiber (Nufern, UHNA3). Spectral broadening by predominantly self-phase modulation resulted in an optical bandwidth of  $> 200$  nm centered at 1060 nm. A 100 m length of single mode fiber (Corning, HI-1060) followed the high NA fiber before launching into a fiber optic 50/50 coupler. The long optical fiber was used to broaden the femtosecond pulse from the oscillator to protect the electro-optic modulator from high peak intensities as well as to reduce the effective exposure at the tissue sample for *in vivo* imaging. A polarization controller was included on the source input to allow for adjustment of the input polarization state. The coupler divided the light between a reference arm and a sample arm, both of which also contained polarization controllers that were used to manipulate the interfering fields to achieve an optimized interference point spread function. The reference arm used an electro-optic waveguide phase modulator (EOSPACE, PM-0K1-12-PFA-PFA-106-UL) designed for use at 1060 nm center wavelength. The modulator consisted of a 72 mm  $\text{LiNbO}_3$  crystal and had an RF electrical bandwidth of  $> 12.5$  GHz. Low optical insertion loss measuring  $< 3$  dB and low  $V_\pi < 5$  V were also desirable characteristics of the device. Light was coupled into and out of the waveguide with polarization-maintaining (PM) optical fiber with the fast and slow axes of the fiber carefully aligned to the fast and slow axes of the modulator. The modulator was driven in a serrrodyne fashion with a sawtooth waveform to produce a roundtrip repetitive phase swing of  $2\pi$ , which resulted in an optical heterodyne frequency shift corresponding to the fundamental frequency of the drive waveform. Frequency shifts of 1-2 MHz depending upon the imaging speed were used for these studies. Use of a pure sawtooth drive with instantaneous flyback resulted in a modulation artifact believed to be due to excitation of mechanical resonances in the modulator by higher harmonics of the waveform. The artifact

was suppressed to below the system dynamic range by using a slightly triangular drive waveform with a 4% flyback component. This caused a slight glitch in the heterodyne signal that was largely eliminated by the bandpass filter applied to the digitized signal. After exiting the modulator, reference arm light passed into a Fourier-domain optical delay line used for dispersion compensation. The delay line also contained a rapid depth scanning galvanometer for adjustment of the coherence gate. Further discussion of the reference arm delay line will follow.

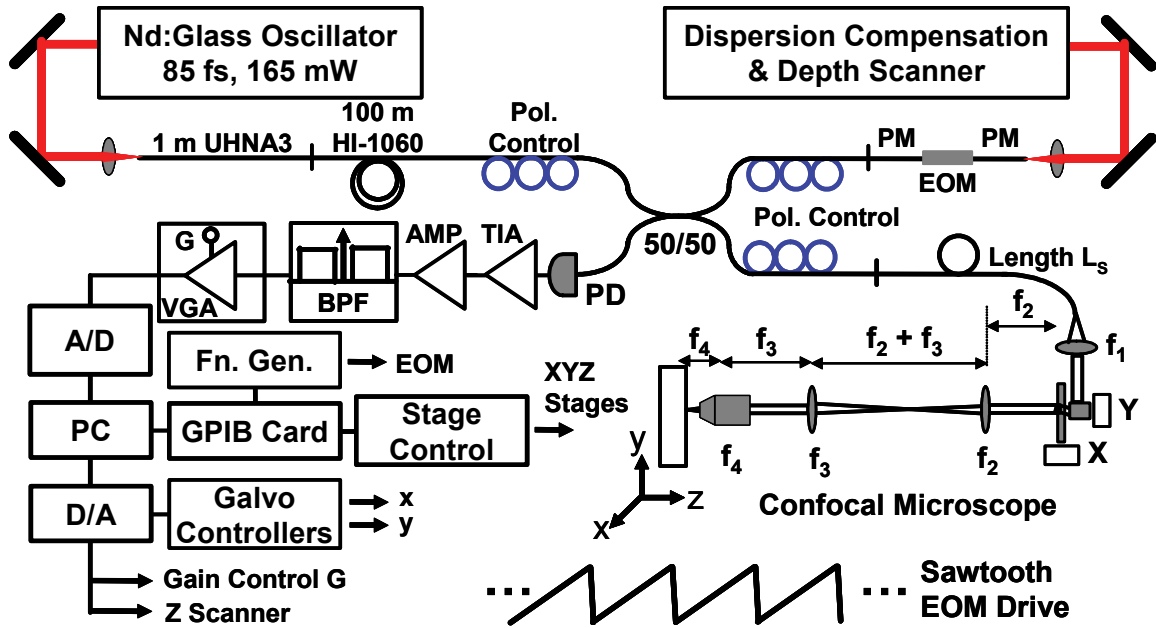


**Figure 5.1.** High-speed OCM imaging system. The system operates at 1060 nm center wavelength using a broadband electro-optic waveguide phase modulator. TIA, transimpedance amplifier. BPF, bandpass filter. PD, photodiode. VGA, variable-gain amplifier. A/D, analog-to-digital converter. PC, personal computer. D/A, digital-to-analog converter. PM, polarization-maintaining. EOM, electro-optic modulator.

The sample arm consisted of fiber-optic confocal microscope, which is shown in detail in figure 5.2. The beam was collimated to a  $1/e^2$  beam diameter of 1.7 mm by a custom Gradium achromat (Lightpath,  $f = 10$  mm) designed for broadband use at 1060 nm. Scanning was performed using a pair of high performance ball-bearing galvanometers capable of high speed non-resonant raster scanning (Cambridge Technologies, 6215H). The scanners enabled image line rates of over 1 kHz using a triangle drive waveform and over 2.5 kHz using a sinusoidal sweep. This provided for imaging at rates of 4-8 frames per second with 500 lines/image using bidirectional acquisition. The galvanometer mirrors had 3 mm aperture and were mounted as close together as possible in an integrated XY housing. The scan lens after the galvanometers consisted of a near-infrared achromat doublet (Edmund Optics, NT45-806) with 100

mm focal length. Several scan lenses were tested, including an expensive telecentric design used in a commercial confocal microscope, but it was found that the performance was not significantly improved over the simple doublet lens for imaging in highly scattering tissues. In addition, the doublet had the advantages of being specifically designed for near-infrared wavelengths and of having relatively little glass thickness compared to multi-element scan lenses. This latter point facilitated dispersion balancing between reference and sample arms for achieving high axial resolution. The third lens in the beam path acted as the tube lens to the infinity-corrected objective lens as well as the second half of the intermediate optics telescope that imaged the scanners to the objective. An identical achromat doublet lens with 100 mm focal length was used. Finally, a 40x/0.8 NA water immersion plan achromat objective lens (Zeiss Achroplan 440095) focused the beam to the specimen. The microscope lateral resolution measured  $< 2$   $\mu\text{m}$  full-width-at-half-maximum (FWHM) and the confocal parameter was  $\sim 19$   $\mu\text{m}$ . The objective lens was significantly underfilled such that the corresponding numerical aperture was only  $\sim 0.32$  rather than the full 0.8. For *ex vivo* imaging experiments, a three-axis translation stage allowed coarse and fine manipulation of the sample position underneath the microscope.

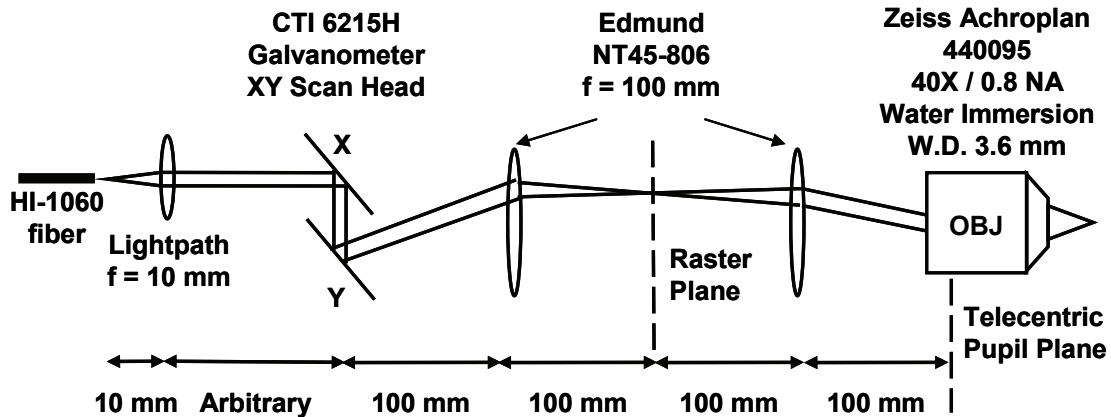


**Figure 5.2.** Detailed schematic of the fiber-optic confocal microscope.

Light returning from the sample and reference arms was recombined by the coupler and produced interference at a photodiode detector. Current to voltage conversion was performed by a custom built wideband transimpedance amplifier and the electrical signal was subsequently amplified by a fixed gain stage before passing through a bandpass filter. The filter consisted of a cascade of a relatively weak 3<sup>rd</sup> order Butterworth high-pass filter and a sharp combination Chebyshev-Butterworth 10<sup>th</sup> order low-pass anti-alias filter. The high-pass cutoff was located at 300 kHz and served only to remove the low-frequency incoherent intensity components to allow for fast boxcar averaging demodulation necessary for high speed real-time display. The anti-alias filter cutoff was set for 2.5 MHz, which corresponded to the

Nyquist frequency limitation of the 5 MHz, 12 bit analog-to-digital (A/D) converter (National Instruments, 6110E). The filter was designed to provide passband to stopband rejection of greater than 50 dB. Following the filtering stage was a low noise, voltage controlled variable gain amplifier (VGA, Miteq) suitable for driving the A/D converter. The amplifier had a gain range spanning from 0 to 40 dB and was controlled by a voltage level generated by the imaging software. The gain of the amplifier after the transimpedance amplifier was selected such that the final variable gain stage clips when the transimpedance amplifier clips. In addition, the A/D converter range was set to the full range of the VGA. During imaging the VGA gain setting was set to bring the image intensity maximum to the A/D maximum allowing the full 12-bit dynamic range to be used for image digitization.

A Pentium IV personal computer (PC) handled the data acquisition and control of the imaging system. The modulator driver (Agilent, 33250A) and stage controller (Newport, ESP300) were interfaced through GPIB communication protocol, while the galvanometer drive signals were controlled directly by a digital-to-analog (D/A) converter card. The VGA gain control and the Z depth scanner were also controlled by the D/A converter. Analog-to-digital conversion of the full interference fringe signal was acquired at a sampling frequency of 5 MHz. Custom Microsoft Windows-based software was written in C++ to handle data streaming through double-buffered acquisition. For real-time imaging, images were demodulated using a fast boxcar averaging algorithm. Boxcar averaging is equivalent to low-pass filtering to remove the carrier waveform, leaving only the envelope of the signal. Before display, the images were renormalized to fill the full grayscale contrast range. Images were written to screen with either no dynamic range compression, with log compression, or with square-root compression.

Offline processing of images used a more accurate Hilbert-transform based demodulation algorithm, which incorporated the digital fast-Fourier transform (FFT) to minimize computation time. Prior to demodulation, digital noise filtering was performed using a 4<sup>th</sup> order Butterworth bandpass filter. Demodulation then began with a real FFT of the digitized fringe signal followed by multiplication of the frequency spectrum by  $2u(t)$ , the scaled unit step function. The multiplication step served to zero the negative frequency components. A complex inverse FFT was next performed and the magnitude of the resulting complex signal taken as the square root of the sum of the squares of the real and imaginary components. The result of the magnitude operation produced the real-valued demodulated envelope function of the original fringe signal.

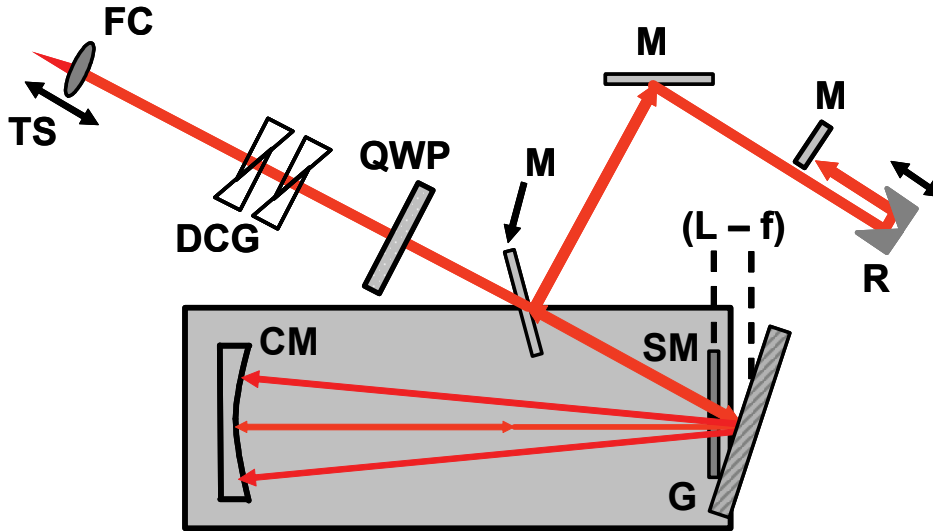


**Figure 5.3.** Schematic of the reference arm optical delay line used for dispersion compensation and path length scanning. FC, fiber collimator. DCG, dispersion compensating glass. QWP, quarter waveplate. M, mirror. R, retroreflector. CM, curved mirror. SM, stationary mirror. G, grating.

The reference optical delay line used for dispersion compensation and depth scanning is shown in top view in figure 5.3. The delay line was an all-reflective geometry modified from rapid scanning optical delay (RSOD) line configurations used for OCT and OCM previously [6, 18]. The grating-lens delay unit was used here only to compensate dispersion rather than to generate group and phase delay, and an additional linear scanning galvanometer was incorporated into the path after the delay unit to allow for depth scanning. After collimation, the input beam was incident at  $\sim 5$  degrees onto a grating with 300 lines/mm and the first diffracted spectral order was captured by a 50 mm focal length curved mirror and focused to a stationary mirror located beneath the grating. The grating and curved mirror combination effectively acted to perform an optical Fourier transform thereby allowing for direct Fourier domain phase manipulation in the focal plane of the focusing mirror. Adjustment of the offset  $(L - f)$  between the grating and the focal plane of the curved mirror allowed variation of second and third order dispersion. Light reflected from the stationary mirror was recaptured by the curved mirror and recombined at the grating. A slight vertical offset was introduced to the beam path to allow a pickoff mirror to redirect the beam toward the linear path scanner. This scanner consisted of a galvanometer with a corner cube retroreflector mounted on an extension arm from the rotating shaft. To improve backcoupling characteristics of the device, it was desirable to adjust the collimating lens so that the beam was focused on the final mirror in the optical path. This was most easily achieved by double-passing the retro-reflector, since focusing on the center corner point of the retro-reflector produced high loss. After

returning from the linear scanner, the beam passed back through the grating delay unit and back to the collimator. Dispersion compensating glass (LakN22, SFL6) was introduced into the input beam path in the form of glass blanks and adjustable prisms. In addition, a quarter wave retarder was used to compensate for wavelength dependent polarization properties of the source. The role of the quarter waveplate will be discussed in a subsequent section. Figure 5.4 presents a photograph of the device. To enable integration into a portable system for clinical imaging, the optical layout was folded to fit onto a 12" x 18" breadboard. The electro-optic modulator was also mounted on to the breadboard such that the entire reference arm assembly was contained in a single unit. Initial alignment of the device required careful adjustments, but once performed, the device was quite robust and required little to no adjustment over weeks of operation.

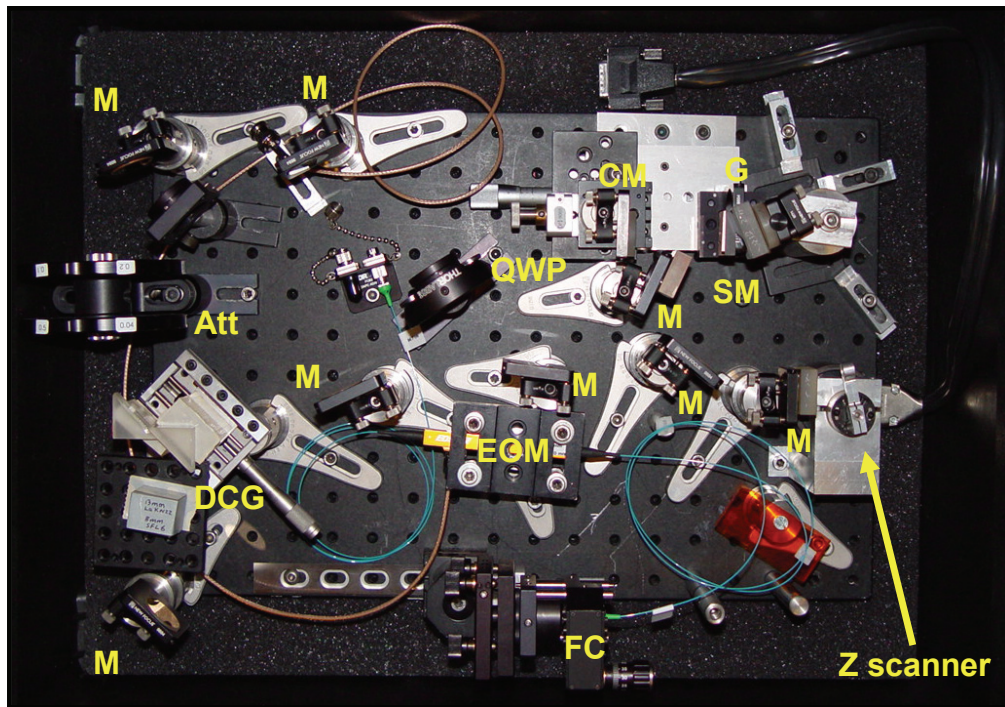


**Figure 5.4.** Photograph of compact reference arm assembly. The entire unit was built on a 12" x 18" breadboard. FC, fiber collimator. DCG, dispersion compensating glass. QWP, quarter waveplate. M, mirror. R, retroreflector. CM, curved mirror. SM, stationary mirror. G, grating. EOM, electro-optic modulator. Att, attenuation.

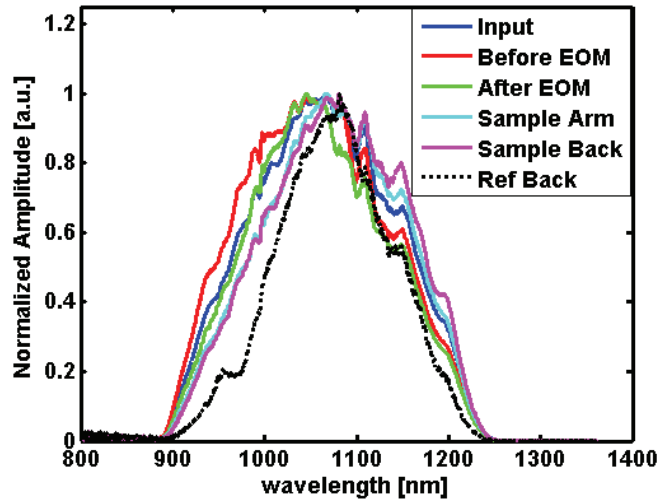


**Figure 5.5.** System optical bandwidth measurements.

Figure 5.5 presents measurements of the optical bandwidth supported by various system components. The source input bandwidth measured more than 200 nm. The EOM cut the long wavelength side of the spectrum slightly but still passed more than 190 nm. The sample arm microscope also weakly shaped the spectrum due to wavelength dependent backcoupling, although the backcoupled spectrum still measured nearly 200 nm in width. The bandwidth limiting component in the system was found to be the dispersion compensating grating delay line. Because the delay line introduced large dispersion for compensation of the EOM, the ratio of  $(L - f)/f$  was large and wavelength dependent backcoupling suffered as a result. The backcoupled reference arm bandwidth measured 152 nm.

### 5.3.2 Dispersion Compensation

To achieve broadband system operation enabled by the continuum source chosen for this system, chromatic dispersion had to be carefully balanced between the reference and sample arms. Two important sources of dispersion mismatch were present in the system. First, the 72 mm LiNbO<sub>3</sub> crystal in the waveguide modulator in the reference arm introduced large amounts of second and third order dispersion that would have destroyed the coherence gated point spread function. Second, the lenses in the confocal microscope also introduced dispersion that could not be ignored. Some of the dispersion from these two sources cancelled since they were in opposite arms of the Michelson interferometer. To achieve the light source transform-limited resolution, however, dispersion balancing had to be performed with fine adjustment in a systematic way. In addition, it was not possible to know the glass types in all of the microscope optics, so it was necessary to use an empirical approach toward dispersion management.

Material dispersion for known optical elements was calculated using the Sellmeier equation for the index of refraction, given as

$$n = \sqrt{1 + \frac{A_1 \lambda^2}{\lambda^2 - B_1} + \frac{A_2 \lambda^2}{\lambda^2 - B_2} + \frac{A_3 \lambda^2}{\lambda^2 - B_3}} \quad (1)$$

where  $A_i$  and  $B_i$  are known as the Sellmeier coefficients and can be found in standard handbooks of optical properties [19]. Dispersion terms were computed by calculating the derivatives of the index as a function of wavelength. Second and third order dispersion terms can be written as

$$\frac{\partial^2 \beta}{\partial \omega^2} = \frac{\lambda^3}{2\pi c^2} \frac{\partial^2 n}{\partial \lambda^2} \quad (2)$$

$$\frac{\partial^3 \beta}{\partial \omega^3} = -\frac{\lambda^5}{4\pi^2 c^3} \frac{\partial^3 n}{\partial \lambda^3} - \frac{3\lambda^4}{4\pi^2 c^3} \frac{\partial^2 n}{\partial \lambda^2} \quad (3)$$

respectively, with  $\beta$  representing the material propagation constant,  $\omega$  is equal to the optical frequency, and  $c$  is the speed of light in vacuum. Second order dispersion has units of  $\text{fs}^2$  while third order has units of  $\text{fs}^3$ .

Second and third order chromatic dispersion introduced into the reference arm by the grating delay line can also be expressed analytically as [12]

$$\phi'' = \frac{\partial \phi(\omega)}{\partial \omega^2} = \frac{-16\pi^2 c}{\omega^3} \frac{m^2}{d^2 \cos^2(\theta_\lambda)} (L-f)(1-\Delta\theta) \quad (4)$$

$$\phi''' = \frac{\partial^3 \phi(\omega)}{\partial \omega^3} = \frac{48m^2 \pi^2 c (L-f)}{d^2 \omega^4 \cos^2(\theta_\lambda)} \left[ 1 + \left( \tan \theta_\lambda + \frac{1}{3} \Delta\theta \right) \left( \frac{2\pi m c}{\omega d \cos(\theta_\lambda)} \right) \right] + \frac{192\pi^3 m^3 c^2 f}{d^3 \omega^5 \cos^3 \theta_\lambda} \Delta\theta \quad (5)$$

where  $c$  represents the speed of light,  $d$  is the grating line spacing,  $m$  is the diffraction order,  $\theta_\lambda$  is the diffraction angle at wavelength  $\lambda$ , and  $\Delta\theta$  is the angle between the diffracted beam and the optical axis of the focusing element. Figure 5.6 plots the second and third order dispersions as a function of wavelength for the RSOD and several materials present in the OCM system. Material dispersion is provided per mm thickness while dispersion from the RSOD is given per mm of separation ( $L-f$ ). It is immediately obvious from the plots that the RSOD can introduce large amounts of dispersion for relatively small displacements of the grating from the focal plane of the curved mirror. Moreover, it can be seen that LiNbO3 has much higher chromatic dispersion than other materials in the system.

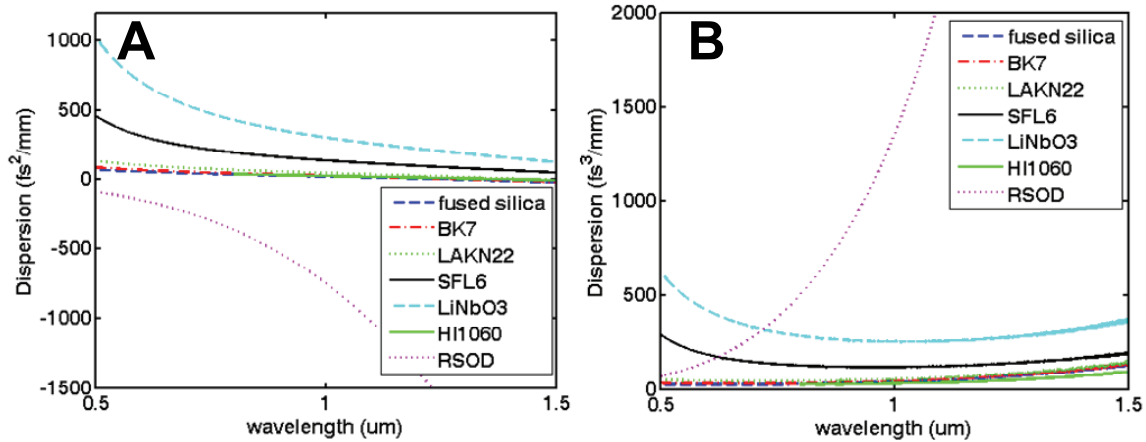


**Figure 5.6.** Second and third order dispersion calculations for system optical components.

With increasing separation ( $L - f$ ) between the grating and the focus plane of the curved mirror, increasing amounts of negative second order dispersion are added by the RSOD. This property has been used to compensate large amounts of second order dispersion introduced by the electro-optic phase modulator [14]. Elimination of second order dispersion, however, comes at the expense of increasing third order dispersion since the third order term for the RSOD is positive. Compensation of second order dispersion is generally sufficient for relatively low bandwidth light sources as have been used in standard resolution OCT systems. For ultrahigh resolution systems, however, higher order dispersion mismatch must be addressed. Chen et al. demonstrated an elegant dispersion balancing solution which allows compensation up to third order. This approach introduced additional dispersion to the sample arm in the form of an extra length of single mode optical fiber. The length of the fiber,  $L_s$ , provided a second independent parameter that could be adjusted along with the offset ( $L - f$ ) to bring both second and third order dispersion mismatch to zero. The optical path length mismatch generated by the length of single mode fiber was then accounted for by introducing additional air gap spacing in the reference optical delay line. This dispersion management strategy allowed them to achieve axial resolution of less than 3  $\mu\text{m}$  at 800 nm.

Table 5.1 presents the dispersion values for the OCM system components extracted from the plots of dispersion in figure 5.6 at the source center wavelength of 1070 nm. The index of refraction of the materials is also provided. Using the method of Chen and colleagues, second and third order dispersion of the  $\text{LiNbO}_3$  EOM was largely eliminated using  $(L - f) \approx 8\text{mm}$  and  $L_s \approx 75\text{cm}$  with reference arm air path length of  $\sim 92.5\text{ cm}$ . Since the computed second and third order dispersions for the EOM and the RSOD were not exact, the settings had to be carefully adjusted empirically in order to achieve an optimal

interference axial point spread function. In particular, the dispersion was quite sensitive to the incident angle of the beam onto the diffraction grating.

The chromatic dispersion introduced by the glass of the confocal microscope was precisely balanced using a modified approach that empirically perturbed the dispersion balancing parameters established for the EOM alone. The known glass of the intermediate optical telescope was exactly balanced by introducing glass blanks with 8 mm of SFL6 and 13 mm of LakN22. Attempts were made to estimate the residual dispersion in the system by Fourier transforming the interference point spread function, but the precision of the measurement was insufficient to get a highly accurate account of remaining third order. To compensate the unknown dispersion, a pair of SFL6 prisms were placed into the reference arm and the point spread function was optimized by iteratively adjusting the prism insertion and the  $(L - f)$  offset in the grating delay line. It was determined by calculation that this approach would work reliably for any range of realistic dispersion imbalance introduced by the microscope optics, which makes this technique a generally useful approach to compensating unknown optical elements in the OCM system. Use of certain pairs of distinct glass types was also found to work, although the ability to introduce so much dispersion using the RSOD adjustment made this the easiest approach.

Optical Components	LiNbO <sub>3</sub> (per mm)	RSOD [per mm (L-f)] single pass	HI-1060 (per mm)	Fused Silica (per mm)	SFL6 (per mm)	LakN22 (per mm)	BK7 (per mm)
Index	2.23	N/A	1.45	1.45	1.77	1.64	1.51
2 <sup>nd</sup> Order (fs <sup>2</sup> )	272.5	-467.9	21.2	16.0	123	39.8	21.84
3 <sup>rd</sup> Order (fs <sup>2</sup> )	257.9	922.06	34.8	44.6	122	59.5	49.25

**Table 5.1.** Dispersion introduced by the optical materials and the grating delay line.

The choice of the layout for reference arm delay line deserves some comment, since it was somewhat nonstandard in terms of the location of the depth scanner. Typically, RSOD configurations place an angular scanning galvanometer at the Fourier transform plane of the grating-lens combination. A tilt of the galvanometer mirror produces a wavelength-dependent phase shift that introduces a group and phase delay during scanning. In principle, the optical path length of the reference arm could be precisely controlled by adjusting the offset of this scanning mirror. In practice, however, three key limitations were discovered with this design. First, at large  $(L - f)$  offset, the backcoupled power dropped off with large angle scans. A much more uniform reference arm power could be obtained across the depth scan using the linear scanner in path after the grating-lens delay unit. Second, for nonzero  $(L - f)$  offset, the dispersion characteristics vary across the scan [12]. This property has been used by others to compensate

for depth dependent dispersion adjustment [12, 20], but it was undesirable in the OCM system constructed for this thesis, which used water immersion objective lenses. Finally, the use of an angle scanner in the Fourier domain delay line generated an image artifact due to the resonances in the galvanometer tuning circuit. The feedback control circuits for modern high speed galvanometer controllers have natural resonances which are suppressed by the manufacturer using tight notch filters on the circuit board. In the scanners tested for this work, the resonances were reduced by several orders of magnitude, but the residual mechanical jitter that they introduced was still visible on the heterodyne signal. This was particularly a problem when the angle scanner was required to hold a position for *en face* scanning rather than depth scanning. Use of a slower scanner with large mechanical inertia in the path after the grating unit produced a much cleaner heterodyne interference signal.

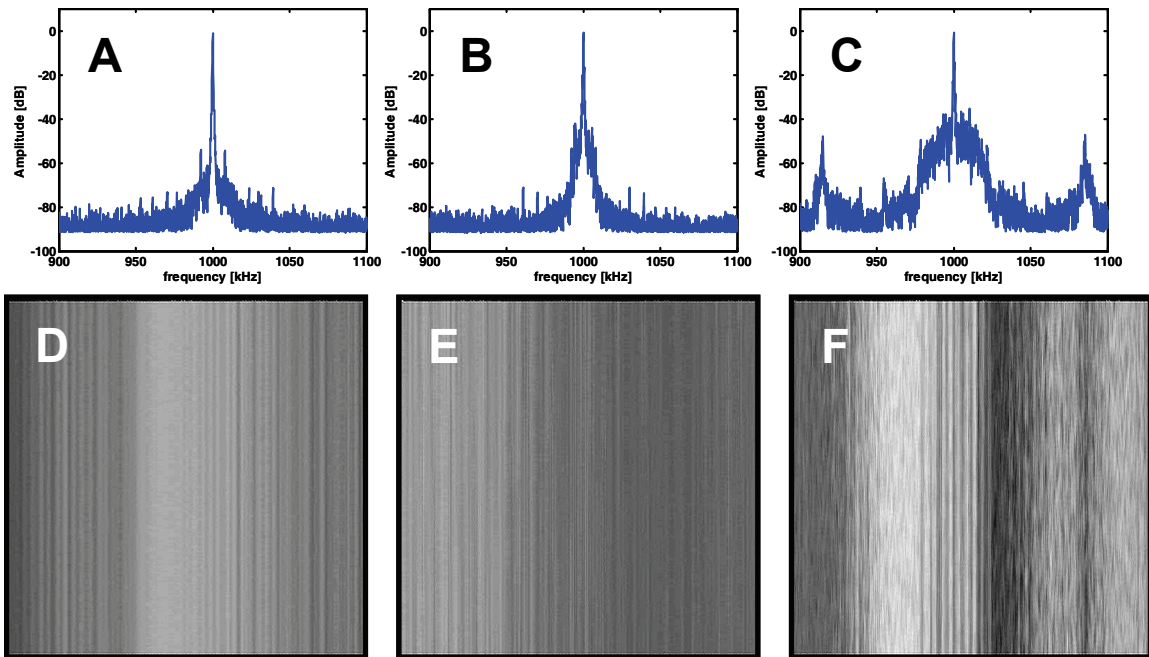


**Figure 5.7.** Image artifacts from the optical path scanner. The RF spectra and OCM images from a mirror are shown for the case of no depth scanner (A,D), a linear galvanometer scanner located after the grating delay unit (B,E), and an angular scanner located at the Fourier focal plane of the grating-lens combination (C,F). The angular scanner in the delay unit generates significant path modulation when trying to hold a fixed position which results in unacceptable image artifact. The linear scanner outside of the Fourier delay line overcomes this problem.

Figure 5.7 presents measurements illustrating this point. In figure 5.7a, the RF spectrum of the heterodyne signal at 1 MHz is shown to fall quickly to the noise floor when no electronically controlled depth scanners were present in the path. With the linear scanner (General Scanning Inc. 300B001) after the grating unit, the RF spectrum as shown in figure 5.7b also falls nicely to the noise floor with only a

slightly higher pedestal compared to the case with no scanner. Finally, with the angular scanner (Cambridge Technologies Inc. 6210) in the RSOD, the RF spectrum in figure 5.7c shows a significantly higher pedestal on the main peak corresponding to the servo controller bandwidth. In addition, sidelobe peaks are present at the resonant frequencies of the circuit despite the notch filtering. The corresponding OCM images of a mirror in figure 5.7d-f further illustrate the influence of this noise. That there is some artifact in all three images due to spurious mechanical vibrations in the optical setup. The image with the angular scanner in the RSOD in 5.7f, however, has significantly worse heterodyne artifact compared to the case of no scanners in 5.7d or the linear scanner in 5.7e. It should also be noted that the position of the angular scanner in the RSOD versus outside of it also contributed to the heterodyne signal artifact, since the RSOD amplified the effective group delay scan produced by the jitter.

### 5.3.3 Wavelength Dependent Source Polarization

A disadvantage of the electro-optic modulator for OCM is the fact that the LiNbO<sub>3</sub> crystal is highly birefringent, with phase modulation preferentially occurring on only one of the polarization axes. This can present problems for use with a polarized light source, particularly in fiber optic systems where there is complex polarization evolution in the optical fiber. Previous work with electro-optic phase modulators has been performed with superluminescent diode sources that are fairly unpolarized compared to femtosecond laser based sources [13, 14]. With unpolarized sources, polarization dependent modulation merely results in effective reference arm signal loss, since half of the intensity on average will not be modulated. In the case of a polarized source, however, alignment of the field polarization with the modulator axis is required. Moreover, any spectral dependence to the polarization state can present a challenge since not all spectral components will see the same modulation. The source used for this work consisted of a linearly polarized femtosecond laser spectrally broadened in 1 m of high numerical aperture optical fiber (Nufern UHNA3). As light propagates in an optical fiber, it sees a core which is not perfectly circular and has essentially randomly varying birefringence [21]. Moreover, the relative birefringence between segments of the fiber can change in time due to changes in environmental conditions. The initially linear polarization state undergoes a transformation to an ill defined elliptical polarization state. Polarization evolution can be further complicated with continuum generation sources due to nonlinear polarization evolution, particularly when the pump wavelength is near the zero dispersion wavelength of the fiber [22, 23].

To understand the polarization state of the light seen by the electro-optic modulator, the spectral dependence of the light source polarization was measured in a simple experiment. The experimental setup and results are presented in figure 5.8. As shown schematically in figure 5.8a, light from the source was collimated and passed through a polarizer before being recoupled into the fiber and measured with an

optical spectrum analyzer. The spectrum after the air gap coupling but without the polarizer is provided in figure 5.8b. Figures 5.8c-f present the wavelength dependence of the polarization in four distinct states, labeled with respect to arbitrary reference as 0, 45, 90, and 135 degrees. A strong wavelength dependence to the polarization was observed in each state. Due to the polarization dependence of the modulator, this effectively resulted in significant spectral modulation in the imaging spectrum. Adjustments to the input polarization using a three-paddle fiber optic controller as shown in figure 5.1 could not produce a reasonable spectrum for imaging and severe distortion of the point spread function resulted.

Two approaches were attempted to eliminate the wavelength dependence to the modulated spectrum. First, a depolarizer was tested for removal of the wavelength dependent polarization. The model used for this study was a combination of a Lyot depolarizer and a wedge depolarizer that was both achromatic and lacked a preferred input polarization state (OFR, DPU-25-YAG). Figure 5.9 illustrates the effect of the depolarizer on the wavelength dependent polarization. The measurement setup shown in 5.9a is similar to that in figure 5.8a but with the depolarizer placed before the polarizer. The depolarizer itself introduced a slight spectral modulation even without the polarizer, as shown in figure 5.9b. Figures 5.9c-f demonstrate that some depolarization of the spectrum was achieved, but fine structural modulation was generated on the spectrum in a given polarization state. This residual wavelength dependence was unacceptable for OCM imaging.

The second strategy tested was the use of a Faraday rotator. Faraday rotators have been long used in fiber optic interferometry to remove the effects of unwanted birefringence from the sensing arm and investigators have also used them in the OCT sample arm [24]. A Faraday rotator uses the magneto-optical Faraday effect to rotate the polarization of incident light by 45 degrees. Importantly, the rotation is non-reciprocal such that light rotates in the same direction going forward or backward through the device and therefore produces a net rotation on double pass of 90 degrees. A Faraday rotator was placed in the reference arm delay line of the OCM system after the EOM to force all wavelengths of the spectrum to see both axes of the LiNbO<sub>3</sub> modulator. The modulator was then driven with a sawtooth wave over  $0 - 2V_{\pi}$  such that a full wave phase shift was acquired on single pass through the device. This strategy worked well to remove the effects of wavelength dependent source polarization and produce a nicely shaped modulated spectrum. The optical bandwidth over which the rotator could maintain the 45 degree rotation, however, was limited to much less than 100 nm, which made the Faraday rotator unsuitable for ultrahigh axial resolution.

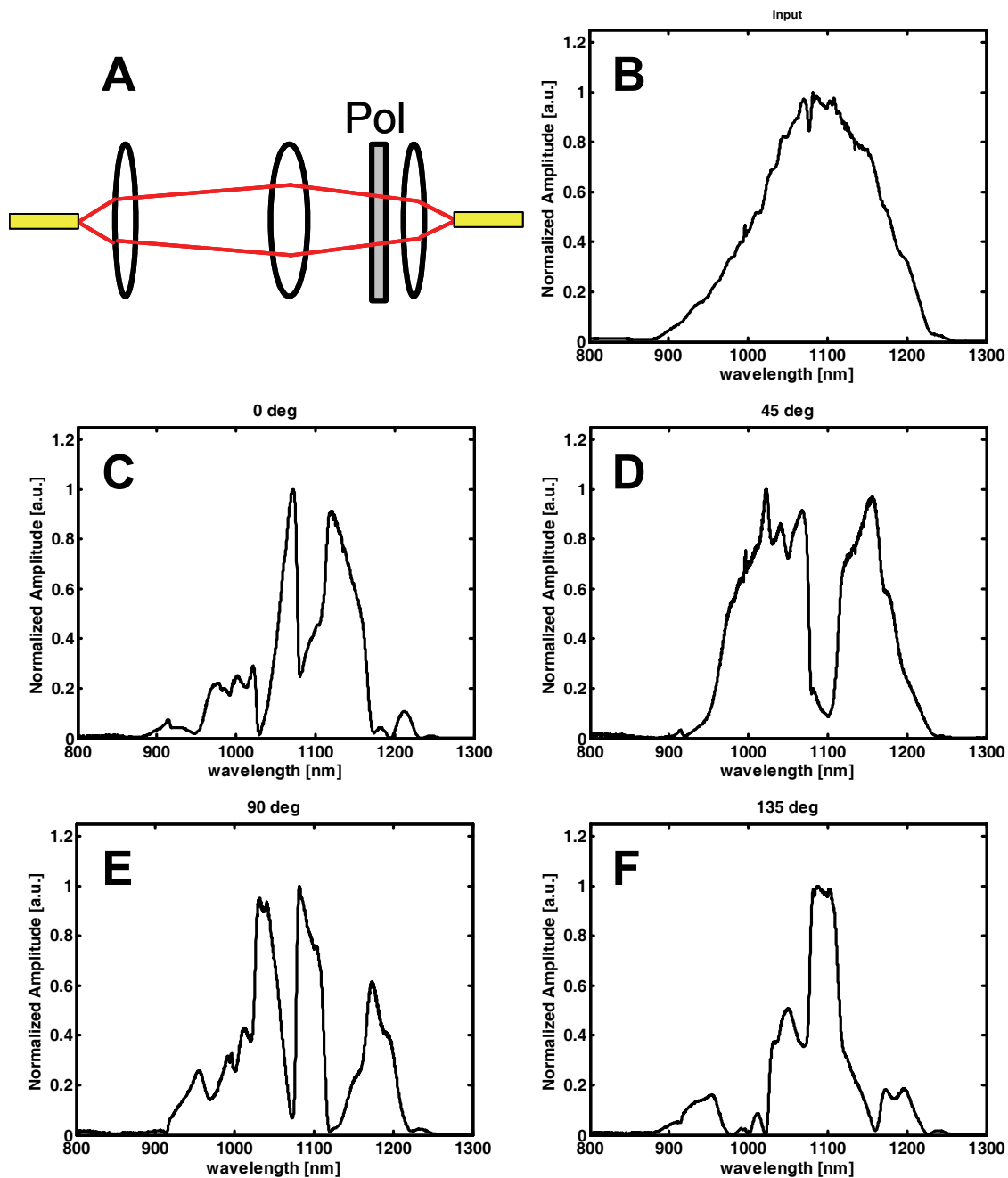


**Figure 5.8.** Wavelength-dependent polarization properties of the light source used for OCM imaging. The setup used to perform the measurements (A) consists of an air gap coupling apparatus with a polarizer inserted into the beam path. The spectral throughput of the air gap coupling is shown in (B) and the transmitted spectra for polarization states defined arbitrarily as 0, 45, 90, and 135 degrees are shown in (C), (D), (E), and (F), respectively.

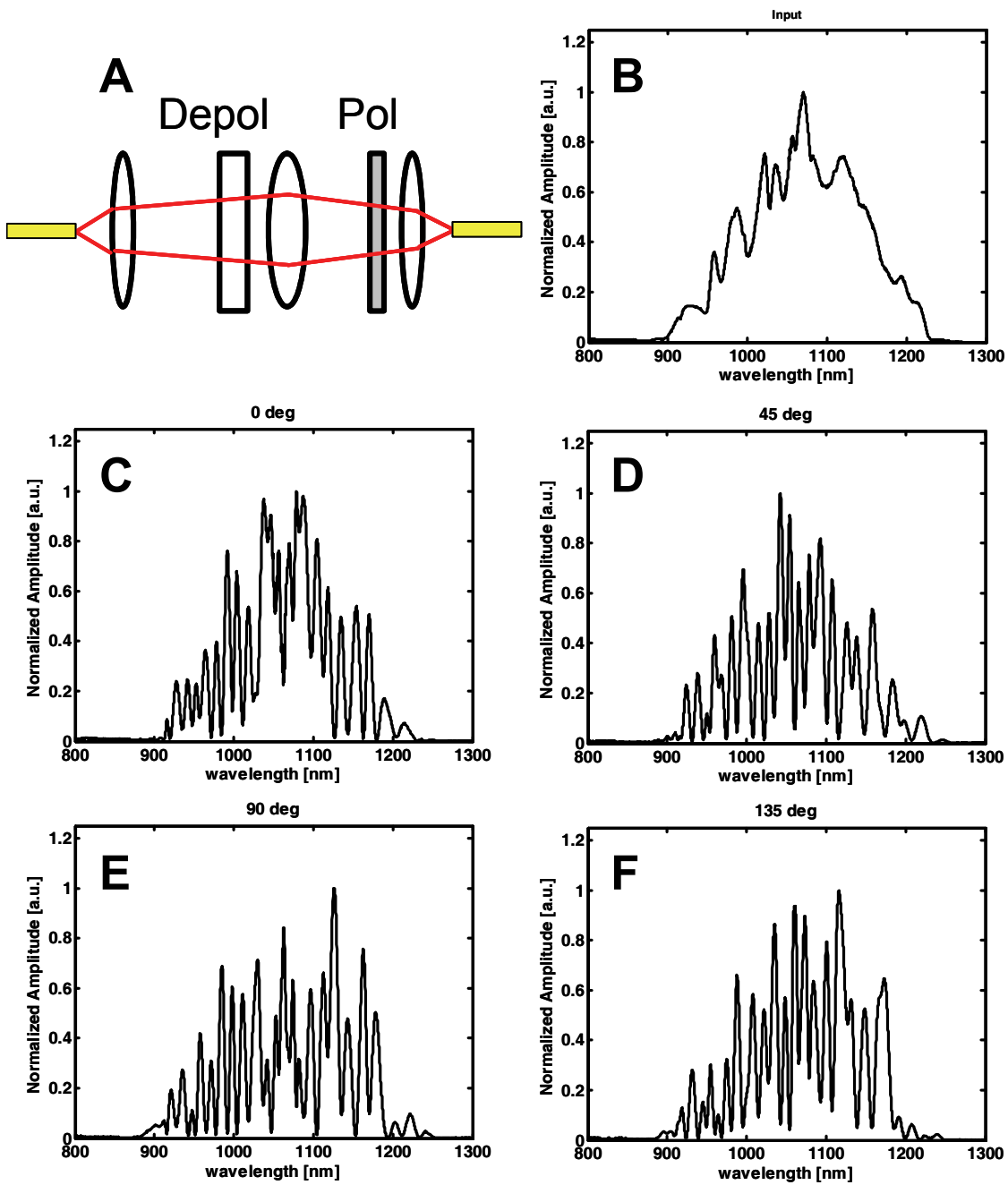
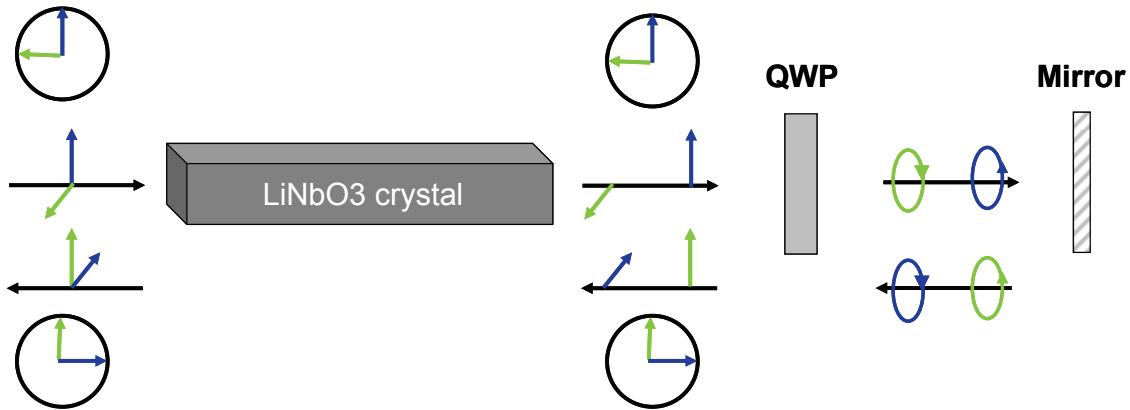
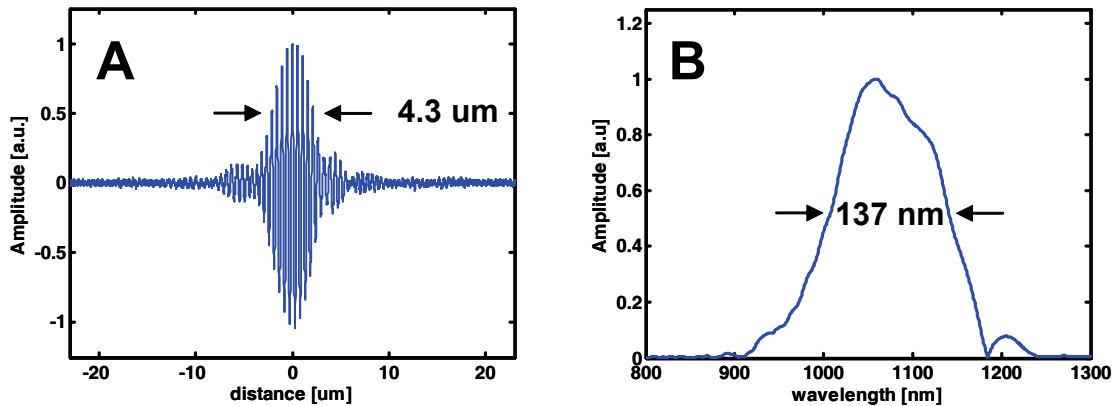


Figure 5.9. Partial depolarization of the spectrum using an achromatic plate depolarizer.

To overcome the bandwidth limitations of the Faraday rotator, a novel polarization compensation approach was developed using a quarter-wave plate (QWP) rather than a Faraday rotator. Achromatic zero order waveplates are now available with nearly constant wavelength dependent retardance over several hundred nanometers of spectrum. These waveplates are constructed by balancing the birefringence properties against the material dispersion characteristics such that uniform fractional wave retardance can be maintained. The QWP used for this study (Thorlabs AQWP05-950) maintained nearly flat spectral dependence of retardance over the wavelength range 800 nm – 1200 nm. The polarization management strategy developed using this QWP takes advantage of the fact that the modulator was fiber pigtailed using polarization-maintaining fiber with the axes of the PM fiber carefully aligned to the axes of the device. The PM fiber ensured that the polarization states of the LiNbO<sub>3</sub> crystal were maintained until the light was launched into the reference delay line. LiNbO<sub>3</sub> has a high birefringence with the ordinary and extraordinary axis indices measuring  $n_o = 2.2273$  and  $n_e = 2.1515$ , respectively. Over the 72 mm length of the crystal, this index difference between the axes lead to a walk-off between polarization states equal to about 5.45 mm. This length corresponds to a temporal group delay much larger than the coherence time of the source, which means that each polarization mode launched from the device could effectively be treated as a linearly polarized input wave to the reference arm. Placement of the QWP in the reference arm with its axes at 45 degrees to the axes of the PM fiber turned each fiber mode into a circularly polarized wave which traveled through the delay line and back to the QWP. Upon passing back through the QWP, the wave was converted to a linear polarization again, but with orientation orthogonal to its initial state. In this manner, the QWP acted to flip the input polarization modes, forcing them back through the EOM along the opposite axis. This was analogous to the operation of the Faraday rotator and ensured that all wavelengths see the modulation axis of the EOM and that the polarization walk-off introduced between orthogonal crystal axes was eliminated. As with the Faraday rotator, the EOM was driven with a sawtooth waveform with amplitude of  $2V_\pi$ . Figure 2.10 illustrates the operation of the device schematically. Note that the method did not require a specific polarization input to the PM fiber coupling into the LiNbO<sub>3</sub> modulator. The technique was insensitive to the reference arm polarization state.



**Figure 5.10.** Schematic illustration of the quarter-wave plate polarization compensation technique. An arbitrary input polarization to the EOM crystal couples to two orthogonal modes which propagate along the ordinary and extraordinary axes of the device. A large group delay walk-off occurs between the modes due to the index difference. The quarter-wave plate (QWP) is positioned at 45 degrees to the orthogonal modes such that it generates two circular polarizations. Upon passing back through the QWP, linear states are generated which are orthogonal to the input states, thereby forcing light to see both axes of the modulator. Polarization mode dispersion in the device is eliminated upon reverse propagation and all spectral components are modulated after double pass.



**Figure 5.11.** Dispersion balanced axial coherence point spread function achieved with polarization management. The axial resolution (A) measured 4.3  $\mu\text{m}$  in air, corresponding to 3.1  $\mu\text{m}$  in tissue. The Fourier transform of the point spread function (B), measures  $\sim 137$  nm in spectral full-width at half maximum

Using this polarization management scheme in combination with the dispersion management techniques described above, the maximum optical bandwidth of the light source could be supported by the EOM. Figure 5.11a presents the point spread function for the dispersion balanced EOM configuration alone, without the additional glass of the confocal microscope. An axial resolution of 4.3  $\mu\text{m}$  in air was

achieved, which corresponds to  $\sim 3.1$   $\mu\text{m}$  in tissue when scaled by an approximate tissue index of refraction of  $n = 1.38$ . The corresponding interference bandwidth determined by Fourier transforming the interference function is presented as figure 5.11b. The spectral bandwidth of 137 nm accounted for the imperfect overlap of the backcoupled reference and sample arm fields and was therefore necessarily lower than the individual limiting component bandwidth of 152 nm shown above in figure 5.4.

Further confirmation of the expected operation of the polarization management scheme was achieved by recording the heterodyne signal over a long depth scan, as presented in figure 5.12. Three main peaks are identified on the plot, corresponding to the distinct paths allowable for light passing through the modulator. Light that was properly rotated by the QWP and coupled into the orthogonal axis contributed to the center interference peak. This light traveled through both the fast and slow axes of the device. The polarization scheme was of course not perfect, however, and some of the light was coupled back into its incident path. Hence, the plot shows the presence of peaks corresponding to passage along the fast axis axis twice or the slow axis twice. Note that the outer peaks are more than 100 times lower in intensity than the main peak, which confirms that the majority of the light followed the desired path. Note also that the delay separation between the fast + fast and slow + slow peaks corresponds to the optical path difference due to the index of refraction difference  $n_o - n_e$ , which was calculated earlier to be  $\sim 5.45$  mm. As expected, the center lobe point spread function was found to be insensitive to the reference arm input polarization state while the two outer peaks were exquisitely sensitive to it. The dispersion along the three optical paths was also obviously different, as evidenced by the relative widths of the peaks. A similar three-peak profile was observed with the Faraday rotator as well. Several smaller peaks are also evident on the depth scan profile. These peaks are believed to be due to slight mismatch between the axes of the polarization maintaining fiber and the axes of the LiNbO<sub>3</sub> crystal, which causes cross-coupling artifacts. The artifacts were relatively weak in amplitude, however, and were all located at least 200  $\mu\text{m}$  away from the peak. They therefore did not affect OCM image quality.

When using the QWP polarization compensation method, a polarization-dependent image artifact was generated. The precise etiology of the signal was not fully understood, but it was believed to be related to either a self-interfering reflection or to interference between cross-coupling components of the PM fiber axes. The artifact showed up with the characteristic frequency of the modulator drive waveform and vanished when the modulator was not driven. It did not present a problem for imaging, however, since it could be very easily and stably suppressed to beyond the dynamic range of the system using adjustment of the source input polarization to the OCM imaging system. This was the primary reason for the presence of the three paddle polarization controller on the input lead of the fiber optic coupler.

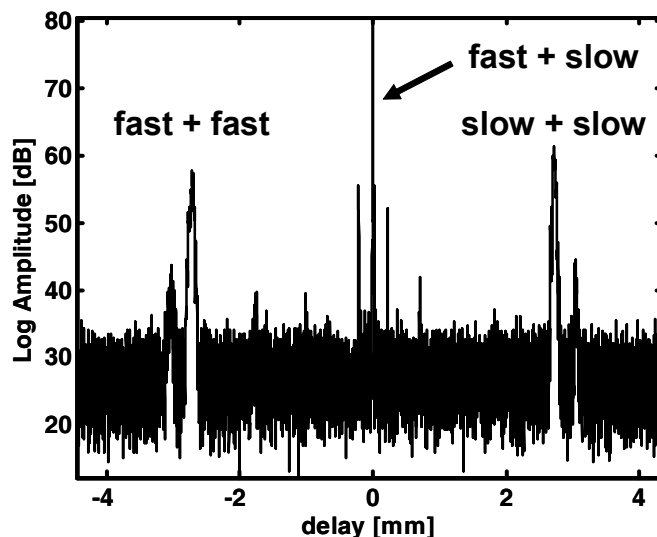


**Figure 5.12.** Long delay scan illustrating the heterodyne signal components generated by the reference arm modulator. Three distinct peaks demonstrate optical paths which include forward and reverse passage through slow + slow axis, fast + slow axes, or slow + slow axes. The majority of the intensity is located in the fast + slow central peak, thereby confirming that the polarization management technique is working as expected.

#### 5.3.4 Performance Characterization

Figure 5.13 presents the resolution characterization for the full OCM instrument. Figure 5.13a displays an image of the standard 1951 USAF calibration target. The smallest elements on the target, measuring 2.2  $\mu\text{m}$  in width with a periodicity of 4.4  $\mu\text{m}$  were clearly visualized. Assuming a Gaussian intensity distribution, the  $1/e^2$  focal spot diameter was measured from the 10-90% width of an edge scan to be 1.08  $\mu\text{m}$ . Moreover, the measured spot diameter over a field of view of 400 x 400  $\mu\text{m}$  did not exceed 1.41  $\mu\text{m}$ . The microscope confocal parameter was measured by translating a mirror through the focal plane and recording the backcoupled intensity. The result is shown in figure 5.13b to be 19  $\mu\text{m}$  full-width-at-half-maximum, which corresponds to a minimum effective numerical aperture of approximately 0.32. Optical aberration clearly degraded the axial response, as evidenced by the long tail extending from the central lobe. Chromatic aberration was likely an important contributing factor since the microscope objective was designed for visible wavelengths rather than the near-infrared imaging wavelength used in this study. The measured coherence gate for the full dispersion balanced OCM system, including the confocal microscope, is also provided in figure 5.13b. The response measured 3.7  $\mu\text{m}$  with water immersion, which is close to the value that would be achieved in tissue. Figure 5.13b clearly illustrates the operating limit for this OCM instrument. The coherence gate provided the dominant axial sectioning, while a relatively relaxed confocal gate provided a window within which the coherence gate operated.

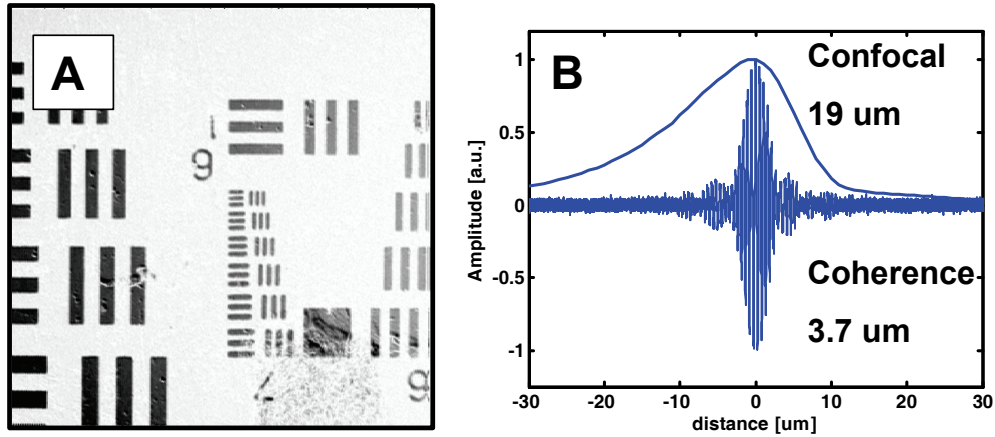


**Figure 5.13.** Resolution characterization for the OCM instrument. High lateral resolution of  $< 2 \mu\text{m}$  is demonstrated through visualization of the smallest elements on the 1951 USAF resolution target (A). The overlapped confocal and coherence gates demonstrate that the dominant axial sectioning is provided by the coherence gate (B).

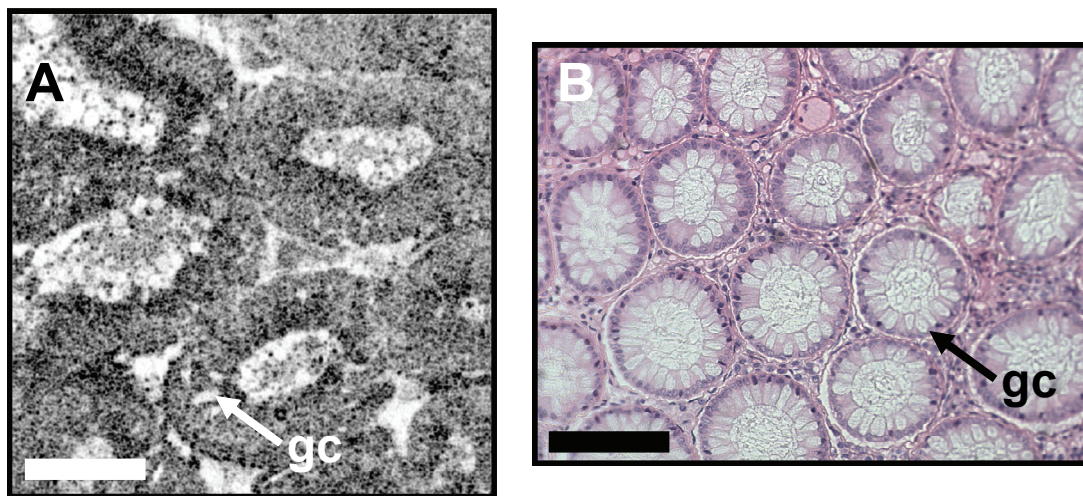


**Figure 5.14.** *Ex vivo* OCM image of human colon with corresponding histology. The OCM image (A) clearly delineates crypt architecture as well as individual goblet cells (gc) in the crypt epithelium. Correspondence with representative histology demonstrates the ability for OCM to perform high resolution imaging without the need for specimen processing (B). Scale bars,  $100 \mu\text{m}$ . Histology is shown at the same scale as the OCM image and exhibits the effects of tissue shrinkage with processing.

The system sensitivity was measured by computing the square of the image amplitude from a mirror with a calibrated attenuator in the sample arm and dividing it by the variance of the noise. The noise variance was computed over an image with the sample arm completely blocked. For approximately  $10 \text{ mW}$  sample power and  $350 \text{ kHz}$  detection bandwidth, the sensitivity measured  $98 \text{ dB}$ . Such high detection sensitivity allowed excellent image quality in scattering tissues. Figure 5.14a presents an

example *ex vivo* image of human colon demonstrating typical image quality. The image was acquired in 0.5 seconds at a depth of 75  $\mu\text{m}$  below the tissue surface. The field of view measured 400  $\mu\text{m}$  x 400  $\mu\text{m}$  and the image contained 500 x 500 pixels. Images provide high contrast between the round crypts and the inner mucous containing crypt lumens, and individual goblet cells are visible within the epithelium. The loose connective tissue lamina propria surrounding the crypts can also be clearly delineated. Representative hematoxylin and eosin stained histology from the same specimen is provided for comparison in figure 5.14b.

#### 5.4 Image Autofocusing

Axial resolution in optical coherence microscopy is determined by the multiplicative effect of the confocal and coherence gates. This has advantages in that it can provide stronger rejection of out of focus scattered light than either gate alone, but it also creates the unique challenge of ensuring that the gates precisely overlap during imaging. As shown by equation 4.9 in the previous chapter, the position of the confocal gate is determined by the position of the focus in the sample while the position of the coherence gate is determined by the relative path length difference between reference and sample arms. As described in the previous chapter, index of refraction differences between air and tissue and within tissue itself, as well as thermal or mechanical perturbations of the optical fiber interferometer can create relative optical path length shifts that cause the coherence and confocal gates to misalign. Gate mismatch effects are most pronounced when both the confocal and coherence gates are very small. For example, use of a gates that are both  $\sim 5 \mu\text{m}$  in width may provide strong optical sectioning but it also makes the signal intensity subject to relative path length fluctuations on the order of 5 – 10  $\mu\text{m}$  or so. The sensitivity to gate mismatch can be reduced by relaxing one of the gates, effectively enlarging the overlap region. Figure 5.13b illustrates this scenario. The larger confocal axial response provides some depth of field over which the coherence gate can operate. Use of water immersion objective lenses also limits the walk-off between the gates when focusing into tissue. For dry objective lenses, however, the coherence and confocal gates will require constant adjustment when changing depth in tissue. Moreover, with the use of fiber-optic catheters or handheld microscopes, the twisting and stretching of the optical fiber will introduce path length shifts that can misalign the gates. Hence, a well-designed OCM system for general use must provide a means for adjustment of the coherence gate to the precise location of the confocal gate in tissue. In essence, this is equivalent to focusing the OCM image.

Most investigators previously have utilized a slow translation stage and have optimized image intensity by manually setting the path length. This process is slow and relatively imprecise and therefore not suitable for high speed *in vivo* imaging. A more appropriate solution would involve an automated adjustment of the coherence gate that can be performed rapidly during real time imaging in a manner

analogous to autofocusing functions on modern digital cameras, camcorders, or light microscopes. Two general types of autofocusing have been implemented in microscopes and cameras. Active autofocusing strategies use a ranging scheme based on ultrasound or infrared light to determine the distance of the object from the lens and adjust the lens position accordingly to bring the object to focus. Passive autofocusing schemes, on the other hand, utilize iterative image processing algorithms to optimize image quality while adjusting the focus in a feedback manner. Metrics such as image sharpness or spatial frequency content are rapidly computed to allow real time focusing [25]. As described previously, the OCM system design described in this chapter included the option for rapid depth adjustment using a linear-scanning galvanometer located in the reference path. This enabled implementation of autofocusing strategies to coordinate the positions of the confocal and coherence gates.

One feasible strategy for OCM is the use of a passive autofocusing scheme where the *en face* image sharpness is optimized while iteratively adjusting the reference path length. Another approach, which is more directly similar to active autofocusing, would be to use the path scanner to perform coherence depth ranging as is done in cross-sectional OCT imaging. This method can be significantly faster than the passive approach because it allows direct location of the position of the confocal gate without iterative acquisition of multiple image frames. Figure 5.15 illustrates the principle. In 5.15a, the depth scanner in the OCM system was used to acquire a lateral priority OCT image, with the lateral scan provided by the fast axis scanner in the confocal microscope. An average depth profile for the image was subsequently generated by averaging all transverse image lines. Averaging of adjacent lines eliminated the effects of scattering inhomogeneities, which could lead to inaccurate estimation of the actual focal position in tissue. This type of depth profile effectively provides a measure of the confocal axial response in the scattering medium. Figures 5.15c-e provide images acquired at different positions of the coherence gate relative to the confocal gate. The in-focus image in 5.15d was generated with the confocal and coherence gates exactly matched. The image in 5.15c was taken at 30  $\mu\text{m}$  above the focal plane, while that in 5.15e was acquired at 30  $\mu\text{m}$  below the focal plane. These out-of-focus images exhibit lower contrast and poorer resolution compared to the in-focus image, as shown in the corresponding zoom views in figures 5.15f-h. The relative positions of the three images are shown on the depth profile in figure 5.15b.

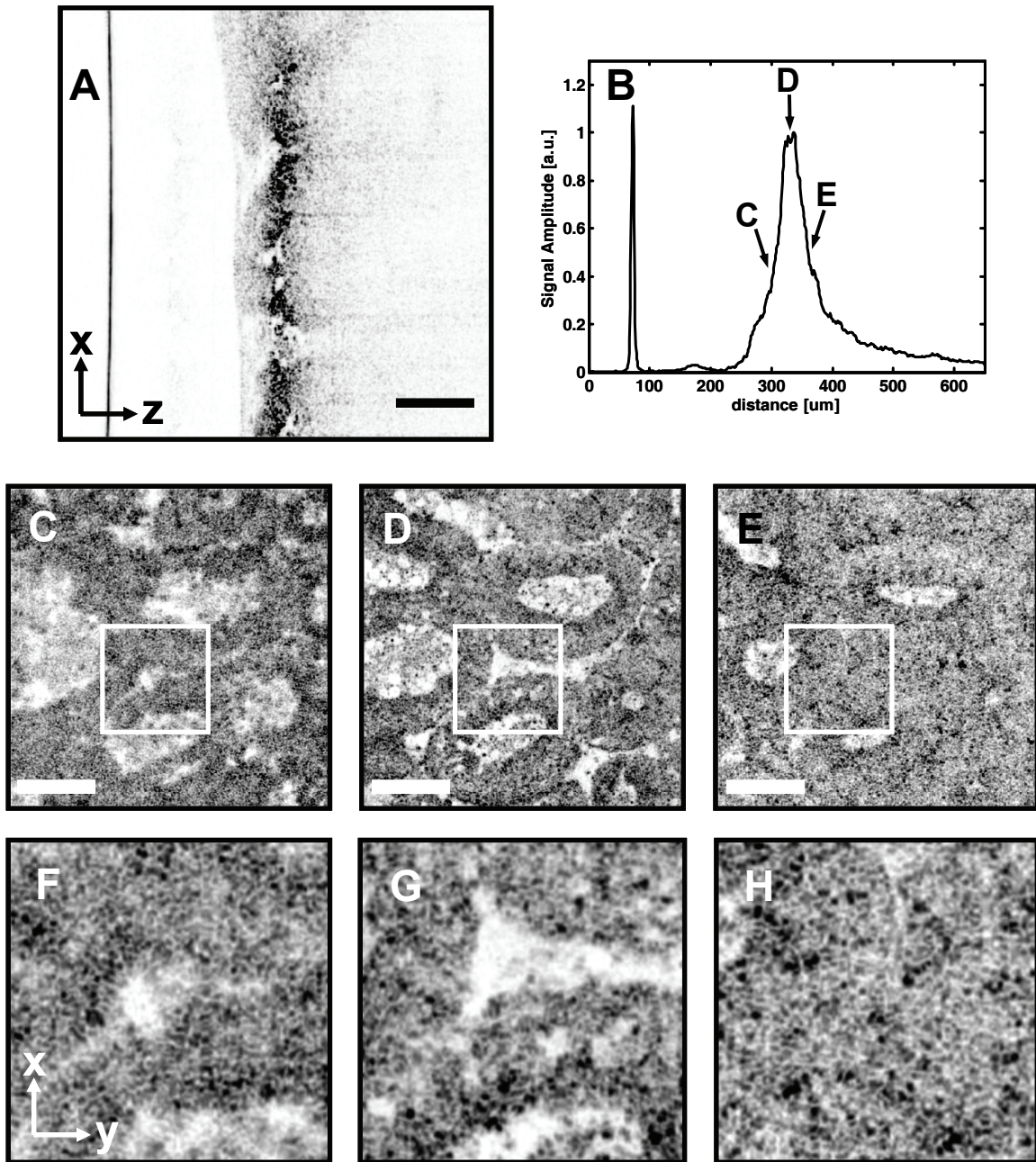


**Figure 5.15.** Measurement of confocal gate position in scattering tissue using coherence ranging. The OCM depth scanner was used to acquire a lateral priority cross-sectional image, which clearly shows the restricted depth of field resulting from high NA focusing (A). Averaging across lateral scans produced an average depth response, which is a measure of the confocal axial response in scattering tissue (B). Images obtained with the coherence and confocal gates misaligned (C,F and E,H) appear out of focus compared to the image obtained with the gates precisely aligned (D,G). Scale bars, 100  $\mu\text{m}$ .

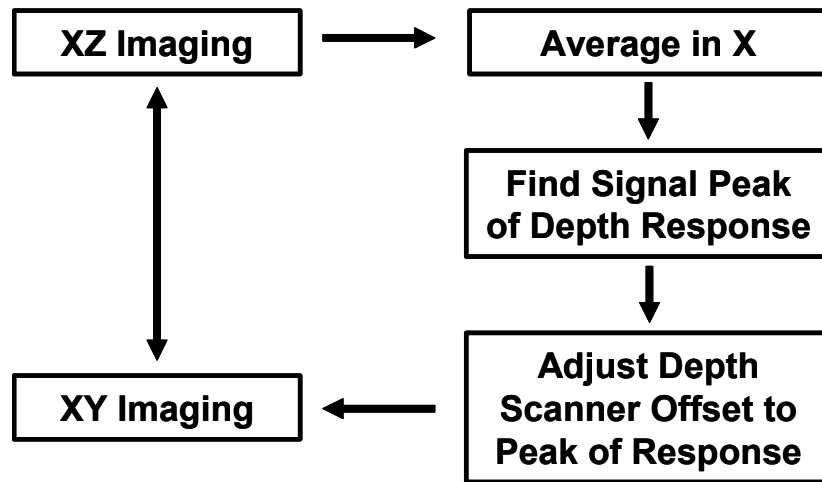


**Figure 5.16.** Algorithm for fast autofocusing in scattering tissues.

An autofocusing algorithm was developed based on the use of lateral-priority cross-sectional images to locate the confocal focus. The algorithm was implemented in the OCM imaging software and allowed for rapid image optimization during real-time display. Figure 5.16 presents the algorithm schematically. The user had the option to flip between *en face* XY imaging and cross-sectional XZ imaging modes. This was useful in itself in allowing the user to rapidly assess the imaging depth in scattering tissue. Autofocusing could be initiated from either XZ or XY imaging mode. During autofocusing, a single XZ cross-sectional image was generated and the average depth profile computed. The offset to the reference arm depth scanner was then adjusted to coordinate the position of the coherence and confocal gates. After adjustment, the software returned to the *en face* imaging mode. The algorithm was fast and required only a single frame loss from the *en face* imaging stream. Moreover, the software interface was user-friendly and greatly simplified the imaging protocol compared to previous OCM imaging systems which required imprecise manual optimization of the reference arm path.

## 5.5 Image Processing and Display

As mentioned previously, minimal image processing was performed during real-time imaging to allow for high speed acquisition and real-time display. Images were demodulated using a fast boxcar averaging algorithm and image compression and gray-level adjustments were applied. As has been pointed out previously with real-time confocal microscopy [26], *in vivo* OCM images viewed during real-time acquisition appeared of higher quality than individual still frames viewed offline. This is due in part to the fact that the human visual system effectively integrates several frames, giving the impression of improved signal to noise. In addition, the viewer has the ability to visually track features in the images *in vivo*, which improves discrimination of the actual features from image degrading coherent speckle noise.

For offline processing, a more rigorous image processing approach was taken to optimize image quality. The raw image lines were first digitally bandpass filtered to remove excess noise outside of the signal bandwidth. The image data was then demodulated from the carrier frequency using a precise Hilbert transform algorithm based on the fast Fourier transform. Next, a spline resampling algorithm (Matlab, *interp1* spline function) was applied to correct for nonlinearity between adjacent lines generated by bidirectional scanning. The images were also resampled to the correct aspect ratio. Following resampling, a slight spatial filter with 3x3 pixel triangle kernel (Matlab, *filter2* function) was applied to reduce the prominence of speckle effects. Finally, image compression and contrast enhancement were implemented and the images were written to JPEG format with an inverse grayscale colormap.

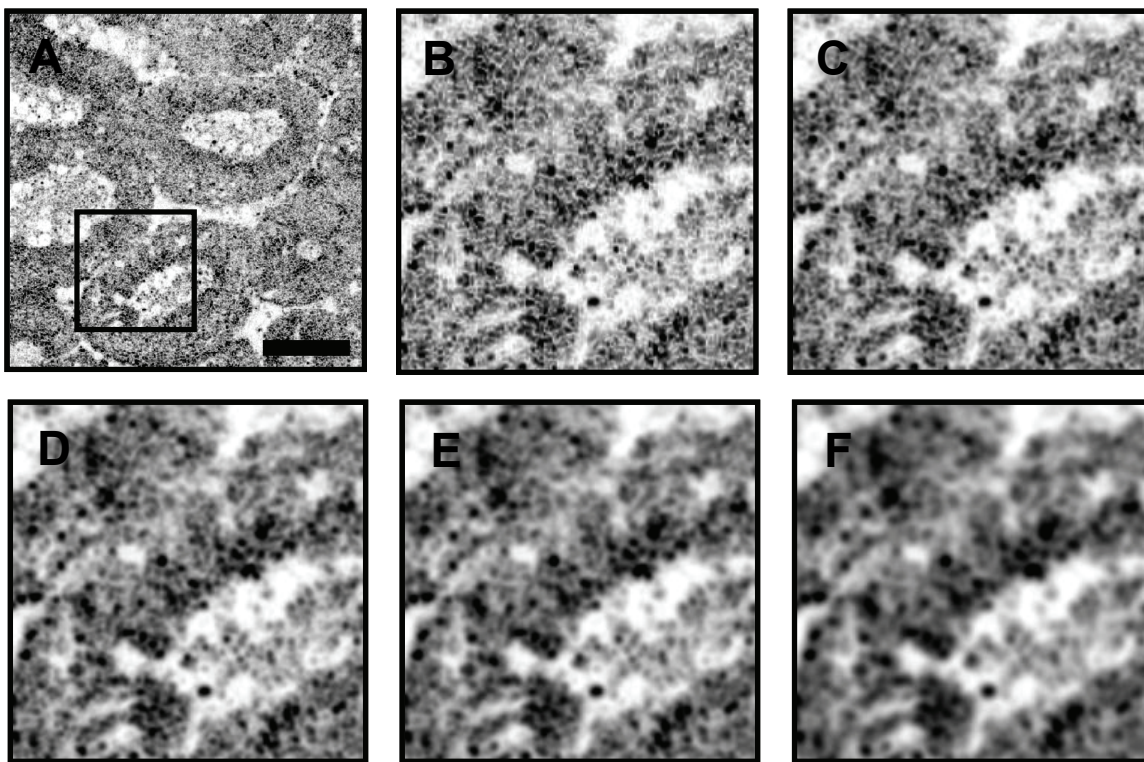


**Figure 5.17.** Comparison of spatial filters for OCM images. Images (B-F) correspond to the boxed region in (A). The unfiltered images (A,B) show the presence of speckle in the OCM images. Iterative application of a 3x3 spatial filter with a triangular kernel reduces speckle at the cost of transverse image resolution. Images (C,D,E, and F) correspond to 1, 3, 5, and 10 applications of the filter, respectively. Scale bar in (A), 100  $\mu\text{m}$ .

Coherent speckle is a well known phenomenon in laser-based imaging modalities, including OCT, as well as in other coherent imaging methods such as ultrasound [27, 28]. Speckle results from interference between mutually coherent waves scattered from tissue microstructure. The speckle pattern carries information about tissue microstructure, and has been investigated for biological diagnostics in certain

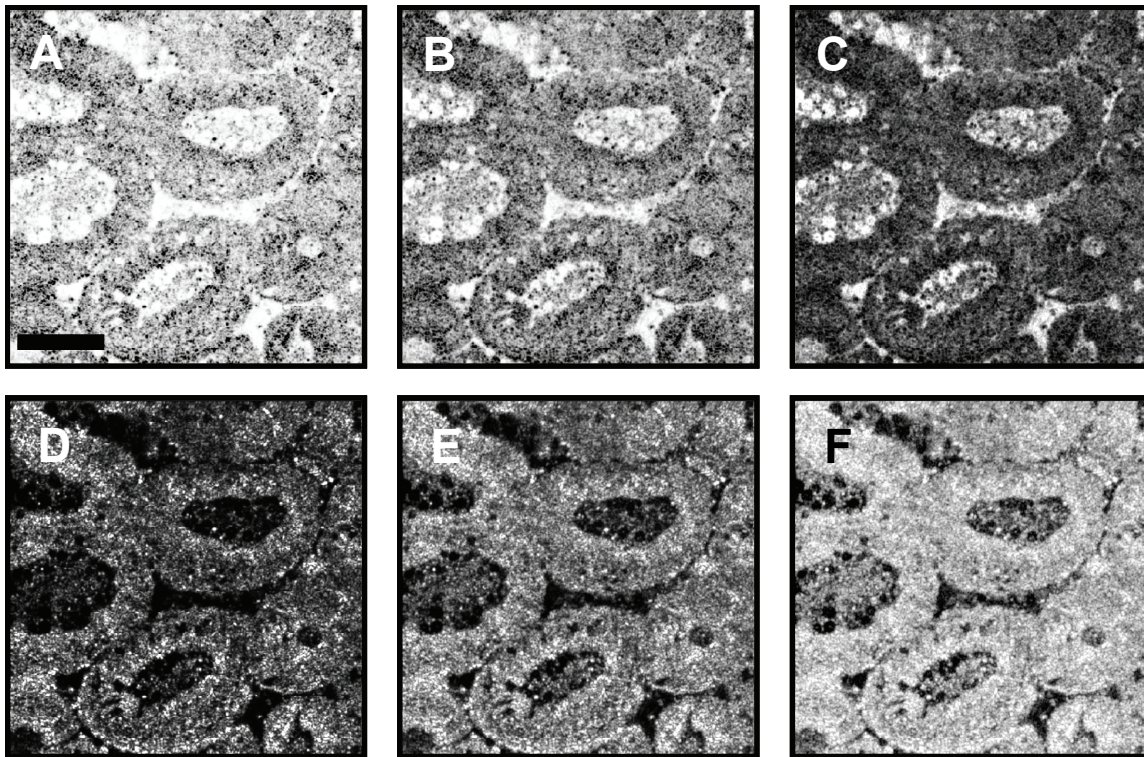
applications [29-31]. For structural imaging, however, speckle is largely a form of image degrading noise and acts to reduce contrast between small scale structures. Speckle in the OCM images is evident by the grainy or mottled appearance of the images and leads to reduction on the effective image resolution. Speckle reduction has been approached in confocal microscopy for *in vivo* cellular imaging applications. The video-rate confocal microscope demonstrated by Rajadhyaksha and colleagues, for example, uses a pinhole detector diameter which is larger than the ideal size for detection of singly-scattered light [32]. The larger pinhole effectively provides multimode detection in the microscope, which reduces speckle and gives higher signal intensity at the cost of slightly reduced axial resolution. The same group employs 3x3 spatial filtering to further smooth the speckle. While multimode detection is not possible in OCM because of the interferometric nature of the technique, spatial filtering is a viable option and has been employed for the work in this thesis. Several additional speckle reduction techniques have been investigated for OCT imaging, including angle compounding [33-35], frequency compounding [36], polarization diversity receivers [37], and novel image processing algorithms [38-40]. Further study of these strategies for OCM imaging is promising.

Several spatial filters were compared for OCM images, including the boxcar filter, median filter, and triangular filter kernels. These well known spatial filter functions were implemented in Matlab using the *medfilt* and *filter2* commands. Each gave reasonable results, although the median and triangular filters produced slightly better looking images. The triangle kernel was selected because of the precedent for its use with confocal images [26]. Figure 5.17 presents the results of filtering using the triangle filter. Images in 5.17a and 5.17b are unfiltered, with 5.17b corresponding to a 3x enlargement of the boxed area of 5.17a. The grainy speckle pattern is readily evident. Figure 5.17c shows the image from 5.17b after application of the triangular filter once. The speckle pattern is slightly blurred with very little visible degradation of image resolution. Images in figure 5.17d, 5.17e, and 5.17f correspond to 3, 5, and 10 applications, respectively, of the 3x3 triangular filter. The speckle pattern is increasingly removed from the images, but with progressively more loss in transverse resolution. Through comparison of images from many tissue types, it was determined that a single application of the filter was the best compromise between speckle reduction and resolution loss.

For this thesis, OCM images are displayed on a negative grayscale colormap with black representing high signal and white representing low signal. This is consistent with the colormap used in the literature for the majority of published OCT images in scattering tissues but inconsistent with the colormap widely used in confocal microscopy and ultrasound. These modalities typically display images on a positive grayscale map with white representing high scattering and black representing low scattering. To first order, one would expect that features would be equally visible on either colormap [41]. However, it was observed in viewing the OCM images that negative contrast improved the appreciation of low scattering,

fine features compared to positive contrast. In addition, the use of negative contrast provided a more direct analogy to histology, which is typically viewed in backlit transmission mode with a light microscope.

A remaining issue in display is that of dynamic range compression. A grayscale colormap has only 256 levels, which corresponds to a dynamic range of 55 dB. An image with greater dynamic range than 55 dB cannot be displayed without clipping high or low values unless some form of compression is used. OCT images typically use log compression because these images can have very large dynamic range due to exponential extinction of light with depth into tissue. *En face* OCM images have lower average dynamic range because they display structure from a uniform depth and therefore do not show the exponential extinction of the signal seen in cross-sectional images. Nonetheless, when using negative contrast display, uncompressed images appeared white saturated. On the other extreme, use of log compression tended to overcompress the black end of the colormap, obscuring fine features. As a compromise, square-root compression was used for image display in this thesis.



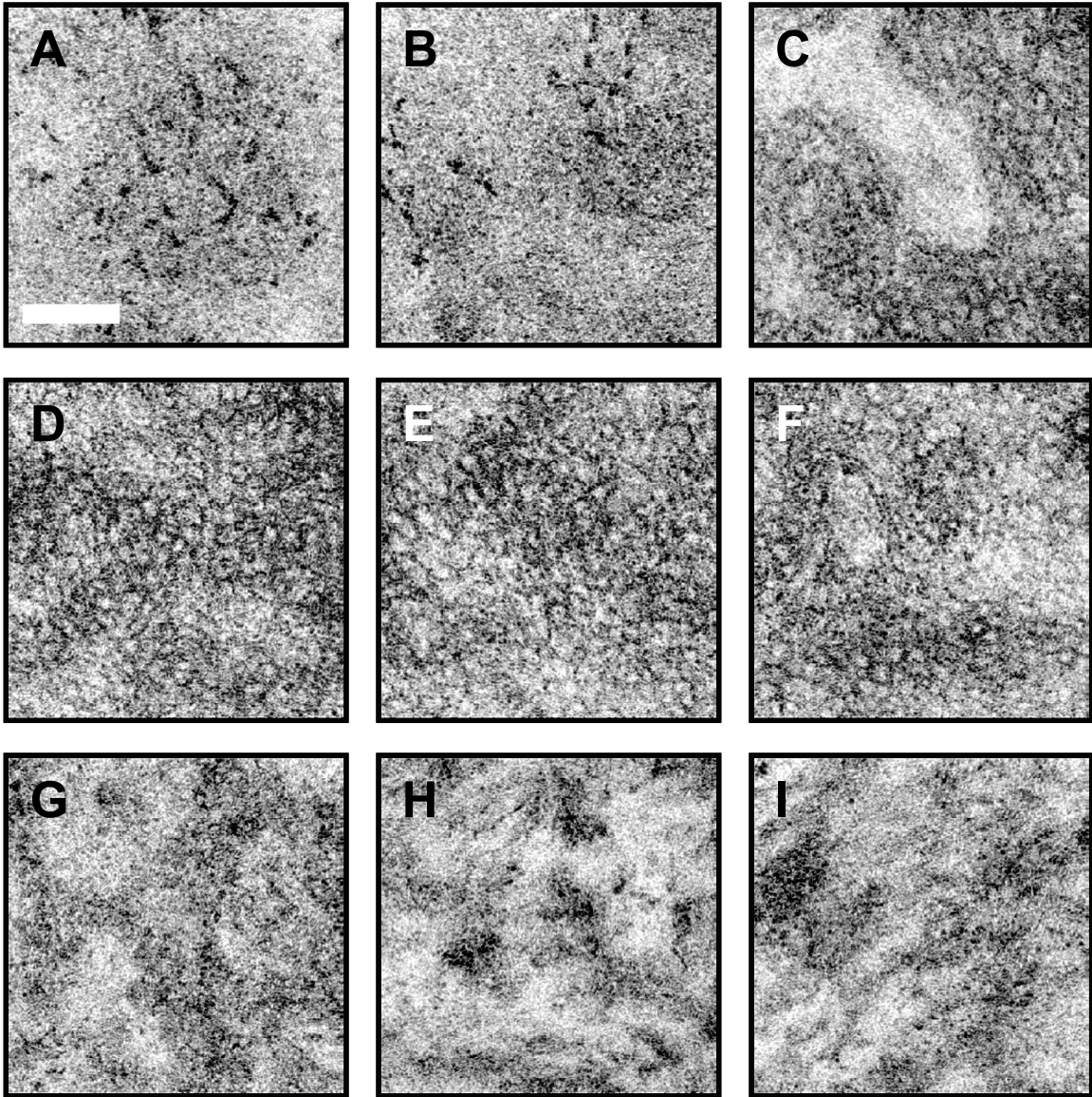
**Figure 5.18.** Comparison of image compression and colormap options. Images A,B and C use an inverse grayscale map with black representing high signal while images D,E, and F use a grayscale map with white corresponding to high signal. Dynamic range compression is provided by square-root (B,E) and log (C,F) display. The uncompressed images are shown in A and D. Scale bar, 100  $\mu\text{m}$ .

Figure 5.18 compares forms of dynamic range compression for both positive and negative contrast. The compression function, sqrt or log, was applied directly to the image signal and the subsequent image was normalized to its maximum intensity. Contrast enhancement was then applied by stretching the gray levels over the range between 1% and 99% of the image histogram. Interestingly, the uncompressed positive contrast images appeared of higher quality than the uncompressed negative contrast images. This supports the notion that the visual system is more sensitive to negative contrast compared to positive contrast. Reduced sensitivity to positive contrast effectively acts to compress the perceived image range. This is an important point to consider when making direct comparisons between OCM and confocal images, since confocal images are typically displayed on an uncompressed positive grayscale map. For the most direct comparison, it would be important to use the same colormap and relative compression.

## 5.6 *In Vivo* Cellular Imaging Results

To demonstrate the capability to the OCM system for high speed, *in vivo* cellular imaging, images of normal human skin were acquired from healthy volunteers. Informed consent was acquired from the volunteers in accordance with approved protocol on file with the Committee on the Use of Humans as Experimental Subjects (COUHES) at the Massachusetts Institute of Technology. Imaging was conducted in the nailfold region of the index finger and on the ventral forearm using a coverslip and water immersion. A ring and template device similar in principal to those used previously for confocal microscopy was used to provide some stabilization of the area being imaged. Images were acquired at 5 frames per second using an image line rate of 2.5 kHz and pixel sampling of 500 x 500 pixels across a field of view of 350  $\mu\text{m}$  x 350  $\mu\text{m}$ . Sample power measured approximately 10 mW at the tissue surface.

Figure 5.19 presents representative imaging results from the nailfold region. The nailfold is a relatively thick region of skin compared to the ventral forearm and was selected here to illustrate the imaging depth ability of the OCM system. A progression through the various layers of the skin is shown, beginning with the uppermost layer of stratum corneum, shown in figures 5.19a thru 5.19c. The junction between the stratum corneum and the epidermis can be readily appreciated in figure 5.19c. Within the stratum corneum, thin fragments of highly scattering corneocytes can be seen. Squamous cells in the epidermis are readily visualized in the images of figures 5.19d thru 5.19f. The cells have strongly scattering borders, and the nuclei do not regularly show up. Ridges marking the transition between the epidermis and the papillary dermis can be appreciated in figures 5.19f and 5.19g, while heterogeneous structure deep into the dermis is pictured in figures 5.19h and 5.19i. The progression of cells was acquired over a depth range spanning from the surface to approximately 400  $\mu\text{m}$  below the surface. In general, image quality compares well with published results using reflectance confocal microscopy.



**Figure 5.19.** *In vivo* OCM images of human skin. A progression is shown from the stratum corneum (A-C) thru the epidermis (D-F) and into the dermis (G-I). The transition regions between the stratum corneum and the epidermis and between the epidermis and the dermis can be appreciated in (C) and (G), respectively. Scale bar, 100  $\mu\text{m}$ , pertains to all images. Approximate image depths: (A,B) 50-100  $\mu\text{m}$ , (C) 175  $\mu\text{m}$ , (D-F) 200 – 250  $\mu\text{m}$ , (G-I) 300 – 400  $\mu\text{m}$ .

## 5.7 Integrated OCM and OCT Clinical Imaging System

One goal of the subsequent studies presented in this thesis was to compare and contrast the ability of OCM and ultrahigh resolution OCT to image tissue microstructure at the architectural and cellular levels. This required development of an integrated OCT and OCM system capable of co-registered imaging of the same tissue sample. Furthermore, for application in clinical imaging studies, the system design was required to be portable. The ability to operate the instrument reliably outside of the optics laboratory enables a host of experiments which are not possible otherwise. These include *in vivo* patient imaging studies as well as *ex vivo* studies of sensitive clinical specimens that cannot be removed from the hospital. The OCM system described in this chapter and the OCT system discussed in chapter 3 both had features that made them amenable to integration into a portable unit. Both used the commercially-available Nd:Glass laser source, which was compact and performed reliably under a variety of environmental conditions. In addition, these systems were largely fiber-optic in nature and therefore required only minimal realignment after transportation outside of the laboratory. Finally, the software user interface provided centralized computer control of the majority of adjustments required during imaging. This enabled the individual components to be installed in a compact enclosure without the need for frequent access to make adjustments.

For portability, the femtosecond laser source was mounted on a compact optical breadboard and enclosed by a fiberglass box. Figure 5.20a shows a photograph of the laser and controller. The breadboard contained the laser head as well as a pair of turning mirrors and a high precision, three axis translation stage for fiber coupling. A combined OCT/OCM microscope was also constructed on a compact breadboard, as shown in the photo in figure 5.20b. The breadboard containing the microscope optics was mounted vertically on a second breadboard containing a three-axis stage for *ex vivo* tissue samples. Fiber optic collimators from both the OCT system and the OCM system were present and the system input could be switched using a flip mirror. Likewise, a green aiming beam could be added to the beam path through a flip mirror also. The OCT and OCM sample arms shared the same scanners and intermediate optics as depicted in figure 5.2. Low and high magnification lenses were mounted on an objective turret to accommodate both OCT and OCM. OCT imaging was performed using a 25 mm focal length near-infrared achromat doublet as the objective lens (Edmund Optics NT45-793), which produced a  $1/e^2$  diameter transverse resolution of 14  $\mu\text{m}$ .

The OCM and OCT imaging engines were integrated into portable instrument carts as shown in figure 5.21. The OCM cart housed the interferometer, photodiode receiver, and the reference arm delay unit, as well as power supplies and controller cards for the galvanometers and the translation stage controller. The OCT cart housed a second interferometer and receiver, the high speed rotating delay line (Lightlab),

power supplies, and the data acquisition computer. Light from the Nd:Glass laser was split between the systems using a 3 dB coupler, with each system receiving approximately 45 - 50 mW of power. The imaging specifications for the integrated system are provided in table 5.2. The combined OCT and OCM system provided high resolution two and three-dimensional imaging over multiple fields of view and allowed investigation of clinical specimens at both the tissue architectural and cellular levels.

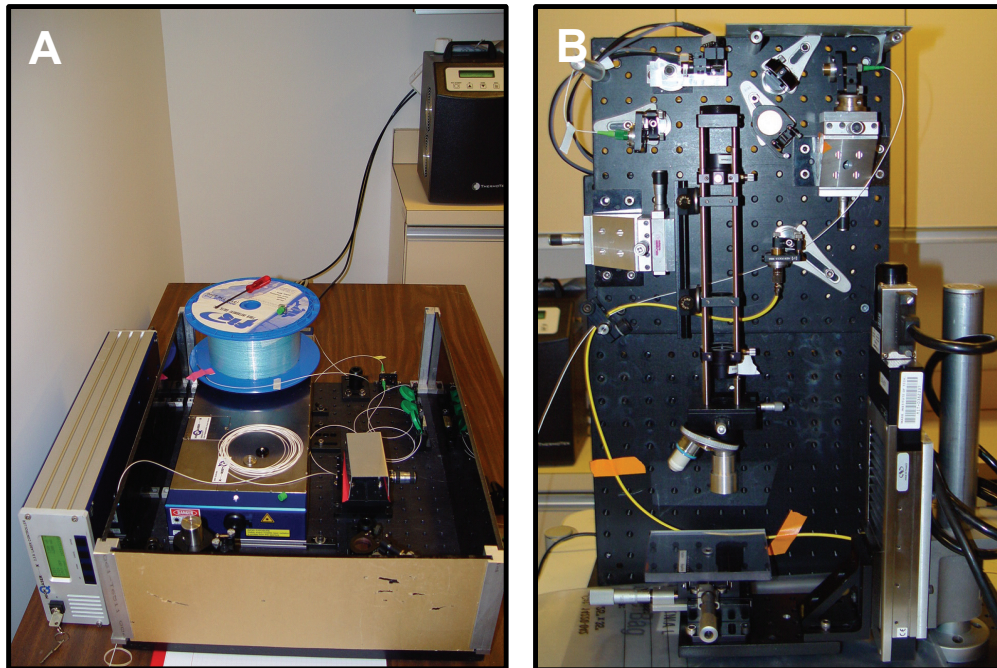


**Figure 5.20.** Photographs of the compact Nd:Glass light source and the portable OCT/OCM microscope. The Nd:Glass laser and nonlinear fiber are mounted together on a breadboard and enclosed in a fiberglass box (A). The portable microscope (B) combines OCT and OCM inputs into a single optical beam path with variable objective lens magnification.

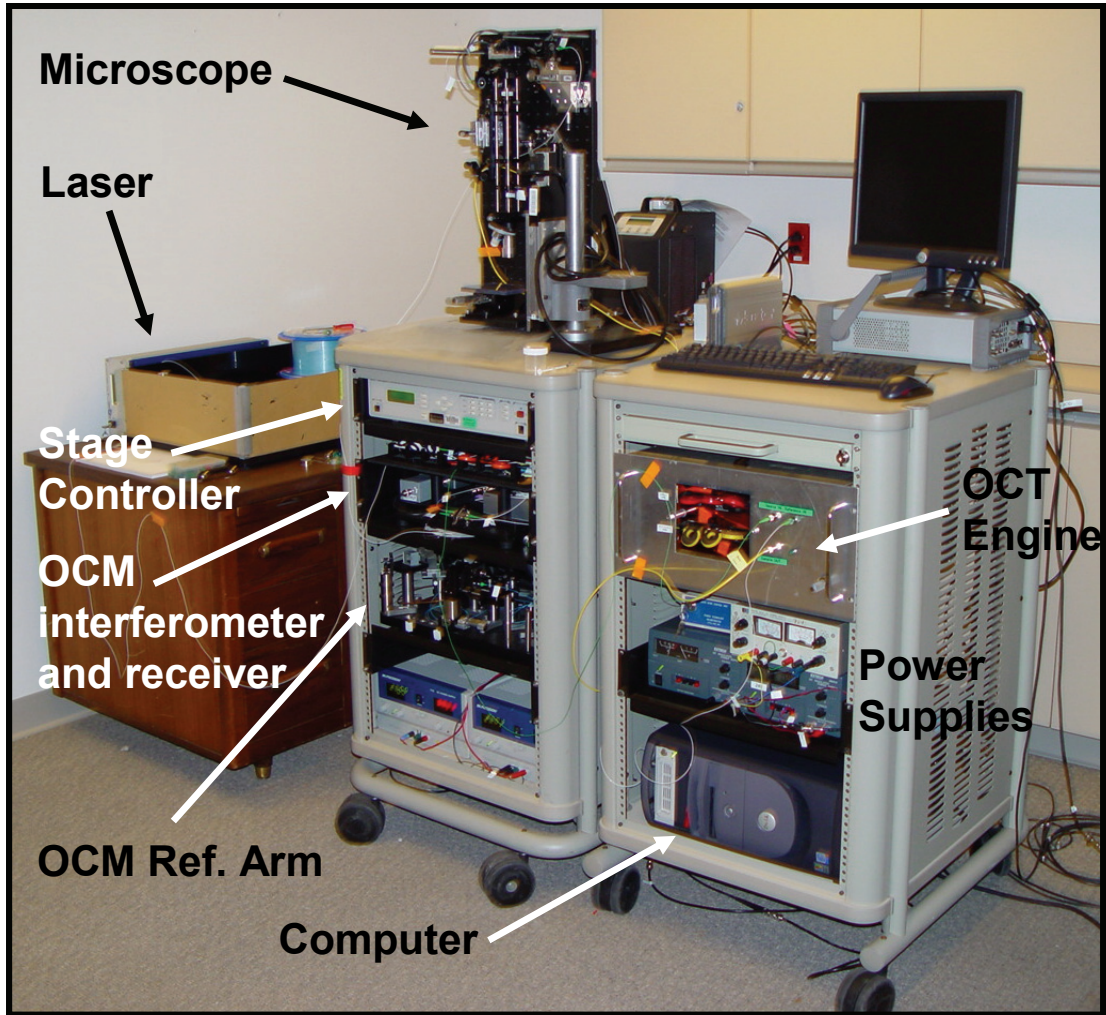


**Figure 5.21.** Photograph of the integrated OCT and OCM portable imaging systems. The photograph was taken of the system installed at the clinical pathology department at the Beth Israel Deaconess Medical Center in Boston Massachusetts.

Specification	OCT	OCM
Light Source	$\lambda_c = 1060 \text{ nm}$ , $\Delta\lambda = 210 \text{ nm}$ , $P_{\text{out}} = 105 \text{ mW}$	
Image Acquisition	Cross-Sectional or Three-Dimensional	<i>En Face</i>
Sample Power	> 16 mW	> 10 mW
Sensitivity	98 dB	98 dB
Axial Resolution (in Tissue)	2.9 $\mu\text{m}$	3.7 $\mu\text{m}$
Lateral Resolution (2w)	14 $\mu\text{m}$	2 $\mu\text{m}$
Field of View	3 mm x 1.45 mm	400 $\mu\text{m}$ x 400 $\mu\text{m}$
Imaging Speed	Up to 2000 XZ lines/sec	Up to 2500 XY lines/sec
Carrier Frequency	5 – 8 MHz	1 – 2 MHz
Image Size	1000 – 1500 lines	400 - 500 lines
Frame Rate	1 – 2 frames/sec	2 – 6 frames/sec

Table 5.2. Specifications for the ultrahigh resolution OCT and OCM imaging systems.

## 5.8 Conclusion

A high speed optical coherence microscopy system was constructed and demonstrated for *in vivo* imaging of human skin and *Xenopus laevis* tadpole. A femtosecond laser and continuum generation light source provided coherence axial resolutions of  $< 4 \mu\text{m}$ . Dispersion and polarization compensation schemes were implemented to enable fast phase modulation using an electro-optic waveguide phase modulator. The system design will scale to very high imaging speeds and is effectively limited only by the maximum rate of the beam raster scanning apparatus. In addition, the system utilized a fast autofocusing technique to ensure optimal alignment of the optical coherence gate with the focal plane of the confocal microscope. The autofocusing solution will enable robust operation *in vivo* with a variety of imaging probes. Finally, the OCM system was integrated with an ultrahigh resolution OCT system to create a clinical imaging unit capable of imaging architectural and cellular features in two and three dimensions over multiple fields of view.

## 5.9 References

- [1] D. Huang, E. A. Swanson, C. P. Lin, J. S. Schuman, W. G. Stinson, W. Chang, M. R. Hee, T. Flotte, K. Gregory, C. A. Puliafito, and et al., "Optical coherence tomography," *Science*, vol. 254, pp. 1178-81, 1991.
- [2] M. Rajadhyaksha, M. Grossman, D. Esterowitz, and R. H. Webb, "In-Vivo Confocal Scanning Laser Microscopy of Human Skin - Melanin Provides Strong Contrast," *Journal of Investigative Dermatology*, vol. 104, pp. 946-952, 1995.
- [3] J. A. Izatt, M. R. Hee, G. M. Owen, E. A. Swanson, and J. G. Fujimoto, "Optical coherence microscopy in scattering media," *Optics Letters*, vol. 19, pp. 590-2, 1994.
- [4] M. Kempe, W. Rudolph, and E. Welsch, "Comparative study of confocal and heterodyne microscopy for imaging through scattering media," *Journal of the Optical Society of America a-Optics Image Science and Vision*, vol. 13, pp. 46-52, 1996.
- [5] J. A. Izatt, M. D. Kulkarni, H.-W. Wang, K. Kobayashi, and M. V. Sivak, Jr., "Optical coherence tomography and microscopy in gastrointestinal tissues," *IEEE Journal of Selected Topics in Quantum Electronics*, vol. 2, pp. 1017-28, 1996.
- [6] A. D. Aguirre, P. Hsiung, T. H. Ko, I. Hartl, and J. G. Fujimoto, "High-resolution optical coherence microscopy for high-speed, in vivo cellular imaging," *Opt Lett*, vol. 28, pp. 2064-6, 2003.
- [7] A. L. Clark, A. Gillenwater, R. Alizadeh-Naderi, A. K. El-Naggar, and R. Richards-Kortum, "Detection and diagnosis of oral neoplasia with an optical coherence microscope," *J Biomed Opt*, vol. 9, pp. 1271-80, 2004.
- [8] W. Drexler, U. Morgner, F. X. Kartner, C. Pitris, S. A. Boppart, X. D. Li, E. P. Ippen, and J. G. Fujimoto, "In vivo ultrahigh-resolution optical coherence tomography," *Optics Letters*, vol. 24, pp. 1221-1223, 1999.
- [9] F. Helmchen, M. S. Fee, D. W. Tank, and W. Denk, "A miniature head-mounted two-photon microscope: High-resolution brain imaging in freely moving animals," *Neuron*, vol. 31, pp. 903-912, 2001.
- [10] C. K. Hitzenberger, P. Trost, P. W. Lo, and Q. Y. Zhou, "Three-dimensional imaging of the human retina by high-speed optical coherence tomography," *Optics Express*, vol. 11, pp. 2753-2761, 2003.
- [11] T. Q. Xie, Z. G. Wang, and Y. T. Pan, "High-speed optical coherence tomography using fiberoptic acousto-optic phase modulation," *Optics Express*, vol. 11, pp. 3210-3219, 2003.
- [12] Y. C. Chen and X. D. Li, "Dispersion management up to the third order for real-time optical coherence tomography involving a phase or frequency modulator," *Optics Express*, vol. 12, pp. 5968-5978, 2004.
- [13] V. Westphal, S. Yazdanfar, A. M. Rollins, and J. A. Izatt, "Real-time, high velocity-resolution color Doppler optical coherence tomography," *Optics Letters*, vol. 27, pp. 34-6, 2002.
- [14] J. F. de Boer, C. E. Saxer, and J. S. Nelson, "Stable carrier generation and phase-resolved digital data processing in optical coherence tomography," *Applied Optics*, vol. 40, pp. 5787-90, 2001.
- [15] Y. Zhao, Z. Chen, C. Saxer, S. Xiang, J. F. de Boer, and J. S. Nelson, "Phase-resolved optical coherence tomography and optical Doppler tomography for imaging blood flow in human skin with fast scanning speed and high velocity sensitivity," *Optics Letters*, vol. 25, pp. 114-16, 2000.
- [16] T. Q. Xie, Z. G. Wang, and Y. T. Pan, "Dispersion compensation in high-speed optical coherence tomography by acousto-optic modulation," *Applied Optics*, vol. 44, pp. 4272-4280, 2005.
- [17] S. Bourquin, A. D. Aguirre, I. Hartl, P. Hsiung, T. H. Ko, J. G. Fujimoto, T. A. Birks, W. J. Wadsworth, U. Bunting, and D. Kopf, "Ultrahigh resolution real time OCT imaging using a compact femtosecond Nd : Glass laser and nonlinear fiber," *Optics Express*, vol. 11, pp. 3290-3297, 2003.
- [18] G. J. Tearney, B. E. Bouma, and J. G. Fujimoto, "High-speed phase- and group-delay scanning with a grating-based phase control delay line," *Optics Letters*, vol. 22, pp. 1811-13, 1997.

- [19] R. E. Hummel, K. H. Guenther, and P. Wissmann, *Handbook of optical properties*. Boca Raton: CRC Press, 1995.
- [20] A. V. Zvyagin, E. D. Smith, and D. D. Sampson, "Delay and dispersion characteristics of a frequency-domain optical delay line for scanning interferometry," *J Opt Soc Am A Opt Image Sci Vis*, vol. 20, pp. 333-41, 2003.
- [21] A. E. Willner, "Chromatic dispersion and polarization-mode dispersion: managing key limitations in optical communication systems," vol. 13, pp. 16-21, 2002.
- [22] T. M. Fortier, S. T. Cundiff, I. T. Lima, B. S. Marks, C. R. Menyuk, and R. S. Windeler, "Nonlinear polarization evolution of ultrashort pulses in microstructure fiber," *Optics Letters*, vol. 29, pp. 2548-2550, 2004.
- [23] Z. M. Zhu and T. G. Brown, "Polarization properties of supercontinuum spectra generated in birefringent photonic crystal fibers," *Journal of the Optical Society of America B-Optical Physics*, vol. 21, pp. 249-257, 2004.
- [24] A. M. Rollins, R. Ung-arunyawee, A. Chak, R. C. K. Wong, K. Kobayashi, M. V. Sivak, Jr., and J. A. Izatt, "Real-time in vivo imaging of human gastrointestinal ultrastructure by use of endoscopic optical coherence tomography with a novel efficient interferometer design," *Optics Letters*, vol. 24, pp. 1358-60, 1999.
- [25] J. M. Geusebroek, F. Cornelissen, A. W. M. Smeulders, and H. Geerts, "Robust autofocusing in microscopy," *Cytometry*, vol. 39, pp. 1-9, 2000.
- [26] M. Rajadhyaksha, S. Gonzalez, J. M. Zavislan, R. R. Anderson, and R. H. Webb, "In vivo confocal scanning laser microscopy of human skin II: Advances in instrumentation and comparison with histology," *Journal of Investigative Dermatology*, vol. 113, pp. 293-303, 1999.
- [27] J. M. Schmitt, S. H. Xiang, and K. M. Yung, "Speckle in optical coherence tomography," *Journal of Biomedical Optics*, vol. 4, pp. 95-105, 1999.
- [28] P. A. Magnin, "Coherent Speckle in Ultrasound Images," *Hewlett-Packard Journal*, vol. 34, pp. 39-40, 1983.
- [29] J. D. Briers, "Laser Doppler, speckle and related techniques for blood perfusion mapping and imaging," *Physiological Measurement*, vol. 22, pp. R35-R66, 2001.
- [30] S. K. Nadkarni, B. E. Bouma, T. Helg, R. Chan, E. Halpern, A. Chau, M. S. Minsky, J. T. Motz, S. L. Houser, and G. J. Tearney, "Characterization of atherosclerotic plaques by laser speckle imaging," *Circulation*, vol. 112, pp. 885-892, 2005.
- [31] C. J. Stewart, R. Frank, K. R. Forrester, J. Tulip, R. Lindsay, and R. C. Bray, "A comparison of two laser-based methods for determination of burn scar perfusion: Laser Doppler versus laser speckle imaging," *Burns*, vol. 31, pp. 744-752, 2005.
- [32] M. Rajadhyaksha, R. R. Anderson, and R. H. Webb, "Video-rate confocal scanning laser microscope for imaging human tissues in vivo," *Applied Optics*, vol. 38, pp. 2105-2115, 1999.
- [33] J. M. Schmitt, "Array detection for speckle reduction in optical coherence microscopy," *Phys Med Biol*, vol. 42, pp. 1427-39, 1997.
- [34] N. Iftimia, B. E. Bouma, and G. J. Tearney, "Speckle reduction in optical coherence tomography by "path length encoded" angular compounding," *J Biomed Opt*, vol. 8, pp. 260-3, 2003.
- [35] A. E. Desjardins, B. J. Vakoc, G. J. Tearney, and B. E. Bouma, "Speckle reduction in OCT using massively-parallel detection and frequency-domain ranging," *Optics Express*, vol. 14, pp. 4736-4745, 2006.
- [36] M. Pircher, E. Gotzinger, R. Leitgeb, A. F. Fercher, and C. K. Hitzenberger, "Speckle reduction in optical coherence tomography by frequency compounding," *J Biomed Opt*, vol. 8, pp. 565-9, 2003.
- [37] P. R. Herz, Y. Chen, A. D. Aguirre, J. C. Fujimoto, H. Mashimo, J. Schmitt, A. Koski, J. Goodnow, and C. Petersen, "Ultrahigh resolution optical biopsy with endoscopic optical coherence tomography," *Optics Express*, vol. 12, 2004.
- [38] D. C. Adler, T. H. Ko, and J. G. Fujimoto, "Speckle reduction in optical coherence tomography images by use of a spatially adaptive wavelet filter," *Opt Lett*, vol. 29, pp. 2878-80, 2004.

- [39] D. L. Marks, T. S. Ralston, and S. A. Boppart, "Speckle reduction by I-divergence regularization in optical coherence tomography," *J Opt Soc Am A Opt Image Sci Vis*, vol. 22, pp. 2366-71, 2005.
- [40] S. Paes, S. Y. Ryu, J. Na, E. Choi, B. H. Lee, and I. K. Hong, "Advantages of adaptive speckle filtering prior to application of iterative deconvolution methods for optical coherent tomography imaging," *Optical and Quantum Electronics*, vol. 37, pp. 1225-1238, 2005.
- [41] S. Brand, J. M. Poneros, B. E. Bouma, G. J. Tearney, C. C. Compton, and N. S. Nishioka, "Optical coherence tomography in the gastrointestinal tract," *Endoscopy*, vol. 32, pp. 796-803, 2000.

## Chapter 6

### ***Ex Vivo* Architectural and Cellular Imaging of Gastrointestinal Tissues with Ultrahigh Resolution OCT and OCM**

#### **6.1 Overview**

This chapter presents *ex vivo* imaging studies performed with the integrated OCT and OCM system described in the previous chapter. The goals of this work were to evaluate the ability for ultrahigh resolution OCT and OCM to visualize tissue architectural and cellular features of normal and diseased tissues of the gastrointestinal tract. Previous *ex vivo* and *in vivo* work has been performed using standard and ultrahigh resolution optical coherence tomography in the upper and lower gastrointestinal tracts, as described in chapter 2 of this thesis. The work presented here, however, provides the first broad survey of cellular resolution OCM in gastrointestinal tissues. In addition, it expands previous *ex vivo* studies of ultrahigh resolution OCT and provides insight into the relative advantages and disadvantages of OCT and OCM.

This work was performed with the help of clinical collaborators from two institutions. Drs. Hiroshi Mashimo and Saleem Desai from the Division of Gastroenterology at the Boston VA Healthcare were instrumental in facilitating the imaging studies in the clinical endoscopy suite. Likewise, Drs. Brad Bryan and James Connolly from the Department of Pathology at the Beth Israel Deaconess Medical Center made possible the imaging experiments in the pathology laboratory. From MIT, Dr. Yu Chen provided assistance with tissue handling and imaging.

#### **6.2 Introduction**

Several advanced optical imaging methods are being developed to supplement conventional white light endoscopy for visualization of mucosal tissues in the gastrointestinal tract. Magnification endoscopy allows the endoscopist to increase the optical power of the scope by 1.5 – 150x, allowing improved visualization of surface architectural features. Magnifying scopes can be combined with topically-applied absorptive dyes [1] or mucous-clearing agents [2] to enhance image contrast. Endocytoscopy, another high resolution technique, provides 450 – 1100 x magnification and has been used in conjunction with methylene blue staining to visualize individual cells in the esophagus *in vivo* [3].

These direct view approaches do not provide insight into subsurface tissue architecture, however. For depth-resolved imaging, endoscopic optical coherence tomography (OCT) has been developed [4]. OCT uses broadband near-infrared light sources to generate cross-sectional images of tissue morphology using low-coherence interferometry. Contrast is due to variations in index of refraction in the tissue, which generates optical reflections in a manner analogous to acoustic reflections used for ultrasound imaging. Standard systems operate with depth resolution of 10 – 15  $\mu\text{m}$  and transverse resolution of 15 – 25  $\mu\text{m}$ . The high resolution of this technique enables visualization of tissue architectural features at a level approaching that of conventional histopathology, but without the need for tissue excision and processing. Numerous studies have been performed in the human esophagus and have established the ability to characterize *in vivo* normal mucosal tissues as well as certain disease states, including Barrett's esophagus and esophageal adenocarcinoma [5-10]. OCT has also been investigated for the detection of high grade dysplasia in the setting of Barrett's esophagus [11, 12], with one report citing sensitivity and specificity of 85% and 75%, respectively [13]. OCT technology is progressing rapidly, with the recent development of ultrahigh resolution endoscopic OCT imaging systems allowing image depth resolutions of better than 5  $\mu\text{m}$  [14, 15]. A major limitation of cross-sectional OCT imaging methods demonstrated to date, though, is the restricted transverse image resolution. This limits the ability to reliably image cellular features, a factor which could be extremely important for the detection and grading of dysplasia and early cancers of the upper and lower gastrointestinal tracts.

Laser scanning confocal microscopy is another subsurface optical imaging method which has shown great promise for *in situ* cellular imaging. Confocal microscopy generates *en face* images by raster scanning a laser beam on tissue through a high numerical aperture objective lens, which produces a small focal spot in the range of 1  $\mu\text{m}$ . Typical depth resolutions of 3-5  $\mu\text{m}$ , or about the thickness of a typical histology slice, are achieved using a pinhole detector to reject scattered light from outside the focal plane. Image contrast can be generated either from direct tissue reflectance, as in OCT, or from exogenous fluorescence dyes. High speed reflectance confocal microscopy using near-infrared lasers has been studied for *in vivo* cellular resolution imaging of human skin [16, 17], cervix [18], and oral mucosa [19]. In addition, a few *ex vivo* studies have investigated the potential role for reflectance confocal microscopy in the gastrointestinal tract [20-22]. Results indicate the ability to visualize cellular and subcellular elements in the esophagus, and to detect with statistical significance a difference between nucleus-to-cytoplasm ratio in normal and cancerous tissue [21]. In the colon, hallmark features of normal, hyperplastic, and adenomatous crypts were identified on confocal images [22]. Development of reflectance confocal endoscopes capable of *in vivo* imaging with equivalent image quality to that obtained *ex vivo* remains a challenging endeavor. These endoscopes require miniaturized optics and raster-scanning schemes. Several approaches toward scanning have been pursued, including fiber bundle

endoscopes [18], microelectro-mechanical systems (MEMS) [23], and spectrally-encoded scanning [24]. Small diameter high numerical aperture objective lenses are also under development [25]. Reflectance confocal microscopy typically demands numerical apertures of 0.7 – 1.0, which presents a daunting task in miniaturized optical design. One very preliminary initial report of endoscopic reflectance microscopy has been published [22], but the method has yet to become widely available in endoscopy.

Fluorescence confocal microscopy, on the other hand, has developed more rapidly for endoscopic imaging in the gastrointestinal tract. Use of visible wavelength excitation and fluorescence contrast provided by exogenous injected fluorescein or topically applied acriflavin dyes can provide a strong signal level compared to reflectance microscopy. Fluorescence confocal systems also offer promise for use with molecularly targeted fluorescence probes currently under development [26]. A confocal endomicroscope with lateral resolution of 1-1.5  $\mu\text{m}$  and axial resolution of 7  $\mu\text{m}$  has been demonstrated for gastrointestinal endoscopy [27]. In this device, the confocal scanner was integrated into a standard clinical endoscope. Outstanding cellular resolution images of normal mucosa have been presented [27] and *in vivo* detection of neoplastic changes in colorectal mucosa has been demonstrated with sensitivity of 97.4% and specificity of 99.4% in a study of 42 patients [28]. More recently, in a study of 63 patients, detection of Barrett's metaplasia and associated intraepithelial neoplasia was shown with sensitivity and specificity of 92.9% and 98.4%, respectively [29]. Fluorescence confocal endoscopy offers great promise going forward, but there are disadvantages compared to reflectance methods. The fluorescence dyes each have toxicities which cannot be ignored and can generate allergic reactions in some patients. In addition, the use of visible wavelength excitation limits image penetration to the upper mucosa. A reflectance method capable of producing high quality cellular images without dyes and to greater depths than existing endoscopic confocal methods would be an important advance.

Optical coherence microscopy (OCM) is a combination of optical coherence tomography and confocal microscopy that has been proposed for cellular resolution imaging in the *en face* plane. OCM has advantages over conventional reflectance confocal microscopy that make it a promising method for endoscopic applications. The combination of optical coherence and confocal detection schemes can provide enhanced optical sectioning in tissue, thereby allowing improved imaging depth compared to confocal microscopy alone [30]. In comparison to the limited confocal imaging depths of 100 – 200  $\mu\text{m}$ , OCT has been shown to image to depths of greater than 1 mm in the gastrointestinal tract [31]. In addition, OCM can image with lower numerical aperture than confocal microscopy, which will facilitate the development of miniaturized probes [32]. Only a few studies with this method have been performed to date largely due to the lack of advanced OCM imaging technology. *Ex vivo* investigations of human tissues performed so far include a very preliminary published report of normal colonic mucosa [33] and a

more extensive report on normal and dysplastic oral mucosa [34]. *In vivo* imaging has been limited to a feasibility demonstration in human skin and developmental biology specimens [32].

Further *ex vivo* studies are essential in the development of this technology to provide a means of evaluation and validation before more advanced *in vivo* studies are performed. Such experiments provide necessary information about imaging parameters and image interpretation criteria that will contribute to the design of future *in vivo* investigations. In addition, the results from *ex vivo* studies serve to motivate further technological developments necessary for *in vivo* imaging, which can be costly and time intensive. The present study was designed to evaluate a newly developed high speed OCM method that can be applied in the future with miniaturized catheter technologies for endoscopic imaging applications. The study consisted of a broad *ex vivo* imaging survey of freshly excised gastrointestinal tissues. Images of normal and diseased tissue specimens were correlated with histology and compared. The ability of the OCM instrument to section in depth was also assessed. In addition, OCM images were precisely correlated to images from an ultrahigh resolution OCT system to allow for comparison between the two methods. The results of this study provide a basis for interpretation of future *in vivo* OCM images in the gastrointestinal tract and will also aid in the interpretation of endoscopic OCT data.

## **6.3 Methods**

### **6.3.1 Imaging System**

This study used an OCM system designed for high-speed imaging at 1060 nm. A detailed description of the system is provided in the previous chapter. Briefly, the system utilized a compact and portable Nd:Glass femtosecond laser source which was spectrally broadened in a high numerical aperture optical fiber to a bandwidth of over 200 nm. High speed phase modulation with an electro-optic waveguide modulator provided a heterodyne carrier frequency of 1 MHz, which enabled fast raster scanning for imaging. Using specialized techniques to compensate for chromatic dispersion and wavelength dependent source polarization, coherence gated axial resolution of  $< 4$   $\mu\text{m}$  was achieved. This corresponds to optical image slices smaller than traditional histologic sections. *En face* imaging was performed through a benchtop fiber-optic confocal microscope consisting of a pair of fast galvanometer scanners, intermediate relay optics, and a water immersion objective lens. The measured lateral optical resolution of the confocal microscope was  $< 2$   $\mu\text{m}$  while the axial response width was  $\sim 19$   $\mu\text{m}$ . Images were acquired at 2 frames/second over a field of view of 400  $\mu\text{m}$  x 400  $\mu\text{m}$  with an effective pixel sampling of 500 x 750 pixels. Sample illumination power measured 10 mW and the recorded detection sensitivity limit was -98 dB, which is close to the shot-noise quantum limit. The system implemented a custom autofocus technique to ensure that the acquired OCM images were in focus. In order of execution, image processing after acquisition consisted of digital demodulation from the carrier

frequency, pixel resampling to remove scanner hysteresis and to correct aspect ratio, slight spatial filtering with a 3x3 triangular kernel, square-root compression of signal values, and contrast enhancement. Images are displayed on an inverse grayscale colormap, which is in agreement with the colormap traditionally used for OCT images but opposite to that used for reflectance confocal microscopy images.

An ultrahigh resolution OCT system operating at 1060 nm was combined with the OCM system to allow for co-registered OCT and OCM imaging. The OCT system was similar to one described for a previous *ex vivo* imaging study [35] and was described in detail in previous chapters. Power from the Nd:Glass laser source was split equally between the OCT and OCM imaging engines to allow for sequential imaging without switching the connections. The OCT sample arm shared the microscope optics with the OCM sample arm, except for the objective lens, which was located on a turret that allowed rapid interchange between high and low magnifications. Cross-sectional images spanning 3 mm in lateral extent by 1.3 mm in depth were acquired with 1000 x 1344 pixels (lateral x depth) at 1 frame/second. The images were scaled to correct for the approximate average index of refraction of tissue of  $n = 1.38$ . The lateral optical resolution of the OCT system was 14  $\mu\text{m}$  while the axial response measured  $< 3 \mu\text{m}$ . The restricted lateral resolution was necessary to maintain sufficient depth of field in the OCT images to keep the entire cross-sectional image in focus. The OCT signal was logarithmically compressed and demodulated using an analog electronic circuit before analog to digital conversion. Image processing after acquisition consisted of pixel resampling to the correct aspect ratio followed by contrast enhancement. Again, images are displayed on an inverse grayscale colormap.

The two systems were integrated into portable instrument carts that were transported to the hospital for imaging experiments. Laser operation was turnkey and stable over hours, requiring little to no adjustment by the user. Microsoft Windows based control software for imaging allowed control of most system parameters, making the instrument operation user-friendly and suitable for the clinical environment.

### **6.3.2 Study Design and Imaging Protocol**

The study was designed as a pilot observational study to evaluate new technology. The design consisted of two separate imaging components. The first portion was performed on freshly excised surgical specimens in the pathology laboratory at the Beth Israel Deaconess Medical Center. The imaging protocol was approved by the institutional review boards at both the Beth Israel Deaconess Medical Center and the Massachusetts Institute of Technology. Informed consent was not required because the study involved only imaging of excess tissue from surgical specimens that was deemed unnecessary for diagnostic protocol by supervising pathologists. Fresh specimens were selected based on the presence of

pathology upon gross examination, prompt arrival to the pathology laboratory, and large specimen size, which allowed normal and pathologic tissues to be collected from each specimen for the study without interfering with routine diagnostic procedures. Specimens that arrived at the pathology laboratory already in formalin were excluded from the study. The approximate length of time between excision and imaging was 2-3 hours. The duration of this component of the study was 5 weeks.

The second portion of the study was performed on freshly excised tissue acquired during upper and lower gastrointestinal endoscopy procedures at the endoscopy suite of Jamaica Plains Veterans Administration Medical Center, a component of the Boston VA Healthcare System. The tissue was imaged as part of ongoing studies investigating the role of endoscopic OCT in the gastrointestinal tract. Subject enrollment was performed in accordance with separate protocols for upper and lower GI imaging approved by institutional review boards at the Massachusetts Institute of Technology, Harvard Medical School, and the Boston VA Healthcare. Both protocols provide for *ex vivo* imaging of excised tissue specimens in addition to the *in vivo* endoscopic OCT imaging. Subjects enrolled under the upper GI protocol were selected from those undergoing surveillance endoscopy and biopsy based upon a history of previously diagnosed Barrett's esophagus, dysplasia, or adenocarcinoma. Subjects enrolled under the lower GI protocol were selected from those undergoing routine screening colonoscopy. Specimens consisted of biopsy samples as well as samples from snare polypectomy procedures. The duration of this component of the study was also 5 weeks.

A two-phase study was chosen because the specimen set imaged during each phase was complementary. Imaging at the pathology laboratory provided access to normal specimens, as well as larger and more intact specimens compared to the pinch biopsy samples obtained in the endoscopy suite. Moreover, full-thickness mucosal samples were taken from the surgical specimens, which allowed more accurate assessment of OCM image penetration depth compared to the partial thickness biopsy samples. On the other hand, biopsy imaging provided access to smaller, more diagnostically sensitive specimens that were not readily available in the pathology laboratory. These included biopsies of Barrett's mucosa and colon polyps, which typically arrive at the pathology lab already fixed in formalin. Furthermore, the biopsies were imaged within minutes of excision compared to the typical 2-3 hour wait for surgical specimens.

In total for both study components, 75 samples were imaged from 39 patients. Sample sizes from surgical specimens typically measured approximately 1 cm x 1 cm. The size of pinch biopsies typically measured 3-4 mm in greatest dimension, while resected polyps ranged from 3 – 7 mm in diameter. The high imaging speed of the OCM system allowed for extensive imaging of each specimen and multiple sites were surveyed in each sample. In total, tens of thousands of images were collected for subsequent review. Normal specimen subtypes included squamous esophagus (10), stomach (3), small intestine (5),

colon (11), and pancreas (2). Pathology specimen subtypes included columnar-lined esophagus (11), esophageal adenocarcinoma (1), celiac disease (1), inflammatory bowel disease (3), acute inflammation (2), chronic colitis (2), melanosis coli (1), tubular adenoma (11), hyperplastic polyp (5), colorectal adenocarcinoma (4), cholecystitis (2), and chronic pancreatitis (1). Specimen classification was done based upon histologic diagnosis made by an experienced pathologist.

To prevent tissue dehydration, specimens were immersed in isotonic phosphate-buffered saline as soon as they were received for imaging. Imaging was performed through a coverslip, but a thin layer of transparent ultrasound gel measuring approximately 100  $\mu\text{m}$  was placed between the coverslip and the tissue surface to prevent from compressing the surface architectural features. Ultrasound gel has excellent optical properties and is commonly used in confocal microscopy as an immersion medium for objective lenses [17]. The sample was placed on a three-axis translation stage to allow panning in three dimensions during imaging. Imaging was first performed using ultrahigh resolution OCT. The larger 3 mm field of view of the OCT system as well as increased familiarity with the cross-sectional OCT images allowed for identification of regions of intact mucosa as well as regions of interesting pathology for higher magnification imaging with OCM. When an area of interest was located, the microscope was quickly switched to the OCM mode and high magnification images were acquired co-registered to the OCT data set. Images were acquired while panning in the transverse dimension and in depth such that the three dimensional structure of the tissue was appreciated on the OCM images. Typical imaging times per sample were in the range of 5-15 minutes. After imaging, the sample was prepared for histologic sectioning. Discarded samples from the pathology laboratory were inked using a small gauge needle to deposit one ink drop at each end of the OCT scan, thereby preserving the OCT imaging plane for histologic sectioning. Slides were cut in both the cross-sectional and *en face* planes relative to the luminal surface to allow comparison to both OCT and OCM images. Specimens from the endoscopy clinic were placed in formalin in accordance with standard of care protocol and sent for routine histologic processing. Slides were stained with hematoxylin and eosin and digital photomicrographs were recorded from a light microscope equipped with a CCD camera and video capture software.

### **6.3.3 Data Analysis**

In this observational study, analysis focused on qualitative image interpretation and correlation with histology. The image database was organized according to specimen, typically with several hundred images per specimen. The entire image database and histology slide set were first reviewed, and representative specimens of normal and pathologic specimens were selected for further evaluation. Selection was based upon several factors, including relative correlation with histology, overall image quality, and the degree to which the selected datasets accurately represented the larger data set.

Representative photomicrographs of histologic specimens were then made with a best effort attempt to provide correlation among features. OCT images proved more useful than OCM for histologic correlations, because the larger field of view allowed appreciation of larger structure in the images. For presentation, OCT and OCM still frames were selected from the individual specimen data set to most accurately correlate with histologic features. Review of the entire data stream consisting of scans of the sample in depth and in transverse dimensions helped to distinguish between actual image features and artifacts, and therefore increased the degree of accuracy to which the histologic correlations were made. Imaging depths for the presented data were determined from depth scans of the sample and from cross-sectional images. Image and histology correlations in this chapter are generally presented with the OCT images and cross-sectional histology sized to the same scale and with the OCM images and transverse or *en face* histology sized to the same scale.

## **6.4 Imaging Results**

### **6.4.1 Upper Gastrointestinal Tract**

Figure 6.1 presents representative ultrahigh resolution OCT (UHR OCT) and histology images of a normal region of squamous esophagus. The OCT image in figure 6.1a clearly delineates the layered esophageal mucosa, including the cellular epithelial layer and the underlying lamina propria and submucosa. As emphasized by the 3x zoom view in figure 6.1b, the high axial resolution of UHR OCT clearly delineates the location of the basement membrane separating the epithelium from the lamina propria. Furthermore, UHR OCT cannot identify cellular features in the epithelium. Images acquired of the same specimen from the same region of mucosa with OCM are presented in figure 6.2. The OCM image has a small field of view compared to the OCT scan. However, the much higher transverse resolution enables visualization of squamous epithelial cells. Figures 6.2a and 6.2b were taken at depths of 30  $\mu\text{m}$  and 125  $\mu\text{m}$ , respectively. In 6.2a, cell nuclei and cell membranes can be readily visualized as highly scattering relative to the weak scattering cytoplasm. The transition region between the stratified squamous epithelium and the underlying lamina propria can be seen in 6.2b, as demarcated by the arrows. Tiny cells are evident on the left portion of this image and point out the change in cell size that is expected in going from the surface to the basement membrane in a stratified squamous epithelium. The lamina propria appears highly scattering and disorganized relative to the cellular epithelium. This is better seen in the images in figure 6.2d and 6.2e, acquired at depths of 210  $\mu\text{m}$  and 400  $\mu\text{m}$ . The images highlight the ability of OCM to visualize tissue structure with high resolution deep into the lamina propria. A vessel can be seen in cross-section in figure 6.2d. Representative *en face* histology is shown for comparison, with figure 6.2c corresponding approximately to OCM image 6.2a and figure 6.2f to the image in 6.2b.

The cellular progression in the stratified squamous esophagus is further highlighted in figures 6.3 and 6.4. Figure 6.3 presents OCM images taken at depths beginning with 30  $\mu\text{m}$  extending below the epithelium to 330  $\mu\text{m}$ . Surface cells are larger and with lower relative nuclear to cytoplasm (N/C) ratio compared to cells found at deeper levels. In this particular specimen, the rete peg ridges projecting from the lamina propria into the epithelium can be visualized, with the squamous cells appearing to swirl around them. At greater depths, the cellular epithelium disappears earlier over the ridges, as evident in figures 6.3f and 6.3g. Figure 6.4 highlights the cell size change by showing 3x zoom views of the boxes identified in figure 6.3. A clear decrease in the cell size as well as an increase in the relative N/C ratio can be appreciated. These images further highlight the high resolution of the OCM images well below the surface. Figure 6.4d corresponds to a depth of 210  $\mu\text{m}$ .

Figure 6.5 demonstrates the squamo-columnar junction marking the transition between the squamous esophagus and the gastric mucosa. The cross-sectional OCT image in figure 6.5b shows a fairly homogeneous squamous epithelium as well as the gastric pit architecture, as verified in the histology shown in figure 6.5a. The *en face* OCM images in figure 6.5c thru 6.5e identify the presence of squamous cells immediately adjacent to the gastric pits. The image depth is approximately 100  $\mu\text{m}$ . Small surface mucous cells can be identified surrounding the lumens of the pits. Figure 6.6 further illustrates the gastric architecture as seen by OCT and OCM. The OCT image in 6.6a shows a typical gastric pit architecture as has been observed previously with endoscopic OCT. The *en face* OCM image shows the field of pits in the orthogonal plane with identification of numerous surface mucous cells. Corresponding histology is provided in both the cross-sectional and *en face* imaging planes.

OCT and OCM images of Barrett's esophagus are shown in figure 6.7. The UHR OCT image in figure 6.7a shows a distinct architecture for the columnar mucosa which differs from either the squamous esophagus or the gastric morphology. Glandular entities at and beneath the mucosal surface can be identified in cross-section, as demonstrated in the magnified view in figure 6.7b. Corresponding cross-sectional histology is presented in 6.7c. Higher magnification images of the histology demonstrate the presence of goblet cells (arrows) within the glandular epithelium, which is the histologic hallmark of specialized intestinal metaplasia. OCM images of this specimen are presented in figures 6.7f – 6.7h. The images demonstrate a villous columnar morphology with glandular lumens of varying shape and size. In addition, the presence of focal regions containing goblet cells can be appreciated in figures 6.7g and 6.7h, as indicated by the arrows. Figure 6.8 further highlights the ability for OCM to identify goblet cells in Barrett's mucosa. The image and corresponding histology were acquired of a pinch biopsy from another patient than those in figure 6.7. The goblet cells appear on OCM as distinct, non-scattering inclusions within the epithelium. Also notable among the OCM images in figures 6.7 and 6.8 is the heterogeneity in scattering properties of the glandular epithelium. Contrast is generated within and between the adjacent

columnar cells, which can be appreciated in certain parts of the epithelium by the striated appearance radiating away from the lumen (open arrows in figure 6.7f).

UHR OCT and OCM images of esophageal adenocarcinoma are presented in figure 6.9. The UHR OCT image in 6.9a was taken in a region of overlying squamous epithelium, with invasive adenocarcinoma underneath. Figure 6.9b is an OCM image demonstrating the characteristic cellular pattern of the surface squamous epithelium. The UHR OCT image of 6.9a exhibits a loss of the typical layered mucosal architecture as seen in figure 6.1. Regions of reactive inflammatory infiltrate surrounding the tumor can be seen as focal areas of high backscattering. As seen in the histology in figure 6.9c, the bulk of the tumor lies almost 1 mm below the surface, which is near the penetration depth limit of the OCT image. A higher magnification view of the tumor histology is shown in figure 6.9d. OCM images acquired directly from the tumor without the overlying squamous epithelium are presented in 6.9e-g. The tumor microarchitecture demonstrates profound heterogeneity on the OCM images and individual features in the images correlate well with the histologic features. Darkly staining nuclei within atypical malignant cells evident on histology appear as highly scattering spots on OCM. In addition, gland forming entities devoid of OCM signal are present throughout the tumor and chords of highly scattering stroma can be seen penetrating the tumor. Images in figures 6.9e and 6.9f were acquired at a depth of 50  $\mu\text{m}$  and the image in figure 6.9g was captured at 125  $\mu\text{m}$  below the surface. In general, the image penetration depth through the tumor was dramatically reduced for both OCT and OCM compared to normal squamous mucosa.

Figure 6.10 presents imaging results from a hyperplastic polyp removed from the gastric mucosa. Hyperplastic polyps are characterized histologically by architectural distortion with irregular and often cystically dilated epithelium. Abundant mucin and a serrated, corkscrew-like appearance to the foveolar epithelium can generally be appreciated [36]. Representative histology in 6.10c thru 6.10e highlight typical features in the imaged specimen. As in the histology, dilated and contorted invaginations of the epithelium can be readily appreciated in the UHR OCT images in 6.10a and 6.10b. An example of the serrated luminal architecture captured in the transverse plane is presented at higher magnification in the histology of 6.10e, and serial *en face* OCM images of similar features are shown in 6.10f-h. The arrows on the images highlight the distorted shape of the lumen. Images for 6.10f-h were acquired sequentially at depths of 100, 150, and 190  $\mu\text{m}$ , respectively, demonstrating the ability to track features in depth using multiple OCM sections.

Images of normal duodenum are presented in figure 6.11. The prominent surface villi seen on the cross-sectional UHR OCT image in figure 6.11a correlate well with the histology in 6.11b. *En face* OCM images in figures 6.11c and 6.11d picture the villi at high resolution, revealing the presence of individual goblet cells in the epithelial layer (arrows). Representative histology from the approximate regions

imaged confirms that the villous architecture is well represented on OCM. Data from a biopsy involving chronic inflammation of the duodenum are shown for comparison in figure 6.12. Consistent with the histology in 6.12b, the UHR OCT image in 6.12a demonstrates a loss of normal villous architecture, which is confirmed by the histology in figure 6.12b. Invaginations of epithelium beneath the surface can be appreciated on OCT. Likewise, the OCM images also show villous blunting. Figure 6.12c demonstrates heterogeneous tissue structure consistent with inflammatory infiltrate, while figure 6.12d pictures the duodenal crypt epithelium compressed, with the lumen collapsed. *En face* histology in 6.12e corresponds well, with an absence of normal villi and diffuse inflammatory infiltrate surrounding distorted crypt epithelium.

#### **6.4.2 Lower Gastrointestinal Tract**

UHR OCT and OCM images of normal colon are presented in figures 6.13 – 6.15. The images in 6.13 and 6.14 are from samples acquired from the cecum regions of different patients and demonstrate variations in normal morphology. Crypt architecture can be appreciated by OCT in both cases with good correspondence to histology. Furthermore, OCM visualizes the individual crypt morphology with high resolution. Corresponding *en face* histology verifies the differences in crypt shape and size between the two specimens as seen on OCM. In figure 6.13, the crypts are larger and have more prominent goblet cells compared to those in figure 6.14. A highly scattering rim surrounds the crypts in figure 6.14, which correlates on histology with the basophilic ring of nuclei at the basal aspect of crypt colonocytes. OCM images were acquired at depths of 75 – 100 um beneath the surface. Figure 6.15 presents yet another OCM image of normal crypt structure with corresponding histology. In this specimen, crypt diameter is larger and prominent goblet cell architecture can be visualized with high resolution.

Imaging of hyperplastic and adenomatous polyps of the colon from multiple patients was conducted. A representative data set from a hyperplastic colonic polyp is shown in figure 6.16. Hyperplastic colon polyps are generally characterized by crypt colonocytes appearing hypermucinous in nature and with small nuclei at their basal aspect. The crypt lumens tend to display a sawtooth or serrated appearance and crypt dilation near the surface is typical. Histology in figures 6.16c – 6.16e confirms many of these features in the imaged specimen. The ultrahigh resolution OCT image in figure 6.16a demonstrates a regular pattern of crypts, with surface dilation, as seen in the magnified view in 6.16b. OCM *en face* images discern the serrated crypt architecture with narrow, irregular lumens. An example data set from a tubular adenoma is presented for comparison in figure 6.17. The selected sample was relatively diminutive in form, measuring less than 3 mm. By definition, all adenomas are considered to have at least low-grade dysplasia. Hallmark features of the tubular adenoma include the presence of long, parallel crypts in cross section without significant villous architecture. The crypts themselves display

enlarged, cigar-shaped nuclei, which typically exhibit mild pseudostratification and occupy the basal half of the cell cytoplasm [36]. Histology in figure 6.17c-e confirms the presence of these features in the imaged specimen. On UHR OCT, the parallel crypt lumens can be identified, and the fine axial resolution enables clear delineation of the columnar epithelial layer lining the crypts, as emphasized by the enlargement in figure 6.17c. OCM *en face* images picture the crypts in the transverse plane and compare well to the representative histology in figure 6.17e. Notably, the elongated, eccentric crypts with varying alignment differ markedly from the uniform field of smaller crypts seen in the normal colon specimens. Moreover, OCM visualizes the characteristic cigar-shaped nuclei in the crypt epithelial layer, with pseudostratification evident at deeper depths. It should be noted that the nuclear arrangement is much better appreciated when viewing the entire data stream, panning in transverse and depth dimensions. Images f thru h were acquired at depths ranging from 80 um to 190 um.

Compared to the images of normal and adenomatous colon, OCT and OCM images of adenocarcinoma of the colon displayed a prominent loss of crypt architecture, as demonstrated in figure 6.18. Similar features could be visualized as in the esophageal adenocarcinoma case presented above. UHR OCT images show relatively poor image penetration and very fine tissue architecture consistent with gland forming morphology as seen in the histology in figure 6.18c. The *en face* OCM images provide a high resolution view of the tissue architecture and clearly identify pockets of gland formation within the tumor. In addition, highly scattering malignant cell nuclei are also prominent in the OCM images. Corresponding histology with the same magnification as the OCM images is provided in figure 6.18d.

Inflammatory conditions in the lower gastrointestinal tract were also investigated with OCT and OCM. Figure 6.19 presents an example of normal small intestinal mucosa recorded from the terminal ileum. The villous architecture is evident on OCT and OCM with nice correlation to cross-sectional and *en face* histology. Images from a region of ileum affected by Crohn's disease are shown in figure 6.20. Both OCT and OCM images demonstrate the absence of villous architecture, which is confirmed by histology. Cross-sectional OCT images fail to display visualize a regular pattern of crypt structures, although faint outlines of irregular crypts can be appreciated in regions of the image. OCM images acquired from the same region confirm an irregular crypt arrangement with relatively poor contrast compared to that observed in images of uninvolved mucosa.

### 6.4.3 Pancreas

Images of normal pancreatic tissue microstructure are shown in figure 6.21. The UHR OCT image in figure 6.21a identifies large regions of high and low scattering interspersed throughout a more homogeneous background. The zoom view in 6.21b more clearly emphasizes this point. The high scattering areas have previously been identified as Islets of Langerhans, part of the endocrine pancreas [37]. *En face* OCM images are presented in figures 6.21d and 6.21e, with representative histology at the same magnification in 6.21c. OCM images visualize a mottled pattern consistent with the clusters of acini which make up the exocrine pancreas. This pattern is readily seen in figure 6.21d. In addition, the image in 6.21e portrays a region of high scattering corresponding to the Islets of Langerhans. Structure within the islet cell cluster can be discerned, which likely corresponds to alpha and beta cells as well as vasculature. Adjacent to the islet cell cluster, a portion of the pancreatic duct system can be seen, including the thin ductal epithelial layer.

### 6.4.4 Measurement of Focusing Properties Below the Tissue Surface

To gain insight into achievable imaging depths with optical coherence microscopy, measurements of the microscope confocal axial response were recorded in scattering tissue. The procedure for these measurements was detailed in the previous chapter. In short, images were acquired with the OCM microscope by scanning in only one transverse dimension while also scanning the depth position of the optical coherence gate relative to the focal position in tissue. This produced cross-sectional images similar in essence to OCT images but with severely restricted depth of field due to high numerical aperture focusing. A single depth profile was created by averaging in the lateral dimension. The averaging served to reduce the effects of tissue heterogeneity and provide an axial response which was more representative of the confocal axial response in scattering media. Figure 6.22 presents the results of these measurements made for a specimen of normal squamous esophagus tissue at two depths. Figures 6.22a and 6.22c correspond to a depth of 215  $\mu\text{m}$  below the surface. The plane of focus is evident clearly on the cross-sectional image, and the equivalent confocal parameter measures  $\sim 27 \mu\text{m}$  full-width-at-half-maximum (FWHM). Although, this deviates slightly from the measurement of 19  $\mu\text{m}$  FWHM made outside of tissue, it indicates nonetheless that the confocal gating function is still effective at this depth. In contrast, figure 6.22b and 6.22d present measurements recorded at a depth of 450  $\mu\text{m}$  below the tissue surface. A defined focal plane is no longer visible in the tissue at this depth, as evidenced by the diffuse scattering seen on the image in 6.22b. Likewise, the depth profile confirms that a significant amount of out of focus light is being collected by the objective lens. This leads to an effective shift of the confocal response toward superficial depths, as seen in 6.22d. In addition, the lateral resolution is reduced due to the degradation in focusing ability of the microscope. Figures 6.22e and 6.22f present OCM *en face* at

the depth locations corresponding to 6.22a and 6.22b. The image in 6.22e is located in the connective tissue lamina propria while that in 6.22f is below the lamina propria at the level of the muscularis mucosa or the superficial submucosa. Importantly, both images still exhibit significant contrast, which relates to the ability of the OCM instrument to detect signal returning from a given depth while rejecting light from other depths. However, the resolution in 6.22e appears better than that in 6.22f.

Figure 6.23 further examines the ability of the microscope to focus deep in tissue. The plot in 6.23a shows the effective confocal response as a function of both the coherence depth scan and the focus translation. After about 400  $\mu\text{m}$ , the microscope's ability to focus degrades rapidly with depth. This is further emphasized by the plot in figure 6.23b of the FWHM response as a function of depth translation. The width is fairly stable until about 350 – 400  $\mu\text{m}$ , after which it degrades rapidly. Note also the shift toward the surface in figure 6.23a.

## 6.5 Discussion

In this study, optical coherence microscopy was investigated for cellular resolution imaging of gastrointestinal tissue *ex vivo*. Conventional cross-sectional optical coherence tomography cannot reliably image cellular features because of restricted transverse imaging resolution. In OCT, the focus is set to a fixed depth in tissue and the optical coherence gate is scanned in depth to generate a profile of optical backscatter collected by the microscope. In order to ensure that all depths can be probed without out of focus signal loss, a low numerical aperture focusing objective lens must be used to provide a long depth of field. The requirement for low numerical aperture practically restricts the transverse optical image resolution to the range of 10 – 15  $\mu\text{m}$ , which is generally insufficient to see cellular and subcellular features in tissue. Optical coherence microscopy overcomes the transverse resolution limitation by acquiring images in the *en face* plane, similar to confocal microscopy. In this manner, the image is generated from a single depth, which allows tight focusing using high numerical aperture optics with severely restricted depth of field. OCM can obtain image resolutions of 2-3  $\mu\text{m}$  in three dimensions, thereby enabling cellular imaging.

Previous work on OCM has been performed with slow scanning systems not suitable for *in vivo* imaging applications. This study was conducted using a state of the art fiber-optic OCM system recently developed for *in vivo* imaging. Using high speed phase modulation techniques in conjunction with a fast scanning microscope and a high power laser source, the system was capable of high speed imaging at several frames per second with excellent detection sensitivity. In addition, the system was highly reliable, compact, and portable, making it suitable for clinical investigations outside of the laboratory. The system can readily be extended for *in vivo* endoscopic imaging applications using miniaturized confocal microscope designs.

The present study sought to validate the new OCM imaging technology through a comprehensive *ex vivo* survey of endoscopically accessible gastrointestinal tissues. This study represents the first such broad investigation of OCM in the gastrointestinal tract, and therefore provides an introduction to OCM for endoscopic imaging applications. Freshly excised normal and pathologic specimens from 39 patients were imaged with system parameters similar to those that would be used *in vivo*, thereby providing an accurate assessment of image quality that can be expected from future endoscopic studies. Furthermore, OCM images were acquired co-registered to ultrahigh resolution OCT images from the same specimen and the data have been presented together. This allows the reader to interpret the *en face* OCM images with respect to the more familiar cross-sectional OCT images which have been published in several studies in the literature. Moreover, the ultrahigh resolution OCT data itself will be of interest to the reader, since it marks a 2-3x improvement in axial resolution compared to the majority of images acquired with standard resolution systems. The data is also taken at a wavelength of 1060 nm, which has been introduced previously [35] but not explored fully in the literature, particularly for imaging in the upper gastrointestinal tract. Together, the OCT and OCM data sets published here provide an important comparison of the state of the art for these two methods.

Careful effort was made to correlate OCT and OCM images with histology. As a result, several conclusions can be drawn about the relative capabilities of the two methods for structural imaging of gastrointestinal tissues. Within scattering tissue, OCT proves most useful at characterizing mucosal layers and overall tissue architecture, and identifying the presence or absence of structures at an intermediate resolution scale. Cross-sectional UHR OCT images provide excellent assessment of layer thicknesses within the first 500  $\mu\text{m}$  – 1 mm of mucosal tissues. In the squamous esophagus, for example, the basement membrane transition zone between the stratified squamous epithelium and the underlying lamina propria can be precisely located. UHR OCT can also frequently visualize crypt and glandular entities, vessels, and ducts at and beneath the surface. Within individual crypts and glands, the columnar cell layers lining the lumen can often be appreciated, although single cells could not be identified. OCT is also capable of very accurate assessment of tissue surface architecture, as exemplified by the images of villous structure from the duodenum and small intestine. Delineation of tissue types based upon these surface architectural features may therefore be possible.

OCM provides an order of magnitude improvement in the transverse resolution compared to ultrahigh resolution OCT. This allows visualization of cellular and subcellular features. Squamous cell nuclei and membranes can generally be identified and the progression of cell size and nuclear to cytoplasm ratio can be appreciated. Nuclei can also be identified in colonic crypts. In the normal crypts, nuclei appear as a thin highly scattering ring at the basal aspect of the crypt. The adenomatous crypts, by contrast, frequently exhibit pseudostratification of oval-shaped nuclei, which is consistent with the presence of low

grade dysplasia. Other cell types visible on OCM include goblet and mucin-containing cells in the stomach and colon as well as in pathologic conditions such as Barrett's esophagus. OCM can also characterize tissue architecture on a smaller scale and in an orthogonal plane compared to OCT. This includes such features as crypt size, shape, and arrangement, and the presence of gland-formation within specimens of adenocarcinoma.

The overall quality of the OCM images compares favorably to previously published reflectance confocal microscopy images [21]. This might be expected, since OCM is inherently confocal in nature and the two methods share a common mode of contrast in tissue, namely variation in the refractive index. The OCM image quality presented here, however, is impressive in light of the use of relatively low numerical aperture by confocal standards. Typical reflectance confocal microscopes utilize a numerical aperture of 0.7 – 1.0 in order to provide a depth response of  $< 5$   $\mu\text{m}$  in width, which is equivalent to a conventional histologic slice thickness [17]. OCM makes use of optical coherence gating in addition to confocal gating, and the combination of the two sectioning methods improves rejection of out of focus scattered light compared to confocal alone. In this work, an effective numerical aperture of  $\sim 0.3 - 0.4$  was used to provide a high lateral resolution of 1-2  $\mu\text{m}$  but a depth response measuring only  $\sim 20$   $\mu\text{m}$  in width. In itself, this slice thickness would be insufficient for high contrast cellular imaging below the tissue surface. The relaxed confocal response, however, was compensated for by using a very short coherence gate measuring  $< 4$   $\mu\text{m}$ . Development of high numerical aperture objective lenses remains a challenging obstacle in the development of reflectance confocal endoscopes. With this in mind, the use of coherence gating to relax the numerical aperture requirements of the confocal microscope should greatly facilitate the development of small diameter endoscopic probes.

Endoscopic OCT has been possible largely because of the relative simplicity of the catheter devices used for *in vivo* imaging. A typical OCT catheter consists of a single mode fiber attached to a graded-index focusing element, with a small microprism or a polished tip to direct the beam orthogonally away from the device [38]. Lateral scanning in a single axis has been performed by either rotating or translating the device from the proximal end. The major factor currently limiting the application of OCM in endoscopy is the widespread availability of two-axis scanning catheters for *en face* imaging. These catheters must incorporate a fast raster scan as well as a means for focus translation in tissue. A number of scanning solutions are currently being explored, including microelectro-mechanical systems (MEMS) [39] and piezo-electric fiber scanners [40, 41]. Moreover, working solutions have already been implemented for fluorescence confocal endoscopy which would work equally well for OCM [27]. Indeed, there are no fundamental limitations which will prevent endoscopic optical coherence microscopy from being a clinically viable alternative to confocal endoscopy in the near future.

There are two limits to consider when evaluating imaging depth in OCM. The first is the quantum sensitivity detection limit. The minimum detectable reflection determines the absolute maximum probing depth. The more practical limit, however, is the point at which image resolution and contrast degrade to the point where the images are no longer useful. Such degradation results from detection of out of focus and multiply scattered light due to insufficient confocal and optical coherence gating. In this work, this limit was explored using a measurement of the confocal axial response in scattering tissue. The confocal response was shown to degrade deep in tissue, leading to a loss of image resolution. From the measurements, the loss of resolution appears to be due to loss of the ability to focus in tissue, as evidenced by the widening confocal response profile in the tissue. The measured depth profiles clearly indicate the limitations on reflectance confocal microscopy. The confocal signal would be the integral of the axial response profile over all depths. As the confocal response degrades, the ratio of light detected from outside the focal plane to light returning from the focal plane increases, and the signal to background limit is reached. The OCM instrument can maintain contrast despite the loss of confocal gating, which points to an intact coherence gating mechanism. As the focus is translated deeper, contrast in OCM also degrades, which suggests detection of increasing amounts of multiply scattered light. The degree of improvement of OCM over confocal microscopy depends heavily upon the tissue scattering and optical properties.

An estimate of the imaging depth for OCM in various tissues can be obtained from the OCT images provided for those tissues. Importantly, however, the perception of depth in OCT images often leads to an overestimate of the useable image depth in OCM because of the role of resolution and contrast loss. OCT is inherently a ranging method, and uses only moderate numerical aperture and transverse resolution, without a significant confocal gate. Hence the loss of lateral resolution in OCT, although still present, is not appreciated as much as in OCM. Furthermore, depth of imaging is generally perceived based on the sensitivity limit in which the signal level falls to the noise floor. The transition to the multiple scattering regime occurs before this and therefore limits the depth at which ballistic, single scattered light can be probed. The multiple scattering regime is evident in nearly all of the images as the diffuse tail of OCT signal that fades into the noise floor. Some features can still be visualized within the multiple scattering regime, but the effective image resolution will be lower.

Imaging depth can be enhanced in OCM through efforts in two areas. First, the confocal microscope optics can be optimized for focusing deep in tissue. Efforts to reduce spherical and other aberrations encountered during deep tissue focusing will lead to an improved point spread function with better resolution and contrast. Studies should be performed over a range of numerical apertures to understand what are the optimal parameters for OCM as compared to confocal microscopy. Use of a lower NA, for example, may actually give better performance because of relative rejection of wide angle multiple scatter

compared to high NA optics. At the increase of system complexity, adaptive optics approaches may also prove useful for improving the axial response [42, 43]. Second, the axial coherence resolution can be improved through the use of broader bandwidth light sources. A shorter coherence gate leads to improved rejection of unwanted scattered light and therefore reduces the contribution of multiple scattering at a given depth. Ultrahigh resolution OCT has been demonstrated with axial resolutions approaching 1  $\mu\text{m}$  [44].

Compared to fluorescence confocal endomicroscopy, OCM images have intrinsic contrast provided by backscattered light. This has the advantage of not requiring exogenous fluorescence dyes, which have associated toxicities. In addition, OCM uses longer wavelength light that penetrates farther into tissue than the visible wavelengths used for fluorescence excitation. Contrast and resolution in OCM are generally lower, however. Fundamentally, OCM contrast is limited by the small refractive index changes in gastrointestinal tissues. Previous work in the cervix and other amelanotic tissues such as the oral mucosa [45, 46] has demonstrated relatively weak cellular contrast compared to images in the skin, where melanin pigmentation provides strong signal [17]. To enhance contrast, a weak solution of acetic acid has been applied to increase nuclear scattering [47]. Although not used in this study, similar contrast improvement can be expected with OCM. Acetic acid solutions are used routinely in endoscopy as mucus clearing agents and would therefore find widespread applicability. Contrast in OCM is also limited by the presence of coherent speckle, which gives a grainy appearance to the images. A number of speckle reduction methods are currently under investigation [48-52]. Implementation of such techniques will further improve OCM image quality.

A limitation of all of the cellular resolution microscopy techniques is the relatively small field of view for the images. These methods are essentially point sampling techniques and are therefore subject to sampling errors in surveillance applications, just as is conventional biopsy. A potential solution to this problem lies in the combination of OCT with confocal microscopy or OCM, as has been suggested by previous investigators [29]. Because OCM is essentially an extension of OCT, integration of OCT and OCM into a single imaging system that can be used clinically is highly feasible. This study was conducted with such a system using an integrated OCT/OCM microscope. The results presented highlight the complementary nature of the information provided by OCT and OCM. OCT images over a larger field of view providing information about architectural morphology while OCM provides a high magnification look at cellular and subcellular structure. OCT technology has advanced rapidly in recent years, with new detection methods leading to improvements in speed of more than a factor of 100 [53, 54]. The increased imaging speed promises to enable wide area coverage, with potential for comprehensive mapping of entire segments of the esophagus or colon [55-57].

With future development of endoscopic devices, OCM may find utility in the range of applications which are currently being studied with confocal microscopy and optical coherence tomography. These include, among others, surveillance for dysplasia in Barrett's esophagus or ulcerative colitis, discrimination between hyperplastic and adenomatous polyps, or identification of tumor margins. In addition, the ability to image with reduced numerical aperture may enable a host of new cellular imaging applications using very small diameter probes. An example of imaging in the pancreas was provided to exemplify the potential image quality that may be obtained in solid organs through needle-based devices. Such applications have been suggested previously for OCT [58], but have been out of reach to confocal devices due to the need for high numerical aperture probes.

Further work is necessary to evaluate clinical indications for optical coherence microscopy. This work was limited to an observational study intended to introduce and validate new technology and to present representative imaging results from throughout the gastrointestinal tract in order to motivate further development. Future work should concentrate on the development of endoscopic imaging probes to enable *in vivo* application. In addition, further *ex vivo* imaging studies must be conducted in a focused manner to investigate specific applications, such as imaging of Barrett's dysplasia, in order to quantify sensitivity and specificity for diagnosis. It will be important in these studies to test blinded interpretation of the images without knowledge of the histopathologic diagnosis. This can be achieved through use of a training data set of histology correlated OCM images to develop image criteria for diagnosis of dysplasia. These criteria should then be applied in a prospective manner to a second validation set of data by observers blinded to the pathologist's histopathology interpretation. Accuracy for diagnosis of dysplasia can then be measured relative to the histologic diagnosis.

## 6.6 Images

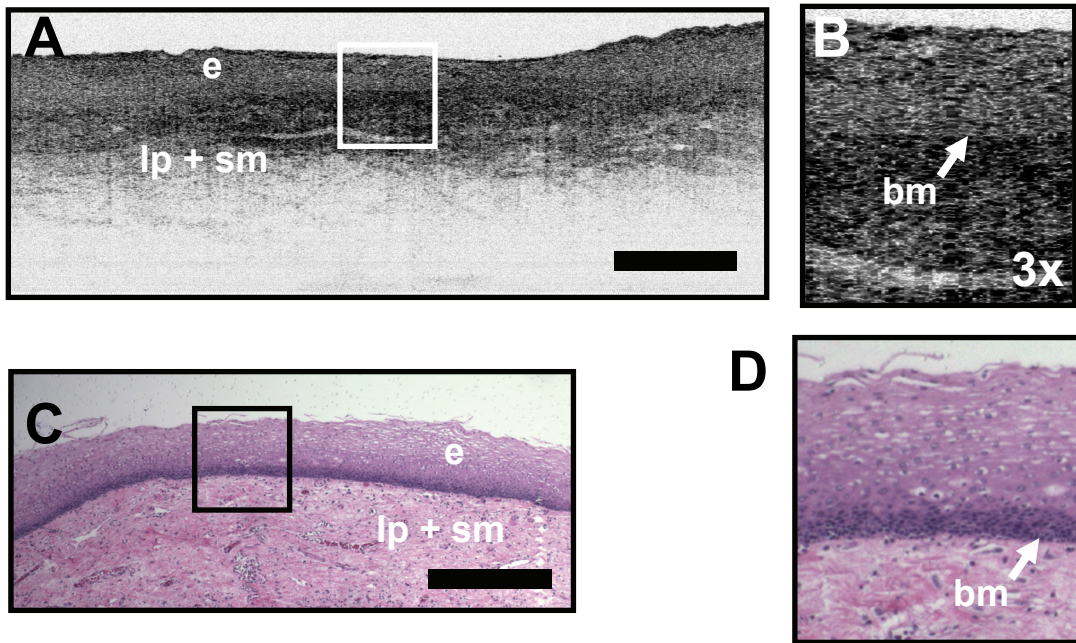


**Figure 6.1.** Ultrahigh-resolution OCT image of normal squamous mucosa. The cross-sectional OCT image (A) and 3x zoom view (B) identify the layered structure of the esophageal mucosa with high resolution. Cross-sectional histology for comparison is provided in (C) and (D). e, epithelium. lp, lamina propria. sm, submucosa. bm, basement membrane zone. Scale bars, 500  $\mu$ m.

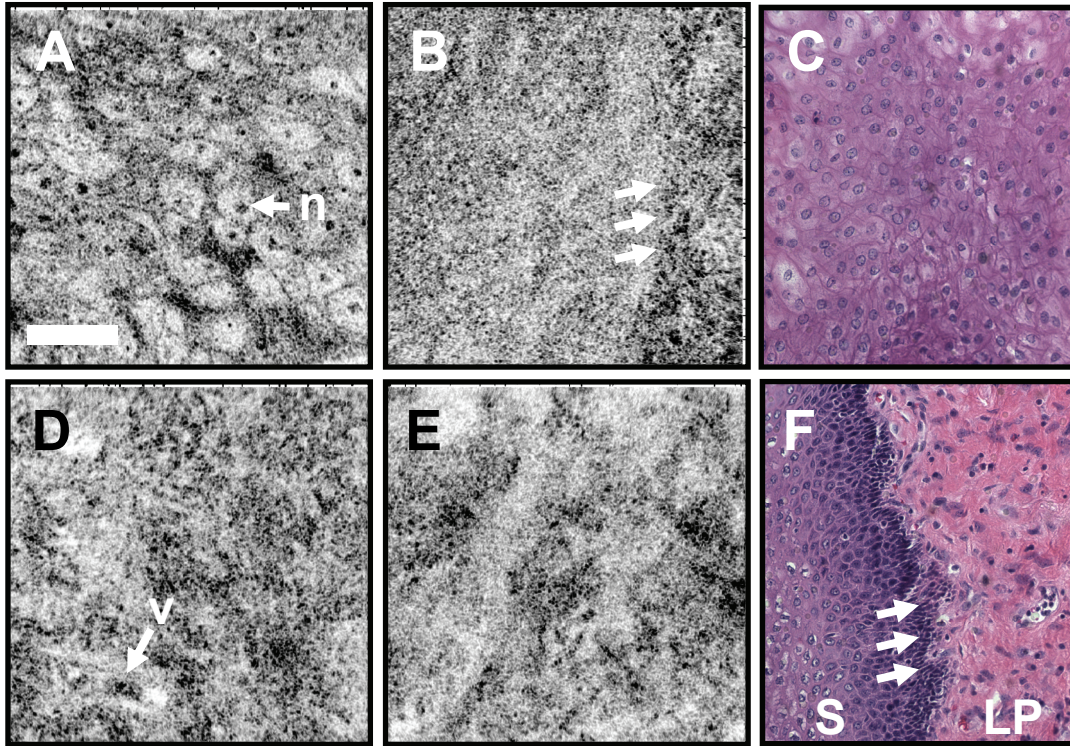


**Figure 6.2.** OCM images of normal squamous mucosa. Cellular features including nuclei (n) and cell membranes are visible in the epithelium (A). The transition between epithelium and underlying lamina propria is also clearly identified (B, arrows). Representative histology in (C) and (F) correlates well with OCM images (A) and (B), respectively. High resolution imaging deep in the lamina propria demonstrates heterogeneous loose connective tissue (D,E). Image depths for (A,B,D,E) are 30, 125, 210, 400  $\mu$ m, respectively. v, vessel. s, squamous epithelium. lp, lamina propria. Scale bar in (A), 100  $\mu$ m, pertains to all images (A-F).

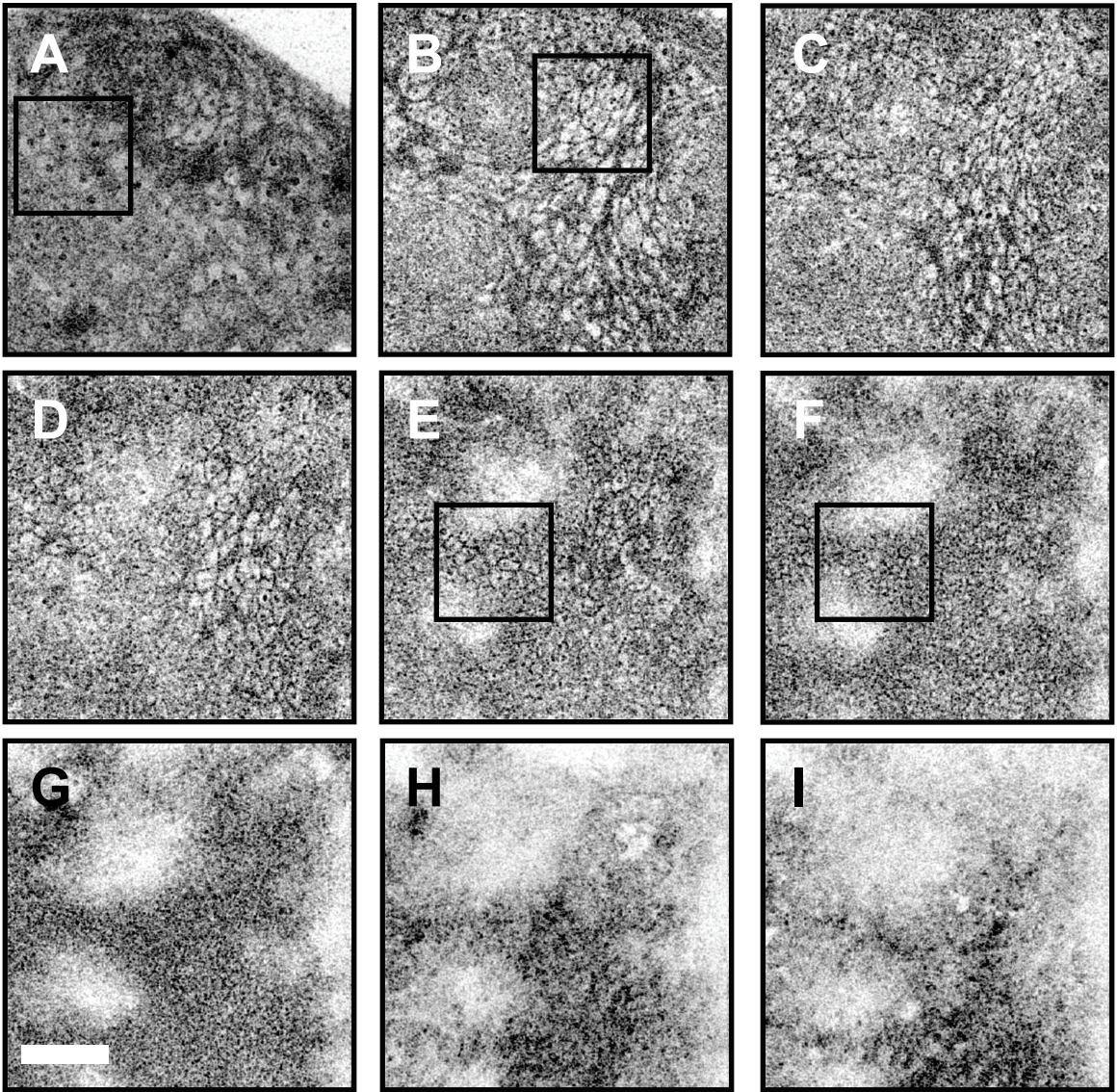


**Figure 6.3.** Progression of cellular architecture with depth in the stratified squamous epithelium. Image depths for (A) thru (I) are: 30, 90, 120, 150, 180, 210, 240, 300, 330  $\mu\text{m}$ , respectively. Scale bar in (G), 100  $\mu\text{m}$ , pertains to all images.

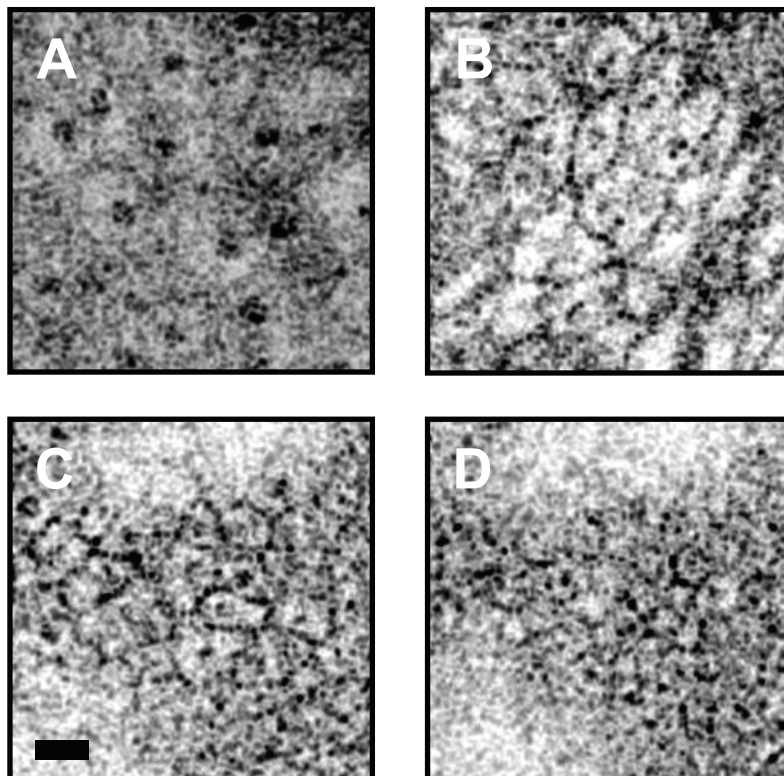


**Figure 6.4.** Zoom views of squamous cells at various depths. High resolution characterization of cell size and arrangement was possible using OCM. Images (A) thru (D) correspond to the boxes shown on images (A), (B), (E), and (F) in figure 6.3. Scale bar in (C), 10  $\mu\text{m}$ , pertains to all images.

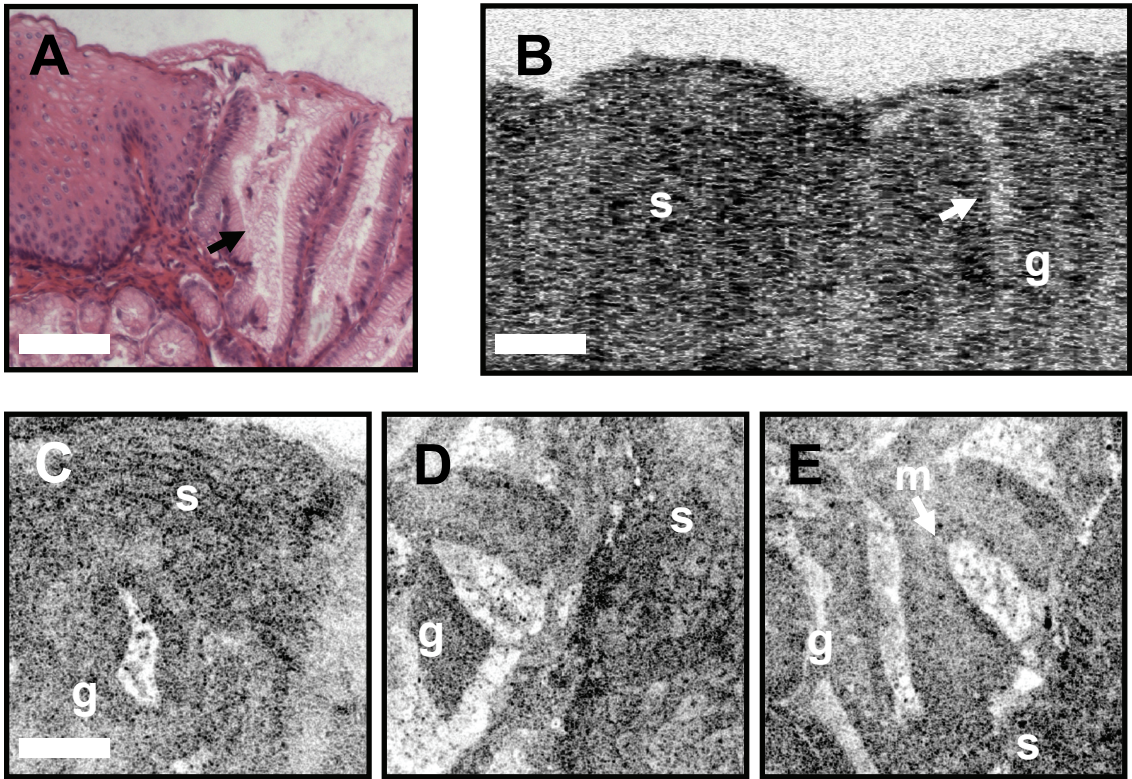


**Figure 6.5** UHR OCT and OCM images of the normal squamo-columnar junction. Gastric (g) and squamous (s) regions of the mucosa can be readily distinguished in both OCT (B) and OCM (C-E) images. OCM also identifies the presence of squamous cells and surface mucous cells (m). Corresponding histology is provided in figure 6.5a. Scale bars, 100  $\mu$ m. Scale bar in (C) pertains to (D) and (E) also.

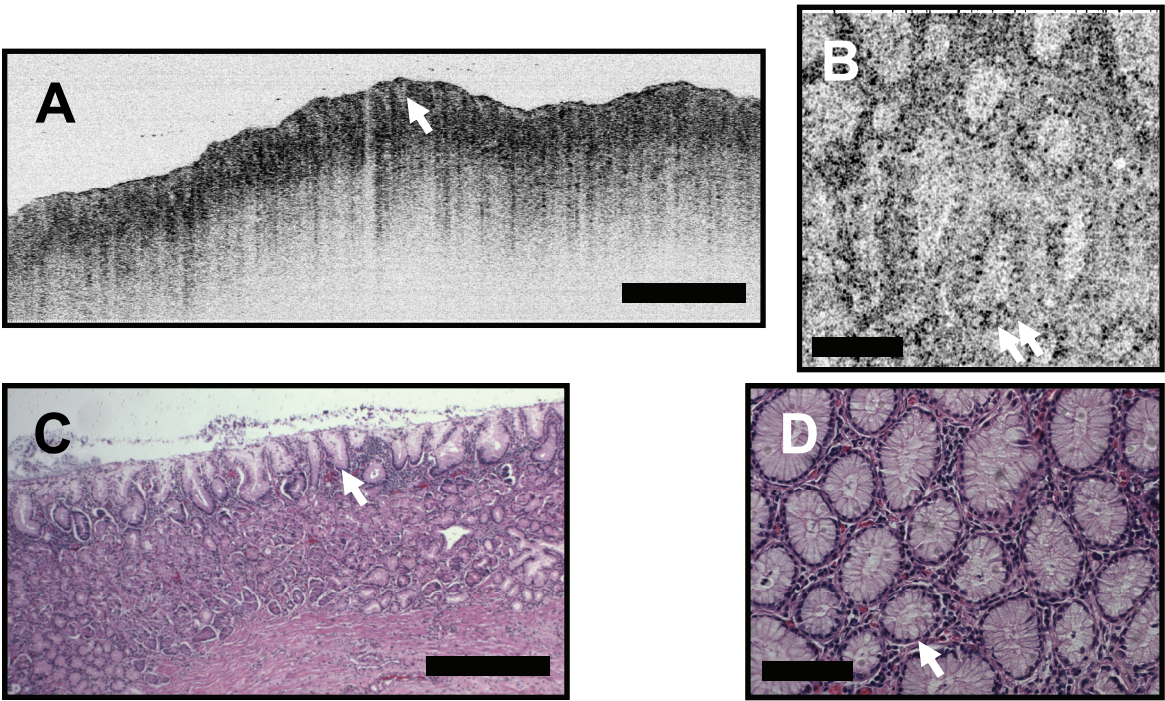


**Figure 6.6.** UHR OCT and OCM images of normal gastric mucosa. The gastric pit architecture is evident in both the OCT (A) and OCM (B) images. Corresponding cross-sectional (C) and en face (D) histology correlates well with the images. Scale bar for (A,C), 500  $\mu\text{m}$ . Scale bar for (B,D), 100  $\mu\text{m}$ .

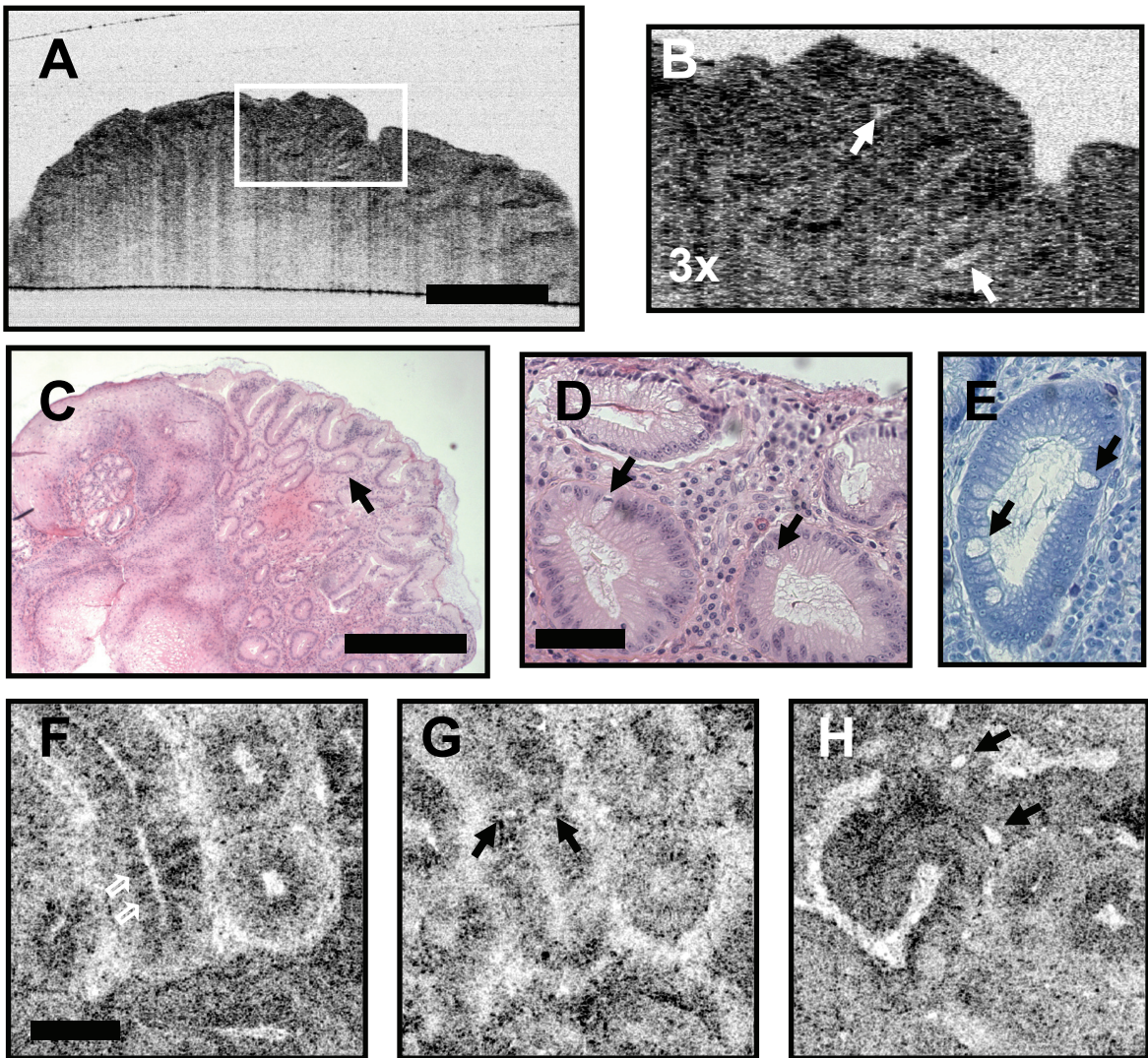


**Figure 6.7.** UHR OCT and OCM images of Barrett's esophagus. The columnar epithelium has a distinct morphology on OCT (A,B) from that seen in the gastric or squamous mucosal tissues. Representative histology in (C) thru (E) demonstrates the glandular architecture with the presence of goblet cells (arrows), the hallmark of specialized intestinal metaplasia. High resolution OCM images in (F) thru (H) visualize the glandular epithelium with the presence of goblet cells (G,H closed arrows). Columnar cell morphology in the glandular epithelium leads to a striated appearance on the OCM images (F, open arrows). Scale bars: (A,C) 500  $\mu$ m; (D-H, 100  $\mu$ m). OCM images in (F-H) were acquired at depths of 90, 150, and 80  $\mu$ m, respectively. Histology in (E) is stained with Alcian Blue to highlight goblet cells.

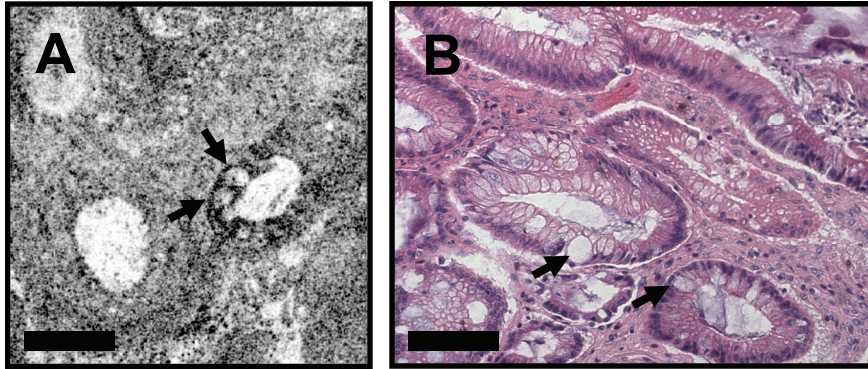


**Figure 6.8.** OCM image of goblet cells in specialized intestinal metaplasia. OCM (A) visualizes low scattering inclusions in the glandular epithelium consistent with goblet cells confirmed on histology (B). Scale bars, 100  $\mu$ m.

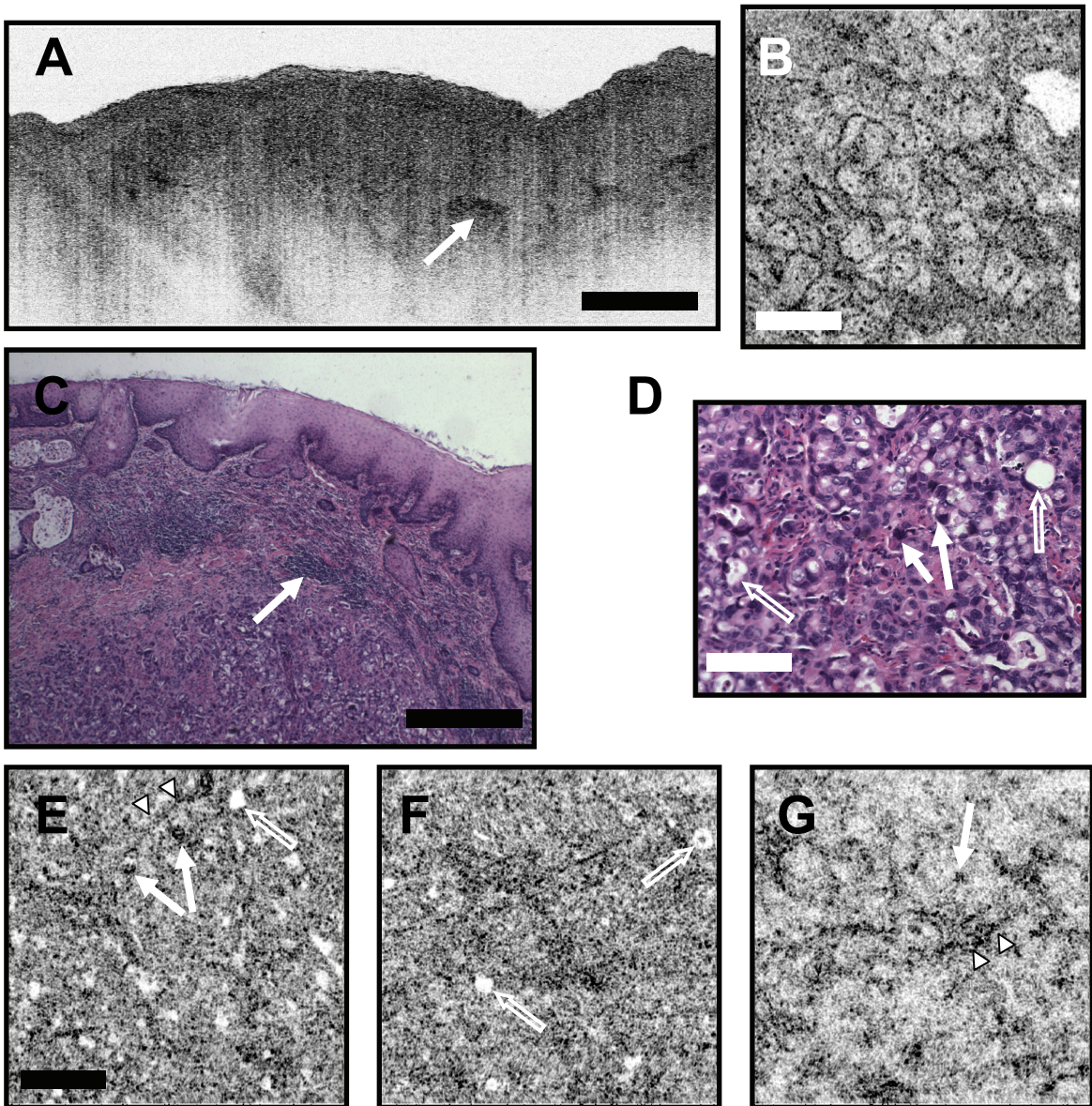


**Figure 6.9.** Images and histology of esophageal adenocarcinoma. The UHR OCT image (A) exhibits loss of characteristic layered pattern of normal squamous mucosa due to the infiltrating tumor, although OCM (B) demonstrates the presence of an intact squamous epithelium. High scattering regions in the OCT image (A, arrow) are consistent with regions of inflammatory infiltrate surrounding the tumor, as seen in the cross-sectional histology (C, arrow). *En Face* OCM (E-G) of the tumor region visualizes the presence of gland forming entities (open arrows) as well as highly scattering cell nuclei (arrows) and elements of tumor stroma (arrowheads). High magnification histology (D) is provided for correlation. Image depths for (E) thru (G) are 50, 50, and 125 um, respectively. Scale bars: (A,C) 500 um; (B,D-G) 100 um.

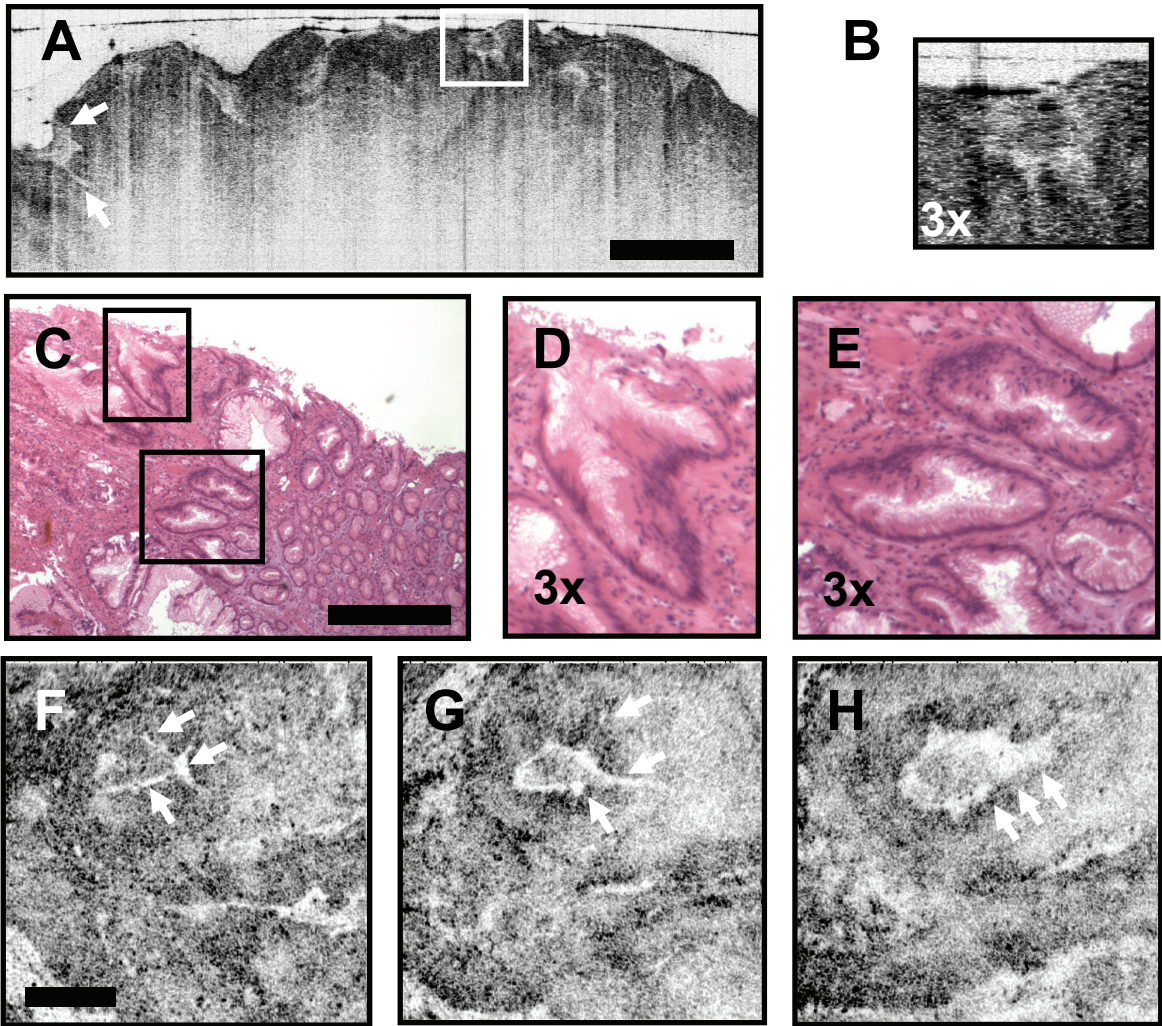


**Figure 6.10.** OCT and OCM of a hyperplastic gastric polyp. UHR OCT (A,B) visualizes serrated epithelial invaginations (arrows, confirmed by histology in (C-D)). Serial *en face* OCM sections (F-H) further highlight the distorted luminal architecture (arrows). Image depths for (F) thru (H) are 100, 150, and 190  $\mu\text{m}$ , respectively. Scale bars (A,C) 500  $\mu\text{m}$ ; (F-H) 100  $\mu\text{m}$ .

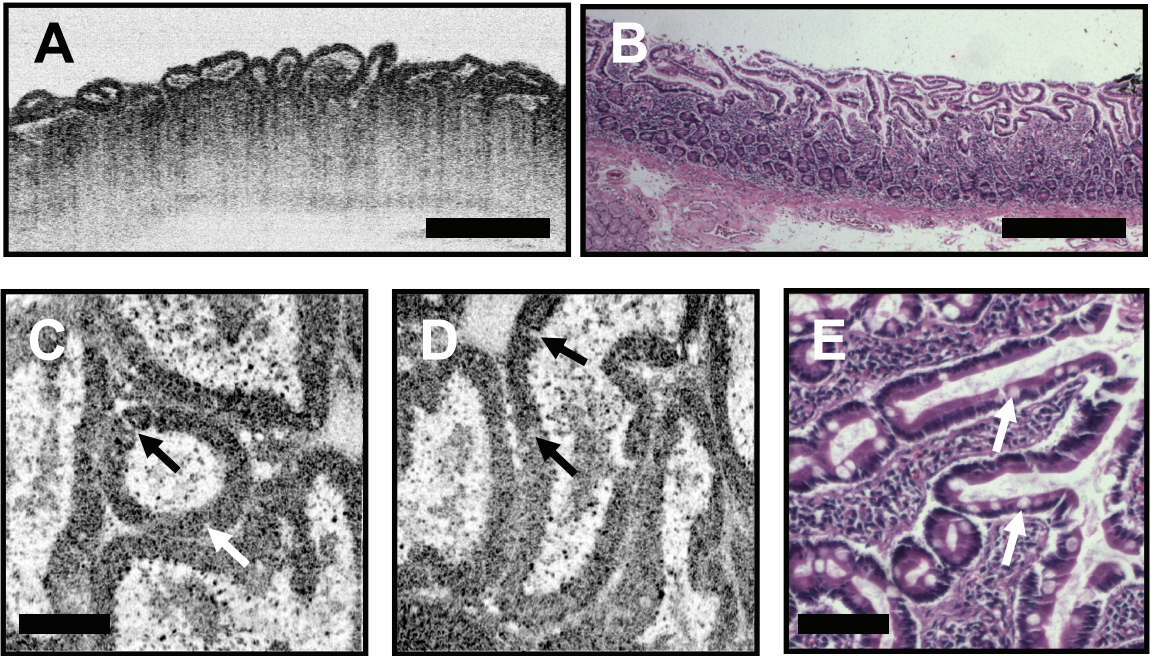


**Figure 6.11.** Corresponding images and histology of normal duodenum. UHR OCT (A) clearly visualizes the villous structure, as evident on histology (B). *En face* OCM images (C,D) display the villous architecture in the transverse plane. Goblet cells are identified in the villous epithelium (arrows) on OCM, with good correspondence to representative *en face* histology (E). Imaging depth for (C) and (D) was 50 – 100  $\mu\text{m}$ . Scale bars: (A,B) 500  $\mu\text{m}$ ; (D-F) 100  $\mu\text{m}$ .

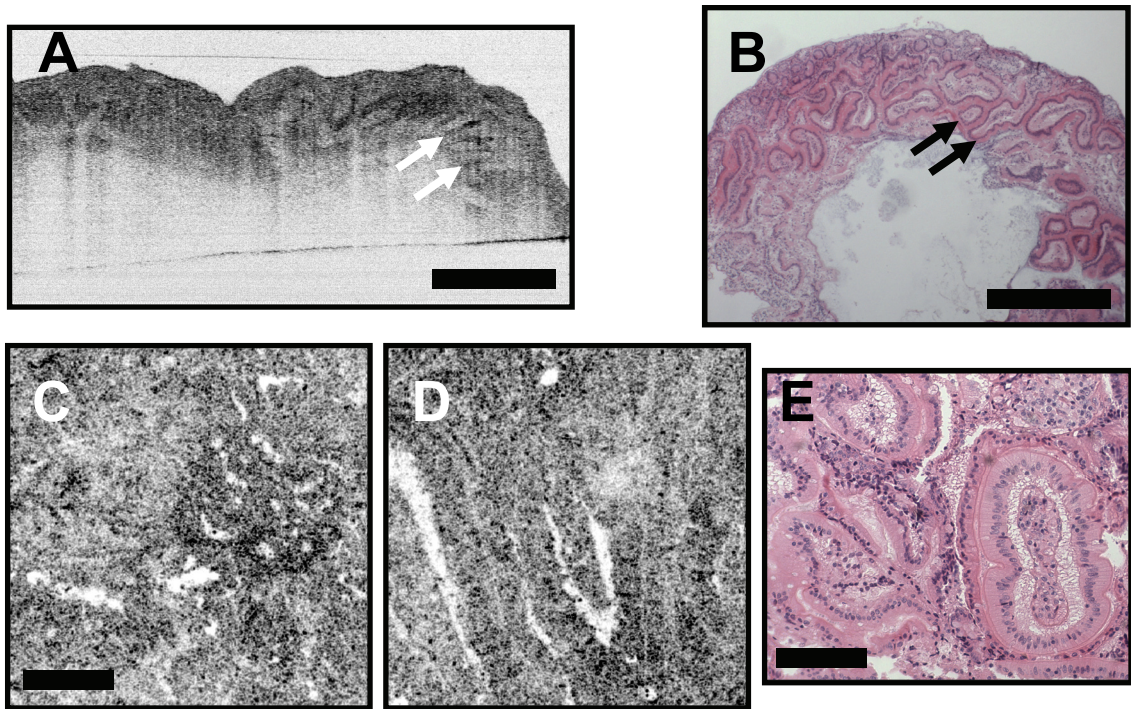


**Figure 6.12.** OCT and OCM images of chronic inflammation in the duodenum. Features in the UHR OCT image (A, arrows) are consistent with blunted villous epithelium seen on histology (B). *En face* OCM (C,D) further confirms the loss of normal villous architecture, although villous epithelium can still be distinguished (D) from surrounding inflammatory infiltrate. OCM image depths for (C) and (D) were 65 and 75  $\mu\text{m}$ , respectively. *En face* histology is provided in (E). Scale bars: (A, B) 500  $\mu\text{m}$ ; (C-E) 100  $\mu\text{m}$ .

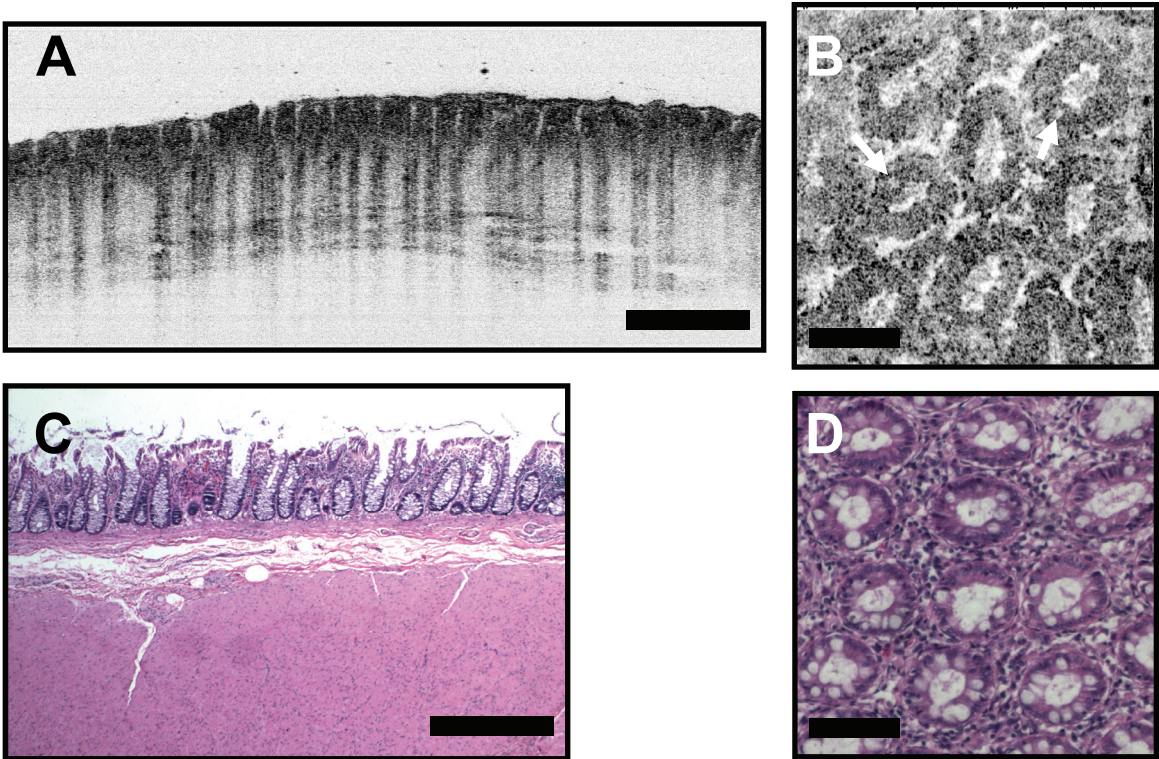


**Figure 6.13.** UHR OCT and OCM images of normal colon. A regular crypt pattern visualized in cross-section on OCT (A) is seen in the transverse plain on OCM (B). Individual goblet cells are seen on OCM (B, arrows). Corresponding cross-sectional (C) and *en face* (D) histology correlate well with the OCT and OCM images, respectively. OCM image depth was 75  $\mu\text{m}$ . Scale bars: (A,C) 500  $\mu\text{m}$ ; (B,D) 100  $\mu\text{m}$ .

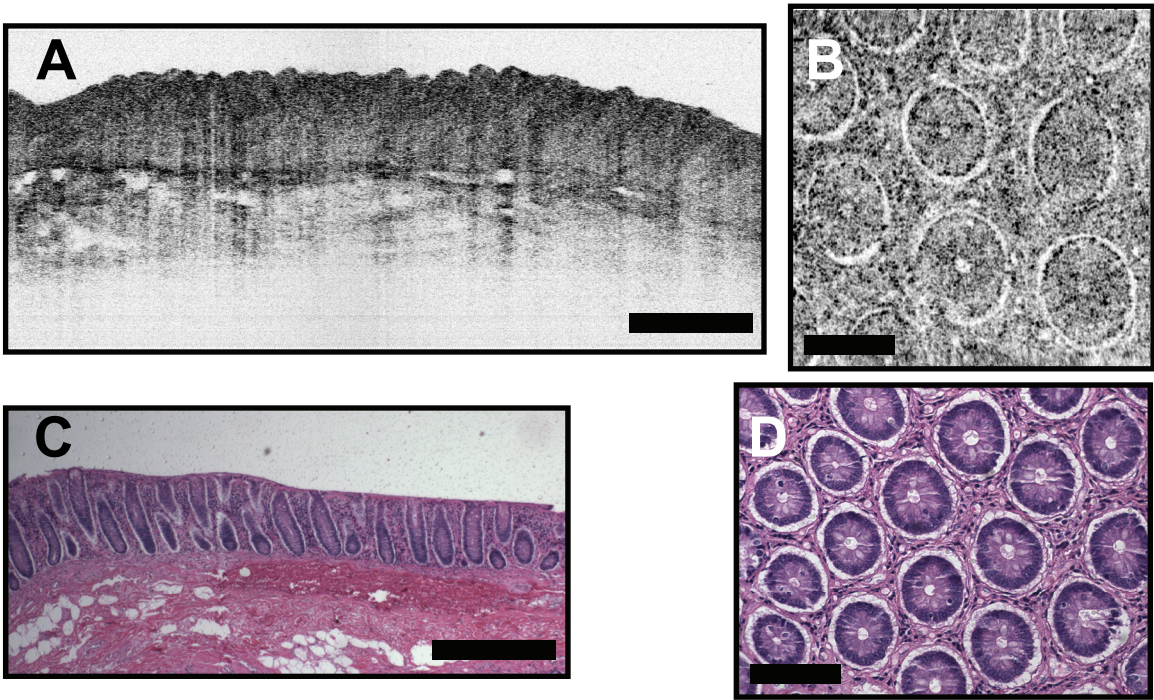


**Figure 6.14.** Variation in normal colon architecture. OCT (A) and OCM (B) picture a crypt morphology with smaller lumens and lower mucin content in the crypt epithelium. Correlation with cross-sectional (C) and *en face* (D) histology confirms these characteristics. OCM image depth was 100 um. Scale bars: (A,C) 500 um; (B,D) 100 um.

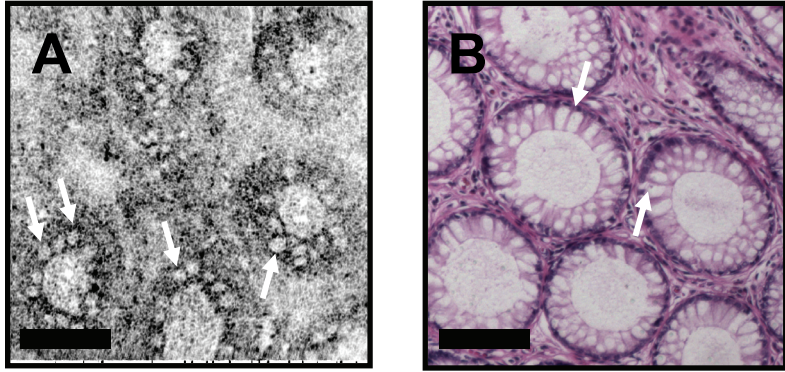


**Figure 6.15.** Goblet cell morphology in colonic crypts visualized with OCM. Numerous goblet cells (arrows) are visible on both the OCM (A) and histology (B) pictures. Scale bars, 100  $\mu\text{m}$ .

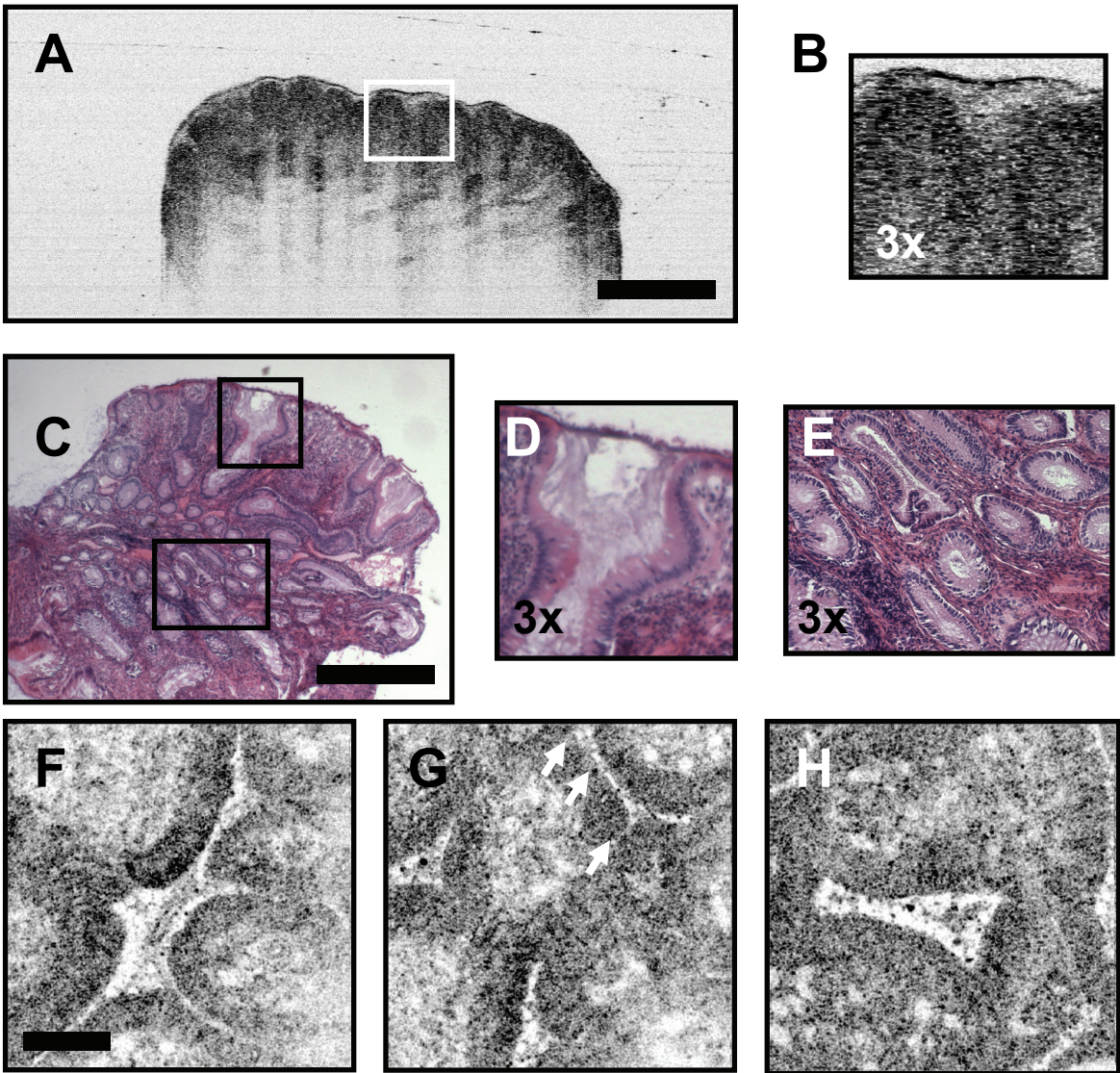


**Figure 6.16.** Images of a hyperplastic polyp of the colon. OCT (A,B) demonstrates a pattern of crypt structure with dilated luminal aspects and poor contrast of the epithelial lining. Representative histology is provided in (C) thru (E) for correlation. *En face* OCM images in (F-H) demonstrate serrated crypt architecture with fairly homogenous scattering of the crypt epithelium. Image depths were 50 – 100  $\mu\text{m}$ . Scale bars: (A,C) 500  $\mu\text{m}$ ; (F-H) 100  $\mu\text{m}$ .

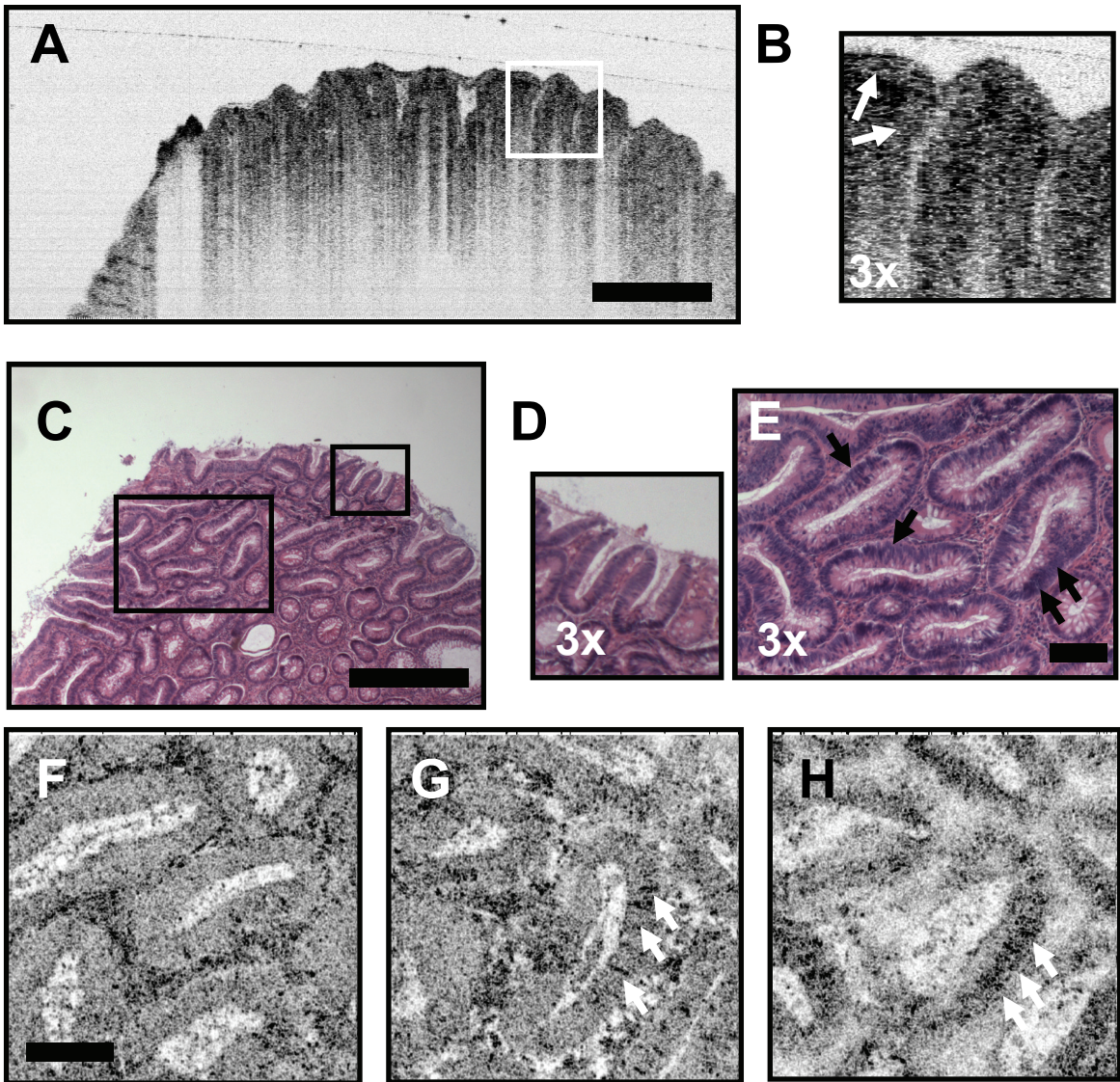


**Figure 6.17.** OCT and OCM images of tubular adenoma of the colon. OCT (A,B) demonstrates a parallel arrangement of long, slender crypt units, with the crypt epithelium identifiable from the lamina propria (B, arrows). Corresponding histology is provided in (C-E). OCM visualizes crypt architecture *en face*, illustrating the eccentric crypt lumens with varying shape and arrangement (F-H). Pseudostratification of oval-shaped nuclei is evident within the crypt epithelium (G,H, arrows). Histology of crypts cut in the transverse plane confirms these features in the specimen (E). OCM image depths for (F) thru (H) were 80, 90, and 190  $\mu\text{m}$ , respectively. Scale bars: (A,C) 500  $\mu\text{m}$ ; (E,F-H) 100  $\mu\text{m}$ .

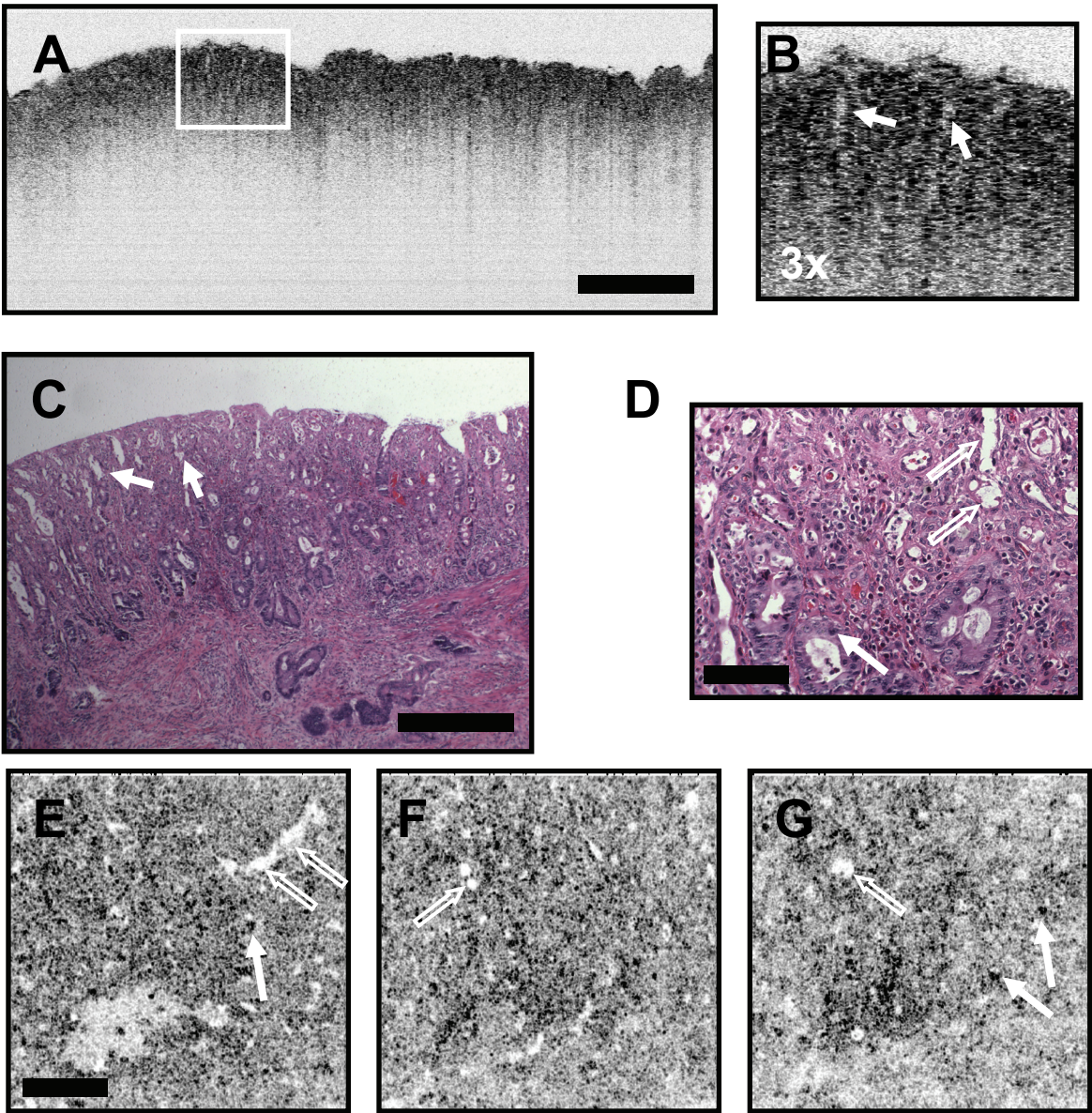


**Figure 6.18.** Imaging of adenocarcinoma in the colon. OCT images (A,B) exhibit limited penetration depth and fine tissue structure consistent with malignant glands seen on histology (C,D, arrows). En face OCM images in (E) thru (G) correlate well with histology, showing small gland forming structures (open arrows) and highly scattering, irregular nuclei (solid arrows). Image depths in tissue for (E) thru (G) were 50, 80, and 125  $\mu\text{m}$ , respectively. Scale bars: (A,C) 500  $\mu\text{m}$ ; (D-G) 100  $\mu\text{m}$ .

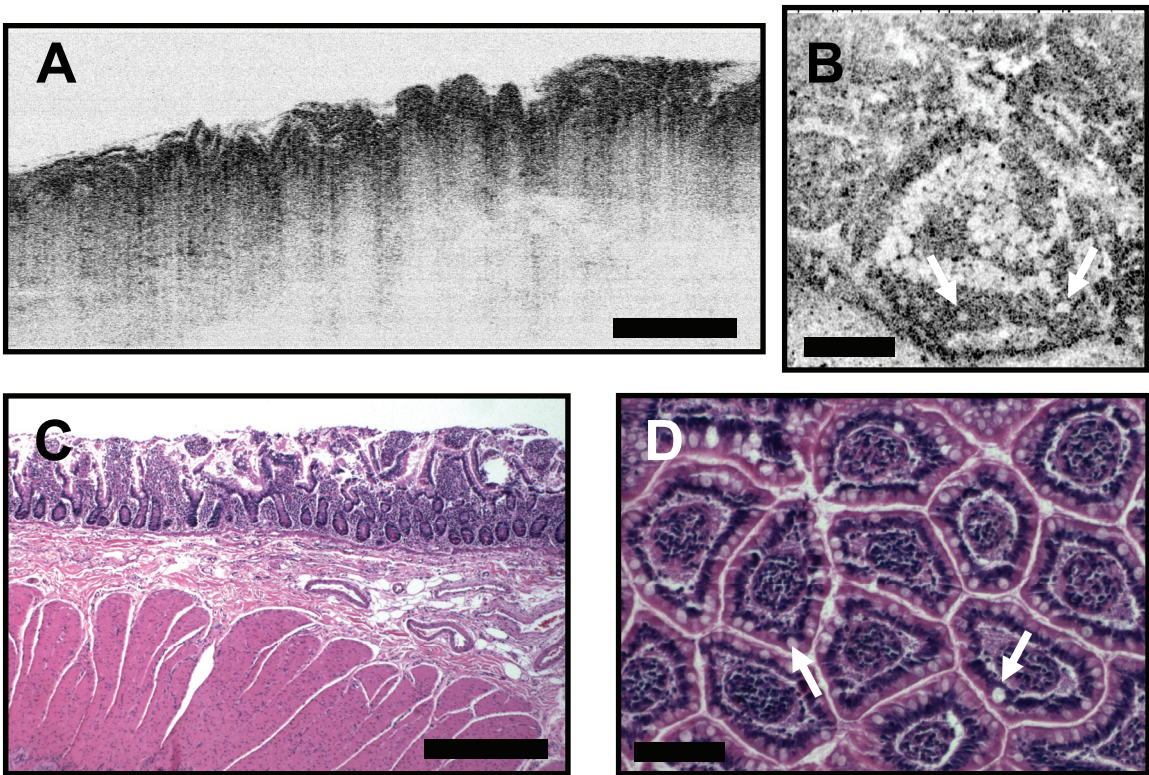


**Figure 6.19.** OCT and OCM images of normal mucosa in the terminal ileum. The UHR OCT image (A) demonstrates villous surface structure, consistent with that seen in histology (C). *En face* OCM provide higher resolution views of the villous epithelium, with prominent goblet cells (arrows). Representative *en face* histology is provided for correlation (D). OCM imaging depth was 135  $\mu\text{m}$ . Scale bars: (A,C) 500  $\mu\text{m}$ ; (B,D) 100  $\mu\text{m}$ .

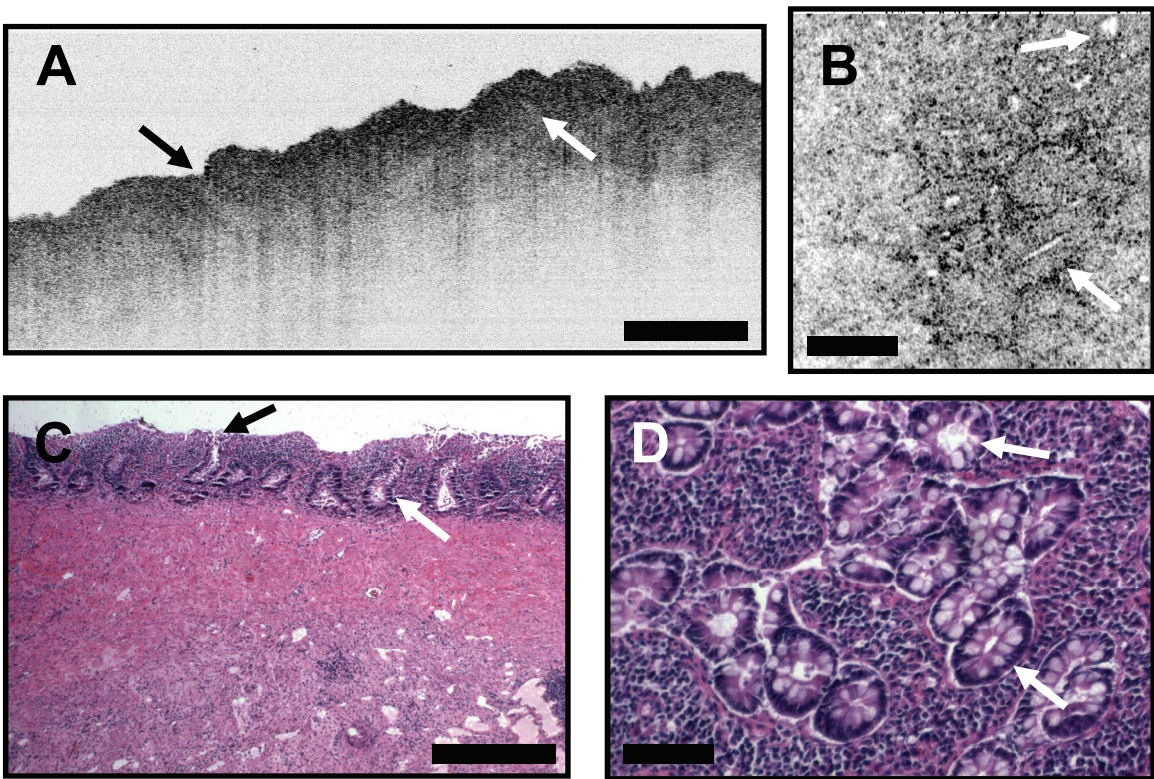


**Figure 6.20.** Imaging of Crohn's disease in the terminal ileum. OCT (A) shows loss of villous architecture with faint outlines of crypts (A, arrows). Cross-sectional histology is provided for comparison (C). OCM images (B) further demonstrate the absence of regular villous structure. Small patches of crypt epithelium are visible (B, arrows), surrounded by inflammatory infiltrate as confirmed by histology (D). OCM imaging depth was 75  $\mu\text{m}$ . Scale bars: (A,C) 500  $\mu\text{m}$ ; (B,D) 100  $\mu\text{m}$ .

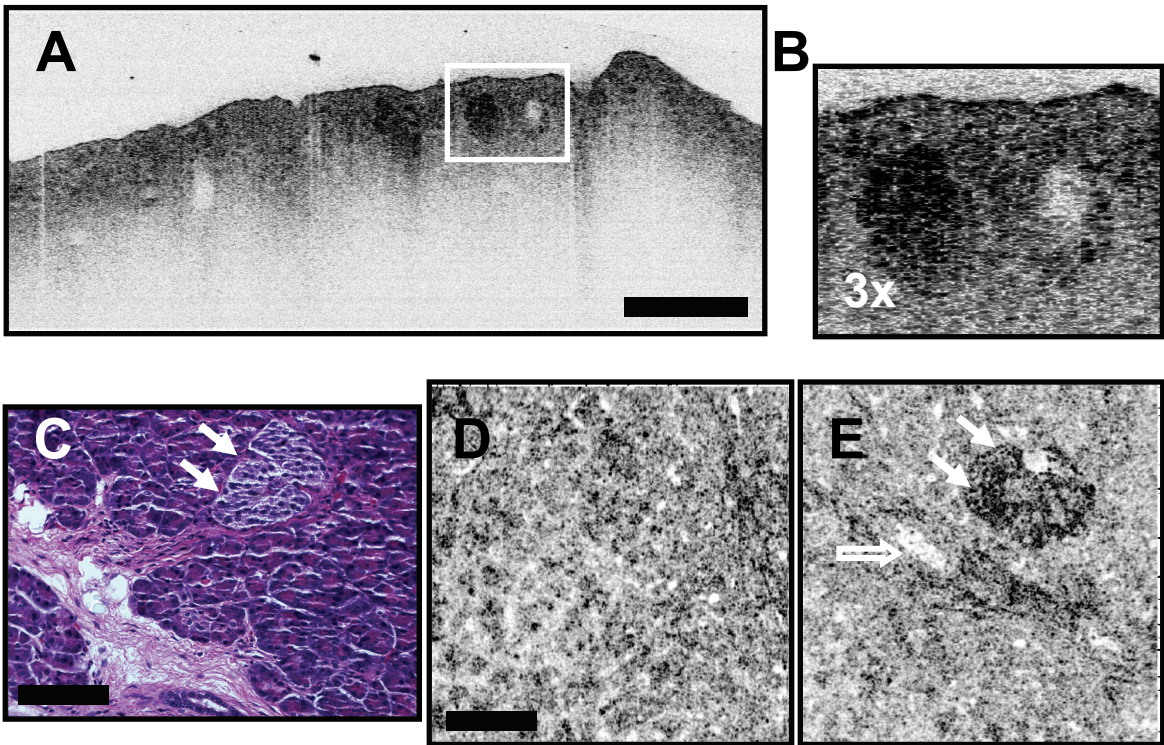


**Figure 6.21.** OCT and OCM images of normal pancreas. OCT (A,B) illustrates the presence of highly scattering islet cell clusters as well as weakly scattering ductal structures. OCM visualizes the mottled appearance of the pancreatic acinar structure (D). In addition, fine features of the islet cell clusters (E, closed arrows) and the ductal epithelium (E, open arrows) can be appreciated. OCM image depths were 75 – 100  $\mu\text{m}$ . Representative histology is provided (C). Scale bars: (A), 500  $\mu\text{m}$ ; (C-E) 100  $\mu\text{m}$ .

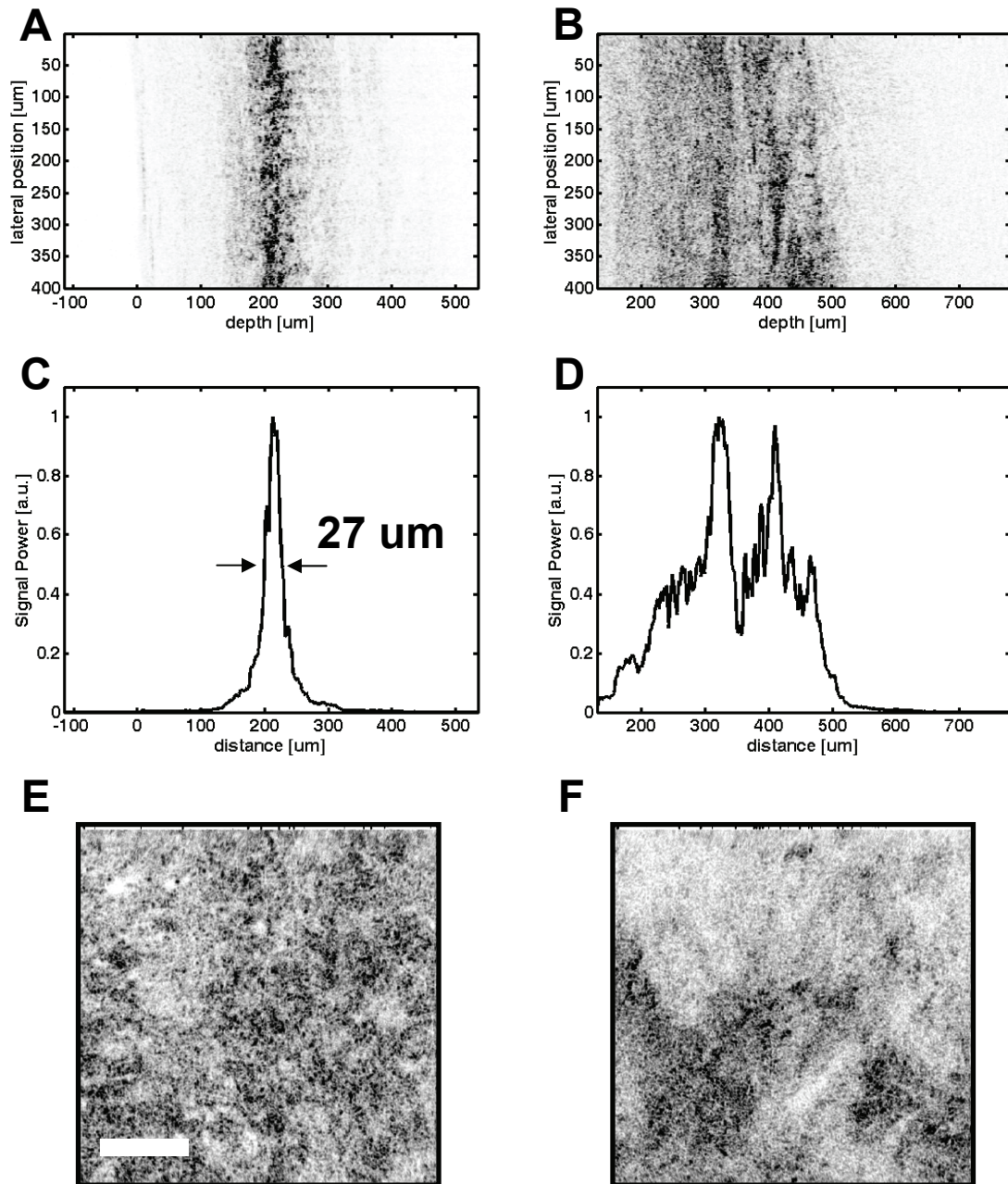


**Figure 6.22.** Measurement of confocal axial response in scattering tissue. At a focal depth of 215 μm, a tight focus is maintained, leading to a restricted depth of field in the cross-sectional image (A) and a narrow axial response (C). At a depth of 450 μm, the ability to focus in tissue has been largely lost (B), resulting in a poor confocal axial response (D). Images at corresponding depths (E, 215 μm and F, 450 μm) indicate that OCM maintains strong signal and contrast at the greater depth, although resolution has degraded relative to the shallow depth. Scale bar, 100 μm.

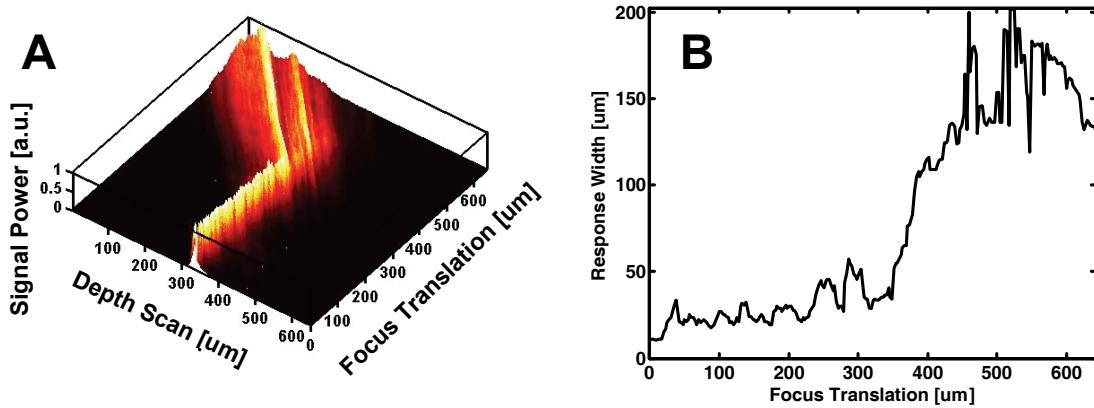


**Figure 6.23.** Focusing properties in scattering tissue as a function of focal depth. (A) 3D representation showing confocal axial response as a function of scanned path length and focus translation. (B) Width of confocal response as a function of focus translation.

## 6.6 References

- [1] E. I. Sidorenko and P. Sharma, "High-resolution chromoendoscopy in the esophagus," *Gastrointest Endosc Clin N Am*, vol. 14, pp. 437-51, vii, 2004.
- [2] M. Guelrud and E. E. Ehrlich, "Enhanced magnification endoscopy in the upper gastrointestinal tract," *Gastrointest Endosc Clin N Am*, vol. 14, pp. 461-73, viii, 2004.
- [3] H. Inoue, T. Kazawa, Y. Sato, H. Satodate, K. Sasajima, S. E. Kudo, and A. Shiokawa, "In vivo observation of living cancer cells in the esophagus, stomach, and colon using catheter-type contact endoscope, "Endo-Cytoscopy system"," *Gastrointest Endosc Clin N Am*, vol. 14, pp. 589-94, x-xi, 2004.
- [4] G. J. Tearney, M. E. Brezinski, B. E. Bouma, S. A. Boppart, C. Pitris, J. F. Southern, and J. G. Fujimoto, "In vivo endoscopic optical biopsy with optical coherence tomography," *Science*, vol. 276, pp. 2037-9, 1997.
- [5] B. E. Bouma, G. J. Tearney, C. C. Compton, and N. S. Nishioka, "High-resolution imaging of the human esophagus and stomach in vivo using optical coherence tomography," *Gastrointest Endosc*, vol. 51, pp. 467-74, 2000.
- [6] M. V. Sivak, Jr., K. Kobayashi, J. A. Izatt, A. M. Rollins, R. Ung-Runyawee, A. Chak, R. C. Wong, G. A. Isenberg, and J. Willis, "High-resolution endoscopic imaging of the GI tract using optical coherence tomography," *Gastrointest Endosc*, vol. 51, pp. 474-9, 2000.
- [7] X. D. Li, S. A. Boppart, J. Van Dam, H. Mashimo, M. Mutinga, W. Drexler, M. Klein, C. Pitris, M. L. Krinsky, M. E. Brezinski, and J. G. Fujimoto, "Optical coherence tomography: advanced technology for the endoscopic imaging of Barrett's esophagus," *Endoscopy*, vol. 32, pp. 921-30, 2000.
- [8] A. M. Sergeev, V. M. Gelikonov, G. V. Gelikonov, F. I. Feldchtein, R. V. Kuranov, N. D. Gladkova, N. M. Shakhova, L. B. Suopova, A. V. Shakhov, I. A. Kuznetzova, A. N. Denisenko, V. V. Pochinko, Y. P. Chumakov, and O. S. Streltzova, "In vivo endoscopic OCT imaging of precancer and cancer states of human mucosa," *Optics Express*, vol. 1, 1997.
- [9] G. Zuccaro, N. Gladkova, J. Vargo, F. Feldchtein, E. Zagaynova, D. Conwell, G. Falk, J. Goldblum, J. Dumot, J. Ponsky, G. Gelikonov, B. Davros, E. Donchenko, and J. Richter, "Optical coherence tomography of the esophagus and proximal stomach in health and disease," *Am J Gastroenterol*, vol. 96, pp. 2633-9, 2001.
- [10] J. M. Ponerros, S. Brand, B. E. Bouma, G. J. Tearney, C. C. Compton, and N. S. Nishioka, "Diagnosis of specialized intestinal metaplasia by optical coherence tomography," *Gastroenterology*, vol. 120, pp. 7-12, 2001.
- [11] P. R. Pfau, M. V. Sivak, Jr., A. Chak, M. Kinnard, R. C. Wong, G. A. Isenberg, J. A. Izatt, A. Rollins, and V. Westphal, "Criteria for the diagnosis of dysplasia by endoscopic optical coherence tomography," *Gastrointest Endosc*, vol. 58, pp. 196-202, 2003.
- [12] G. Isenberg, M. V. Sivak, Jr., A. Chak, R. C. Wong, J. E. Willis, B. Wolf, D. Y. Rowland, A. Das, and A. Rollins, "Accuracy of endoscopic optical coherence tomography in the detection of dysplasia in Barrett's esophagus: a prospective, double-blinded study," *Gastrointest Endosc*, vol. 62, pp. 825-31, 2005.
- [13] J. A. Evans, J. M. Ponerros, B. E. Bouma, J. Bressner, E. F. Halpern, M. Shishkov, G. Y. Lauwers, M. Mino-Kenudson, N. S. Nishioka, and G. J. Tearney, "Optical coherence tomography to identify intramucosal carcinoma and high-grade dysplasia in Barrett's esophagus," *Clin Gastroenterol Hepatol*, vol. 4, pp. 38-43, 2006.
- [14] P. R. Herz, Y. Chen, A. D. Aguirre, J. G. Fujimoto, H. Mashimo, J. Schmitt, A. Koski, J. Goodnow, and C. Petersen, "Ultrahigh resolution optical biopsy with endoscopic optical coherence tomography," *Optics Express*, vol. 12, pp. 3532-3542, 2004.
- [15] Y. Chen, A. D. Aguirre, P. L. Hsiung, S. Desai, P. R. Herz, M. Pedrosa, Q. Huang, M. Figueiredo, S. W. Huang, A. Koski, J. M. Schmitt, J. G. Fujimoto, and H. Mashimo, "Ultrahigh

- resolution optical coherence tomography of Barrett's esophagus: preliminary descriptive clinical study correlating images with histology," *Endoscopy*, vol. 39, pp. 599-605, 2007.
- [16] S. Gonzalez, K. Swindells, M. Rajadhyaksha, and A. Torres, "Changing paradigms in dermatology: Confocal microscopy in clinical and surgical dermatology," *Clinics in Dermatology*, vol. 21, pp. 359-369, 2003.
- [17] M. Rajadhyaksha, S. Gonzalez, J. M. Zavislan, R. R. Anderson, and R. H. Webb, "In vivo confocal scanning laser microscopy of human skin II: Advances in instrumentation and comparison with histology," *Journal of Investigative Dermatology*, vol. 113, pp. 293-303, 1999.
- [18] K. B. Sung, R. Richards-Kortum, M. Follen, A. Malpica, C. Liang, and M. R. Descour, "Fiber optic confocal reflectance microscopy: a new real-time technique to view nuclear morphology in cervical squamous epithelium in vivo," *Optics Express*, vol. 11, pp. 3171-3181, 2003.
- [19] W. M. White, M. Rajadhyaksha, S. Gonzalez, R. L. Fabian, and R. R. Anderson, "Noninvasive imaging of human oral mucosa in vivo by confocal reflectance microscopy," *Laryngoscope*, vol. 109, pp. 1709-1717, 1999.
- [20] P. W. Chiu, H. Inoue, H. Satodate, T. Kazawa, T. Yoshida, M. Sakashita, and S. E. Kudo, "Validation of the quality of histological images obtained of fresh and formalin-fixed specimens of esophageal and gastric mucosa by laser-scanning confocal microscopy," *Endoscopy*, vol. 38, pp. 236-40, 2006.
- [21] H. Inoue, T. Igari, T. Nishikage, K. Ami, T. Yoshida, and T. Iwai, "A novel method of virtual histopathology using laser-scanning confocal microscopy in-vitro with untreated fresh specimens from the gastrointestinal mucosa," *Endoscopy*, vol. 32, pp. 439-43, 2000.
- [22] M. Sakashita, H. Inoue, H. Kashida, J. Tanaka, J. Y. Cho, H. Satodate, E. Hidaka, T. Yoshida, N. Fukami, Y. Tamegai, A. Shiokawa, and S. Kudo, "Virtual histology of colorectal lesions using laser-scanning confocal microscopy," *Endoscopy*, vol. 35, pp. 1033-8, 2003.
- [23] D. L. Dickensheets and G. S. Kino, "Micromachined scanning confocal optical microscope," *Optics Letters*, vol. 21, pp. 764-6, 1996.
- [24] G. J. Tearney, R. H. Webb, and B. E. Bouma, "Spectrally encoded confocal microscopy," *Optics Letters*, vol. 23, pp. 1152-1154, 1998.
- [25] C. Liang, K. B. Sung, R. R. Richards-Kortum, and M. R. Descour, "Design of a high-numerical-aperture miniature microscope objective for an endoscopic fiber confocal reflectance microscope," *Appl Opt*, vol. 41, pp. 4603-10, 2002.
- [26] T. D. Wang, "Confocal microscopy from the bench to the bedside," *Gastrointest Endosc*, vol. 62, pp. 696-7, 2005.
- [27] A. L. Polglase, W. J. McLaren, S. A. Skinner, R. Kiesslich, M. F. Neurath, and P. M. Delaney, "A fluorescence confocal endomicroscope for in vivo microscopy of the upper- and the lower-GI tract," *Gastrointest Endosc*, vol. 62, pp. 686-95, 2005.
- [28] R. Kiesslich, J. Burg, M. Vieth, J. Gnaendiger, M. Enders, P. Delaney, A. Polglase, W. McLaren, D. Janell, S. Thomas, B. Nafe, P. R. Galle, and M. F. Neurath, "Confocal laser endoscopy for diagnosing intraepithelial neoplasias and colorectal cancer in vivo," *Gastroenterology*, vol. 127, pp. 706-13, 2004.
- [29] R. Kiesslich, L. Gossner, M. Goetz, A. Dahlmann, M. Vieth, M. Stolte, A. Hoffman, M. Jung, B. Nafe, P. R. Galle, and M. F. Neurath, "In Vivo Histology of Barrett's Esophagus and Associated Neoplasia by Confocal Laser Endomicroscopy," *Clin Gastroenterol Hepatol*, 2006.
- [30] J. A. Izatt, M. R. Hee, G. M. Owen, E. A. Swanson, and J. G. Fujimoto, "Optical coherence microscopy in scattering media," *Optics Letters*, vol. 19, pp. 590-2, 1994.
- [31] S. Brand, J. M. Ponomarev, B. E. Bouma, G. J. Tearney, C. C. Compton, and N. S. Nishioka, "Optical coherence tomography in the gastrointestinal tract," *Endoscopy*, vol. 32, pp. 796-803, 2000.
- [32] A. D. Aguirre, P. Hsiung, T. H. Ko, I. Hartl, and J. G. Fujimoto, "High-resolution optical coherence microscopy for high-speed, in vivo cellular imaging," *Opt Lett*, vol. 28, pp. 2064-6, 2003.

- [33] J. A. Izatt, M. D. Kulkarni, H.-W. Wang, K. Kobayashi, and M. V. Sivak, Jr., "Optical coherence tomography and microscopy in gastrointestinal tissues," *IEEE Journal of Selected Topics in Quantum Electronics*, vol. 2, pp. 1017-28, 1996.
- [34] A. L. Clark, A. Gillenwater, R. Alizadeh-Naderi, A. K. El-Naggar, and R. Richards-Kortum, "Detection and diagnosis of oral neoplasia with an optical coherence microscope," *J Biomed Opt*, vol. 9, pp. 1271-80, 2004.
- [35] P. L. Hsiung, L. Pantanowitz, A. D. Aguirre, Y. Chen, D. Phatak, T. H. Ko, S. Bourquin, S. J. Schnitt, S. Raza, J. L. Connolly, H. Mashimo, and J. G. Fujimoto, "Ultrahigh-resolution and 3-dimensional optical coherence tomography ex vivo imaging of the large and small intestines," *Gastrointest Endosc*, vol. 62, pp. 561-74, 2005.
- [36] R. D. Odze, J. R. Goldblum, and J. M. Crawford, *Surgical Pathology of the GI Tract, Liver, Biliary Tract, and Pancreas*, 1st ed. Philadelphia: Saunders, 2004.
- [37] G. J. Tearney, M. E. Brezinski, J. F. Southern, B. E. Bouma, S. A. Boppart, and J. G. Fujimoto, "Optical biopsy in human pancreatobiliary tissue using optical coherence tomography," *Dig Dis Sci*, vol. 43, pp. 1193-9, 1998.
- [38] G. J. Tearney, S. A. Boppart, B. E. Bouma, M. E. Brezinski, N. J. Weissman, J. F. Southern, and J. G. Fujimoto, "Scanning single-mode fiber optic catheter-endoscope for optical coherence tomography," *Optics Letters*, vol. 21, pp. 543-5, 1996.
- [39] W. Jung, D. T. McCormick, J. Zhang, L. Wang, N. C. Tien, and Z. P. Chen, "Three-dimensional endoscopic optical coherence tomography by use of a two-axis microelectromechanical scanning mirror," *Applied Physics Letters*, vol. 88, pp. -, 2006.
- [40] X. Liu, M. J. Cobb, Y. Chen, M. B. Kimmey, and X. Li, "Rapid-scanning forward-imaging miniature endoscope for real-time optical coherence tomography," *Opt Lett*, vol. 29, pp. 1763-5, 2004.
- [41] J. Sawinski and W. Denk, "Miniature random-access fiber scanner for in vivo multiphoton imaging," *Journal of Applied Physics*, vol. 102, pp. -, 2007.
- [42] M. J. Booth, M. A. Neil, R. Juskaitis, and T. Wilson, "Adaptive aberration correction in a confocal microscope," *Proc Natl Acad Sci U S A*, vol. 99, pp. 5788-92, 2002.
- [43] M. Schwertner, M. J. Booth, M. A. Neil, and T. Wilson, "Measurement of specimen-induced aberrations of biological samples using phase stepping interferometry," *J Microsc*, vol. 213, pp. 11-9, 2004.
- [44] W. Drexler, U. Morgner, R. K. Ghanta, F. X. Kartner, J. S. Schuman, and J. G. Fujimoto, "Ultrahigh-resolution ophthalmic optical coherence tomography," *Nat Med*, vol. 7, pp. 502-7, 2001.
- [45] T. Collier, A. Lacy, R. Richards-Kortum, A. Malpica, and M. Follen, "Near real-time confocal microscopy of amelanotic tissue: Detection of dysplasia in ex vivo cervical tissue," *Academic Radiology*, vol. 9, pp. 504-512, 2002.
- [46] A. L. Clark, A. M. Gillenwater, T. G. Collier, R. Alizadeh-Naderi, A. K. El-Naggar, and R. R. Richards-Kortum, "Confocal microscopy for real-time detection of oral cavity neoplasia," *Clinical Cancer Research*, vol. 9, pp. 4714-4721, 2003.
- [47] R. A. Drezek, T. Collier, C. K. Brookner, A. Malpica, R. Lotan, R. R. Richards-Kortum, and M. Follen, "Laser scanning confocal microscopy of cervical tissue before and after application of acetic acid," *American Journal of Obstetrics and Gynecology*, vol. 182, pp. 1135-1139, 2000.
- [48] D. L. Marks, T. S. Ralston, and S. A. Boppart, "Speckle reduction by I-divergence regularization in optical coherence tomography," *J Opt Soc Am A Opt Image Sci Vis*, vol. 22, pp. 2366-71, 2005.
- [49] D. C. Adler, T. H. Ko, and J. G. Fujimoto, "Speckle reduction in optical coherence tomography images by use of a spatially adaptive wavelet filter," *Opt Lett*, vol. 29, pp. 2878-80, 2004.
- [50] M. Pircher, E. Gotzinger, R. Leitgeb, A. F. Fercher, and C. K. Hitzenberger, "Speckle reduction in optical coherence tomography by frequency compounding," *J Biomed Opt*, vol. 8, pp. 565-9, 2003.

- [51] J. M. Schmitt, "Array detection for speckle reduction in optical coherence microscopy," *Phys Med Biol*, vol. 42, pp. 1427-39, 1997.
- [52] A. E. Desjardins, B. J. Vakoc, G. J. Tearney, and B. E. Bouma, "Speckle reduction in OCT using massively-parallel detection and frequency-domain ranging," *Optics Express*, vol. 14, pp. 4736-4745, 2006.
- [53] S. H. Yun, G. J. Tearney, J. F. de Boer, N. Iftimia, and B. E. Bouma, "High-speed optical frequency-domain imaging," *Optics Express*, vol. 11, pp. 2953-2963, 2003.
- [54] R. Huber, M. Wojtkowski, and J. G. Fujimoto, "Fourier Domain Mode Locking (FDML): A new laser operating regime and applications for optical coherence tomography," *Optics Express*, vol. 14, pp. 3225-3237, 2006.
- [55] S. H. Yun, G. J. Tearney, B. J. Vakoc, M. Shishkov, W. Y. Oh, A. E. Desjardins, M. J. Suter, R. C. Chan, J. A. Evans, I. K. Jang, N. S. Nishioka, J. F. de Boer, and B. E. Bouma, "Comprehensive volumetric optical microscopy in vivo," *Nat Med*, vol. 12, pp. 1429-33, 2006.
- [56] B. J. Vakoc, M. Shishko, S. H. Yun, W. Y. Oh, M. J. Suter, A. E. Desjardins, J. A. Evans, N. S. Nishioka, G. J. Tearney, and B. E. Bouma, "Comprehensive esophageal microscopy by using optical frequency-domain imaging (with video)," *Gastrointest Endosc*, vol. 65, pp. 898-905, 2007.
- [57] D. C. Adler, Y. Chen, R. Huber, J. Schmitt, J. Connolly, and J. G. Fujimoto, "Three-dimensional endomicroscopy using optical coherence tomography," *Nature Photonics*, vol. 1, pp. 709-716, 2007.
- [58] J. H. Hwang, M. J. Cobb, M. B. Kimmey, and X. Li, "Optical coherence tomography imaging of the pancreas: a needle-based approach," *Clin Gastroenterol Hepatol*, vol. 3, pp. S49-52, 2005.

## Chapter 7

### Three-Dimensional Projection OCT Imaging of Gastrointestinal Tissues

#### 7.1 Overview and Introduction

OCT imaging speeds have rapidly increased in recent years due to the advent of Fourier-domain OCT imaging methods [1-8]. With imaging speeds more than 100 times greater than those available with time-domain OCT approaches, *in vivo* volumetric imaging is now possible, and has already been demonstrated by multiple groups in the retina [9-11] as well as the gastrointestinal and cardiovascular systems [12-14]. With OCT systems now capable of producing large amounts of volumetric data, a need exists for new OCT visualization methods that capture the richness of the three-dimensional data sets.

For the application of gastrointestinal endoscopy, *en face* views provide an important complement to the conventional cross-sectional OCT images. *En face* OCT allows interpretation of tissue features in the plane of the standard endoscopic view and can generate views similar in principle to those provided by magnification endoscopes used clinically. The ability to register OCT image data sets with standard clinical views will facilitate interpretation by clinicians and will improve localization of images to important tissue landmarks.

In contrast to OCT, white light and magnification endoscopes lack the ability to section in depth and individual images therefore represent a sum of light returning from all depths. Analogous views can be reconstructed from three-dimensional OCT data sets by summing along the depth dimension to generate a projection from a stack of images. In chapter 2, the concept of projections for OCT data sets was introduced briefly. Projection methods create a two-dimensional representation from a three-dimensional data set by projecting rays through the data to a specified plane. The projection is composed using a defined set of rules along the rays. One approach, termed maximum intensity projection, displays the maximum voxel intensity encountered along the projection ray. Minimum intensity and sum or mean intensity projections can also be used. The sum intensity projection is particularly useful for display of 3D OCT datasets in the gastrointestinal tract because of its analogy to magnification endoscopy techniques. This chapter further explores sum intensity projections for OCT in gastrointestinal imaging by contrasting projection views from normal and pathologic tissue specimens.

## 7.2 Methods

The OCT imaging system and the combined OCT and OCM imaging study were described in detail in chapters 5 and 6, respectively. Briefly, an ultrahigh resolution OCT imaging system operating at 1060 nm center wavelength with  $< 3$   $\mu\text{m}$  axial resolution and  $\sim 14$   $\mu\text{m}$  transverse resolution was used for these studies. The system used a pair of galvanometer scanners to generate a two-dimensional scan for volumetric imaging. OCT volumes consisted of 672 cross-sectional images, each spanning 3 mm in lateral extent by 1.3 mm in depth, and spaced over 1.5 mm in the orthogonal lateral dimension. Each OCT image had 1344 x 1000 pixels and was acquired at 1 frame/second. Image data was logarithmically demodulated from the carrier frequency using analog electronics before acquisition by a computer.

All imaging was conducted in accordance with protocols approved by the human subjects committees at the Massachusetts Institute of Technology and at participating hospitals. Tissue samples were placed on a three-axis stage to allow translation with respect to the microscope optics. Imaging was performed through a glass coverslip with a thin layer of ultrasound gel (Aquasonic) between the coverslip and the tissue specimen. The gel was important to preserve tissue surface architecture for three-dimensional visualization, which may otherwise be compressed by contact with the glass. One or more volumetric OCT scans were acquired of 75 freshly excised samples taken from 39 patients. Normal specimen subtypes included squamous esophagus (10), stomach (3), small intestine (5), colon (11), and pancreas (2). Pathology specimen subtypes included columnar-lined esophagus (11), esophageal adenocarcinoma (1), celiac disease (1), inflammatory bowel disease (3), acute inflammation (2), chronic colitis (2), melanosis coli (1), tubular adenoma (11), hyperplastic polyp (5), colorectal adenocarcinoma (4), cholecystitis (2), and chronic pancreatitis (1). In addition, one formalin fixed specimen of Barrett's esophagus with dysplasia was imaged. Specimen classification was done based upon histologic diagnosis made by an experienced pathologist. Representative results were selected from the database for discussion here.

Data processing was performed in Matlab. Individual cross-sectional images were resampled to the correct aspect ratio and the *en face* OCT projection was computed from the 3D volume by summing the image amplitude along the depth direction for each lateral pixel element. The sum was computed of the logarithmically demodulated data, and the result displayed with linear mapping on an inverse grayscale colormap. On this colormap, black represents high signal and white represents low signal. This colormap has traditionally been used in OCT due in part to its analogy with white light transmission microscopy used in histopathologic analysis, although it is opposite to the grayscale map used by most radiologic methods including ultrasound. Projection images were contrast enhanced for display.

The projection views were generated from images with logarithmic dynamic range compression. Log scale compression is used to enable display of the full dynamic range of cross-sectional OCT images in

scattering tissue, which is typically at least 40 – 50 dB and cannot be represented in a single 8-bit image on a linear scale. Virtually all other *en face* endoscopy methods integrate intensity along the depth dimension without use of log-compression images, which is an important point to appreciate when comparing the projection views shown in this chapter to other images in the published literature. Summation of log-compressed images along the depth dimension preferentially weights deeper structures below the surface compared to projection views generated from images on a linear dynamic range scale. A systematic comparison of log versus linear projection OCT views was not performed in this thesis work, but would be an important follow-on investigation to more fully understand the implications for image interpretation.

### **7.3 Results**

OCT projection views of normal squamous esophagus and gastric mucosa are compared in figure 7.1. The projections are noticeable at once for their relative absence of speckle compared to conventional cross-sectional OCT images and *en face* OCM images. The squamous esophagus in 7.1a demonstrates a fine pattern of tissue architecture. Surprisingly, some larger cellular elements also appear to be visible, as evidenced by the magnified 3x view in 7.1b (arrows). In contrast, the gastric mucosal architecture exhibits a characteristic regular pattern of pits, as shown in 7.1c and 7.1d. The entire diameter of the pits appears dark on the projection compared to much lighter surrounding regions. The lumen of the pits is not readily visible.

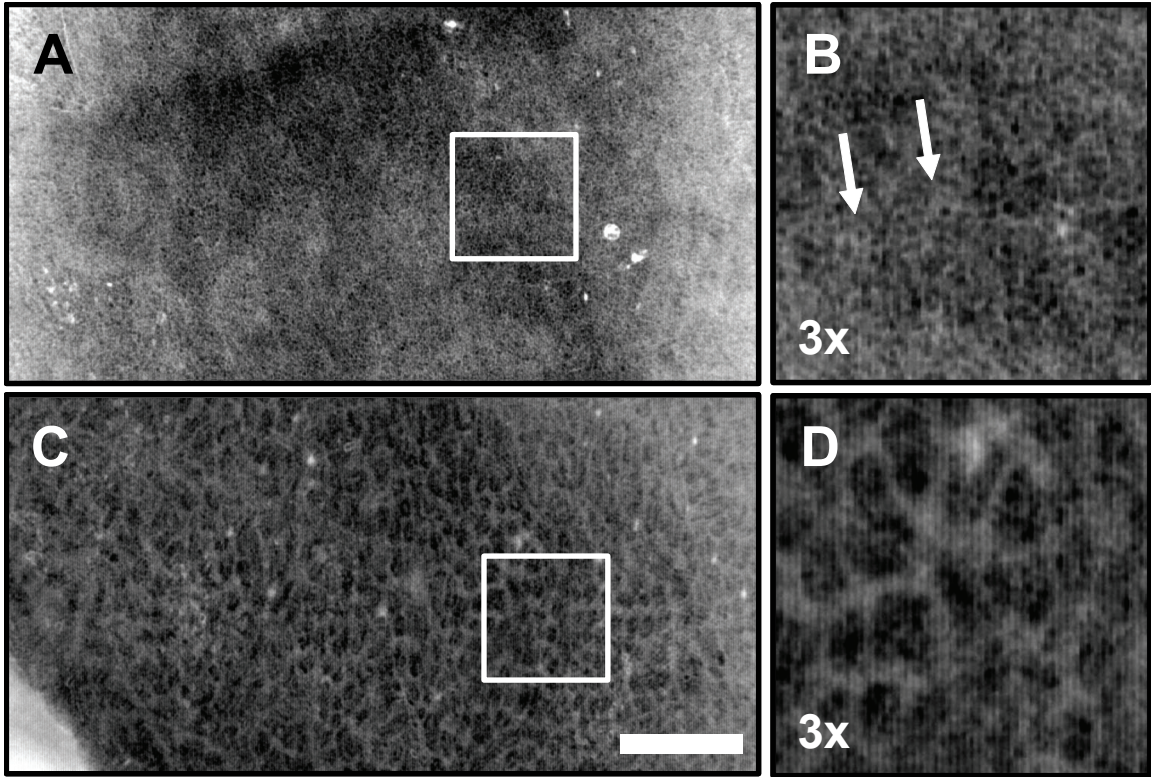


**Figure 7.1.** Projection OCT views of normal squamous and gastric mucosal tissues. Gastric mucosa (C,D) exhibits a regular pattern characteristic of pit architecture compared to the finer tissue structure seen in the squamous esophagus (A,B). Squamous cell features may be visible in the *en face* projection (arrows). Scale bar, 500  $\mu$ m.

Columnar metaplasia of Barrett's esophagus is shown in figure 7.2. Two separate specimens are shown in figures 7.2a and 7.2c with corresponding 3x magnifications in 7.2b and 7.2d. These specimens were noted to have specialized intestinal metaplasia with the presence of goblet cells on histology. The projection views visualize glandular elements lined by a rim of highly scattering columnar epithelium. Although individual cells cannot be clearly visualized, the lumens of the glands are apparent. Notable variation in size, shape, and orientation of the glands can be appreciated, which differs markedly from the consistent round pattern of pits in the gastric mucosa. The specimen in 7.2c and 7.2d was imaged after approximately 12 hours in formalin, and was diagnosed on histology with mild to moderate dysplasia.

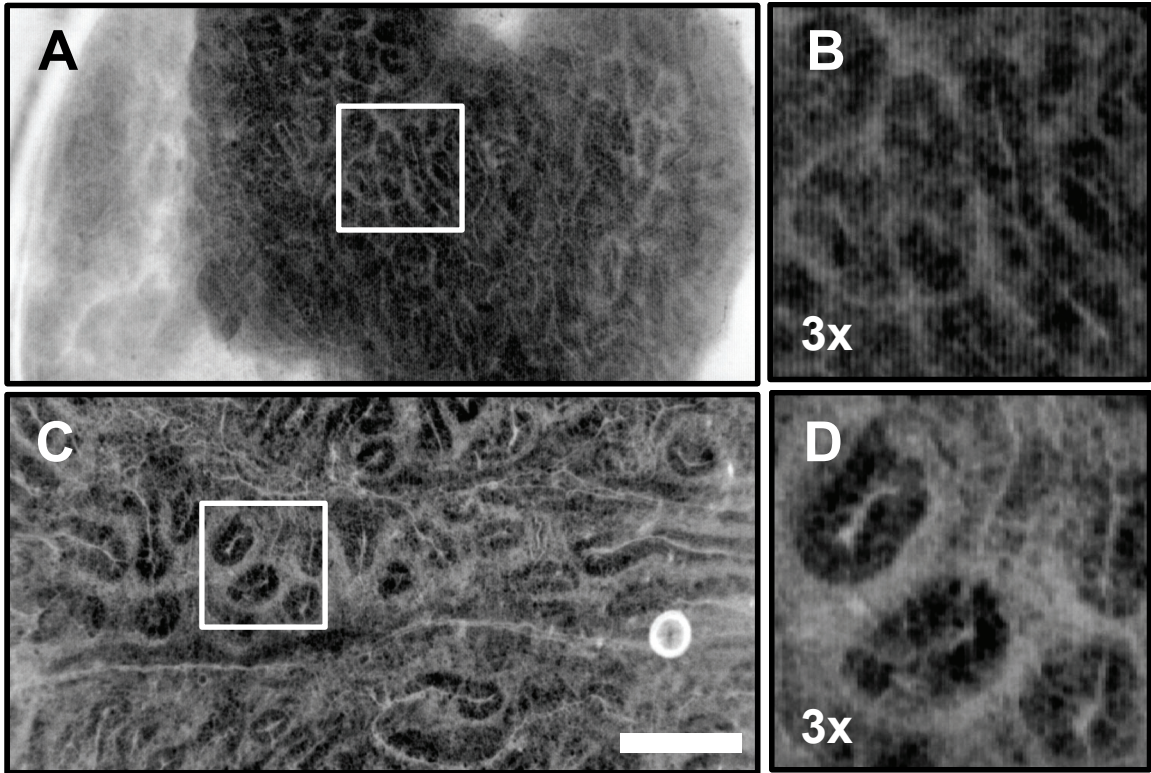


**Figure 7.2.** OCT projections of Barrett's esophagus. (A,B) Projection from a specimen with focal specialized intestinal metaplasia (SIM). (C,D) Projection from a specimen with diffuse SIM and moderate dysplasia. This specimen was formalin fixed when imaged. Scale bar, 500  $\mu$ m.

Projections from normal colon and tubular adenoma of the colon are presented in figure 7.3. The normal colon exhibits a highly ordered, uniform arrangement of crypts, with individual crypts demonstrating high signal in the columnar epithelium and low signal in the crypt lumens as well as the surrounding lamina propria. As in the cases of Barrett's esophagus, the adenoma shows heterogeneity in crypt size, shape, and orientation. Elongated crypts with elliptical lumens are prevalent, and the crypt epithelium is thicker compared to the normal colonic epithelium. The magnified views in figure 7.3b and 7.3d demonstrate this point. In addition, the crypt epithelium shows variation in signal intensity, which may be correlated with pseudostratification of nuclei.

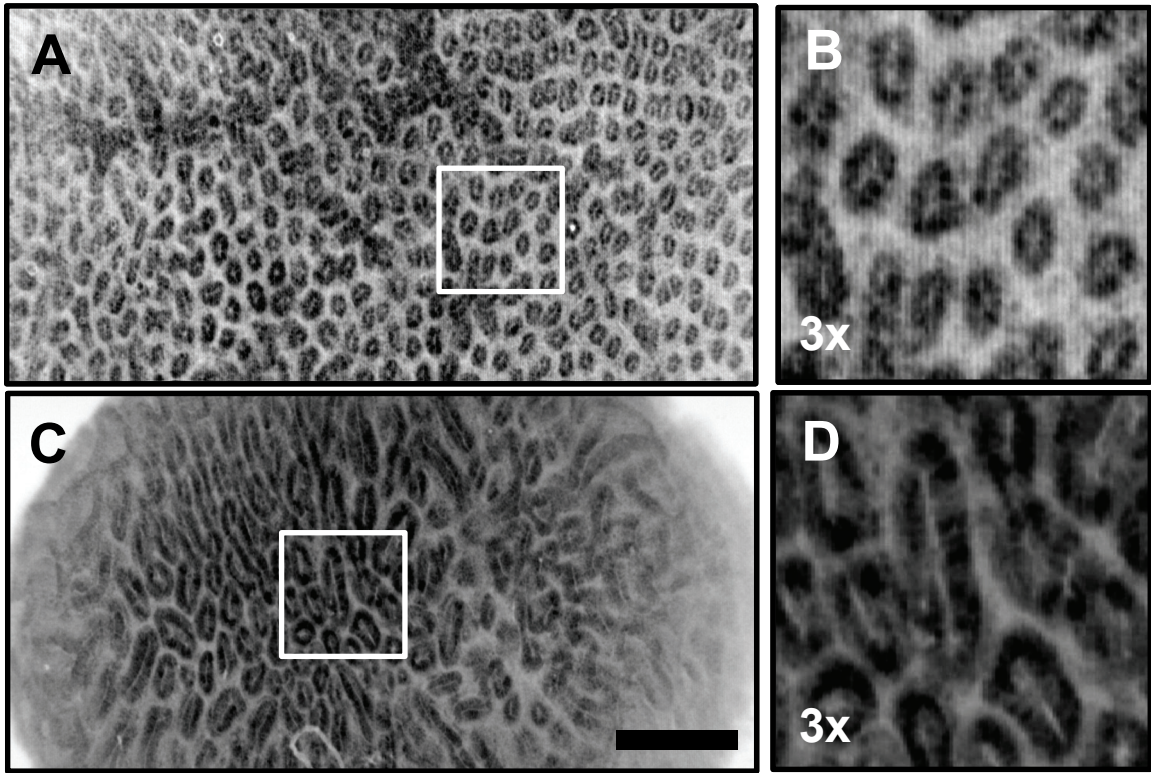


**Figure 7.3.** Projection OCT of normal and adenomatous colon. (A,B) Projection from normal colon showing uniform crypt pattern. (C,D) Projection from a specimen of tubular adenoma with elongated crypt architecture. Scale bar, 500  $\mu$ m.

Results from two separate specimens of adenocarcinoma of the colon are presented in figure 7.4. The projection in 7.4a is a composite made from two overlapping scans and shows features of the adenocarcinoma in the region of the tumor margin. Ulceration is present in the center, and an irregular distribution of highly scattering structures believed to be malignant glands can be seen across the field. The 3x magnification in 7.4b highlights a suspected area of tumor glandular structure. In addition, the projection shows what appears to be an irregular tumor margin, as delineated by the arrows. Figures 7.4c and 7.4d present projections from a region of another tumor that also exhibits significant architectural distortion. Normal crypt morphology has been replaced by fine gland forming structure (7.4d, arrows) and structural heterogeneity.

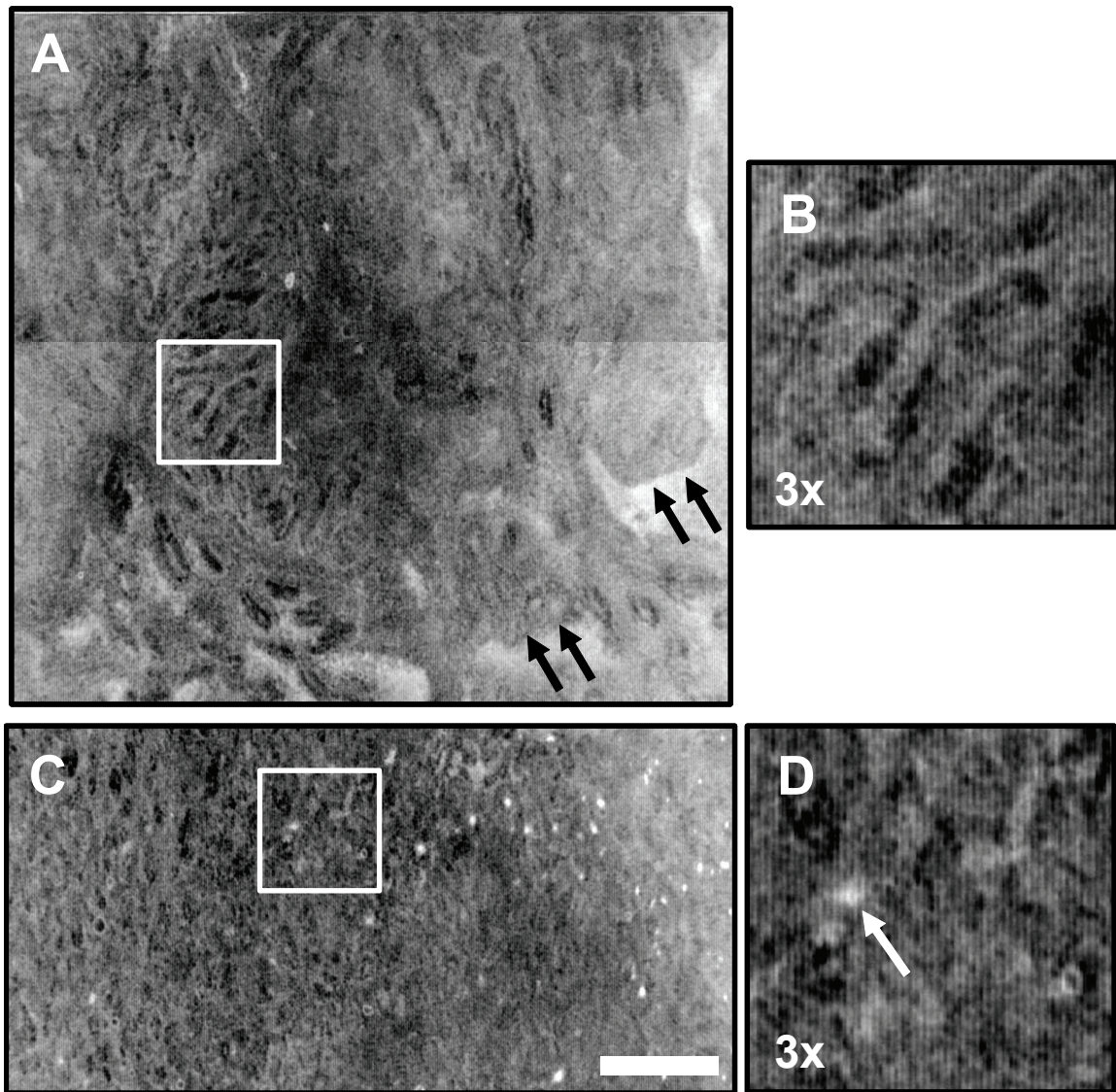


**Figure 7.4.** Projection OCT views of adenocarcinoma of the colon. (A,B) Projection from a region in the area of the tumor margin. Irregular glands and the tumor margin (arrows) can be visualized. (C,D) Projection from a second tumor specimen exhibiting finer tissue architecture with gland formation (arrow). Scale bar, 500  $\mu$ m.

Figure 7.5 compares projection views from a region of normal small intestine and an area affected by Crohn's disease, a chronic inflammatory condition. The samples were taken from the terminal ileum of the same patient. In figure 7.5a and 7.5b, the projection shows a pattern representative of normal villous architecture. The specimen with Crohn's inflammation exhibits a total loss of the villous architecture and an irregular tissue pattern.

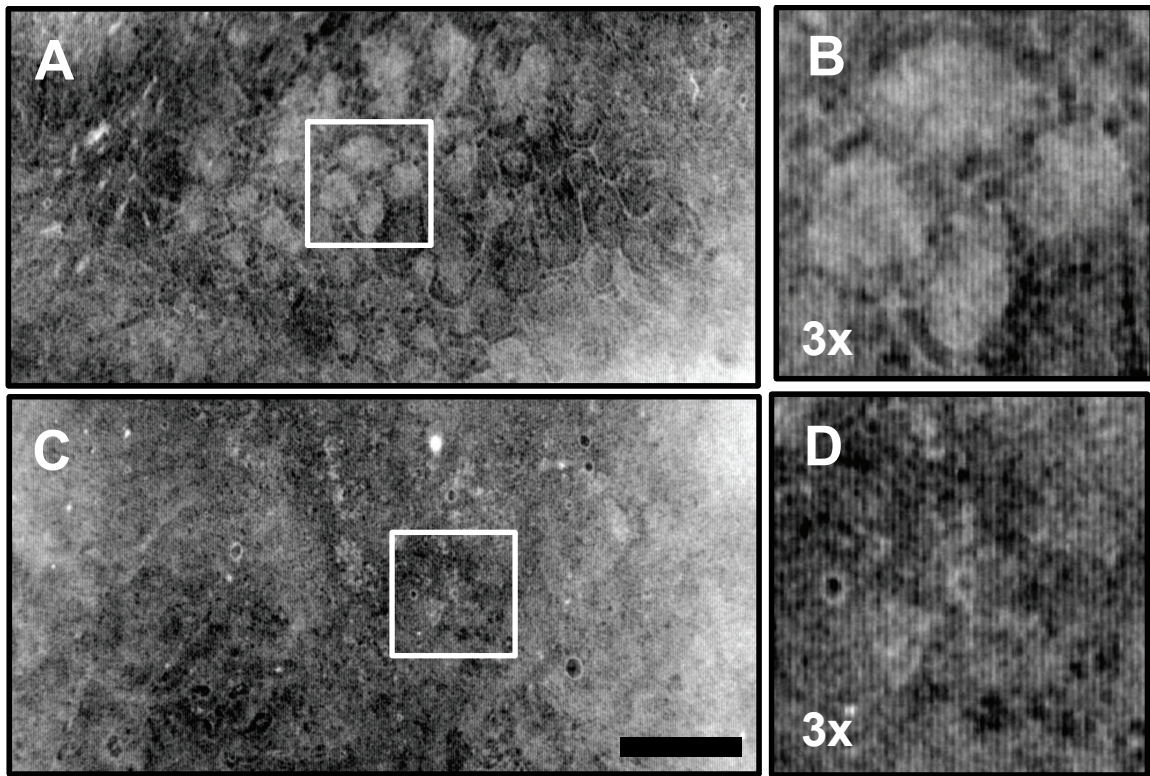


**Figure 7.5.** OCT projections of normal and diseased terminal ileum. (A,B) Normal ileum shows the presence of villous surface architecture while ileum affected with Crohn's disease exhibits a loss of villi (C,D). Scale bar, 500  $\mu$ m.

#### 7.4 Discussion

This study investigates a simple *en face* projection approach to processing volumetric OCT data sets of gastrointestinal tissues. While applied ubiquitously for 3D data sets from other imaging modalities such as magnetic resonance imaging and computed tomography (CT), this method has yet to be investigated thoroughly for OCT. The intensity sum or average projection view has particular relevance in gastrointestinal endoscopy because of its relationship to the standard endoscopic view. A standard endoscope records an *en face* view consisting of the integrated light intensity from all depths in the tissue, and consequently does not have the ability to gate out light from a single depth. Optical coherence tomography, by contrast, can provide high resolution cross-sectional, and depth resolved, images of tissue microstructure. By acquiring OCT images in two lateral dimensions with respect to the tissue surface, a 3D data set can be generated. The *en face* projection removes the depth dimension of the data set by integrating the light from all depths, thereby creating a view which is in principle similar to the conventional *en face* endoscopic view.

More accurately, the OCT *en face* projection is analogous to the view created with magnification endoscopes. Indeed, the projection views presented in this study resemble some of the published images acquired with magnification endoscopy. Importantly, however, the projection view is precisely co-registered to the individual cross-sectional scans which were used to construct it. Areas of interest in the projection view can be looked at in cross-section to appreciate features resolved in depth. Future three-dimensional endoscopic OCT systems will therefore enable visualization of gastrointestinal mucosal tissues from multiple perspectives while maintaining the familiar *en face* view that is the clinical standard in endoscopy.

Projection methods are attractive for use with high speed OCT imaging methods. The projection processing technique can be executed rapidly, which makes it amenable for real time imaging display of three-dimensional datasets. In addition, selective subsets of the volume data set can be projected to look at individual layers rather than the entire tissue block. For the views presented here, all depths were included in the projections. It is possible, however, to project only the stratified squamous epithelium or only the lamina propria, for example.

Comparison of the projection views to the cross-sectional OCT images from the previous chapter highlight some important points regarding the averaging effects of the projection. First, speckle is dramatically reduced in the projections. This results from averaging of multiple speckles, despite the fact that they are generated by entirely different structures. Second, averaging of tissue heterogeneity occurs. Regions of connective tissue typically have weak signal on the projection due to the fact that connective tissue organization is relatively random compared to other more defined structures such as crypts or villi. Finally, the projection averaging in the work presented here was performed on a logarithmic scale. This has the effect of enhancing the contribution of scattering from below the surface compared to linear projections. This is a difference between the OCT projection technique used here and conventional direct view methods such as magnification endoscopy, which integrate depth in a linear fashion. Further work is necessary to understand optimal depth weighting schemes for projection averaging.

## 7.5 References

- [1] R. Leitgeb, C. K. Hitzenberger, and A. F. Fercher, "Performance of Fourier domain vs. time domain optical coherence tomography," *Optics Express*, vol. 11, pp. 889-894, 2003.
- [2] M. A. Choma, M. V. Sarunic, C. H. Yang, and J. A. Izatt, "Sensitivity advantage of swept source and Fourier domain optical coherence tomography," *Optics Express*, vol. 11, pp. 2183-2189, 2003.
- [3] J. F. de Boer, B. Cense, B. H. Park, M. C. Pierce, G. J. Tearney, and B. E. Bouma, "Improved signal-to-noise ratio in spectral-domain compared with time-domain optical coherence tomography," *Opt Lett*, vol. 28, pp. 2067-9, 2003.
- [4] M. Wojtkowski, T. Bajraszewski, P. Targowski, and A. Kowalczyk, "Real-time in vivo imaging by high-speed spectral optical coherence tomography," *Opt Lett*, vol. 28, pp. 1745-7, 2003.
- [5] S. H. Yun, G. J. Tearney, J. F. de Boer, N. Iftimia, and B. E. Bouma, "High-speed optical frequency-domain imaging," *Optics Express*, vol. 11, pp. 2953-2963, 2003.
- [6] N. Nassif, B. Cense, B. H. Park, S. H. Yun, T. C. Chen, B. E. Bouma, G. J. Tearney, and J. F. de Boer, "In vivo human retinal imaging by ultrahigh-speed spectral domain optical coherence tomography," *Opt Lett*, vol. 29, pp. 480-2, 2004.
- [7] M. Wojtkowski, V. J. Srinivasan, T. H. Ko, J. G. Fujimoto, A. Kowalczyk, and J. S. Duker, "Ultrahigh-resolution, high-speed, Fourier domain optical coherence tomography and methods for dispersion compensation," *Optics Express*, vol. 12, pp. 2404-2422, 2004.
- [8] R. Huber, M. Wojtkowski, and J. G. Fujimoto, "Fourier Domain Mode Locking (FDML): A new laser operating regime and applications for optical coherence tomography," *Optics Express*, vol. 14, pp. 3225-3237, 2006.
- [9] N. A. Nassif, B. Cense, B. H. Park, M. C. Pierce, S. H. Yun, B. E. Bouma, G. J. Tearney, T. C. Chen, and J. F. de Boer, "In vivo high-resolution video-rate spectral-domain optical coherence tomography of the human retina and optic nerve," *Optics Express*, vol. 12, pp. 367-376, 2004.
- [10] U. Schmidt-Erfurth, R. A. Leitgeb, S. Michels, B. Povazay, S. Sacu, B. Hermann, C. Ahlers, H. Sattmann, C. Scholda, A. F. Fercher, and W. Drexler, "Three-dimensional ultrahigh-resolution optical coherence tomography of macular diseases," *Invest Ophthalmol Vis Sci*, vol. 46, pp. 3393-402, 2005.
- [11] M. Wojtkowski, V. Srinivasan, J. G. Fujimoto, T. Ko, J. S. Schuman, A. Kowalczyk, and J. S. Duker, "Three-dimensional retinal imaging with high-speed ultrahigh-resolution optical coherence tomography," *Ophthalmology*, vol. 112, pp. 1734-46, 2005.
- [12] S. H. Yun, G. J. Tearney, B. J. Vakoc, M. Shishkov, W. Y. Oh, A. E. Desjardins, M. J. Suter, R. C. Chan, J. A. Evans, I. K. Jang, N. S. Nishioka, J. F. de Boer, and B. E. Bouma, "Comprehensive volumetric optical microscopy in vivo," *Nat Med*, vol. 12, pp. 1429-33, 2006.
- [13] B. J. Vakoc, M. Shishko, S. H. Yun, W. Y. Oh, M. J. Suter, A. E. Desjardins, J. A. Evans, N. S. Nishioka, G. J. Tearney, and B. E. Bouma, "Comprehensive esophageal microscopy by using optical frequency-domain imaging (with video)," *Gastrointest Endosc*, vol. 65, pp. 898-905, 2007.
- [14] D. C. Adler, Y. Chen, R. Huber, J. Schmitt, J. Connolly, and J. G. Fujimoto, "Three-dimensional endomicroscopy using optical coherence tomography," *Nature Photonics*, vol. 1, pp. 709-716, 2007.

## Chapter 8

### Two-axis MEMS Scanning Catheter for Ultrahigh Resolution Three-Dimensional and *En Face* Imaging

#### 8.1 Overview

As shown through the *ex vivo* studies from the previous two chapters, three-dimensional OCT and *en face* OCM have great potential for endoscopic imaging applications. The ability to implement these methods for *in vivo* endoscopic imaging, however, hinges on the development of miniaturized two-axis scanning catheters. This chapter details efforts to develop such devices based on micro-electro-mechanical systems (MEMS) mirrors.

The results presented here were achieved in collaboration with the research group of Prof. Ming Wu from the University of California, Los Angeles. In particular, Dr. Wibool Piyawattanametha was responsible for fabrication of the MEMS mirrors and integration into the endoscopic package. Dr. Li Fan designed the MEMS package and provided advice on the design of amplifiers for driving the mirrors. From MIT, Paul Herz and Dr. Yu Chen assisted with imaging experiments.

#### 8.2 Introduction

Optical coherence tomography (OCT) is a promising technique for high-resolution *in situ* cross-sectional imaging of biological tissues. Development of scanning fiber-optic catheters has enabled *in vivo* endoscopic OCT imaging [1, 2], and results to date have shown the ability to distinguish tissue architectural layers and to differentiate normal from certain pathologic conditions within the human gastrointestinal tract [3-7]. In recent years, OCT technology has improved significantly. High speed Fourier domain detection has enabled *in vivo* three-dimensional imaging [8-17], and new technology for *en face* imaging has paved the way for high speed, *in vivo* cellular imaging using optical coherence microscopy [18]. Implementation of 3D OCT and OCM imaging endoscopically, however, requires improvement in catheter device designs. Current endoscopic OCT catheters consist of a single-mode fiber fused to a focusing lens and a microprism to deflect the beam orthogonally away from the fiber axis [1]. These devices are scanned by proximally rotating or translating the fiber. Proximal catheter actuation, however, has poor precision and repeatability and is limited to relatively slow imaging rates

due to the physical inertia of the device and the friction between the catheter and its outer sheath. Furthermore, proximal scanning can generally only be performed in one dimension for the generation of a two-dimensional OCT image. For three-dimensional and *en face* imaging applications, a need exists for new flexible catheter designs which implement high speed two-axis scanning at the distal tip of the device.

Distal scanning for microscopy applications can be performed either by scanning the fiber tip in the back image plane of the objective or by beam steering using micromirror technologies. Fiber scanning has been performed using piezo-electric devices [19-23] or a balanced tuning fork and lever approach [24]. Micro-electro-mechanical systems (MEMS) mirrors have been demonstrated for beam steering in confocal microscopy [25-30] and in OCT [31-38]. Most fiber scanning approaches require resonant scanning in order to generate sufficient deflection for a reasonable field of view. MEMS mirrors, on the other hand, can perform large angle scanning without resonance, which enables arbitrary scan patterns as well as features such as panning or image rotation. MEMS scanners can also be actuated on resonance to provide high speed raster scanning necessary for *en face* imaging. Furthermore, MEMS devices can operate reliably and with low power consumption, making them suitable for integration into *in vivo* imaging devices.

In this work, a two-dimensional MEMS scanning endoscope was developed and demonstrated for OCT imaging. The MEMS scanning mirror was capable of both DC and resonant operation and could produce arbitrary beam scan patterns, enabling cross-sectional, *en face*, and three-dimensional imaging. The integrated endoscope measured approximately 5 mm in diameter and produced a transverse spot size of ~12  $\mu\text{m}$ . Using the miniaturized catheter probe, ultrahigh resolution two and three-dimensional OCT imaging with < 5  $\mu\text{m}$  axial resolution was demonstrated both *in vivo* and *ex vivo*.

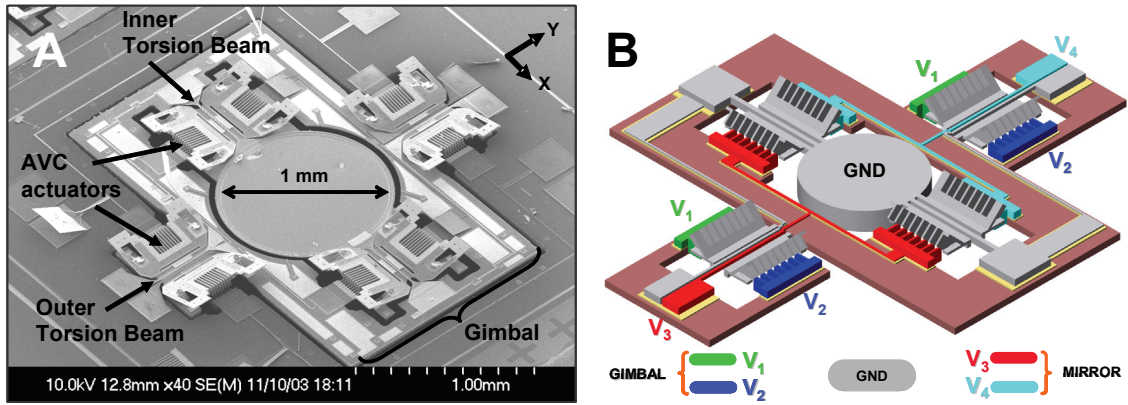
### **8.3 Catheter Design and Characterization**

A scanning electron micrograph of the MEMS optical scanner used in the OCT endoscope is shown in figure 8.1a. A large 1 mm diameter mirror was driven by angular vertical comb (AVC) actuators, which provided large scan angles for the same comb dimensions compared to standard vertical comb actuators [39]. The comb fingers were self-aligned with a single etching step. The device was realized by combining a foundry surface-micromachining process (MUMPS) with a 3-mask deep-reactive-ion-etching (DRIE) post process. Surface micromachining provides versatile mechanical design and electrical interconnect while bulk micromachining offers flat micromirrors and high-force actuators. The scanner utilized torsion beams and a gimbal-mounting configuration to scan the MEMS mirror on two axes. This design had the advantage of combining the two scan axes to provide a true XY integrated scanner, with a single pivot point. The complete scanner die with the mirror and the actuators measured 3

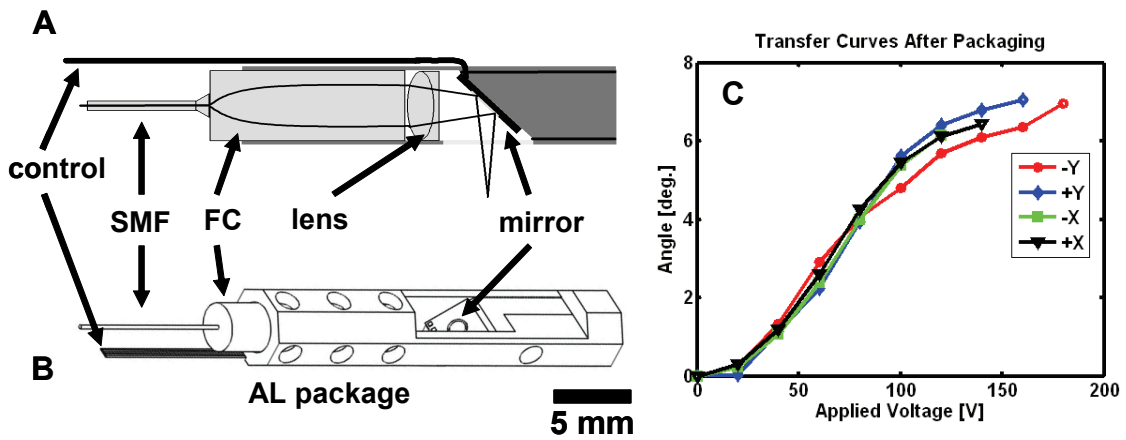
mm x 3 mm square. Electrical interconnects are shown in figure 8.1b. To achieve full scanner performance, application of four separate control signals was required, one for each of two sets of comb actuators on both the X and Y axes. Electrostatic actuators have a capacitive load and therefore draw very small amounts of current for low frequency actuations, generally less than 1 to 10 nA.

Figure 8.2 presents the optical and mechanical designs for the MEMS scanning catheter as well as the scanner characteristics measured in the device package. As shown in the optical schematic in figure 8.2a, light was first collimated by a graded-index (GRIN) fiber collimator fused to a single mode optical fiber. A small achromatic lens ( $f = 10$  mm) focused the light onto the specimen. The MEMS optical scanner was mounted at 45 degrees to the optical axis of the lens and redirected the beam out of the endoscope in a similar side-view fashion as used in the conventional OCT catheter [1]. The scanner performed post-objective scanning, which eliminated the off-axis optical aberrations that would be generated if the beam was scanned on the objective lens. Figure 8.2b provides a mechanical drawing of the catheter package design. The optics and scanner were mounted in a compact aluminum package with a transparent ITO-coated glass window covering the beam opening (not shown). Use of the glass window reduced aberration generated by the plastic sheath used in a conventional catheter. The inexpensive outer housing was machined from a single piece of aluminum, which minimized the number of steps required for assembly. The custom package design allowed for precise lateral alignment of the optics using tiny set screws. In addition, the scanner was mounted on an inner carrier block which could be adjusted along the catheter axis to account for lenses with different focal lengths or to set the working distance according to the specific application. The working distance of the catheter used for this study measured  $\sim 2$  mm, and the outermost diameter of the device was  $\sim 5$  mm. This is consistent with confocal scanners which have been integrated into the endoscope head [24] but is larger than the typical accessory working channel in a standard endoscope. Further efforts in the future should lead to reduction of device design below the 3 mm threshold necessary for use in the working channel.

The non-resonant mechanical scanning angle responses for the four mirror drive controls are presented in Figure 8.2c. Importantly, these measurements were made with the mirror mounted in the package, which demonstrates the ability of the scanner to function at its optimal performance within the endoscope. Careful attention had to be devoted to bonding issues in mounting the scanner to ensure that device performance was not compromised. The scanner achieved  $\pm 6$  degrees mechanical at slightly more than 100 V for both the inner X and outer Y axes. In addition, the optical scanner also had excellent frequency response with resonances in the hundreds of Hz for both axes, as shown in figure 8.3. Resonant operation of the mirror would enable high-speed raster scanning for *en face* microscopy.



**Figure 8.1.** Scanning electron micrograph (A) and electrical schematic (B) of the MEMS two-axis optical scanner. The scanner has a larger 1 mm diameter mirror and uses angled vertical comb (AVC) actuators to produce a large angle scan for high resolution imaging.



**Figure 8.2.** MEMS catheter design and performance characteristics. (A) Optical schematic. (B) Mechanical drawing. (C) Non-resonant drive characteristics for the MEMS optical scanner after packaging in the catheter endoscope. SMF, single mode fiber. FC, fiber collimator. AL, aluminum.

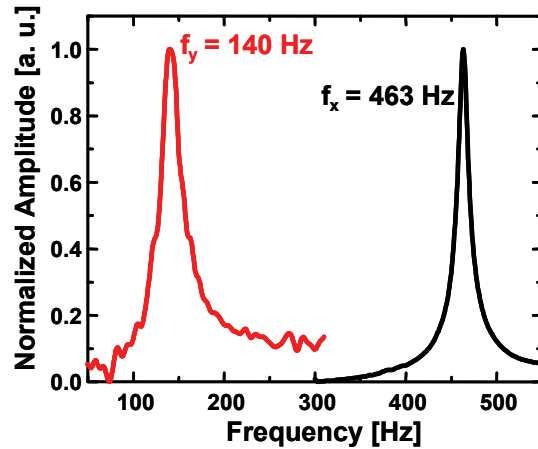


**Figure 8.3.** Resonance characteristics of the MEMS scanner. The mirror resonance was at 463 Hz and the gimbal axis resonance was 140 Hz.

To illustrate the scanner drive control scheme used for imaging, figure 8.4 presents measurements of the position response for the X mirror axis for two different drive waveforms. The position was recorded by detecting an optical beam reflected from the mirror with a two-dimensional position sensor. The response to a triangle drive waveform applied to only one side of the comb actuators is shown in figure 8.4a. The mirror angle responds as the square of the applied voltage, as shown by the plotted response curve. To compensate for the nonlinear response, a modified drive scheme consisting of a square root function with a DC offset was applied. In addition, the mirror was driven on both axes in a differential manner, which effectively doubled the scan range that could be achieved with a single axis. The resulting angle response had excellent linearity, as shown in figure 8.4b.

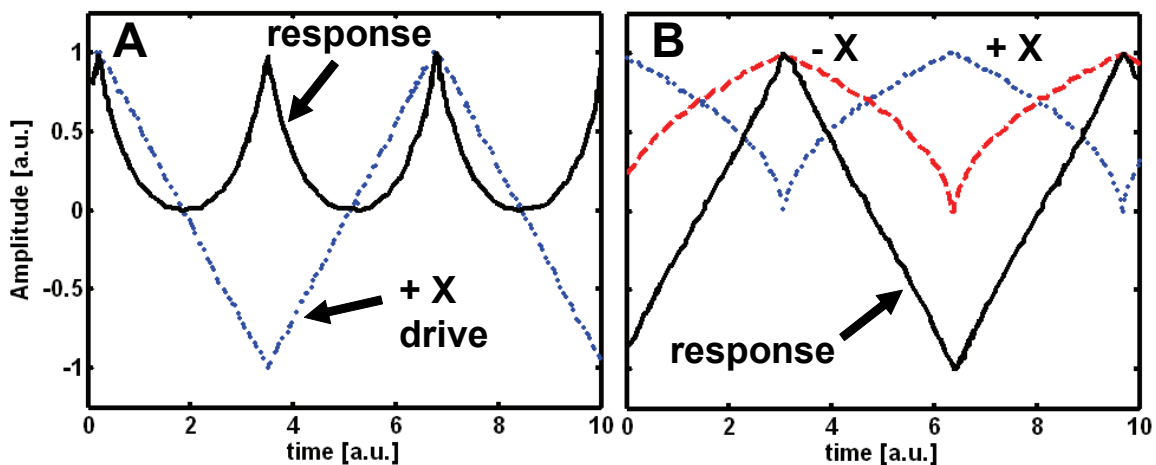


**Figure 8.4.** Drive control scheme for the MEMS optical scanner. (A) Response to a linear drive waveform. (B) Linearized response to a differential, square-root drive function.

## 8.4 Two and Three-dimensional Imaging Results

The MEMS OCT endoscope was incorporated into an ultrahigh resolution OCT imaging system. The system diagram is shown in figure 8.5. A broadband laser light source with more than 200 nm bandwidth centered at 1.06  $\mu\text{m}$  was coupled into a fiber-optic interferometer and split between a reference and a sample arm. Reference delay scanning was performed at  $\sim 2000$  axial scans per second. The MEMS endoscope was placed in the sample arm with an air gap to allow for dispersion compensation of the reference arm air path. The interference signal was recorded by a photodetector, and the electronic signal was amplified, filtered, and demodulated before being sampled by a 12-bit, 5 MHz A/D converter and processed by computer. Axial resolution measured  $< 4 \mu\text{m}$ , while transverse resolution as set by the focusing optics was  $\sim 12 \mu\text{m}$  ( $1/e^2$  spot diameter). Imaging was performed with the endoscope at a rate of 4 frames per second over a three-dimensional field of view (X x Y x Z) of 1.8 mm x 1.0 mm x 1.3 mm with 500 x 500 x 1000 pixels.

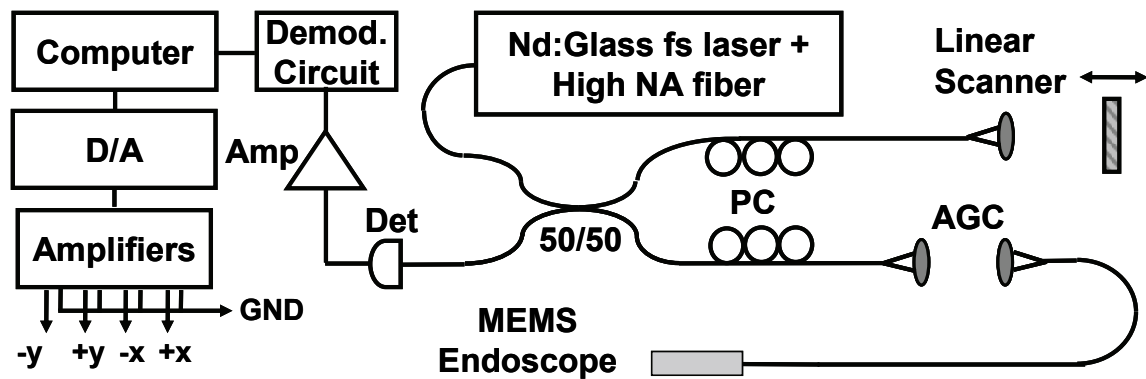


**Figure 8.5.** OCT system schematic for imaging with the MEMS endoscope. PC, polarization control. AGC, air-gap coupling. Det, detector. Amp, amplifier. D/A, digital to analog converter.

Imaging results achieved with the catheter endoscope are presented in figure 8.6. Figure 8.6a and 8.6b present *in vivo* images acquired in human skin. Image quality compares very well with that obtained with the system using a conventional benchtop microscope [40]. Skin from two different locations is shown. A thinner stratum corneum (sc) can be appreciated in 8.6a, which is from the dorsal aspect of the hand, compared to 8.6b, which is from the palmar finger tip. The epidermis and underlying dermis can be seen in both images. Fine structure within the stratum corneum can also be visualized in figure 8.6b. Figure 8.6c presents an image of lime pulp, which was used here illustrate the very high axial resolution of the catheter imaging system. Some image stretching at the edges occurs from residual scanner nonlinearity encountered when the rotation angle reverses.

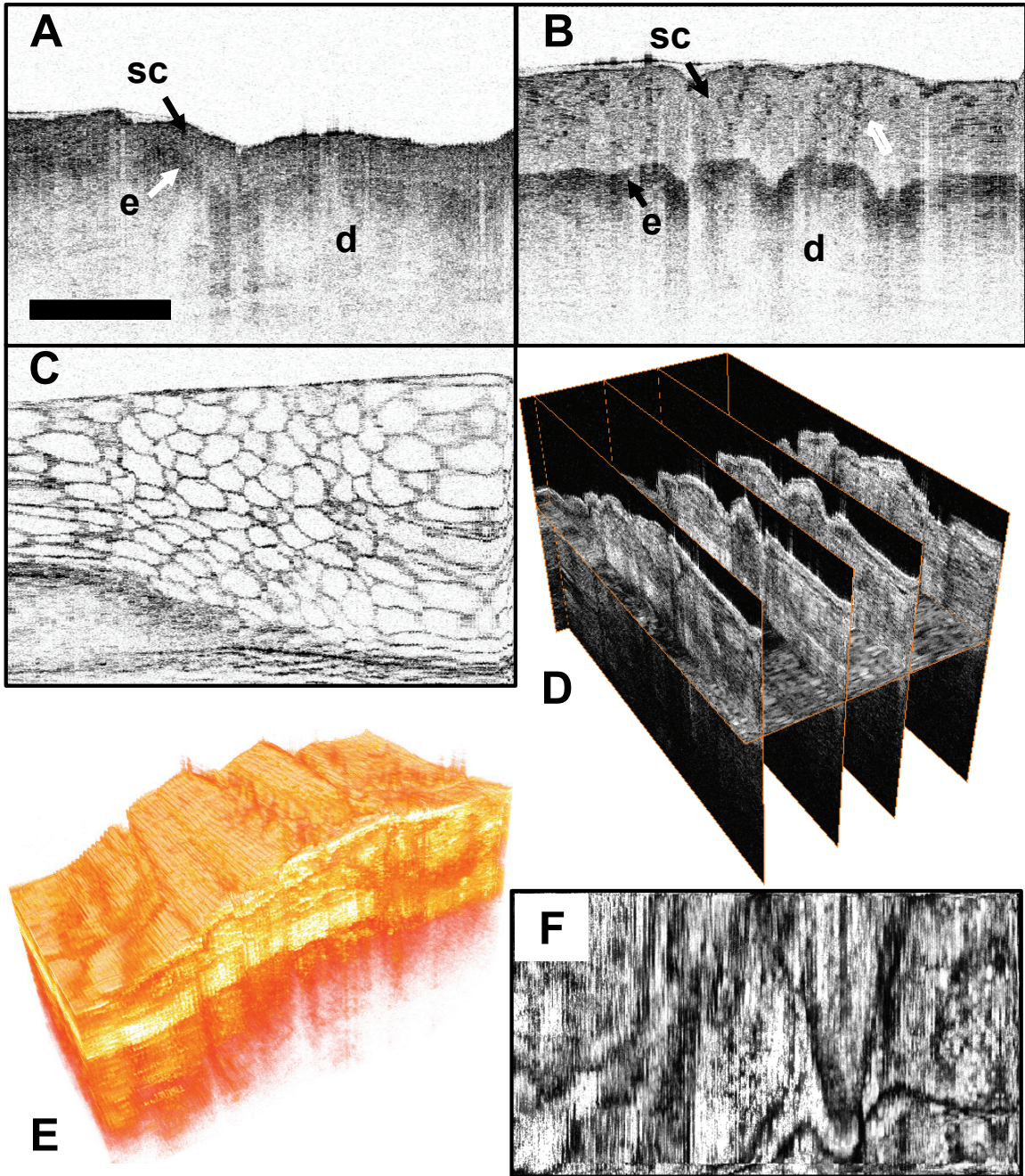


**Figure 8.6.** OCT images acquired with the MEMS scanning catheter. (A,B) *In vivo* cross-sectional images of human skin. sc, stratum corneum; e, epidermis; d, dermis. (C) Cross-sectional image of lime pulp. (D) Serial cross-sections and *en face* plane extracted from a three-dimensional OCT volume of hamster cheek pouch acquired *ex vivo*. (E) Three-dimensional rendering of OCT volume data set from the hamster cheek pouch. (F) OCT intensity projection of the 3D volume. Scale bar, 500  $\mu$ m.

Three-dimensional imaging was performed *ex vivo* of hamster cheek pouch with the MEMS scanning catheter, and representative results are presented in figures 8.6d thru 8.6f. Volumetric imaging allows visualization of serial two-dimensional sections or reconstruction of a two-dimensional image at an arbitrary image plane, as shown in figure 8.6d. The volume can also be rendered in three-dimensions to produce a topographical surface representation, illustrated here in figure 8.6e. To represent the entire data set in a two-dimensional plane, projection techniques can be applied. Figure 8.6f shows an *en face* integrated intensity projection. This view removes the depth dimension, giving a composite perspective which weights structures in depth by scattering intensity. Prominent surface features seen in the projection compare well to those in the rendering. The length of time for acquisition of the 3D volume data set was approximately 2 minutes. These times can be significantly reduced using high speed, Fourier domain OCT techniques.

## 8.5 Discussion

A two-axis MEMS scanning catheter with 5 mm outer diameter has been demonstrated for high quality two and three-dimensional ultrahigh resolution OCT imaging. The device produced optical resolution of 12  $\mu\text{m}$  in the transverse dimension and was combined with an OCT system capable of  $< 4$   $\mu\text{m}$  axial resolution. The scanner had excellent DC response characteristics in packaged form, and a differential drive scheme for linearization of the scanner response was demonstrated for enhanced imaging performance.

The device design used in this study has several advantages which make it attractive for further development for clinical imaging applications. Post-objective side-view scanning allows for a simplified optical layout and ease of alignment compared to more complex designs, which require folding of the beam with multiple reflections. Optical aberrations due to pre-objective scanning are eliminated, resulting in improved imaging performance. In addition, the inexpensive aluminum package and standard optical components combined with the ability to fabricate the micromirrors in bulk keeps the overall device cost low. Using such designs, it is foreseeable that MEMS based scanning catheters could be disposable if required by the specific application. Finally, the catheter design described here can be made waterproof for future *in vivo* imaging applications by sealing the glass window and coating the remainder of the device using a plastic sheath.

The MEMS scanner itself had excellent performance characteristics for imaging applications. A 1 mm diameter mirror and good angle response allowed imaging with a large number of resolvable spots. The large mirror aperture would allow for even shorter focal length to reduce transverse spot sizes to  $< 5$   $\mu\text{m}$ . For example, use of a lens with 5 mm focal length can provide  $1/e^2$  radius of  $\sim 3$   $\mu\text{m}$  with a working distance from the optical window of several hundred micrometers. For the imaging results

presented in this chapter, the MEMS scanner was directly driven off resonance with a square-root waveform to produce a linearized response, and DC mechanical angles of  $\pm 6$  degrees were achieved. Response angles of 2-3 times larger will be possible, however, when driving the mirror on resonance. In addition, using bidirectional resonant scanning with scanner responses as shown in figure 3, fast image line rates of over 900 Hz and higher should be possible with these devices. The fast raster scanning capability combined with tighter focusing optics should enable *en face* optical coherence microscopy for cellular resolution imaging.

The capability for *in vivo* 3D imaging was limited in our study by the relatively slow scan rate of the time-domain OCT system. Future incorporation of these devices with Fourier / spectral domain or swept-source OCT systems will allow much faster 3D imaging. With the advent of very high speed Fourier-domain mode-locked lasers, real-time volumetric imaging at rates of several volumes per second will soon be a reality [41].

In recent years, several groups have made progress toward the development of reliable MEMS based scanners for endoscopic imaging, and a growing body of literature on the subject exists. The task of implementing MEMS-scanning devices for clinical imaging studies remains challenging, however. High speed and linear scanner responses, compact and waterproof device packaging, and development of depth focusing and tissue stabilization schemes are key areas of consideration for future development efforts. Furthermore, the devices presented to date operate in an open-loop mode and lack the precise control that can be achieved with modern galvanometer scanners. Addressing this concern will require increasingly sophisticated scanner technology. Finally, the use of relatively high voltages *in vivo* demands a greater level of engineering effort to ensure safety for human studies compared to previous catheter designs, which utilized simple mechanical translation or rotation for scanning. Despite these challenges, development of two-dimensional scanning endoscopes is essential to harness rapid advances in imaging speed and resolution that promise to bring three-dimensional and cellular-level OCT imaging to a clinical reality.

## 8.6 References

- [1] G. J. Tearney, S. A. Boppart, B. E. Bouma, M. E. Brezinski, N. J. Weissman, J. F. Southern, and J. G. Fujimoto, "Scanning single-mode fiber optic catheter-endoscope for optical coherence tomography," *Optics Letters*, vol. 21, pp. 543-5, 1996.
- [2] G. J. Tearney, M. E. Brezinski, B. E. Bouma, S. A. Boppart, C. Pitris, J. F. Southern, and J. G. Fujimoto, "In vivo endoscopic optical biopsy with optical coherence tomography," *Science*, vol. 276, pp. 2037-9, 1997.
- [3] B. E. Bouma, G. J. Tearney, C. C. Compton, and N. S. Nishioka, "High-resolution imaging of the human esophagus and stomach in vivo using optical coherence tomography," *Gastrointest Endosc*, vol. 51, pp. 467-74, 2000.
- [4] M. V. Sivak, Jr., K. Kobayashi, J. A. Izatt, A. M. Rollins, R. Ung-Runyawee, A. Chak, R. C. Wong, G. A. Isenberg, and J. Willis, "High-resolution endoscopic imaging of the GI tract using optical coherence tomography," *Gastrointest Endosc*, vol. 51, pp. 474-9, 2000.
- [5] S. Jackle, N. Gladkova, F. Feldchtein, A. Terentieva, B. Brand, G. Gelikonov, V. Gelikonov, A. Sergeev, A. Fritscher-Ravens, J. Freund, U. Seitz, S. Schroder, and N. Soehendra, "In vivo endoscopic optical coherence tomography of esophagitis, Barrett's esophagus, and adenocarcinoma of the esophagus," *Endoscopy*, vol. 32, pp. 750-5, 2000.
- [6] X. D. Li, S. A. Boppart, J. Van Dam, H. Mashimo, M. Mutinga, W. Drexler, M. Klein, C. Pitris, M. L. Krinsky, M. E. Brezinski, and J. G. Fujimoto, "Optical coherence tomography: advanced technology for the endoscopic imaging of Barrett's esophagus," *Endoscopy*, vol. 32, pp. 921-30, 2000.
- [7] J. M. Poneros, S. Brand, B. E. Bouma, G. J. Tearney, C. C. Compton, and N. S. Nishioka, "Diagnosis of specialized intestinal metaplasia by optical coherence tomography," *Gastroenterology*, vol. 120, pp. 7-12, 2001.
- [8] R. Leitgeb, C. K. Hitzenberger, and A. F. Fercher, "Performance of Fourier domain vs. time domain optical coherence tomography," *Optics Express*, vol. 11, pp. 889-894, 2003.
- [9] M. A. Choma, M. V. Sarunic, C. H. Yang, and J. A. Izatt, "Sensitivity advantage of swept source and Fourier domain optical coherence tomography," *Optics Express*, vol. 11, pp. 2183-2189, 2003.
- [10] J. F. de Boer, B. Cense, B. H. Park, M. C. Pierce, G. J. Tearney, and B. E. Bouma, "Improved signal-to-noise ratio in spectral-domain compared with time-domain optical coherence tomography," *Opt Lett*, vol. 28, pp. 2067-9, 2003.
- [11] S. H. Yun, G. J. Tearney, J. F. de Boer, N. Iftimia, and B. E. Bouma, "High-speed optical frequency-domain imaging," *Optics Express*, vol. 11, pp. 2953-2963, 2003.
- [12] N. A. Nassif, B. Cense, B. H. Park, M. C. Pierce, S. H. Yun, B. E. Bouma, G. J. Tearney, T. C. Chen, and J. F. de Boer, "In vivo high-resolution video-rate spectral-domain optical coherence tomography of the human retina and optic nerve," *Optics Express*, vol. 12, pp. 367-376, 2004.
- [13] R. A. Leitgeb, W. Drexler, A. Unterhuber, B. Hermann, T. Bajraszewski, T. Le, A. Stingl, and A. F. Fercher, "Ultrahigh resolution Fourier domain optical coherence tomography," *Optics Express*, vol. 12, pp. 2156-2165, 2004.
- [14] M. Wojtkowski, V. Srinivasan, J. G. Fujimoto, T. Ko, J. S. Schuman, A. Kowalczyk, and J. S. Duker, "Three-dimensional retinal imaging with high-speed ultrahigh-resolution optical coherence tomography," *Ophthalmology*, vol. 112, pp. 1734-46, 2005.
- [15] R. Huber, M. Wojtkowski, J. G. Fujimoto, J. Y. Jiang, and A. E. Cable, "Three-dimensional and C-mode OCT imaging with a compact, frequency swept laser source at 1300 nm," *Optics Express*, vol. 13, pp. 10523-10538, 2005.
- [16] M. A. Choma, K. Hsu, and J. A. Izatt, "Swept source optical coherence tomography using an all-fiber 1300-nm ring laser source," *J Biomed Opt*, vol. 10, pp. 44009, 2005.

- [17] R. Huber, M. Wojtkowski, and J. G. Fujimoto, "Fourier Domain Mode Locking (FDML): A new laser operating regime and applications for optical coherence tomography," *Optics Express*, vol. 14, pp. 3225-3237, 2006.
- [18] A. D. Aguirre, P. Hsiung, T. H. Ko, I. Hartl, and J. G. Fujimoto, "High-resolution optical coherence microscopy for high-speed, in vivo cellular imaging," *Opt Lett*, vol. 28, pp. 2064-6, 2003.
- [19] S. A. Boppart, B. E. Bouma, C. Pitris, G. J. Tearney, J. G. Fujimoto, and M. E. Brezinski, "Forward-imaging instruments for optical coherence tomography," *Optics Letters*, vol. 22, pp. 1618-20, 1997.
- [20] F. Helmchen, M. S. Fee, D. W. Tank, and W. Denk, "A miniature head-mounted two-photon microscope: High-resolution brain imaging in freely moving animals," *Neuron*, vol. 31, pp. 903-912, 2001.
- [21] E. J. Seibel and Q. Y. J. Smithwick, "Unique features of optical scanning, single fiber endoscopy," *Lasers in Surgery and Medicine*, vol. 30, pp. 177-183, 2002.
- [22] X. Liu, M. J. Cobb, Y. Chen, M. B. Kimmey, and X. Li, "Rapid-scanning forward-imaging miniature endoscope for real-time optical coherence tomography," *Opt Lett*, vol. 29, pp. 1763-5, 2004.
- [23] J. Sawinski and W. Denk, "Miniature random-access fiber scanner for in vivo multiphoton imaging," *Journal of Applied Physics*, vol. 102, pp. -, 2007.
- [24] A. L. Polglase, W. J. McLaren, S. A. Skinner, R. Kiesslich, M. F. Neurath, and P. M. Delaney, "A fluorescence confocal endomicroscope for in vivo microscopy of the upper- and the lower-GI tract," *Gastrointest Endosc*, vol. 62, pp. 686-95, 2005.
- [25] D. L. Dickensheets and G. S. Kino, "Silicon-micromachined scanning confocal optical microscope," *Journal of Microelectromechanical Systems*, vol. 7, pp. 38-47, 1998.
- [26] M. Sakashita, H. Inoue, H. Kashida, J. Tanaka, J. Y. Cho, H. Satodate, E. Hidaka, T. Yoshida, N. Fukami, Y. Tamegai, A. Shiokawa, and S. Kudo, "Virtual histology of colorectal lesions using laser-scanning confocal microscopy," *Endoscopy*, vol. 35, pp. 1033-8, 2003.
- [27] H. Miyajima, N. Asaoka, T. Isokawa, M. Ogata, Y. Aoki, M. Imai, O. Fujimori, M. Katashiro, and K. Matsumoto, "A MEMS electromagnetic optical scanner for a commercial confocal laser scanning microscope," *Journal of Microelectromechanical Systems*, vol. 12, pp. 243-251, 2003.
- [28] W. Piyawattanametha, P. R. Patterson, G. D. J. Su, H. Toshiyoshi, and M. C. Wu, "A MEMS non-interferometric differential confocal scanning optical microscope," presented at Proceedings of 11th International Conference on Solid State Sensors and Actuators Transducers '01/Eurosensors XV, 10-14 June 2001, Munich, Germany, 2001.
- [29] W. Piyawattanametha, R. P. Barretto, T. H. Ko, B. A. Flusberg, E. D. Cocker, H. Ra, D. Lee, O. Solgaard, and M. J. Schnitzer, "Fast-scanning two-photon fluorescence imaging based on a microelectromechanical systems two-dimensional scanning mirror," *Opt Lett*, vol. 31, pp. 2018-20, 2006.
- [30] J. T. Liu, M. J. Mandella, H. Ra, L. K. Wong, O. Solgaard, G. S. Kino, W. Piyawattanametha, C. H. Contag, and T. D. Wang, "Miniature near-infrared dual-axes confocal microscope utilizing a two-dimensional microelectromechanical systems scanner," *Opt Lett*, vol. 32, pp. 256-8, 2007.
- [31] Y. Pan, H. Xie, and G. K. Fedder, "Endoscopic optical coherence tomography based on a microelectromechanical mirror," *Optics Letters*, vol. 26, pp. 1966-8, 2001.
- [32] J. M. Zara, S. Yazdanfar, K. D. Rao, J. A. Izatt, and S. W. Smith, "Electrostatic micromachine scanning mirror for optical coherence tomography," *Opt Lett*, vol. 28, pp. 628-30, 2003.
- [33] A. Jain, A. Kopa, Y. T. Pan, G. K. Fedder, and H. K. Xie, "A two-axis electrothermal micromirror for endoscopic optical coherence tomography," *Ieee Journal of Selected Topics in Quantum Electronics*, vol. 10, pp. 636-642, 2004.
- [34] B. Qi, A. P. Himmer, L. M. Gordon, X. D. V. Yang, L. D. Dickensheets, and I. A. Vitkin, "Dynamic focus control in high-speed optical coherence tomography based on a microelectromechanical mirror," *Optics Communications*, vol. 232, pp. 123-128, 2004.

- [35] W. Piyawattanametha, L. Fan, S. Hsu, M. Fujino, M. C. Wu, P. R. Herz, A. D. Aguirre, Y. Chen, and J. G. Fujimoto, "Two-dimensional endoscopic MEMS scanner for high resolution optical coherence tomography," presented at Conference on Lasers and Electro-Optics (CLEO), San Francisco, CA, USA, 2004.
- [36] J. T. W. Yeow, V. X. D. Yang, A. Chahwan, M. L. Gordon, B. Qi, I. A. Vitkin, B. C. Wilson, and A. A. Goldenberg, "Micromachined 2-D scanner for 3-D optical coherence tomography," *Sensors and Actuators a-Physical*, vol. 117, pp. 331-340, 2005.
- [37] W. G. Jung, J. Zhang, L. Wang, P. Wilder-Smith, Z. P. Chen, D. T. McCormick, and N. C. Tien, "Three-dimensional optical coherence tomography employing a 2-axis microelectromechanical scanning mirror," *Ieee Journal of Selected Topics in Quantum Electronics*, vol. 11, pp. 806-810, 2005.
- [38] W. Jung, D. T. McCormick, J. Zhang, L. Wang, N. C. Tien, and Z. P. Chen, "Three-dimensional endoscopic optical coherence tomography by use of a two-axis microelectromechanical scanning mirror," *Applied Physics Letters*, vol. 88, pp. -, 2006.
- [39] P. R. Patterson, D. Hah, H. Nguyen, H. Toshiyoshi, R.-m. Chao, and M. C. Wu, "A scanning micromirror with angular comb drive actuation," presented at Technical Digest. MEMS 2002 IEEE International Conference. Fifteenth IEEE International Conference on Micro Electro Mechanical Systems, 20-24 Jan. 2002, Las Vegas, NV, USA, 2002.
- [40] S. Bourquin, A. D. Aguirre, I. Hartl, P. Hsiung, T. H. Ko, J. G. Fujimoto, T. A. Birks, W. J. Wadsworth, U. Bunting, and D. Kopf, "Ultrahigh resolution real time OCT imaging using a compact femtosecond Nd : Glass laser and nonlinear fiber," *Optics Express*, vol. 11, pp. 3290-3297, 2003.
- [41] R. Huber, D. C. Adler, and J. G. Fujimoto, "Buffered Fourier domain mode locking: unidirectional swept laser sources for optical coherence tomography imaging at 370,000 lines/s," *Optics Letters*, vol. 31, pp. 2975-2977, 2006.

## Chapter 9

# Depth-Resolved Imaging of Functional Activation in the Rat Cerebral Cortex Using Optical Coherence Tomography

### 9.1 Overview

The previous chapters demonstrated methods for high resolution OCT imaging of tissue architectural and cellular features, with particular focus on applications in the gastrointestinal tract. OCT is also advancing rapidly as a tool for basic science investigations, including small animal imaging. The noninvasive, high speed character of OCT enables longitudinal imaging *in vivo*, which opens a host of opportunities for study of structure and function in living organisms.

The present chapter expands upon this concept by describing an application of OCT imaging in the area of functional neuroimaging. Co-registered optical coherence tomography and video microscopy images of the rat somatosensory cortex were acquired simultaneously through a thinned skull during forepaw electrical stimulation. Fractional signal change measurements made by OCT revealed a functional signal timecourse that correlates with the well understood hemodynamic signal measurement made with video microscopy. These results demonstrate that OCT can provide high-resolution, cross-sectional images of functional neuro-vascular activation and may offer a new tool for basic neuroscience research in the important rat cerebral cortex model.

Dr. Yu Chen, Ms. Lana Ruvinskaya, Dr. Anna Devor, Prof. David Boas, and Prof. James G. Fujimoto were direct collaborators on this study. E. Hillman also provided helpful discussions. This research was supported by the Air Force Office of Scientific Research Medical Free Electron Laser Program FA9550-040-1-0046 and FA9550-040-1-0011, and the National Institutes of Health R01-EB00790, R01-EY011289-20, and R01-CA75289-09.

### 9.2 Introduction

Several distinct technologies have been used to noninvasively probe neuronal response to external stimuli. Among available methods, hemodynamic techniques, including positron emission tomography (PET), single-photon emission computed tomography (SPECT), and functional magnetic resonance imaging (fMRI), have proven useful for visualizing spatial localization of neural activity, but they have limited temporal resolution. In contrast, electrophysiological techniques, such as electroencephalography (EEG), can measure neural responses on the millisecond time scale, but with limited spatial resolution.

Optical methods can offer both high spatial and high temporal resolutions and are therefore particularly promising for making full-field measurements of hemodynamic, metabolic, and neuronal activity *in vivo*. Optical approaches can provide highly sensitive measures of neuronal and vascular responses to brain activation, both invasively [1], and noninvasively [2], and are currently being used extensively for study of the neuro-vascular relationship [3, 4].

Most optical methods used to date do not provide depth resolution of the functional response. To overcome this shortfall, multiphoton fluorescence microscopy has been used for functional neuronal imaging [5]. In addition, new methods such as laminar optical tomography are being developed [6]. Optical coherence tomography (OCT) is another promising method for high resolution, depth-resolved imaging in turbid tissues such as the cerebral cortex. OCT is a real-time imaging method which generates cross-sectional images of tissue architecture based solely on scattered light, without the need for exogenous dyes to enhance contrast [7]. Furthermore, OCT is very sensitive for the measurement of small scattered signals over several orders of magnitude in dynamic range and can potentially image with enhanced depth compared to multiphoton microscopy. Relatively few studies exist to date using OCT for measurement of functional activation in neuronal tissues. Maheswari et al. demonstrated depth resolved stimulus specific profiles of slow processes during functional activation in the cat visual cortex [8]. Lazebnik et al. recorded scattering changes corresponding to action potential propagation in the sea slug abdominal ganglion [9]. Other groups have explored low coherence interferometry methods for measurement of functional retinal activation [10-12] as well as nerve axon displacement [13, 14].

The rat somatosensory cortex is an important model system in neuroscience research and has been extensively studied using optical methods [3-5]. This chapter demonstrates OCT as a method for high-resolution, cross-sectional measurement of functional hemodynamic response to electrical stimulation in the rat cortex model. OCT data are correlated with simultaneously acquired video microscopy data to allow comparison of OCT results with the extensively studied intrinsic optical signal timecourse.

### **9.3 Methods**

Figure 9.1 shows a schematic of the combined OCT and video microscopy imaging system. The time-domain OCT engine consisted of a balanced interferometer configuration, a rapid linearly scanning reference delay line operating at 1140 Hz, and logarithmic demodulation. The image acquisition rate was set at 3 Hz, and each frame had 380 x 1000 pixels over 3 mm transverse by 2.8 mm depth dimensions. The light source was a Nd:Glass femtosecond laser centered at 1060 nm wavelength which was spectrally broadened in a standard single mode fiber (HI-1060) to generate an output bandwidth of 30 nm. The optical bandwidth was deliberately reduced compared with previous studies using this light source in order to provide a larger resolution voxel for enhanced integration of small signals [15]. The measured

axial resolution was  $\sim 18 \mu\text{m}$  in air, corresponding to  $\sim 13 \mu\text{m}$  in tissue. The OCT microscope included a collimating lens followed by a pair of galvanometer scanners to allow precise two-dimensional control of the OCT scan orientation. The scanned OCT beam was focused by a near-infrared achromat lens ( $f = 60 \text{ mm}$ ) and then redirected onto the specimen by a dichroic hot mirror which reflected the near-infrared light while passing visible light. The focal spot of the microscope had a  $1/e^2$  waist diameter of  $\sim 36 \mu\text{m}$ . The demodulated OCT signal was recorded to the computer via a 12-bit, 5 MHz analog to digital converter.

The video microscope system has been described previously [16]. For these studies, the Hg: Xenon lamp illumination was spectrally filtered to a narrow band at 570 nm, which is located at an isosbestic point for hemoglobin absorption. Therefore, cortical reflectivity at 570 nm provided a measurement of total hemoglobin, which is proportional to total blood volume if hematocrit is assumed constant. Reflected visible light from the cortex was collected with a camera lens and imaged onto a high sensitivity CCD, which was read by a second computer. The acquisition card on this computer drove the electrical stimulus generator and served as the master clock for the experiment by simultaneously acquiring relevant synchronization signals on a timebase locked to the stimulus drive. The signals acquired included the stimulus drive itself, a separate trial initiation pulse which denotes the beginning of a stimulus sequence, the CCD camera exposure, the OCT image frame synchronization, and a blood pressure trace used for monitoring animal physiology.

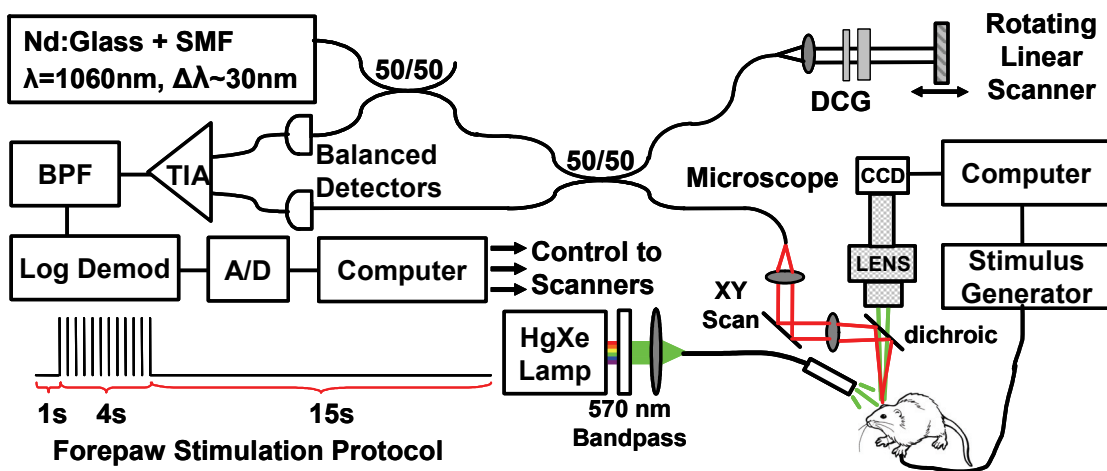


**Figure 9.1.** Schematic of combined optical coherence tomography (OCT) and video microscopy system. Dispersion compensating glass (DCG); Transimpedance amplifier (TIA); Bandpass filter (BPF). Also shown is the forepaw stimulation protocol used in the experiments.

All experiments were conducted according to protocols approved by the animal care committees at the Massachusetts Institute of Technology and the Massachusetts General Hospital. Rats were anesthetized with isoflurane and immobilized stereotactically before beginning the cranial preparation. An area of skull overlying the primary somatosensory cortex on the contralateral side of the stimulated forepaw was thinned with a dental burr until transparent. A barrier of petroleum jelly was built around the thinned skull and filled with mineral oil to reduce surface reflection from the skull. Forepaw stimulation was performed using 20 second stimulation blocks, as shown in the inset in figure 9.1. Each block consisted of a 1 second pre-stimulus period, followed by 4 seconds of stimulation with  $\sim 1.8$  mA pulses at 3 Hz. The stimulus amplitude was chosen to be just below the animal's twitch threshold as determined by palpation. A 15 second post-stimulus period was then used to allow full recovery to baseline. The stimulus block was repeated 60 times during data acquisition over a 20 min period. Prior to data processing, digitized OCT images were converted from log to linear. Block average OCT signals were then computed to reduce the effects of physiologic noise in the measurements.

#### 9.4 Results

Figure 9.2 illustrates the co-localization of the OCT scan to the region of functional activation, as measured by video microscopy. The functional signal was computed as a ratio of the cortical reflectance at each time point to the mean reflectance in the pre-stimulus period and is therefore representative of a percent signal change from baseline. Figure 9.2a presents the overlay of the functional signal taken at its peak amplitude on the structural image of the cortex. The precise OCT scan location is shown over the region of activation. The corresponding temporal trace for functional activation in the boxed region of figure 9.2a is shown in figure 9.2b. As expected, the cortical reflectance shows a drop of  $\sim 2-3\%$  corresponding to increased absorption from blood volume and total hemoglobin increase in the region of activation. The mean OCT structural image during the prestimulus period is shown in figure 9.2c. OCT enables precise measurement of skull thickness and the identification of cortical surface vessels and meningeal layers separating the skull from the underlying cortex. Figure 9.2d shows an image of the standard deviation of the OCT signal divided by the mean across the total block averaged data set. This form of display highlights the very low signal variation in the immobilized skull compared with the cortex and the smaller vessels located above the dura.

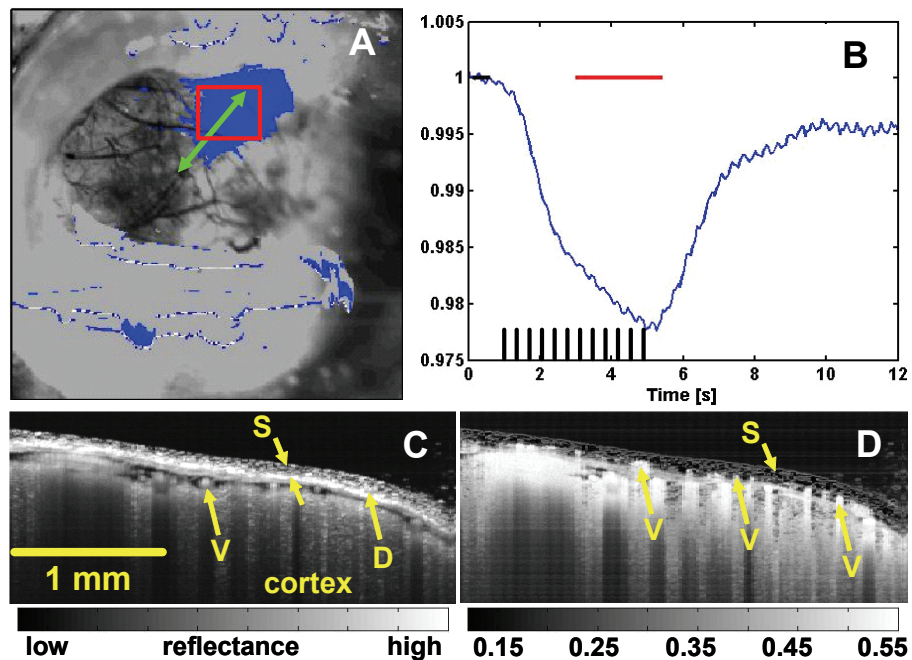


**Figure 9.2.** Precise co-registration of OCT imaging to the region of functional activation. The OCT scan is directed across the region of interest as measured with video microscopy (A,B). Horizontal bars in (B) mark the activated and baseline time windows used to generate the functional map overlaid on the structural view in (A). Structural OCT imaging (C) reveals high resolution visualization of the skull (S), surface vasculature (V), and meningeal layers, including the dura mater (D). Percent variation maps extracted from the multiple trial data set reveal smaller vessels located above the dura, while also highlighting the low signal fluctuation in the immobilized skull compared to the cortex.

The OCT functional response measurements are presented in figure 9.3. As with the video microscopy data, a fractional change map was computed by normalizing all time points to the baseline prestimulus period. The functional image taken at the peak of maximal activation is shown in figure 9.3a. Both positive and negative signal changes are present. Warm colors at the red and yellow end of the colormap represent positive signal changes, while cool colors at the blue end represent negative changes. The temporal sequence of images during activation reveals the persistence of highly localized, distinct “hot spots” of activation in the cortex. Figure 9.3b shows a magnified view of the temporal sequence for the corresponding boxed region in figure 9.3a. Time point zero represents the baseline. At four and six seconds, bright areas of signal increase emerge and subsequently return to baseline after eight and ten seconds. Note that there is some baseline drift due to physiological noise. Figure 9.3c shows a second magnified region of the functional OCT image. The colormap has been switched to gray scale, with positive signal change in black, to allow clear color coded delineations of regions of interest. The corresponding temporal sequences of activation for the boxed regions in 9.3c are provided in figure 9.3d.

The OCT functional signal timecourses reveal clear increases and decreases that deviate from baseline, reach a peak near the cessation of the stimulus, and then gradually return to baseline.

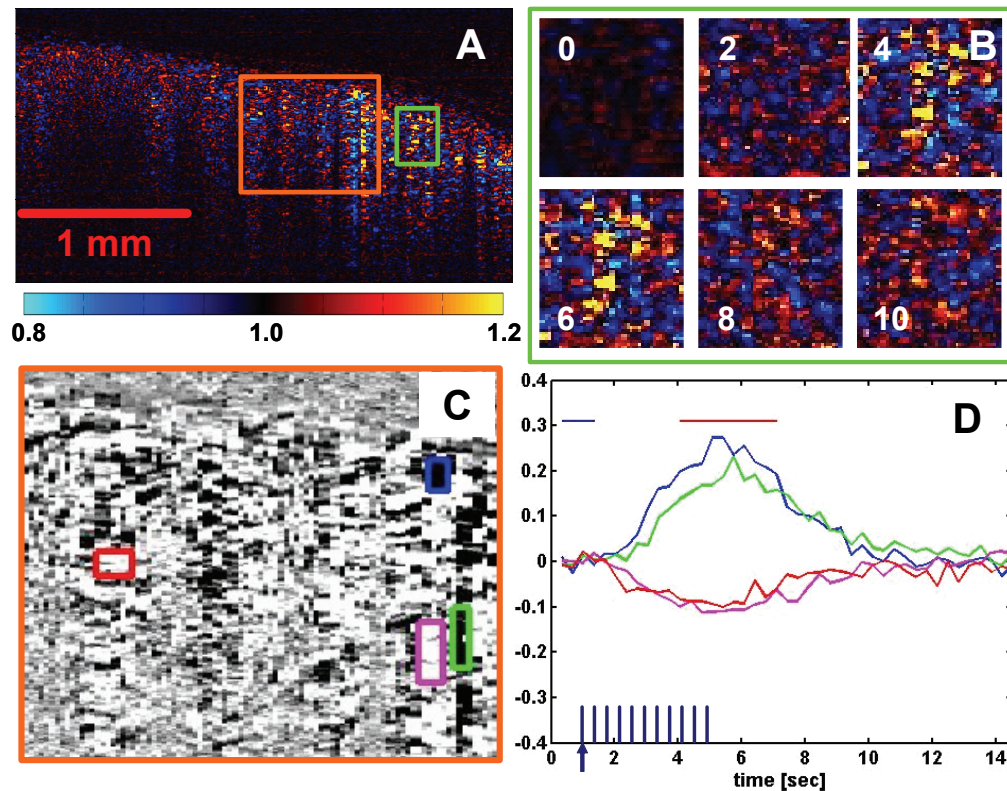


**Figure 9.3.** Functional OCT measurements in the rat cortex. A fractional change map (A) demonstrates the presence of positive (warm colors) and negative (cool colors) changes in OCT signals during stimulation. Temporal sequences (B) reveal the presence of highly localized regions of activation in the cortex that persist throughout stimulation. Further analysis of the localized regions of interest (C,D) shows a functional OCT timecourse that correlates well with that of the intrinsic hemodynamic optical signal but with both positive and negative going responses. The horizontal bars in (D) indicate the time windows of interest used to generate the functional map (A, B, C).

## 9.5 Discussion

Understanding the exact etiology and timecourse of the OCT functional signal will require additional investigation. The results presented here have been validated in more than 10 animals to date, and in each case, a robust and highly localized OCT response is seen corresponding with the hemodynamic response measured by video microscopy. Moreover, the timecourse and spatial localization of the OCT responses track those measured by video microscopy. The response is absent outside of the region of hemodynamic activation and is absent when the ipsilateral forepaw is stimulated. Furthermore, the blood pressure traces reveal no signs of vagal response, which could suggest shock-induced motion artefact. The presence of positive and negative going OCT signals and the relatively speckled appearance of the response under

differential signal analysis implicate swelling mechanisms as an important contributor. Furthermore, the presence of highly localized regions of activation in the cortex suggests that localized swelling or vascular dilation, rather than simply bulk brain swelling, is contributing. Finally, the possibility exists for localized scattering increases and decreases that reflect local changes in linear red cell density, an observation that would have some support in previous literature [5]. Additional work will focus on careful characterization of the response, including the use of techniques such as three-dimensional and Doppler OCT. With further study, this technique has potential to become a new tool for basic and applied neuroscience research in animal models.

## 9.6 References

- [1] H. S. Orbach, L. B. Cohen, and A. Grinvald, "Optical mapping of electrical activity in rat somatosensory and visual cortex," *J Neurosci*, vol. 5, pp. 1886-95, 1985.
- [2] A. Villringer and B. Chance, "Non-invasive optical spectroscopy and imaging of human brain function," *Trends Neurosci*, vol. 20, pp. 435-42, 1997.
- [3] A. Devor, A. K. Dunn, M. L. Andermann, I. Ulbert, D. A. Boas, and A. M. Dale, "Coupling of total hemoglobin concentration, oxygenation, and neural activity in rat somatosensory cortex," *Neuron*, vol. 39, pp. 353-9, 2003.
- [4] S. A. Sheth, M. Nemoto, M. Guiou, M. Walker, N. Pouratian, and A. W. Toga, "Linear and nonlinear relationships between neuronal activity, oxygen metabolism, and hemodynamic responses," *Neuron*, vol. 42, pp. 347-55, 2004.
- [5] D. Kleinfeld, P. P. Mitra, F. Helmchen, and W. Denk, "Fluctuations and stimulus-induced changes in blood flow observed in individual capillaries in layers 2 through 4 of rat neocortex," *Proc Natl Acad Sci U S A*, vol. 95, pp. 15741-6, 1998.
- [6] E. M. Hillman, D. A. Boas, A. M. Dale, and A. K. Dunn, "Laminar optical tomography: demonstration of millimeter-scale depth-resolved imaging in turbid media," *Opt Lett*, vol. 29, pp. 1650-2, 2004.
- [7] D. Huang, E. A. Swanson, C. P. Lin, J. S. Schuman, W. G. Stinson, W. Chang, M. R. Hee, T. Flotte, K. Gregory, C. A. Puliafito, and et al., "Optical coherence tomography," *Science*, vol. 254, pp. 1178-81, 1991.
- [8] R. U. Maheswari, H. Takaoka, H. Kadono, R. Homma, and M. Tanifuji, "Novel functional imaging technique from brain surface with optical coherence tomography enabling visualization of depth resolved functional structure in vivo," *J Neurosci Methods*, vol. 124, pp. 83-92, 2003.
- [9] M. Lazebnik, D. L. Marks, K. Potgieter, R. Gillette, and S. A. Boppart, "Functional optical coherence tomography for detecting neural activity through scattering changes," *Opt Lett*, vol. 28, pp. 1218-20, 2003.
- [10] X. C. Yao, A. Yamauchi, B. Perry, and J. S. George, "Rapid optical coherence tomography and recording functional scattering changes from activated frog retina," *Appl Opt*, vol. 44, pp. 2019-23, 2005.
- [11] K. Bizheva, R. Pflug, B. Hermann, B. Povazay, H. Sattmann, P. Qiu, E. Anger, H. Reitsamer, S. Popov, J. R. Taylor, A. Unterhuber, P. Ahnelt, and W. Drexler, "Optophysiology: depth-resolved probing of retinal physiology with functional ultrahigh-resolution optical coherence tomography," *Proc Natl Acad Sci U S A*, vol. 103, pp. 5066-71, 2006.
- [12] V. J. Srinivasan, M. Wojtkowski, J. G. Fujimoto, and J. S. Duker, "In vivo measurement of retinal physiology with high-speed ultrahigh-resolution optical coherence tomography," *Opt Lett*, vol. 31, pp. 2308-10, 2006.
- [13] C. Fang-Yen, M. C. Chu, H. S. Seung, R. R. Dasari, and M. S. Feld, "Noncontact measurement of nerve displacement during action potential with a dual-beam low-coherence interferometer," *Optics Letters*, vol. 29, pp. 2028-2030, 2004.
- [14] T. Akkin, D. P. Dave, T. E. Milner, and H. G. Rylander, "Detection of neural activity using phase-sensitive optical low-coherence reflectometry," *Optics Express*, vol. 12, pp. 2377-2386, 2004.
- [15] S. Bourquin, A. D. Aguirre, I. Hartl, P. Hsiung, T. H. Ko, J. G. Fujimoto, T. A. Birks, W. J. Wadsworth, U. Bunting, and D. Kopf, "Ultrahigh resolution real time OCT imaging using a compact femtosecond Nd : Glass laser and nonlinear fiber," *Optics Express*, vol. 11, pp. 3290-3297, 2003.
- [16] A. K. Dunn, A. Devor, H. Bolay, M. L. Andermann, M. A. Moskowitz, A. M. Dale, and D. A. Boas, "Simultaneous imaging of total cerebral hemoglobin concentration, oxygenation, and blood flow during functional activation," *Opt Lett*, vol. 28, pp. 28-30, 2003.

## Chapter 10

### Summary and Conclusions

#### 10.1 Summary of Work

The majority of this thesis explores the importance of resolution improvement for endoscopic applications of optical coherence tomography. Inspiration for this work was provided by the parallel development over the last 10 – 15 years of optical coherence tomography and confocal microscopy as techniques for high resolution reflectance imaging of tissue microstructure. Optical coherence tomography provides depth resolved cross-sectional images of tissue architecture and can be performed through flexible fiber-optic catheter devices, making it readily available for investigations in clinical endoscopy. The inability to visualize cellular features in human tissues with conventional OCT, however, has limited its effectiveness in applications such as imaging of early cancer, which is characterized fundamentally by cellular abnormalities. Reflectance confocal microscopy, on the other hand, has shown tremendous promise for cellular resolution imaging *in vivo*, but has been limited to applications such as dermatology that can be performed using large benchtop microscopes. The promise of combining the endoscopic advantages of optical coherence tomography and the cellular resolution capability of confocal microscopy was a fundamental motivation for this thesis.

The investigations for this thesis included a combination of *in vivo* clinical studies, technological development, and *ex vivo* biological imaging experiments. Extensive studies were conducted using ultrahigh resolution endoscopic OCT for the clinical evaluation of patients with Barrett's esophagus. These studies demonstrated unprecedented resolution and imaging quality for endoscopic OCT and established the feasibility of using advanced femtosecond laser technology for clinical investigations in endoscopy. In addition, the studies inspired new ideas for other applications of ultrahigh resolution OCT in gastrointestinal endoscopy. These include monitoring of therapeutic interventions, assessment of margins during endoscopic mucosal resection, and surveillance in the setting of polyposis syndromes of the upper or lower gastrointestinal tracts. The experiments with ultrahigh resolution endoscopic OCT also highlighted the limitations of the technology, however. Despite axial resolutions of  $< 4 \mu\text{m}$  in tissue, cellular features were not visible. Moreover, the Cr:Forsterite femtosecond laser system proved too unreliable for more general application by personnel untrained in optics.

To address the limitations posed by the clinical endoscopic studies and to enable the next generation of clinical investigations, several new technologies were developed in this thesis. New light sources for ultrahigh resolution OCT were developed based on commercially-available femtosecond lasers and the phenomenon of supercontinuum generation in highly nonlinear optical fibers. A compact, portable, and highly reliable Nd:Glass oscillator was shown to enable ultrahigh resolution imaging throughout the near-infrared wavelength band by precisely controlling the continuum generation with specific optical fibers. Spectrum broadening by self-phase modulation in fibers with strong normal dispersion proved particularly useful for OCT imaging. Ultrahigh resolution OCT with  $< 3$   $\mu\text{m}$  axial resolution in tissue was achieved at 1060 nm using this mechanism. The light source had  $> 100$  mW output power and was suitable for reliable use in the clinical environment. Furthermore, the light source is commercially available and presents a user-friendly option for research groups interested in ultrahigh resolution OCT.

Optical coherence microscopy was developed for cellular resolution imaging. OCM combines OCT and confocal microscopy, and generates images in the *en face* plane rather than the cross-sectional plane of conventional OCT. OCM imaging parameters were investigated to understand the advantages of the combined technique over confocal microscopy alone. Through the use of ultrahigh coherence axial resolutions provided by broadband femtosecond laser sources, OCM was shown to enable cellular resolution imaging with lower numerical aperture than confocal microscopy. Fundamentally, this realization facilitates the development of small diameter endoscopic probes, since the method no longer depends upon a large numerical aperture to provide depth resolution.

OCM imaging systems for high speed *in vivo* imaging were demonstrated. Two important technical challenges were overcome. First, high speed phase modulation schemes were implemented for use with broadband femtosecond laser sources. A modulator based upon the Fourier domain rapid scanning optical delay line (RSOD) was demonstrated for use at 800 nm, and an electro-optic phase modulator was used at 1060 nm. The electro-optic modulator (EOM) was shown to have several advantages and was further developed for clinical imaging experiments. Use of the EOM required careful dispersion management and development of a novel photonic solution to manage the polarization dependence of the modulator. Second, techniques for alignment of the optical coherence and confocal gates were studied. A novel autofocusing scheme was demonstrated to ensure optimal image quality in scattering tissue. The optimized OCM system was integrated into a portable unit compatible with clinical investigations outside of the laboratory. Cellular resolution OCM imaging of human skin was demonstrated with  $< 2$   $\mu\text{m}$  transverse resolution and  $< 4$   $\mu\text{m}$  axial resolution in tissue at frame rates of 5 – 8 Hz. Studies conducted in this thesis represent essentially the first demonstrations of real time *in vivo* cellular imaging in human tissues using optical coherence microscopy and will pave the way for future clinical applications of the method.

Extensive *ex vivo* imaging studies of gastrointestinal tissues were conducted using an integrated ultrahigh resolution OCT and OCM imaging system. The studies were designed to assess the feasibility of three-dimensional OCT and OCM cellular imaging for future applications in endoscopy. Normal and relevant pathology specimens from the upper and lower GI tracts were imaged and compared with corresponding histology. OCM imaged with high resolution features that were not visible with ultrahigh resolution OCT, including individual cells and cell nuclei and distinct features of glandular epithelium and extracellular stroma in normal, dysplastic, and cancerous tissues from the esophagus and colon. Results suggest that cellular resolution fundamentally improves the ability of OCT to identify early pathologic changes in human gastrointestinal tissues. The studies also highlighted the complementary nature of OCT and OCM. OCM can image cellular features *en face* with high resolution, while OCT provides a cross-sectional view of tissue architecture over a larger field of view. Furthermore, three-dimensional OCT data sets can be processed in novel ways to provide additional important information about tissue architecture not appreciated in the cross-sectional view. Projection-based methods for *en face* visualization were explored and shown to generate high quality views comparable to those of magnification endoscopy.

To enable future endoscopic imaging studies, novel catheter designs capable of three-dimensional and *en face* OCT imaging were developed based upon MEMS micromirror technology. High performance mirrors based on angled vertical comb (AVC) actuators were integrated into a flexible catheter with 5 mm outer diameter. High quality ultrahigh resolution cross-sectional, three-dimensional, and *en face* OCT were demonstrated with the device.

Finally, a new application of OCT outside of endoscopy was explored in this thesis. OCT was demonstrated for depth-resolved imaging of functional neuronal activation in the important rat somatosensory cortex model. This work highlights the ability of OCT to provide quantitative information about tissue functional state as well as structural morphology. It also suggests that OCT can provide a new tool for further investigations in basic and applied neuroscience.

## **10.2 Future Studies**

The ability to image with cellular resolution promises to significantly improve current endoscopic OCT methods. Work in this thesis has fundamentally enabled high speed optical coherence microscopy for *in vivo* imaging and has made progress on catheter devices for endoscopic imaging. Similarly, development of high speed Fourier-domain OCT methods by other investigators has enabled real-time volumetric OCT imaging. Successful implementation of these methods for clinical endoscopy will require further work on catheter and endoscope device technology. MEMS mirror technology as well as piezo-electric fiber scanners should enable fast *en face* imaging using resonant scanning at line rates of

several kHz. For cellular imaging, catheter designs compatible with high numerical aperture focusing must be implemented. These devices must also allow for tissue stabilization and focal depth translation. In addition, packaging must be made watertight and must be compatible with safety requirements for *in vivo* applications. Previous work with endoscopic OCT benefited from the relative simplicity of the catheter devices. It is clear that extension of cross-sectional OCT to *en face* and three-dimensional imaging poses a greater engineering challenge. This is an active area of research, however, and it is fully expected that reliable catheter device technology for three-dimensional OCT and cellular resolution OCM will become available in the near future.

New technological developments in optical coherence microscopy will surely follow this work. Although OCM has inherent similarities to both OCT and confocal microscopy, there are certainly subtleties to the method that make it a distinct technology. The method will benefit from further efforts to understand system design parameters. Studies on the optimization of resolution deep in scattering tissues will be essential to reaching the full potential of OCM to improve upon confocal microscopy. In addition, implementation of techniques from OCT, such as polarization diversity detection and speckle reduction strategies, promise to improve OCM image quality. It is also important to explore new approaches to OCM. This thesis work focused on time domain, point-scanning OCM, but cellular resolution optical coherence imaging has also been demonstrated with non-scanning full-field OCM [1, 2], line scanning OCM [3], and Fourier domain OCM [4, 5]. Full-field and line-scan OCM simplify the scanning requirements for catheter devices, and may therefore find applicability in endoscopy [6]. These OCM approaches have distinct differences in their mechanisms of image generation, and comparative studies between OCM techniques would be warranted to understand the relative advantages and disadvantages of the techniques for imaging in scattering tissues.

Additional clinical *ex vivo* tissue imaging studies will be important to further optimize OCT and OCM and to motivate future *in vivo* studies. This thesis has explored ultrahigh resolution and three-dimensional OCT and cellular resolution OCM for imaging in the gastrointestinal tract through a broad survey of relevant tissues, using qualitative comparison with histology as the metric of success. Further studies in this area should focus upon careful statistical assessment of diagnostic accuracy for the detection of dysplasia and cancer. These studies are necessarily more complex than the imaging experiments performed for this thesis. They require expanded participation by clinician investigators in data analysis and interpretation and prospective study designs which incorporate blinded interpretation of images. As OCT technology becomes more mature, such expanded collaborative efforts are rightfully becoming the standard for OCT imaging studies.

The complementary nature of OCT and OCM revealed in this thesis through *ex vivo* imaging studies warrants further consideration of combined clinical endoscopic OCT and OCM imaging approaches.

Combination of cellular resolution OCM with high speed Fourier-domain OCT could enable sequential wide-area imaging and cellular resolution imaging. One can envision the use of optical coherence imaging in a manner similar to the way a pathologist uses a light microscope. Pathologists use a combination of gross assessment followed by histologic analysis at varying magnifications to interpret a pathologic lesion. At each magnification scale, there are features that stand out prominently, while other features are obscured by the size scale. In the endoscopy clinic, the white light endoscopic view provides the equivalent of gross specimen assessment. High speed OCT in turn can provide two and three dimensional visualization at the 2 – 4 X magnification level over a field of view spanning several millimeters to centimeters. Finally, OCM offers cellular resolution imaging at 20 – 40X magnification. For optimum performance, it would be desirable to have an OCT/OCM instrument which can transition seamlessly between resolutions. In endoscopy, this once again necessitates advanced two-axis scanning catheter endoscope designs, which are capable of varying magnification as well as varying the size of the scan field. Moreover, integrated imaging engines compatible with both OCT and OCM would be desirable for simplification of overall system design.

Further investigations of ultrahigh resolution and three-dimensional OCT and cellular resolution OCM in other organ systems besides the gastrointestinal tract are also warranted. OCM and 3D OCT would likely provide significant improvement over standard cross-sectional OCT for endoscopic imaging of pathologies in the bladder [7-9] and cervix [10], for example. Moreover, ultrahigh resolution and cellular imaging may have a role in tumor margin or lymph node assessment during laparoscopic or open-field surgery for cancers of the prostate [11, 12] or breast [13, 14]. The capability of OCM to image with much lower numerical aperture compared to confocal microscopy also encourages the development of needle-based cellular imaging techniques for imaging soft tissue and solid organs [15]. *Ex vivo* survey imaging studies similar to the one performed for this thesis will be important to establish the feasibility for OCM and 3D OCT in these and other applications.

In the area of functional neuroimaging, OCT has tremendous promise for future studies. Additional experiments and analysis are necessary to fully understand the etiology of the neurovascular response observed with OCT. In addition, the high speed capability of OCT makes it attractive as a method for studying the fast neuronal response. The ability to measure the fast response in the intact cortex with an optical method would be a major advance. Furthermore, these are just the initial studies to establish the method. OCT could be applied for a host of studies in basic and applied neuroscience. These include studies in the rat cortex to understand the neurovascular coupling, imaging in models of stroke, and investigations of cortical plasticity.

### 10.3 Conclusions

The development of methods for ultrahigh resolution optical coherence tomography and cellular-resolution optical coherence microscopy represent important advances toward realization of “optical biopsy” and promise to significantly improve the ability for endoscopic detection of dysplasia and cancer in the gastrointestinal tract compared to conventional endoscopic OCT techniques. Important technical advances for ultrahigh resolution OCT and OCM were achieved in this thesis including development of compact broadband laser sources, novel high speed microscopy systems, and MEMS catheter probe technology to enable endoscopy. *In vivo* ultrahigh resolution endoscopic OCT studies demonstrated significant improvement in image quality compared to conventional endoscopic OCT. *Ex vivo* clinical OCM imaging studies subsequently established the feasibility of high resolution optical coherence cellular imaging in human gastrointestinal tissues without the need for tissue staining. Furthermore, combined OCT and OCM imaging was demonstrated for sequential wide-field, cross-sectional and high magnification *en face* imaging. Combined with recent developments in high speed, three-dimensional Fourier domain OCT by other investigators, the work in this thesis generates exciting opportunities for OCT imaging in endoscopy and in several other clinical scenarios where high resolution views of tissue microstructure from the architectural to the cellular level are required.

As described in the introduction to this thesis, advances in OCT have occurred in the setting of a larger revolution in optical imaging in the past two decades that has led to a number of new methods including fluorescence techniques, molecular imaging, and multiphoton microscopy. The success or failure of OCT in endoscopy, as well as in other clinical applications, is closely tied to improvements in these other optical methods as well as continued advances in OCT technology. Moreover, research on non-image based molecular diagnostic assays and cytology techniques also target an overlapping set of applications with OCT research in the area of cancer diagnostics. Future progress in OCT will require ongoing assessment of the strengths and weaknesses of the technology compared to competing methods as well as continued efforts to understand the niche applications where optical diagnostics can provide valuable information to the clinician.

Despite the numerous challenges of translational biomedical research, OCT imaging in 2008 remains an exciting and dynamic field with outstanding opportunities for young investigators. Technology development continues to proceed in parallel with exploration of key clinical and scientific applications of OCT and with commercialization of imaging systems for widespread availability. At the time of publication of this thesis, there exist dozens of academic research groups around the world focusing on optical coherence tomography. The first commercial OCT system for clinical ophthalmology became available in 1996, and OCT is now rapidly becoming a standard of care for retinal imaging. Efforts to develop OCT for other clinical applications, including cardiovascular and gastrointestinal imaging, are

also progressing, and there currently exist more than 17 companies working toward the development of commercial OCT systems for a range of applications. The impact of OCT will undoubtedly multiply in years to come. It is the challenge of the OCT research community to continue to push the limits of technology while simultaneously identifying and capitalizing on the most promising opportunities to improve human health.

## 10.4 References

- [1] A. Dubois, K. Grieve, G. Moneron, R. Lecaque, L. Vabre, and C. Boccara, "Ultrahigh-resolution full-field optical coherence tomography," *Appl Opt*, vol. 43, pp. 2874-83, 2004.
- [2] A. Dubois, L. Vabre, A. C. Boccara, and E. Beaurepaire, "High-resolution full-field optical coherence tomography with a Linnik microscope," *Appl Opt*, vol. 41, pp. 805-12, 2002.
- [3] Y. Chen, S. W. Huang, A. D. Aguirre, and J. G. Fujimoto, "High-resolution line-scanning optical coherence microscopy," *Opt Lett*, vol. 32, pp. 1971-3, 2007.
- [4] C. Xu, C. Vinegoni, T. S. Ralston, W. Luo, W. Tan, and S. A. Boppart, "Spectroscopic spectral-domain optical coherence microscopy," *Opt Lett*, vol. 31, pp. 1079-81, 2006.
- [5] S. W. Huang, A. D. Aguirre, R. A. Huber, D. C. Adler, and J. G. Fujimoto, "Swept source optical coherence microscopy using a Fourier domain mode-locked laser," *Optics Express*, vol. 15, pp. 6210-6217, 2007.
- [6] W. Y. Oh, B. E. Bouma, N. Iftimia, R. Yelin, and G. J. Tearney, "Spectrally-modulated full-field optical coherence microscopy for ultrahigh-resolution endoscopic imaging," *Optics Express*, vol. 14, pp. 8675-8684, 2006.
- [7] C. A. Jesser, S. A. Boppart, C. Pitris, D. L. Stamper, G. P. Nielsen, M. E. Brezinski, and J. G. Fujimoto, "High resolution imaging of transitional cell carcinoma with optical coherence tomography: feasibility for the evaluation of bladder pathology," *Br J Radiol*, vol. 72, pp. 1170-6, 1999.
- [8] E. V. Zagaynova, O. S. Streltsova, N. D. Gladkova, L. B. Snopova, G. V. Gelikonov, F. I. Feldchtein, and A. N. Morozov, "In vivo optical coherence tomography feasibility for bladder disease," *J Urol*, vol. 167, pp. 1492-6, 2002.
- [9] Y. Pan, J. P. Lavelle, S. I. Bastacky, S. Meyers, G. Pirskhalaishvili, M. L. Zeidel, and D. L. Farkas, "Detection of tumorigenesis in rat bladders with optical coherence tomography," *Med Phys*, vol. 28, pp. 2432-40, 2001.
- [10] C. Pitris, A. Goodman, S. A. Boppart, J. J. Libus, J. G. Fujimoto, and M. E. Brezinski, "High-resolution imaging of gynecologic neoplasms using optical coherence tomography," *Obstet Gynecol*, vol. 93, pp. 135-9, 1999.
- [11] G. J. Tearney, M. E. Brezinski, J. F. Southern, B. E. Bouma, S. A. Boppart, and J. G. Fujimoto, "Optical biopsy in human urologic tissue using optical coherence tomography," *J Urol*, vol. 157, pp. 1915-9, 1997.
- [12] A. V. D'Amico, M. Weinstein, X. Li, J. P. Richie, and J. Fujimoto, "Optical coherence tomography as a method for identifying benign and malignant microscopic structures in the prostate gland," *Urology*, vol. 55, pp. 783-7, 2000.
- [13] S. A. Boppart, W. Luo, D. L. Marks, and K. W. Singletary, "Optical coherence tomography: feasibility for basic research and image-guided surgery of breast cancer," *Breast Cancer Res Treat*, vol. 84, pp. 85-97, 2004.
- [14] P. L. Hsiung, D. R. Phatak, Y. Chen, A. D. Aguirre, J. G. Fujimoto, and J. L. Connolly, "Benign and malignant lesions in the human breast depicted with ultrahigh resolution and three-dimensional optical coherence tomography," *Radiology*, vol. 244, pp. 865-74, 2007.
- [15] X. Li, C. Chudoba, T. Ko, C. Pitris, and J. G. Fujimoto, "Imaging needle for optical coherence tomography," *Optics Letters*, vol. 25, pp. 1520-2, 2000.